The Dissertation Committee for Jae Gu Yoo
certifies that this is the approved version of the following dissertation:

Actuator Performance Envelope Through Nonlinear Test Bed

Committee:

Delbert Tesar, Supervisor

Benito Fernandez

S.V. Sreenivasan

Chetan Kapoor

J. Wesley Barnes

Ben Mooring

Actuator Performance Envelope Through Nonlinear Test Bed

by

Jae Gu Yoo, B.S., M.S.

DISSERTATION
Presented to the Faculty of the Graduate School of
The University of Texas at Austin
in Partial Fulfillment
of the Requirements
for the Degree of

DOCTOR OF PHILOSOPHY

THE UNIVERSITY OF TEXAS AT AUSTIN
December 2004

With my deepest love and respect, I dedicate this work to my parents, Chowoong Yoo and Okjoo Oh. I also dedicate this work to my beautiful wife, Eunjoo and my lovely sweet daughter, Gina.

Acknowledgments

I am very grateful to my supervisor, Prof. Delbert Tesar, for his continuous guidance and support throughout my graduate studies. He always encouraged me to accomplish my work to be an outstanding job and gave me the motivation to build the nonlinear test bed with a full support. Thanks to his deepest concerns and advices, I could have finished a successful research topic.

Also, I would like to thank Dr. Chetan Kapoor and Dr. Mitch Pryor of the Robotics Research Group for our discussions that have been very useful throughout this work. I thank many of the colleagues in the Robotics Research Group in the University of Texas at Austin for having their time with me to discuss a various of engineering topics.

I would like to express my deep gratitude to Prof. Melba Crawford of the Operational Research and Information Department at The University of Texas at Austin for many enlightening and inspiring discussions about statistical methods.

Finally, this work was supported by U.S. Department of Energy grant number DE-FG04-94EW37966. Equipment was graciously donated by National Instruments of Austin, TX. Their support is greatly appreciated.

Actuator Performance Envelope Through Nonlinear Test Bed

Publication No. ____________________

Jae Gu Yoo, Ph.D.
The University of Texas at Austin, 2004

Supervisor: Delbert Tesar

With the increased importance of actuator performance in robotic applications, many robot manufacturers have focused on assuring quality, reliability, conformance to design, and application suitability in their actuators. Performance metrics for actuator evaluation have been proposed to improve understanding of an actuator's nonlinear characteristics. Thorough actuator testing can provide necessary feedback information on the effectiveness of the robot actuator for a specific task. This report describes the development and use of performance maps and performance envelopes for electromechanical actuators using an advanced dynamic dynamometer test bed. Initial test data in the form of performance maps is created for a range of rated output power and dynamic loading for brushless DC motors.

The core contributions of this research are the creation and manipulation of actuator performance maps and envelopes, and the design and development of a nonlinear test bed for electromechanical actuators. To create a performance map, specific criteria must be developed to describe the performance characteristics of an actuator. The **performance criteria** are formulated to define, anticipate,

and evaluate the performance responses of the system and can provide metrics for measuring and controlling actuator performance and help identify nonlinear components in actuator modeling. These criteria form the basis for **performance maps**, which is basically a data representation of the criteria over a range of input and output conditions. A representative set of ten actuator performance maps are suggested based on several independent control parameters such as current and voltage, and output conditions such as torque and speed. After completing the development and analysis of these ten performance maps, the process for building unique performance envelopes is described. **Performance envelopes** are created from performance maps and are defined as the combined optimum surface in the full set of maps, which satisfy a combination of criteria in each operational region. Performance envelopes can safely increase the number of control surfaces without violating actuator constraints. This provides more choices in an operational range as compared to statically developed torque-speed curves.

For the creation of these performance maps, five test regimes are suggested such as dynamic loading, static loading, transient response, torque ripple and statically changing temperature tests. Test regimes are evaluated under two types of loads: a static loading and a sinusoidal loading. For these test protocols, a Nonlinear Test Bed for Actuators (NTBA) has been designed and built to measure and record an array of physical performance properties. The test bed is specifically designed with the capability to emulate high bandwidth complex duty cycle loads. It is comprised of a 7.2 kW servo motor (which serves as a dynamic load emulator), a 26 Nm hysteresis brake, an electromechanical clutch, full sensor array (includes current, temperature, torque, magnetic flux density sensors) for comprehensive monitoring of test variables, and supporting motion control hardware to operate the test bed.

Ten performance maps (i.e., operational margin, efficiency, power losses, rise time, torque-current, torque ripple, acceleration, max magnetic flux energy, magnetic flux density, and temperature) for a commercial brushless DC motor are developed in 3D surface displays using the test bed. The performance maps collected from repeated tests (more than 20 times for each test protocol) of the test motor provide an insight into the complexity of the electromechanical response and also provide metrics for measuring motor current states during operation. Standard deviation and average values are also calculated and used to develop the upper and lower error bounds of the magnetic flux energy performance map. In addition, the Box-Jenkins ARIMA method is used to analyze all of the test data and build a mathematical representation of sensor derived data with respect to time. This stochastic ARIMA equation is used to create each data point in a performance map. The performance map plots are normalized by using the maximum values over the range of motor operation. One performance envelope plot with respect to torque and speed is illustrated in this research.

Finally, the performance data plots used in the trade literature and research papers are compared with the test result plots presented as actuator performance maps. The performance plots in the literature have several drawbacks for users, which are the lack of operational values in abnormal operating conditions and the lack of reference plots to fully describe and enable the management of the performance of the motor considering all of the operational conditions. On the other hand, the maps obtained in the experiments using the NTBA provide enough metric values to manage the actuator to achieve optimum performance for a multitude of desired operating conditions (maximum efficiency, soft start, low noise, maximum life, etc.).

Table of Contents

Chapter 3. Actuator Criteria Development 44

Chapter 4. Nonlinear Test Bed Development 67

Chapter 5. Test Regime and Stochastic Processes 101

Chapter 6. Development of Performance Maps and Performance Envelopes 137

List of Tables

List of Figures

Chapter 1

Introduction

To improve the overall performance of actuator systems, most researchers concentrate on finding or developing control algorithms with improved attributes including: stability, robustness, disturbance rejection, etc [17], [107]. The belief is that control techniques could reject most nonlinear disturbances, enhance transient responses, and determine the best output performance for the system. However, traditional control theories do not tell us the system response when operating under extreme or abnormal conditions. For example, when an actuator runs at high speed with a temperature greater than $200°C$, control techniques do not predict whether or not the output torque will deteriorate at a certain time. Furthermore, traditional control methods do not determine how fast the rotor accelerates when the actuator is subjected to a very high current surge for a brief interval.

Up until now, most control theories have required comprehensive physical modeling to convey mathematical meaning. However, it is difficult to represent the system completely, and to model even simple mechanical and electrical systems with particular parameters. This is primarily due to the nonlinear properties of these physical systems. The nonlinear properties include Coulomb friction, saturation, dead-zone, backlash, hysteresis, quantization error, etc. Modeling electromechanical systems including these nonlinearities has been attempted by using the differential equations to operate and guide all of the responses for the system. Typically, pedestrian electromechanical motor users do not care whether the electromechanical system contains certain nonlinear properties. These users are more interested in at which speed a motor runs into a limitation of maximum torque output, how the efficiency of the system can be improved under certain environmental conditions, and whether their motor can generate the maximum torque under different conditions. Also, users often realize how much power is lost during one period of a machine process and develop some way to improve the machine's cooling mechanism. To better accommodate the average user, this research focuses on the motor responses in operational regimes for electromechanical actuators. These regimes are interpreted as criteria spaces that represent aspects of system performance (outputs) or as aspects of system control (inputs).

Typically in research, modeling of the system is accomplished using spring, mass, and damper components to form the governing linear differential equations. However, due to the complexity of the real system, it is still difficult to find the appropriate PID control gains, which can cover all of the operational range in the system. For improved control, gains should be adjusted for different operational areas based on the difficulty of control, increment of uncertainty, and reduction of the error. Managing the overall processing range of the real mechanical and electrical applications by changing controller gains is called *gain scheduling.*

Gain scheduling is a form of nonlinear feedback method of a special type which has a linear controller whose control parameters are changed as a function of operating conditions in a preprogrammed way. It has the drawback that it may be time and cost consuming to build a schedule. Currently, auto-tuning, which is used in adaptive control, is used to build gain schedules but it should be improved to cover much larger range of control parameters to obtain better operational performance of electromechanical actuators [5]. Auto-tuning also needs incorporate automatic modeling and design in a controller, so it simplifies the use of the controller and it does not apply for complex system any more. Similarly, the control engineers developed adaptive controllers to track small variations in system parameters in the case of time-invariant or steady state operations[1]. However, this controller could lose its effectiveness in certain domains of operation due to the uncertainties found in any model. Another control systems approach for doing this is to use the concept of a robust controller, but it also has similar limitations due to system dynamic equations with a limited operational region. Based on these limitations a different approach to intelligent control is developed in RRG. This approach will be implicitly time dependent and generate 90% of control efforts for the overall control strategy of the physical system. The rest of 10% can be managed by the traditional control methods as mentioned above.

In this report, performance maps, based on the complete knowledge of all operational restrictions and regimes, are suggested and provide the knowledge to help attempting to develop the highest performance actuator controller. If all of the responses and conditions in an electromechanical motor are identified before it is actually used in a real application, the system might be more effectively controlled for the best performance in the overall operational region. All of the possible control parameters need to be identified and the extreme ranges of the actuator performance need to be determined. After accomplishing this, the burdensome role of feedback controller gains can possibly be reduced dramatically.

To create a performance map, specific criteria must be developed to cover the entire possible control regime that describes the performance characteristics of

---

[1] In real world, system parameters are time-variant.

an actuator. These criteria can provide metrics for measuring and controlling system performance and can reduce the complexity when trying to identify nonlinear components in actuator modeling. All of the performance maps are represented in statistical forms presented in Section 5.2. Based on the ARIMA methods suggested in Section 5.2, all of the nonlinear phenomena including the physical responses of testing an electromechanical motor can be expressed in algebraic equations which reduce the system complexity. In Chapter 3, actuator criteria will be explained in detail. The tests needed for an actuator must consider all of the possible situations if we are to obtain the guiding maps necessary to drive the actuator in good conditions. The plots generated in the major tests, which are described in Chapter 6, will visually illustrate a clearer picture of the operational management. They will describe the property of the system better than the model-based approaches that rely on ordinary or partial differential equations. Generally, a greater number of performance maps will provide more choices of control efforts.

The ultimate goal of this research is to develop the performance envelopes of an actuator in terms of several control parameters. The parameter values recorded when testing an actuator are obtained from physical sensors, which have their own limitations and constraints. The performance envelopes are constructed from one, two, or several sets of these performance maps which are acquired by testing the actuator in question. The performance envelopes are the guiding surfaces in particular regions which dominate and govern the control parameters for the best performance. This region can be expanded depending on the operational conditions. The envelope indicates the peak metric points in a critical range and the safe metric values in a particular region to the motor user. These performance envelopes are determined based on a statistically proven optimization process. In

Chapter 5, performance envelopes are described thoroughly.

1.1 Intelligent Control Architecture Development

Over the years engineers have realized that a robot's performance is directly limited by the performance parameters (such as power density, accuracy, stiffness, etc.) of its actuators. The reconfigurability of the system also demands modular actuators with standardized interfaces and embedded intelligent controllers. This central importance of the actuator has led to the development of an Electro-Mechanical Actuator Architecture (EMAA) that includes ten different classes of actuators [102]. Each class in the EMAA represents a specific application domain such as: low cost volume use in manufacturing automation, high ruggedness in construction machinery, delicateness in microsurgery, intelligence to support condition based maintenance, or fault tolerance for aircraft safety. Each class is represented by both rotary and linear motion configurations. The detailed explanation about the intelligent control architecture for an actuator is given in Ref. [42].

Intelligent actuators as described in the EMAA are highly nonlinear under abnormal conditions and some of them include redundant resources for fault tolerance. The purpose of initiating this intelligent control study is explained as follows. The conventional linear models using feedback control [23] are insufficient to obtain the maximum performance that can be derived from an increased set of resources. By using the linear model for a physical system, the desired output can be obtained quite easily, but if the mathematical expression for the system model includes nonlinear terms, the selection of the gains will be much more difficult. Moreover, most of controllers concentrate on improving their stabilities in order to provide the fastest response in a complex system, but they worked correctly only

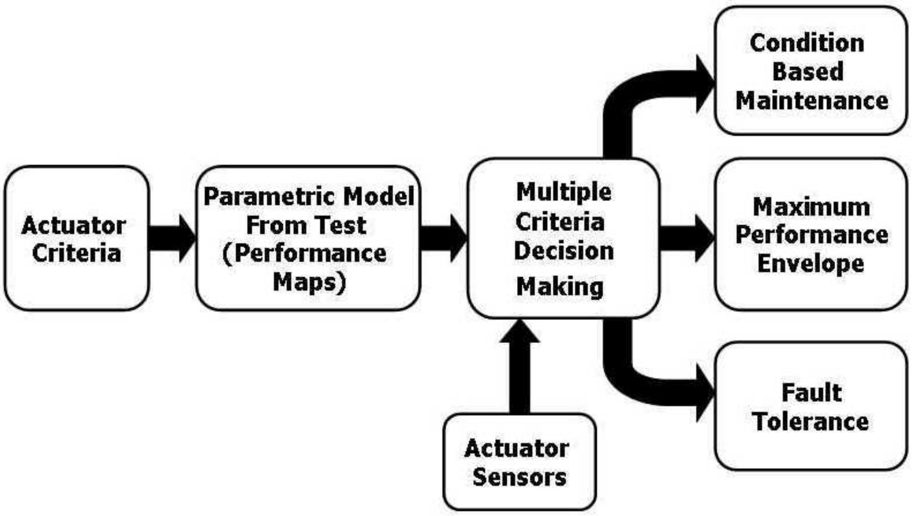

Figure 1.1: Actuator management diagram

when the range of the operating parameters was quite small [5], [93]. Because of this, it is not possible to design the controller gains to operate satisfactorily tracking at one operating state and expect it to perform equally well elsewhere without re-tuning the gains. This is due to the substantial changes of the operating states in different conditions. To solve this problem, control engineers used *gain scheduling* to change the controller gains by monitoring the operating conditions of the process as mentioned above.

The conceptual diagram of the actuator control architecture, which uses a decision-making system to determine the best performance output for an intelligent actuator, is shown in Figure 1.1. The key building blocks of this intelligent control approach are the actuator criteria and performance maps of which are constructed in this research. The performance criteria are defined as the decisive factors to define, anticipate, and evaluate the performance responses of the system. The quality of an actuator's outputs can be evaluated quantitatively based on the properly defined performance criteria. The criteria, built in this research, are diverse enough to characterize as many aspects of performance as can be deduced from the physical state of an actuator during a task. These criteria become the basis to create the performance maps, which is the metric visual expression of performance criteria, when considering all possible situations and conditions. The performance maps developed from tests are based on independent operational parameters and states, and represents all nonlinear properties of the actuator. A generalized actuator parametric model that represents all nonlinear properties will then be developed using these performance maps. Also, in order to complete the intelligent control, the decision-making algorithm necessitates sensor models that are based on real-time sensor data. Actuator criteria, which are the focus of this paper, will be the references against which to compare the collected sensor data, and the sensor data are based on the parametric models.

Once effective actuator performance criteria are developed, the next step is to send collected data to a decision-making system that can use these criteria which we have developed to achieve performance goals specified by the user. Key requirements of this decision-making system are its ability to combine and resolve conflicts among performance criterion that are nonlinear and coupled. Research done at the system level (i.e., the full robot software) has suggested the use of direct-search techniques, heuristics, and nonlinear optimization. Limitations of these approaches have been their inability to handle global optimums, computational inefficiency when nonlinear optimization is used, and a lack of physical meaning of some of the criteria. Decision-making at the actuator level should be relatively direct as the criteria themselves have clear physical meanings and are less volatile when compared to the system level criteria.

The decision-making system can be used to determine the maximum performance envelope for an actuator from a complete set of performance maps. These maps are based on a specific set of performance criteria. These particular maps will have several different layers in terms of the same reference control parameters regarding different input loadings. The performance envelope is the combined optimum surface in the full set of maps, which satisfies the desired criteria in each operational region. Performance envelopes can be used both to aid in the actuator design process and they can also be used as the constraints for high performance control. For design, a wide variety of actuators will be tested so that their performance maps can be correlated with design parameters. Once an array of maps is available, it will be possible to accurately estimate the performance map and envelope for untested actuator designs.

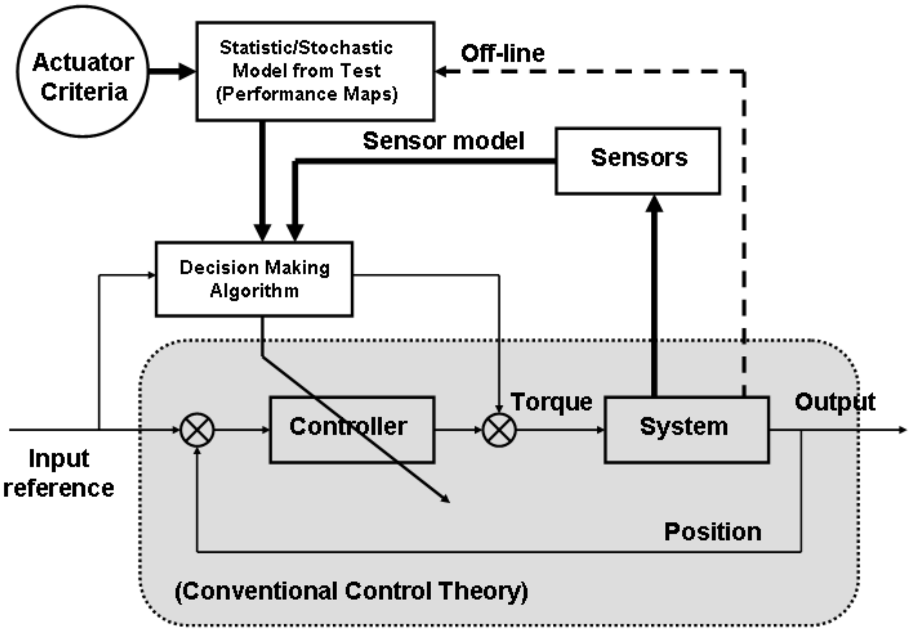

Figure 1.2: New control strategy based on actuator criteria

Figure 1.2 shows how the decision-making algorithm based on the performance maps and envelopes is added to normal conventional control theory. The decision-making algorithm is used just like a feedforward controller. The feedforward design has been used to significantly reduce the reference error in trajectory following systems. This method is an open loop control method, so it does not affect the loop stability and dynamic response. The educated guidance directed by the decision-making algorithm will generate a bias signal through the feedforward path. The feedback signal from the output sensor eliminates the very small portion of the residual error. The input command to the plant (i.e., a system model) is a torque signal which is combined from the controller and decision-making algorithm. The decision-making algorithm accepts two inputs. One is from the performance maps/envelopes based on actuator criteria and the other comes from the real time sensing signals from the sensors installed in the test model. As mentioned before, the performance maps/envelopes have already been built in for guiding and constraining the operational performance of the actuator. The sensors installed in the test actuator will send the signals to the decision-making algorithm in real time in order to determine the optimum torque control value for the best performance. During the operation of the system, the controller gains (i.e., Proportional, Integrated, and Derivative gains) will be changed with the proper combinations of the gain values as scheduled in off-line. The detailed explanation for the decision-making control of the intelligent actuator is in [42]. This research is focused on the development of the actuator criteria and the generation of performance maps, which are the most crucial and foundation work for the construction of the described intelligent actuator architecture system.

There are some application areas that are keys to the intelligent control above the decision-making system as shown in Figure 1.1. For example, fault tolerance will be useful for high cost systems in space and aircraft, whereas Condition-Based Maintenance (CBM) will be essential for low cost maintainability (say in manufacturing). All these application areas will be dealt with by using a unified description of an actuator as represented by the performance criteria. This leads to a clean architecture that separates the specifications of an actuator from these applications. It should be noted that each of these application areas may put specific demands on the criteria and that new criteria may need to be added to address them. The CBM component shown in Figure 1.1 will track all performance criteria and develop a historical map of all their indices. Any deviations from this map could be as a result of impending failure. Multivariate analysis can then be used to detect this variation and relate it to a bounded list of fault classes [42]. The advantage of the approach (that uses criteria as a basis for decisions) is that it best combines the best parametric model and sensor data into a unified decision making structure.

Fault tolerance will also benefit from this research. Fault tolerance in an intelligent actuator results from duality in every active component of the actuator such as motor, brakes, gear trains, etc. and allows the system to function with degraded performance after a fault. To fully utilize the redundancy in this system (under normal conditions) and reallocate resources (when under fault), new actuator criteria must be developed. Under faults, conflict resolution and resource allocation in near real time will be the key responsibilities of the decision-making system.

At the core of the EMAA is the prime mover. Currently, the prime mover under consideration is a Permanent Magnet Synchronous Motor (PMSM). Since the prime mover is the most actively controlled part of the actuator, we are currently focused on the development of performance criteria for its operation. The availabilities of the performance criteria is described in Section 1.2.

1.2 Literature Survey of Performance Criteria and Maps

To evaluate the performance of a specific actuator, many researchers and manufacturers have investigated to try and find out the best way to quantify the performance metrics for actuators. Several efforts for performance evaluation of the electromechanical actuators were introduced, but none of them included the complete set of performance maps and envelopes to maneuver for the best operational conditions.

Morrell and Salisbury proposed performance criteria for electromechanical actuator evaluation [64]. They asserted that quantitative metrics for the task performance would improve understanding of an actuator's nonlinear characteristics. They described how the performance of the manipulator was affected by the control system for the actuator. Most of their performance criteria were also obtained in the frequency domain. The approach using the performance criteria to improve and evaluate the response of the real electric actuator was introduced in Ref. [80]. The performance criteria of the switched reluctance motor (SRM) were described and they were used to optimize the performance of the SRM. Some of them are used in this report, such as efficiency, torque ripple, torque output, and noise. These reference control parameters used in [80] were turn-on angle, turn-off angle, reference current, and size of the hysteresis band. Note that the permanent magnet synchronous motor (PMSM) has only one reference control parameter (such as current). The 3D plots of performance criteria in [80] represented efficiency and torque plots based on those four reference control parameters. Also, they mentioned the control parameters should be selected using optimizing strategies for different operational regimes in order to maximize the benefits that can be derived from properly chosen performance criteria. For example, at higher speed, a torque ripple is less important. Due to the kinetic energy of the system, the inertia of the system will mash the torque ripple.

Neumeyer et. al. [67] introduced seven performance limiting factors to evaluate if the operational conditions of a motor were out of range. In practice, the rating values attached in the nameplates of the electric machines (motors) were mostly non-feasible and they usually operated over a wide range of load, speed, and power factor about varying pulse repetition. The overall machine performance maps were shown as a function of power factor and cyclic frequency. The limiting factors for the best performance were also divided into two categories: those that required a long period to register their values, such as stator and field winding temperatures, and those for which the values could be changed instantaneously such as stator and field currents, stator voltage, and instantaneous torque.

Nine quantitative performance criteria were presented in [94] and most of them were used to meet the design specification for electromechanical actuators in reference to robot applications. They discussed the roles of compliance and inertia in the structure of a robot actuator in the context of force and motion control. Their approach for performance criteria was, also, a model-based method since the performance criteria suggested in the paper were used to determine the location of poles and zeros on the complex plane in an effort to design proper mechanical parameters. However, Smith and Jacobsen mentioned that the difficulty of modeling complex systems reduced their utility in design. Kuribayashi [50] used power and energy divided by mass and volume to evaluate ten linear and rotary actuators, and he named them as power density per unit mass (PDM), power density per unit volume (PDV), energy density per unit mass (EDM), and energy density per unit volume (EDV). He compared several different kinds of actuators, such as hydraulic cylinder, pneumatic cylinder, stepping motor, piezoelectric actuator, etc., by using the four different values along the force and speed axes. However, these four values were not enough to evaluate the actuator in such a manner that one could evaluate the overall actuator performance capability. Performance criteria which can cover all of the possible operational conditions needs to be developed in further study.

Visualizing and quantifying performance criteria of mechanical systems has been used in other industrial applications for a long time [7], [19], [28], [70], [72]. Engineers obtain the sensible data in a variety of different experimental settings. By analyzing the data and graphically displaying them, the users can predict the response in many different situations and evaluate the performance of the particular system. These complex systems have been difficult to model mathematically due to the requirement that they need to demonstrate the performance improvement in a physically understandable way.

The Performance Criteria and Maps Approach (PCMA) has been use to understand automobile engine systematically for more than 30 years. Baker and Darby developed an engine mapping method to determine engine calibration [7]. The task of engine calibration was very complex because of the large number of engine variables in the overall range of engine operation. For optimum engine calibration, they developed torque-speed look-up tables in different transmission ratios. Based on these tables, several engine control parameters were determined by experiments. Another good example of the PCMA applied to automobile engines was presented in [97]. To evaluate the performance of a spark ignition engine, Stevens et. al. [97] built a map of engine stability and combustion performance parameters. Their approach was valuable because they showed a statistically generated matrix of test data and performance maps from this experimental design method. Based on [97], an idea of first collecting the experimental data from engine tests and then using a post processing technique, a statistical approach was formulated. They showed qualitative and quantitative trends of engine behavior in the graph. Golverk generated the generalized normalized diesel engine performance maps through experiments [29], [30]. The engine performance maps were obtained for both constant and variable load under normal and extreme conditions. He also developed parametric equation models in the form of second order polynomials. The polynomial coefficients were determined empirically with less than 0.5% error. Also, he developed the mathematical expression of the performance maps for an internal combustion engine based on the mathematical correlation among the parameters [28]. The coefficients in each term were determined by a statistical regression method. Onder et. al. [70] generated loop-up tables to represent the nonlinear operational conditions for the internal combustion engine using a dynamic test bench. The test procedures that he created in the engine tests were very similar to the test method which are contained in this report. They measured several engine signals to decide the optimum values of the spark advance and the air-to-fuel ratio, which then became the main control parameters for the best performance in internal combustion engine.

In addition to the usage of these engine performance mapping methods in automobile industry, PCMA has been a useful tool for the evaluation and control of hybrid electric vehicles including internal combustion engines and electric motors. For high fuel economy and exhaust emission targets, which were their performance optimization goal, automobile drivetrain hybridization (using two types of energy converters rather than just one) has been considered by the government and industry Partnership for the New Generation of Vehicles (PNGV) effort for last ten years [19]. The initial studies at National Renewable Energy Laboratory (NREL) derived the development of the vehicle performance simulator, ADvanced VehIcle SimulatOR (ADVISOR). By using this performance analyzing software, they created the performance maps for the operational regime and predicted the electric vehicle performance, range, and fuel economy. To do this, ADVISOR used the fundamental equations of vehicle dynamics coupled with efficiency and power loss component. Rizzoni et. al. [82] also developed a simulation package using performance maps to find the operational optimizing solution of the control parameters for hybrid electric vehicles. Paganelli et. al. [72], [73] used the concept of engine performance maps to formulate the instantaneous power split between an internal combustion engine and electric motor in parallel hybrid vehicles. By using the appropriate scaling and parametrization of their efficiency characteristics combined with their control strategy, they were able to provide a powerful performance simulation environment.

There are some more examples that apply PCMA in machine industry. Sieros et. al. [89] described a method to model the performance maps of compressors and turbines in a jet engine. They generated the performance maps for a jet engine in order to monitor the engine conditions and to diagnose for faults. They used tabulated functions as well as interpolation to cover all of the operational range. The maps were created by tests and compared the experimental data to estimated values with scaled independent variables. Other methods include the analytical functional method, a least-square method and a nonlinear regression which were used to determine the coefficient values of the polynomial equations using the experimental data. Chen et. al. [15] presented the effect of the power loss of a rubber V-belt continuous variable transmission (CVT) at constant running speeds and during acceleration in a continuous changes of speed ratio. The dynamometer constructed in [15] was very similar to the test bed in this report. The dynamometer measured the speeds and torques of the driving and driven pulleys so as to identify the losses and efficiency of the CVT. In order to identify torque or speed loss in transient operational condition, more efficiency plots were drawn with respect to different operational conditions of torque and speed.

1.3 Research Objectives and Overview

The goal of this research is to generalize actuator test data in the form of performance maps which would document the characteristics of a representative permanent magnet synchronous motor, with a range of rated output power, under dynamic load operations. A collection of performance maps is our approach to representing the complexity of the actuator response to control inputs (in both the model and the sensor data) and also provides metrics for measuring the actuator states. These actuator criteria maps can be used to build performance envelopes, and to provide a reference basis for CBM and fault tolerance. Figure 1.3 shows the overall procedure to obtain a performance map.

The state values of interest from the sensors in the test bed are position, velocity, torque, temperature, voltage, current, and magnetic flux density. However, the parameters measured by the embedded sensors in the test bed include signal noise, so mathematical tools are utilized to reduce this noise content. The

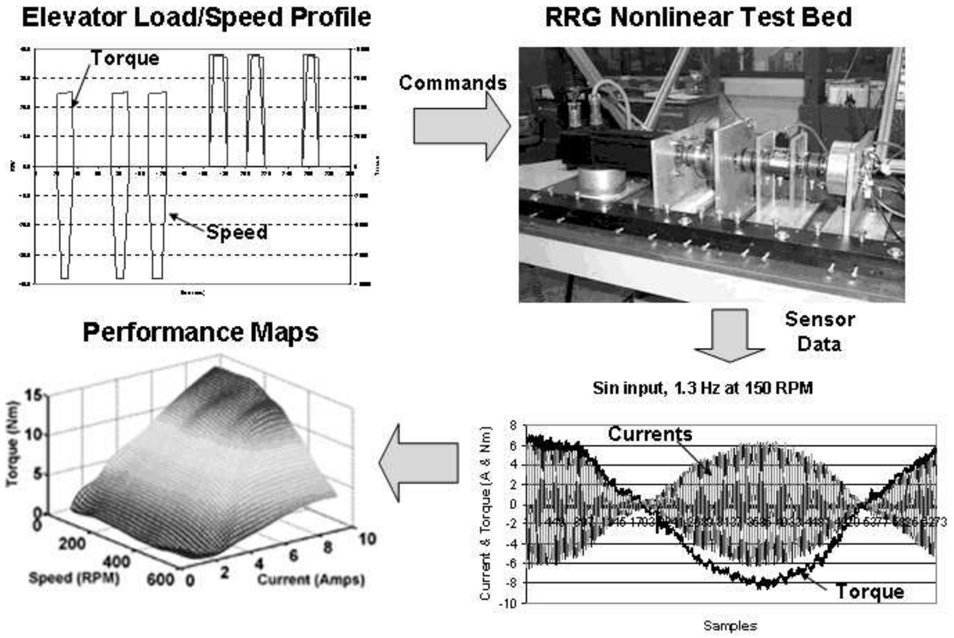

Figure 1.3: Procedure for the development of performance maps

raw data from the test bed are conditioned by a stochastic processes, developing dynamic regression models, and tracking the test protocol of the actuator. Additionally, the data obtained in real time will have associated upper and lower error bounds to indicate the uncertainties in the sample data. Once all of the data sets are collected, they are combined based on each actuator criterion. The preferred maps are continuous, limited in magnitude, implicitly time dependent, graphically clear, and vary significantly over the actuator's regime of operation. A full set of performance maps based on operating criteria can be generated using appropriate operational parameters monitored during the full range of tests.

The actuator test bed data can be used to determine the maximum performance envelope for a specific actuator (based on a specific set of performance criteria) from a complete set of performance maps. Figure 1.4 represents the conceptual idea for generating the performance envelope from several criteria maps. A particular map will have several different layers based on the different input loads with the same reference control parameters. The performance envelope is the enclosing line with the maximum performance capacity from the full set of maps which meets with the desired criteria for the specific actuator.

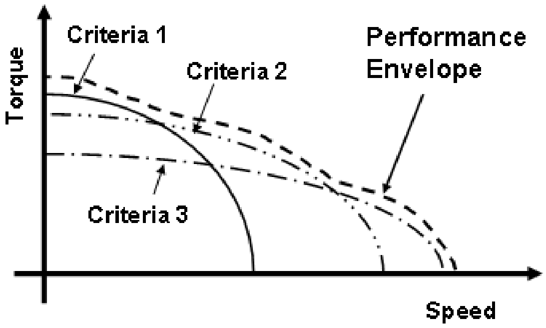

Figure 1.4: Conceptual idea for a performance envelope

Performance maps can aid in the actuator design process, they can be used to increase control performance, and they can be used to generate performance envelopes for use in CBM and in other decision-making functions. For design, a wide variety of actuators will ultimately be tested so that their performance maps (perhaps 20) can be correlated with design parameters. Once an array (i.e., from 30 or more different actuator types) of maps is available, it will be possible to estimate the performance maps and envelopes for untested actuator designs. Further, we will show how to guide the designer and operator to mix a selected set of performance maps to create a performance envelope to best meet the operating requirements of a given application at the end of this research effort.

Chapter 2

Background Study

2.1 Overview of Prime Mover Technology

There are two major types of DC motors. The first is a brushed DC motor and the second is a brushless DC (BLDC) motor. The DC motors shown in [49], [83] have in common the use of brushes and commutators to distribute current through the windings as the motor rotates. The DC brushed motor has two main parts: the stator part and the rotor part. The rotor may be of cylindrical or disk shaped and contain a symmetric winging made of identical coils connected in series to the insulated copper sectors of the mechanical commutator. The current injected through the brushes is sent to the rotor coils through the commutator copper sectors in pace with the rotor position. The mechanical commutator is an inverter which changes the switching frequency depending on the number of poles and the rotor speed.

In case of the brushless DC motor, this mechanical switching is replaced with electronic switching. These motors are not called AC motors even though alternating currents (ACs) are supplied to the motor. The shape of the motor command voltage is a sine wave but the output current from the motor is a direct current (DC). A brushless DC motor driven by three sinusoidal currents in three phases adds further confusion because all phases are active and the current waveforms are sinusoidal. Bose [10] refers to this motor as a permanent magnet synchronous motor (PMSM).

BLDC motors use position feedback to keep input waveforms synchronous with the rotor position. The motors and theory described in this section are specifically limited to the continuous rotation motors that commutate electronically and have the same basic motor operation characteristics as the DC servo motor. The BLDC motors with the proper electronic control system can be substituted directly for the mechanically commutated DC motors and provide the same output performance.

2.1.1 Electric Motor Fundamentals

The fundamental equations for a simple electric motor include two magnetic field equations as shown in Equations (2.1) and (2.2). When a current carrying wire is placed in a magnetic field such that the current flow is perpendicular to the direction of the field, a force is exerted between the field producing element and the wire as shown in Figure 2.1. The conductors are shown wrapped around the square stator. The force is the product of the strength of the field, the length of the wire, and the current in the wire as follows

$$F = ilB \tag{2.1}$$

where F is in newtons, B is magnetic flux density in Tesla, l is the length of conductor in meters, i is current in amperes. The direction of the force will depend on the orientation of the magnetic field and the current direction in the wire.

The exact opposite effect on the foregoing discussion is observed. If the wire is disconnected from the current source and the field is moved in a direction perpendicular to the wire, a voltage will be measured across the ends of the wire. The magnitude of the voltage, E, depends on the flux density, B, the length of the

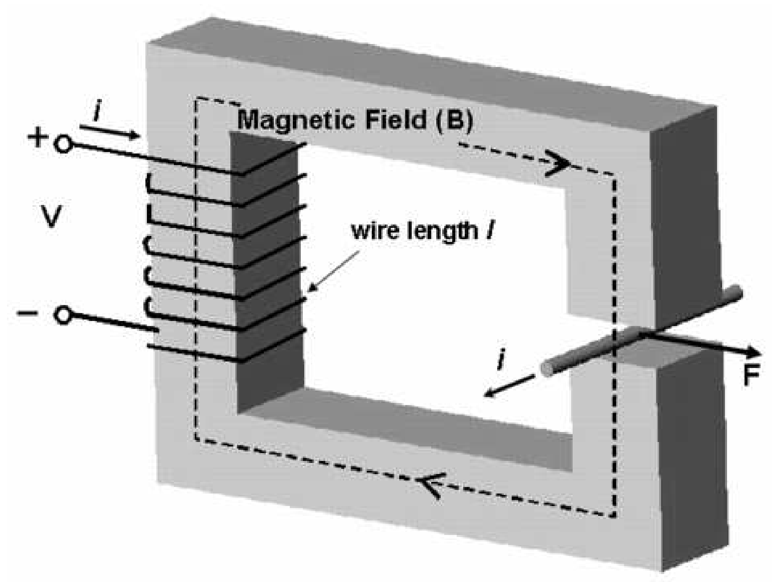

Figure 2.1: Current carrying wire exposed to a magnetic field

wire, l, and the velocity of the rotor, v, with which the wire is moved through the field, or

$$E = Blv \tag{2.2}$$

The force on the conductor in the magnetic field can be controlled by changes in B, l, or i. In motor design, B is affected by the type of permanent magnet material and magnetic circuit design, l is affected by the length and number of active windings, and i is the current carried in the wire. The generated voltage is similarly controlled by changes in B and l and by velocity (rotor speed). Figure 2.2 represents a wound two pole brushless DC motor. The windings are wrapped around the stator. The magnetic flux density is developed in the magnetic circuit comprised of the north and south permanent magnets and two parts of the stator core. If current is applied to the conductors as shown, the force F from Equation (2.1) is imparted tangentially to the rotor, and torque results in the direction of the arrow. If the current source is removed and the rotor turned, an alternating voltage will appear across the terminals as shown in Figure 2.2.

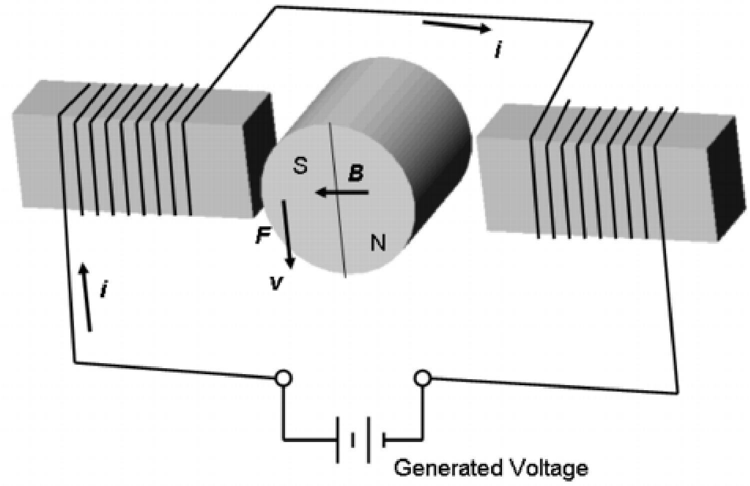

Figure 2.2: Basic one phase, two pole brushless motor

2.1.2 General Permanent Magnet Motor

In permanent magnet actuation technology, there are two kinds of motors, Permanent Magnet Synchronous Motor (PMSM) and Brushless DC (BLDC) Motor. The difference between them is in the shape of the back EMF. That is, the PMSM has a sinusoidal back EMF while the BDCM has a trapezoidal back EMF [76]. This section focuses on the model of a PMSM. This motor consists of a steel rotor, a position sensor mounted on the rotor, an electronic circuitry, a logic controller, and a stator [95]. The steel rotor has strips of permanent magnets mounted on its surface. These magnets create magnetic fields that interact with the magnetic fields produced in the stator windings to generate torque. The position sensor, which is connected to the rotor, is generally either an encoder or a resolver. This sensor provides accurate information about the angular position of the rotor, which is used in the commutation of the currents in the stator windings. The electronic circuitry commutates the currents in the stator windings according to control signals provided by a logic controller. This controller sends low voltage signals to the electronic circuitry to produce the commutation of the currents in the stator windings. The controller uses the angular position provided by the position sensor to produce the torque demanded by the actuator. Finally, the stator is constructed with three phases, which are generally Y-connected. Constant switching of the currents in the phases of the stator intends to produce a constant torque on the rotor of the motor.

A set of first order differential equations that explains the dynamic behavior of a PMSM can be obtained as in [36]. This set can be simplified by using a general mathematical transformation known as the d-q transformation. The d-q transformation uses the properties of trigonometric identities to remove the sinusoidal terms that appear in the equations due to the back EMF. The simplified set of equations, known as d-q equations, is simpler to use than the original set [36]. However, the set of equations was obtained under the assumption that the flux linkage and the currents in the phases are linearly related. In the presence of magnetic saturation, this assumption is not valid. The flux linkage terms in the set of equations are no longer linear functions of the currents and the angular position of the rotor. Therefore, a new set of equations that takes into account this condition should be obtained to explain the dynamic behavior of the motor under the saturation phenomenon. Previous efforts [36], [18] have been made to obtain the nonlinear relations of the flux linkage, the currents, and the angular position. In this report, based on the fully explained mechanism of brushless DC motor, actuator performance will be evaluated.

2.1.3 Sinusoidal Commutation

Figure 2.3 schematically shows a typical brushless motor wound with three phases and the voltages between the phases when the motor is run as a generator at a constant speed. The motor is wound to provide overlapping, sinusoidal three phase voltages, electrically 120° apart. In this case, the motor has two poles, so the electrical angles equal the mechanical angles. Increasing the number of poles will increase the number of electrical cycles for each complete rotation of the rotor. The points of north and south balance for each winding occur where the voltages go through zero and reverse polarity. It is the method and type of winding, as well as the geometric and physical characteristics of the rotor and stator that create the sinusoidal shape of the terminal voltage, the back EMF (electromotive force) of the motor.

In general, the best position for commutation is that point at which the back EMF waveform is centered between commutation points. Commutating at the zero crossing of the back EMF waveform is ineffective since there is no resultant torque no matter how much current is applied to the phase. Peak torque per unit current for a running motor is achieved by using a maximum in the current at the peak of the back EMF waveform.

2.2 Magnetism in Permanent Magnet Motor

2.2.1 Magnetization and Ferromagnetism

The quantities used to describe the strength of a magnetic field are the magnetic flux, φ, in units of Webers (Wb) and the magnetic flux density, B, in units of Webers per square meter (Wb/m^2), or Teslas (T). Magnetic field strength, or magnetizing force, H, in units of Ampere per meter (A/m), is the current

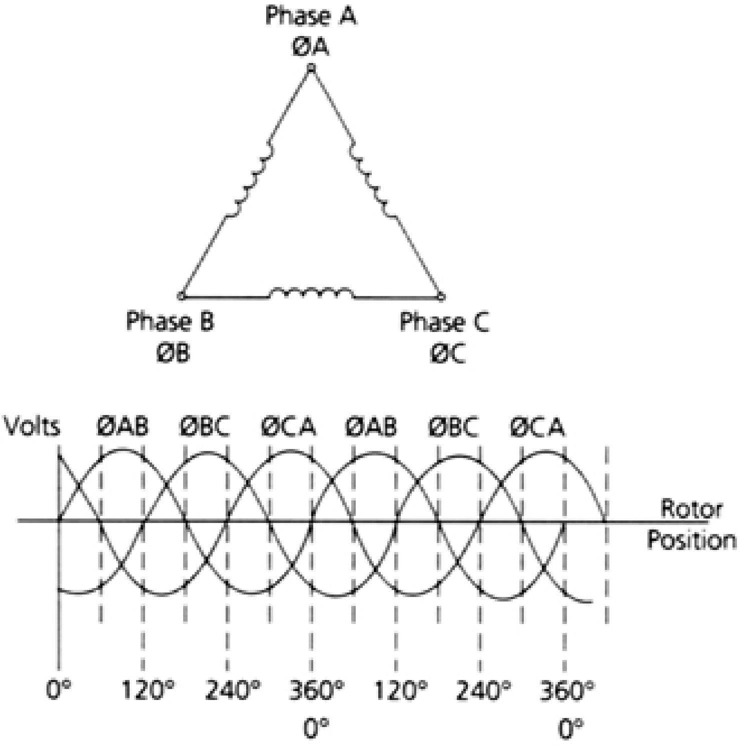

Figure 2.3: Commutation in delta winding [47]

used to generate magnetic flux density. Also, it is a physical property to measure the magnetization of the ferromagnetic material. Magneto-motive force (mmf) is defined by the total current (Ni) encircling the flux path. N is the total number of wound coils. The unit of magneto-motive force, F, is often called an Ampere-turn. Magnetic reluctance, R, also can be defined by the constant of proportionality between magnetic flux, φ, and magneto-motive force, F [25], [74]. When a material is placed in a magnetic field with strength, H, the interaction between the external and internal atomic moments increases the resultant flux density, B. If the induced magnetism is denoted by the magnetic moment density or magnetization, M, the flux density due to M alone is given by $B = \mu_\circ M$, where the magnetic constant,

$\mu_\circ$, has a value of $\mu_\circ = 4\pi \times 10^{-7}\ H/m$ in SI units. The total flux density due to M and the external field, H, is $B = \mu_\circ M + \mu_\circ H$. Slemon and Parker [92], [74] define magnetic susceptibility, χ, as the ratio of magnetization, M, and magnetic filed strength, H. Therefore, the total flux density becomes

$$B = \mu_\circ(\chi + 1)H = \mu_\circ \mu_r H = \mu H \tag{2.3}$$

where μ_r is the relative permeability of the material to free space and μ refers to the permeability of the material.

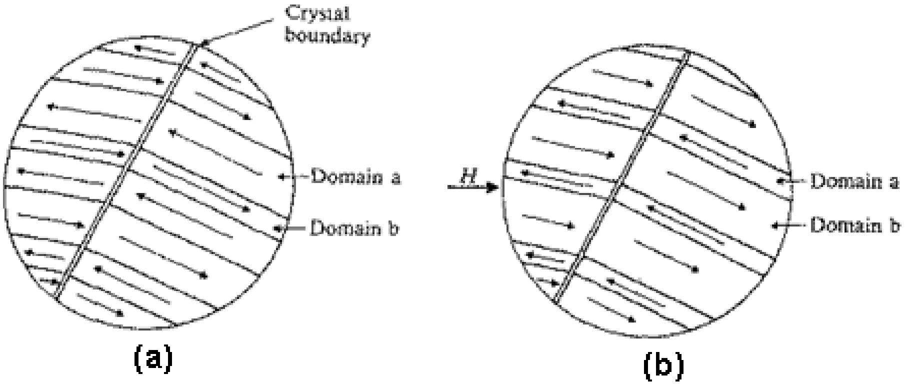

Figure 2.4: Ferromagnetic domains. (a) No applied magnetic field. (b) Applied magnetic field intensity H [92]

If an iron core of identical dimensions replaces a free space, the total flux produced by the same coil current is significantly increased. This increase is due to the phenomenon of ferromagnetism, which is a very important factor in the process of energy conversion by electromagnetic machines like motors. The direction of alignment of the magnetic moments in a ferromagnetic material is normally along the magnetized direction. It has been shown experimentally that a specimen of ferromagnetic material is divided into so-called magnetic domains, usually of microscopic size, in each of which the atomic moments are aligned. The alignment direction differs from one domain to another [92]. Figure 2.4 shows ferromagnetic domains.

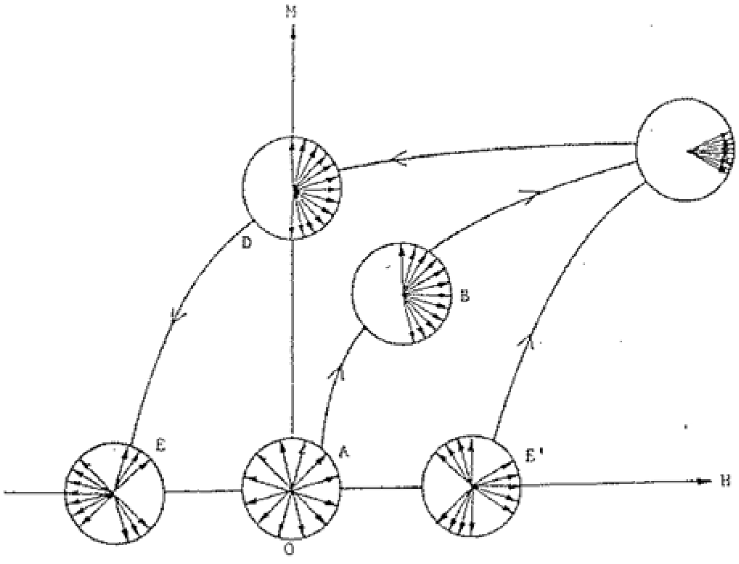

Figure 2.5: Domain arrangement for various states of magnetization [20]

When a ferromagnetic material is placed in a magnetic field, the magnetic moments of the atoms tend to rotate into alignment with the direction of the applied field. Domains in the material in which the magnetic moments are more or less aligned with the applied magnetic field increase in size at the expense of neighboring domains that are more or less oppositely aligned to the applied field. The consequence of such domain wall motion is that the material acquires a magnetic moment that may be considered as the resultant of all of its atomic moments. Therefore, the magnetic moment of the specimen provides a measure of the degree of alignment of the atomic moments [74].

2.2.2 Definition of Magnetic Saturation

The magnetization of ferromagnetic material is caused by the movement of magnetic domain walls and the rotation of magnetic domains. Figure 2.5 shows several states of magnetization. In the figure, the arrows represent the direction of spontaneous magnetization of each magnetic domain. The ideal demagnetized state is shown at point O. A direction of spontaneous magnetization in each magnetic domain is distributed randomly. When a positive magnetic field is applied, domains magnetized in the minus direction are eliminated first, by 180 ° wall motion, leading to the distribution shown at B. Further increase in magnetic field rotates vectors into the state of saturation shown at C. The magnetic saturation of the material is defined in this state. When the field is now removed, the domain vectors fall back to the easy direction in each grain nearest to the positive direction of H. The domain vectors are uniformly spread over one half of a sphere, as indicated at D. In Figure 2.5, we can see the states at O and D are different. If we apply a magnetic field in the other direction, the magnetization arrives at E and its state is also different from the state of the grain at O. When the rotor which has permanent magnets on its surface rotates for several cycles, this process is repeated.

2.2.3 Change of Magnetic Saturation

As mentioned in Section 2.2.1, the magnetic moments of materials are held in parallel or anti-parallel by exchanging forces. This is due to the sharing or exchange of electrons between neighboring atoms in the crystal structure of the material. When the temperature of a material is increased, each atom oscillates about its mean position in the crystal lattice, and this oscillation disturbs the alignment of the spin magnetic moments [92], [20]. Consequently, as the temperature of a ferromagnetic material is increased, its magnetization decreases as shown in Figure 2.6. At a temperature known as the Curie temperature, T_c, the parallel alignment completely disappears and the magnetic moments become randomly aligned. The definition is given in the American Institute of Physics handbook [27], "Curie point, as the temperature increases, at which the transition from ferromagnetic to paramagnetic properties of a substance is complete". For this paper, an iron magnetic core has been assumed. The Curie temperature for iron is $770°C$ [20]. Since the temperature in most electric machines is usually below $150°C$, the effect of the temperature on the ferromagnetic property of iron is small. Nd-Fe-B, rare earth material, is used for a permanent magnetic material. It has a very low Curie temperature of $320°C$ compared with the other pure materials in a motor [74].

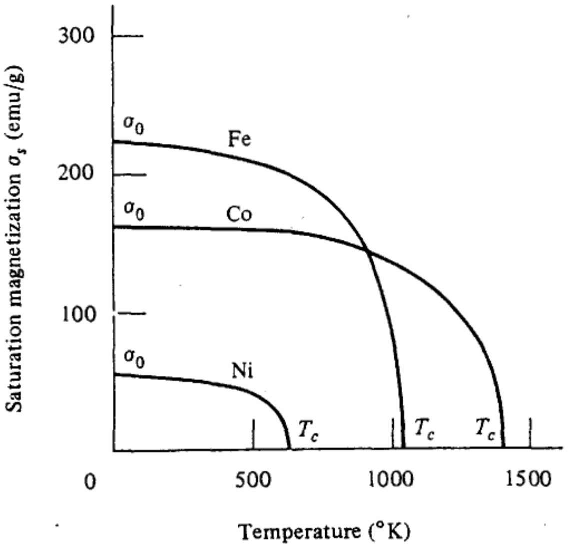

Figure 2.6: Saturation of Fe, Co, and Ni as a function of temperature [92]

However, the bend point of the saturation magnetization curve in Figure 2.6

is of interest in this research. The magnitude of magnetic flux of a magnet starts to reduce from this bend point when it loses its magnetization at a high temperature. The Nd-Fe-B permanent magnet material has a property of a negative high slope of its magnetic flux value with temperature as shown in Figure 2.7. Therefore, it is hard to decide the exact bend point because the tendency of magnetization is different from the case of a pure material. When the temperature, $65°C$ ($338°K$), is applied to Figure 2.7, then the corresponding magnetic flux density, B, is 1.24 Teslas and the magnetic susceptibility, χ, is 1, and the value of Boron component is 8. The reduction of magnetic flux density from 1.3 T to 1.24 T means the magnetic material reaches its saturation state faster by increased temperature of operation of the PM motor. Moreover, the magnetic flux density curve decreases linearly between $50°C$ and $150°C$ in Figure 2.7. This means that magnetic flux density and temperature have a linear negative relationship. Therefore, based on this information, magnetic flux density is 1.1 Teslas at $150°C$ ($423°K$) which is a 15% reduction.

2.3 Simulation for Generating Performance Maps

This section addresses some example plots for performance maps obtained from a permanent magnet synchronous motor (PMSM) simulation. This simulation focuses on how the prime mover performance criteria and maps are obtained. Therefore, the description of PMSM system model, mechanical model of the whole test system, and explanation of MATLAB simulation blocks will be described.

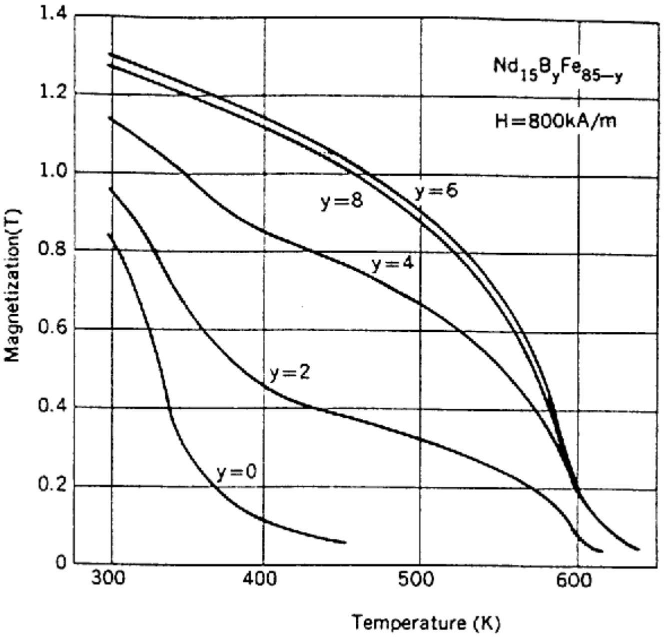

Figure 2.7: Magnetization curves of Nd-Fe-B magnets containing different percentages of Boron [84]

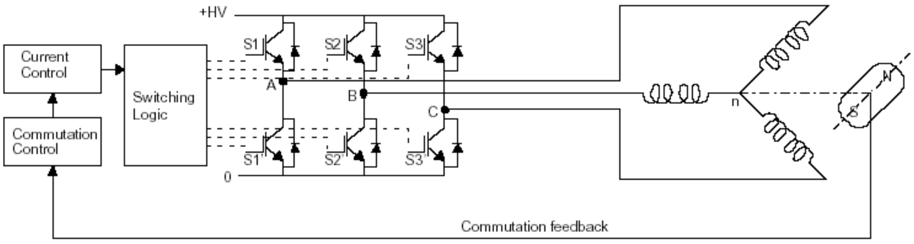

Figure 2.8: Brushless servo system [2]

2.3.1 Mathematical Model of a Permanent Magnet Synchronous Motor (PMSM)

A PMSM consists of a permanent magnet rotor, a position sensor mounted on the rotor, and an electronic circuitry that provide signals to the stator winding as shown in Figure 2.8. The stator is constructed by three phases, generally Y-connected, and the rotor has permanent magnets which are mounted on the surface of the rotor [4]. The physical contact between the mechanical brushes and commutators are eliminated, and the electronic switching is used to commutate electric currents in the stator windings. The appropriate winding is switched on by solid state amplifiers according to the current rotor position.

The PMSM has a sinusoidal back EMF and requires sinusoidal stator currents to produce constant torque. The following assumptions are made in the derivation [35].

- Magnetic saturation is neglected.
- The back EMF is perfectly sinusoidal.
- Copper losses and core losses are negligible.
- The stator windings have the same resistances and inductances.
- The self inductances and mutual inductances between windings are equal.

With these assumptions, the governing differential equations describing the dynamic behavior of PMSM is written as

$$V_k = Ri_k + \frac{d\lambda_k}{dt} \qquad for\ k = 1, 2, 3 \tag{2.4}$$

The flux linkages λ_j can be written as [4]

$$\lambda_1 = L_{11}i_i + L_{12}i_2 + L_{13}i_3 + \lambda_{m1} \tag{2.5}$$

$$\lambda_2 = L_{21}i_i + L_{22}i_2 + L_{23}i_3 + \lambda_{m2} \tag{2.6}$$

$$\lambda_3 = L_{31}i_i + L_{32}i_2 + L_{33}i_3 + \lambda_{m3} \tag{2.7}$$

where L_{ii} is the self inductance of winding i and L_{ij} is the mutual inductance between windings i and j. λ_{mi} is the magnetic flux linkage of winding i related to the permanent magnet. The windings in the stator are sinusoidally distributed and separated by 120° apart in each other. λ_{mi} may be written as

$$\lambda_{mi} = k_e \; sin(n\theta - \frac{2(k-1)\pi}{3}) \quad for \; k = 1, 2, 3 \tag{2.8}$$

where k_e is the back EMF constant and n is the number of pole pairs of the permanent magnet in the rotor. The self inductance is expressed as L and the mutual inductance is denoted as M. R represents the terminal resistance measured between two power wires of the test motor. Then, the mutual inductances, L_{ij} equal to M as mentioned in the assumptions above. Note that the sum of the currents in a Y-connected circuit is equal to zero. Equation (2.8) is applied in Equations (2.5), (2.6), and (2.7) then the flux linkage equations are

$$\lambda_1 = (L-M)i_1 + k_e \sin(n\theta) \tag{2.9}$$

$$\lambda_2 = (L-M)i_2 + k_e \sin(n\theta - \frac{2\pi}{3}) \tag{2.10}$$

$$\lambda_3 = (L-M)i_3 + k_e \sin(n\theta + \frac{2\pi}{3}) \tag{2.11}$$

By differentiating Equations (2.9), (2.10), and (2.11) with respect to time, the dynamic equations of the PMSM become

$$V_1 = Ri_1 + (L-M)\frac{di_1}{dt} + nk_e\omega \cos(n\theta) \tag{2.12}$$

$$V_2 = Ri_2 + (L-M)\frac{di_2}{dt} + nk_e\omega \cos(n\theta - \frac{2\pi}{3}) \tag{2.13}$$

$$V_3 = Ri_3 + (L-M)\frac{di_3}{dt} + nk_e\omega \cos(n\theta + \frac{2\pi}{3}) \tag{2.14}$$

where ω is the angular velocity of the rotor. In Equations (2.12), (2.13), and (2.14), the first terms are the losses in the stator windings, the second terms are the induced voltages due to the change in current, and the third terms represents the back EMF force.

The torque produced by the PMSM can be expressed as change of magnetic co-energy by [25]

$$T(i,\theta) = \frac{\partial W_c(i,\theta)}{\partial \theta} \tag{2.15}$$

The co-energy is expressed as

$$W_c(i,\theta) = \int_{i(0)}^{i(t)} \lambda di \tag{2.16}$$

Refer to Woodson and Melcher's Electromechanical Dynamics [105] for a comprehensive examination. Equations (2.9), (2.10), and (2.11) are substituted into Equation (2.16), then the expression for the co-energy becomes

$$W_c(i,\theta) = k_e \sin(n\theta)i_1 + k_e \sin(n\theta - \frac{2\pi}{3})i_2 + k_e \sin(n\theta + \frac{2\pi}{3})i_3 \tag{2.17}$$

Using Equation (2.15), the expression for the electromechanical torque is evaluated as follows [4]

$$T(i,\theta) = nk_e \cos(n\theta)i_1 + nk_e \cos(n\theta - \frac{2\pi}{3})i_2 + nk_e \cos(n\theta + \frac{2\pi}{3})i_3 \tag{2.18}$$

Therefore, the motor torque is determined as a function of the phase currents and rotor displacement. In Section 2.3.2, the simplification of the nonlinear differential equations that described the dynamic behavior of the PMSM is introduced.

2.3.2 Transformation of the Dynamic Equations

Equations (2.12), (2.13), (2.14), and (2.18) can be simplified in a more manageable form for obtaining solutions. These equations can be simplified by using a general mathematical transformation known as the *d*-*q* transformation. The *d*-*q* transformation uses the properties of trigonometric identities to remove the sinusoidal terms that appear in the equations due to the back EMF. The transformation can be represented in terms of the electrical angle θ between the

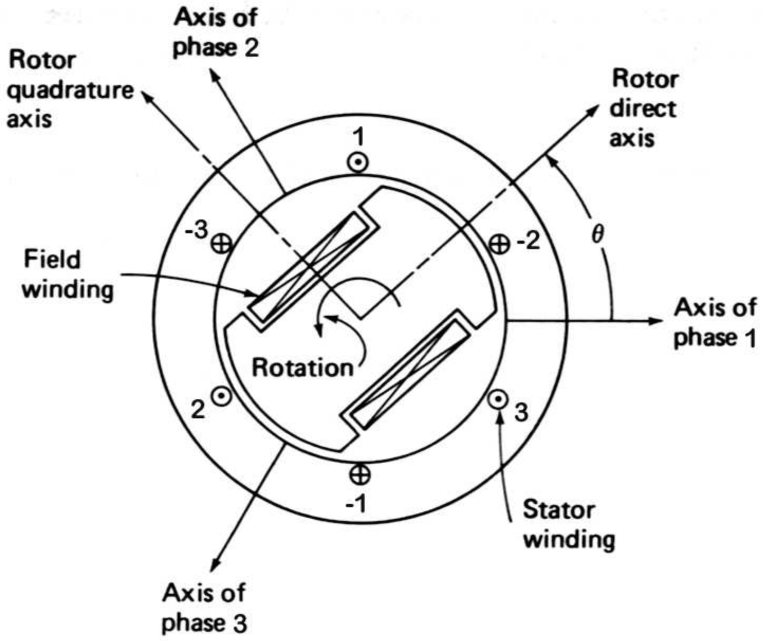

Figure 2.9: Brushless servo system [25]

rotor direct axis and the stator axis 1 as shown in Figure 2.9. For sinusoidally distributed windings, the following *d*-*q* transformation, which is also referred to as the Park's transformation, is used for convenience [35].

$$\begin{bmatrix} S_d \\ S_q \\ S_0 \end{bmatrix} = \sqrt{\frac{2}{3}} \begin{bmatrix} \cos\theta & \cos(\theta - 120^\circ) & \cos(\theta + 120^\circ) \\ -\sin\theta & -\sin(\theta - 120^\circ) & -\sin(\theta + 120^\circ) \\ \frac{1}{\sqrt{2}} & \frac{1}{\sqrt{2}} & \frac{1}{\sqrt{2}} \end{bmatrix} \begin{bmatrix} S_1 \\ S_2 \\ S_3 \end{bmatrix} \tag{2.19}$$

where the subscripts d, q, 0 correspond to the fictitious windings rotating with the rotor, and S represents voltage, current, or flux linkage.

Applying Park's transformation to Equations (2.12), (2.13), and (2.14), the new set of equations are

$$V_q = Ri_q + (L - M)\frac{di_q}{dt} + n(L - M)i_d\frac{d\theta}{dt} + nk_e\frac{d\theta}{dt} \tag{2.20}$$

$$V_d = Ri_d + (L - M)\frac{di_d}{dt} - n(L - M)i_q\frac{d\theta}{dt} \tag{2.21}$$

$$V_0 = Ri_0 + \frac{d\lambda_0}{dt} \tag{2.22}$$

In addition, Park's transformation is now applied in Equation (2.18) for the electromechanical torque as shown in

$$T = \frac{3}{2} n k_e i_q \tag{2.23}$$

The equations that we obtained here are used to simulate the PMSM drive. Solving the new equations is obviously a much simpler task than attempting to solve Equations (2.12)-(2.18). The solution of the system of equations in the rotating frame must be transformed back into the solution in terms of the actual variables. This can be done by using the inverse of Park's transformation as follows [25]

$$\begin{bmatrix} S_1 \\ S_2 \\ S_3 \end{bmatrix} = \sqrt{\frac{2}{3}} \begin{bmatrix} \cos\theta & -\sin\theta & \frac{1}{\sqrt{2}} \\ \cos(\theta - 120^\circ) & -\sin(\theta - 120^\circ) & \frac{1}{\sqrt{2}} \\ \cos(\theta + 120^\circ) & -\sin(\theta + 120^\circ) & \frac{1}{\sqrt{2}} \end{bmatrix} \begin{bmatrix} S_d \\ S_q \\ S_0 \end{bmatrix} \tag{2.24}$$

2.3.3 Mathematical Model of the Nonlinear Test Bed

The mechanical design includes the mechanical test components of the testing system, such as the brake, clutch, couplings, and load motor. The schematic diagram in Figure 2.10 illustrates how the mechanical components in the test bed can be rearranged depending on the desired test purpose and procedure. If the test actuator includes a gear train, the load source will require a gear train with a higher power rating.

The linear dynamic equation for the test motor is

$$T_m = J_m \frac{d\omega_m}{dt} + B_m \omega_m + T_a \tag{2.25}$$

where J_m is the inertia and B_m is the viscous friction of the test motor. T_m is the electromotive driving torque generated at the test motor. ω_m is the desired speed of the test motor. T_a is the measured torque from the torque sensor. Also, T_a can be represented as

$$T_a = J_l \frac{d\omega_l}{dt} + B_l \omega_l + T_e \tag{2.26}$$

where J_l stands for the total inertia of load motor, couplings, brake, clutch, and torque sensor shaft. B_l is considered as the friction coefficient of load motor, and T_e is the electrical driving torque generated at the load motor. The load motor sets the rotational speed of the system during testing. The motion controller controls the electrical driving torque, T_e, and the torque sensor feeds back the measured torque, T_a, as a reference signal. If Equations (2.25) and (2.26) are combined together, then, the linear dynamic equation for the test motor and the load motor becomes

$$T_m = (J_l + J_m) \frac{d\omega_l}{dt} + (B_l + B_m)\omega_l + T_e \tag{2.27}$$

where ω_l represents the speed of the load motor. Equation (2.27) is obtained only if ω_l equals to ω_m. The whole structure will rotate with the speed of the load motor.

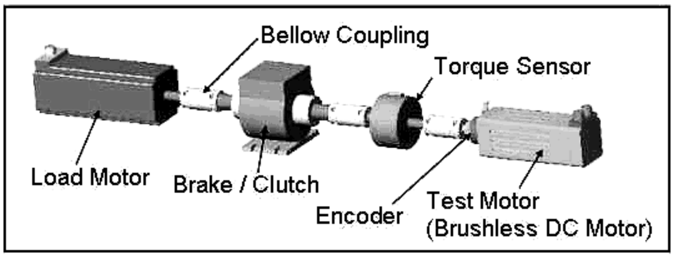

Figure 2.10: A schematic conceptual diagram of actuator test bed

In order to decide the control gain of the system, the dynamic linear model of the electric machine is derived. The set of differential equations for a PMSM given in Equations (2.20) and (2.21) becomes

$$
\begin{aligned}
\frac{di_q}{dt} &= -\frac{R}{L-M}i_q - ni_d\omega - \frac{nk_e}{L-M}\omega + \frac{1}{L-M}V_q && (2.28)\\
\frac{di_d}{dt} &= -\frac{R}{L-M}i_d + ni_q\omega + \frac{1}{L-M}V_d && (2.29)
\end{aligned}
$$

Because the controller gains are decided based on the system inertia, damping factor, the ratio of the resistance and inductance, and the rotating speed of the system, the state space form was established using Equations (2.27), (2.28), and (2.29). The driving torque, T_e, is not included because this term is considered as a disturbance. Also, recall that the torque generated by the PMSM is expressed in Equation (2.23). Combining Equations (2.27), (2.28), (2.29), and (2.23), the state space form can be obtained

$$
\begin{bmatrix} \dot{i}_q \\ \dot{i}_d \\ \dot{\omega} \end{bmatrix} = \begin{bmatrix} -\frac{R}{(L-M)} & 0 & \frac{nk_e}{(L-M)} \\ 0 & -\frac{R}{(L-M)} & 0 \\ \frac{3}{2}\frac{nk_e}{J_{eq}} & 0 & -\frac{B_{eq}}{J_{eq}} \end{bmatrix} \begin{bmatrix} i_q \\ i_d \\ \omega \end{bmatrix} + \begin{bmatrix} \frac{1}{(L-M)} & 0 \\ 0 & \frac{1}{(L-M)} \\ 0 & 0 \end{bmatrix} \begin{bmatrix} V_q \\ V_d \end{bmatrix} \quad (2.30)
$$

The total inertia of the test system is J_{eq} and the total damping factor in the test motor and load motor is B_{eq}. The state space matrix forms can be transferred to the transfer function form. Equations (2.31) and (2.32) show the state space form to decide gains.

$$
\begin{aligned}
\dot{x}(t) &= Ax(t) + Bu(t) && (2.31)\\
y(t) &= Cx(t) + Du(t) && (2.32)
\end{aligned}
$$

The matrices A, B, C, and D are determined as shown in Equation (2.33). These values are obtained by plugging the values of Table 2.1 in Equation (2.30).

$$
A = \begin{bmatrix} -2.8949 & 0 & -171.23 \\ 0 & -2.8949 & 0 \\ 312.41 & 0 & -0.1758 \end{bmatrix}, \ B = \begin{bmatrix} 567.8 \\ 0 \\ 0 \end{bmatrix}, \ C = \begin{bmatrix} 1 & 0 & 0 \end{bmatrix}, \ D = 0 \quad (2.33)
$$

Then, the root locus is drawn based on the transfer function with a single input as shown in Figure 2.11. From this plot, there are three poles and two zeros, and the dominant pole, which is the closest one to the imaginary axis, approaches the zero on its right as the proportional gain increases. The detailed drawing on the right in Figure 2.11 explains this. Therefore, the proportional gain should be small to avoid the system becoming unstable. Also, two imaginary poles meet at the point "A" and the proportional gain value at this location is one, which is the closest integer number of a controller gain. In order to increase the stability of the system, a derivative gain is added. The integral gain is based on the feedback parameter associated with the steady state error.

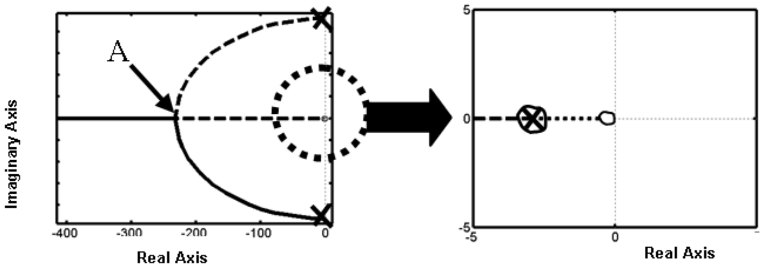

Figure 2.11: Root locus used to decide the control gains

2.3.4 Development of Two Performance Maps in Simulation

The PMSM system model obtained for simulation in Section 2.3.3 is modified for this actuator application. All of the values used for each variable are specified in Table 2.1. This demonstration illustrates the use of the PMSM in a closed-loop speed and current control on 25 Nm torque at 600 RPM which is designed in [47]. When the system model (i.e., motor and test bed components) is tested in the Matlab simulation, some portions can be modified with proper block sets to describe the action on the model. All of the values used in each variable are specified in Matlab simulation blocks. One of the given inputs, torque, is varied from 1 Nm to 20 Nm static constant loads. The other three inputs are the electrical connections of the machine's stator. The Permanent Magnet Synchronous Machine block assumes a linear magnetic circuit with no saturation of the stator and rotor iron [71].

Property	**Measure**	**Unit**
No. of Poles	12	pc
Peak Current	17.2	Amps
Base Voltage	120	Volt
No Load Speed	650	RPM
Peak Torque	26.3	Nm
Max. Cont. Stall Torque	5.1	Nm
Inertia of the Rotor	7.8×10^{-4}	kgm^2
Terminal Resistance	5.8	Ω
Terminal Inductance	20.5	mH
Torque Constant	1.52	Nm/Amp
Voltage Constant	159.66	V/KRPM

Table 2.1: PMSM parameter values

Two of the example simulations are described in this section. The plots shown in Figure 2.12 and 2.13 will represent the efficiency performance map and the temperature performance. All of the performance maps including these two must undergo further definition both analytically and experimentally to improve their usefulness in decision making for intelligent actuators.

The efficiency is the ratio of output power to input power with the assumption that the measurement error of these two quantities is ignored. The input power is divided into output power and power loss. The power loss consists of copper loss and core loss in this simulation. The copper loss may be determined for any condition of operation if the winding currents and their resistances are known.

The core loss depends on the peak flux density produced in the core and in turn depends on the terminal potential difference. In order to implement these terms, the mathematical expression for output power and total power loss are defined as follows

$$Output\ Power = T_e \times \omega_e \tag{2.34}$$

$$Power\ Loss = \frac{\omega_e^2}{R_c}[(L_1 I_1)^2 + (L_2 I_2)^2 + (L_3 I_3)^2] + R_s[I_1^2 + I_2^2 + I_3^2] \tag{2.35}$$

where R_c is the resistance of the rotor core, and R_s is the resistance of the winding. L_1, L_2, and L_3 are the root mean square values of inductance. I_1, I_2, and I_3 are the root mean square values of excited currents in three phases. T_e is the electrical torque generated from the excitation of phase currents, and ω_e is the rotor speed. Several parameters can affect the efficiency of the motor, but the most important factors are load torque and rotor speed as shown in Figure 2.12. The plot is obtained for steady state constant load at each constant speed. Efficiency depends on the increase in speed above the reference speed and the desired continuous torque. There exists an optimum rated speed to get the highest efficiency, which is around 200 RPM in this case.

As one of the operational criteria, the torque-speed curve is dependent on temperature. The torque speed curve is the most meaningful performance graph to show the output capacity of an actuator. To cover a more general situation, one more governing parameter such as temperature needs to be included. Temperature is an important parameter to describe the actual condition of a prime mover and is a principal cause of failure [96]. Prime mover (i.e., an electromechanical motor) temperature rise is a result of energy losses from various sources, and is affected by the ability of the motor to dissipate heat and the effectiveness of the cooling system of the prime mover to remove that heat. In this study, motor temperature

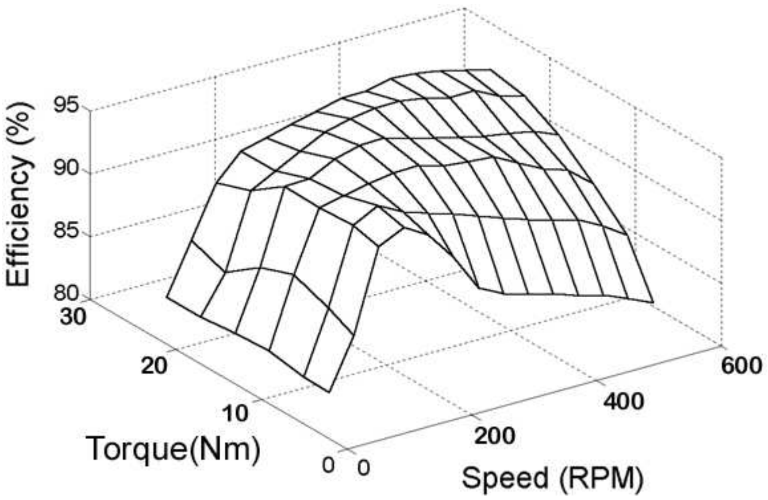

Figure 2.12: Efficiency plot from simulation

is estimated by adding an interactive resistance model in the PMSM Simulink block diagram model as shown in

$$R_s = R_0(1 + a_s(T - T_0)) \tag{2.36}$$

where T is the stator winding temperature, a_s is the temperature coefficient of resistance, and R_0 is the resistance at a temperature of T_0 [53]. Figure 2.13 is obtained from this simulation for temperature variations relative to torque and speed. We can see the temperature gets higher as the motor's maximum torque and maximum continuous speed increases.

The simulation study above confirms the validity of the model for both steady state and dynamic conditions. However, these performance maps do not provide transient response. That would be needed for fault tolerance. Although the basic linearized equation of the model is used, the usefulness of the performance maps has been established, and thus, the analytical study of modeling an electric machine has been performed. The dynamic modeling equations including nonlinear

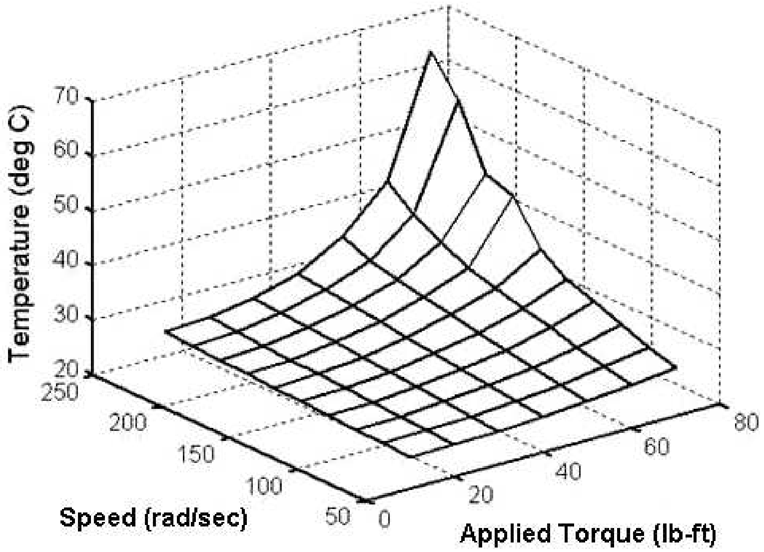

Figure 2.13: Temperature plot from simulation

terms are referred to Hvass and Tesar [42]. Based on this simulation study, ten performance maps will be developed though experiments.

Chapter 3

Actuator Criteria Development

3.1 Introduction

From discussions with electromechanical motor suppliers, it is apparent that only general performance descriptions are provided. Examples of these are motor power, torque-speed relationship, motor efficiency, etc. Most of these parameters are one-dimensional or two-dimensional at the most.

In reality, an electromechanical motor has a multitude of parameters that affect overall performance. A detailed understanding of these cross couplings and parameters is an essential first step towards increased performance. Development of these criteria and the relationships among them is the foundation to this problem. An initial listing of l0 actuator performance criteria is given in Table 3.1. For example, the torque generated by a motor is closely tied to its temperature. Understanding of this relationship allows us to address the cooling needs of the actuator. Also, of interest is the acceleration response of a motor under a given load. Analysis of this property can provide us with an operational acceleration margin that can tell us how fast the acceleration follows the input torque command (i.e., in terms of step input). The difference between real output power and theoretical power computed via an analytical model is important for CBM. Such information can also allow us to anticipate power drop at higher temperatures. Superimposed cyclic variations in the normal load (called torque ripple) affect actuator performance. This torque ripple has a distinct sound signature that can

Criteria	**Descriptions**
Operational Margin	Indicates the maximum speed and torque with dynamic loads.
Temperature	Higher torque builds up high temperature in a short time.
Efficiency	Output power divided by input power. Max efficiency is at rated torque and speed.
Motor Losses	How much copper and core losses are generated.
Acceleration	Limit of acceleration at various levels of torque.
Torque Ripple	Percentage of cyclic variation in the output torque.
T - i Ratio	The effect of magnetic saturation to torque-to-current ratio.
Rise Time	How fast the response follows the input torque signal.
Magnetic Flux Density	Magnetic flux density is deteriorated in higher temperature.
Max Magnetic Flux Energy	Produce Hysteresis loop and obtain $(BH)_{\text{max}}$ by measuring magnetic flux density.

Table 3.1: Initial set of actuator criteria

be detrimental for low noise applications such as deployment on submarines. A detailed description of the proposed actuator criteria is presented in the next section. This report addresses electromechanical motor criteria. Additional research is ongoing to expand the range of criteria that can be used to describe actuator performance (mainly, including gear train, brake, clutch, and sensors). Ten prime mover criteria are described and some of them will undergo further definition both analytically and experimentally to improve their usefulness in decision making for intelligent actuators. Most of them have been shown to be important issues to evaluate the performance of electromechanical actuators. Also, these criteria are reviewed thoroughly and added to supplements for complete coverage of the operational range of the actuator.

3.2 Operational Margin

The torque-speed characteristics have been important to users of general electric machine systems, so that they could graphically trace motor speed regulation in response to load and voltage changes. With the performance profile of the motor, it is possible to estimate the operational range of the motor within the specified temperature and torque limitations. On the other hand, the practical torque response in the application of the motor does not have a steady state response. The responses are more like exaggeratedly nonlinear periodic loads. Figure 3.1 describes a realistic torque response demand in an electromechanical motor in a periodic machine operation. When the impact wrench tool installed on Mr2Arm Robot at RRG is operated to tighten and loosen bolts, the nonlinear loads are repeatedly applied to the bolt head. In this case, the operational margin criteria, related in a torque-speed curve, will guide an operator to manage the control parameters.

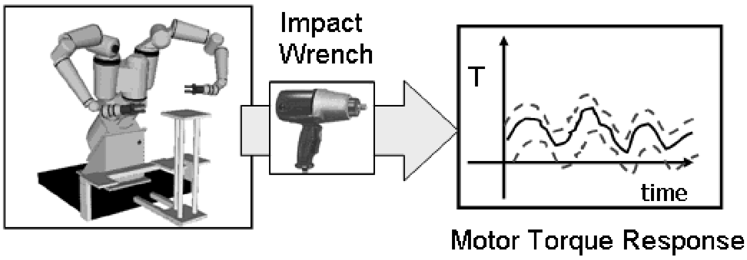

Figure 3.1: Creating a periodic loading in use of impact wrench

A typical torque-speed curve for a permanent magnet DC motor shows the expected torque performance of the motor for a specific duty cycle at a given speed presented in Figure 3.2. The continuous operating region is determined by operating the motor to the maximum allowable winding temperature at various speeds and recording the output torque. The duty cycle is characterized by cycle times, cycle durations, and load. The intermittent operating region is defined by a period of constant loadings followed by an interval of no load. Also, the steady state model for the motor can be used to derive the torque-speed curve directly.

However, motor users can not depend on this description of the torque output with applications which have varying speeds combined with periodic nonlinear loading because general torque-speed plots, obtained by a static load such as a brake, are heavily effected by dynamic loads. The alternating dynamic loads and speeds are expressed as root mean square values because they generate alternating wave motion. Also, they must be applied for several minutes in order to give enough time to characterize the input (torque or speed). Since torque and speed have a causal relationship, one of these inputs should be dependent on the other at a certain condition and the other will have a nonlinear varying value.

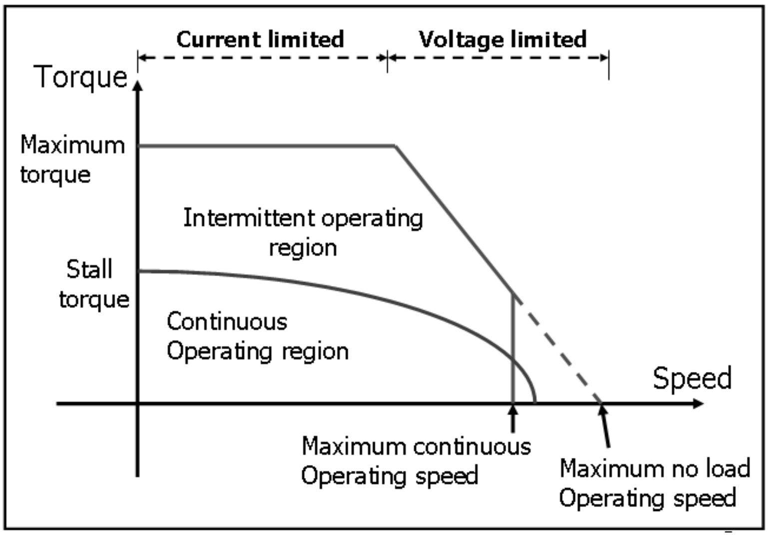

Figure 3.2: General torque-speed curve

On the test bed, the test motor will be tested based on the variation of the load motor. The test motor will govern the whole system as a torque control and the load motor will be run with a speed control in this research. While the load motor runs at a certain static speed, the load torque will be applied to it through several torque profiles from the test motor. The variations of torque, speed, current, voltage, and temperature will be measured at this time. Then, the operational margin will lead to the test motor with the best performance and avoid the limits of operating parameters.

3.3 Efficiency

In order to evaluate energy savings of an electromechanical motor, the entire energy converting mechanism should be considered as one of the actuator criteria. The electromechanical motor drive system starts from electric power system terminals at the plant via the motor drives, and includes the driven mechanical device. Thus, the motor efficiency is a measure of the effectiveness with which a motor converts electrical energy into mechanical energy.

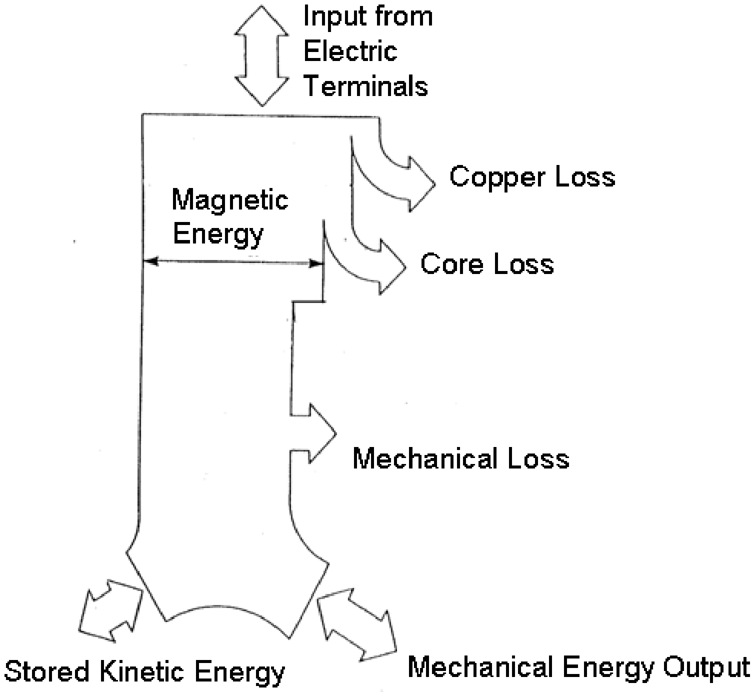

Figure 3.3: Energy flow diagram

There are many methods pertinent to motor efficiency evaluation in the literature [41]. The most obvious way is to connect the motor to a known load and measure the electrical power into the motor. Assuming we know both the power (or work) output and power going in, the ratio of these is efficiency. A mathematical way of stating this is shown below:

$$Efficiency = \frac{Power\ Output}{Power\ Input} = \frac{Power\ Output}{Power\ Output + Losses} \tag{3.1}$$

Losses can occur at the stator (stator copper loss, core loss and stator stray loss) and at the rotor (friction and windage, rotor stray loss). If there is no power loss in the system, the generated power is expressed by the conversion from electrical power to magnetic power and from magnetic power to mechanical power as shown in Figure 3.3. However, power losses are always present and they are mathematically separated from the storage mechanism. The losses will be explained in Section 3.4 in detail. The input power, which is the electrical energy, is expressed as follows

$$Power\ In = V_{1,rms}I_{1,rms} + V_{2,rms}I_{2,rms} + V_{3,rms}I_{3,rms} \tag{3.2}$$

where $V_1,\ V_2,\ and\ V_3$ stands for the phase one, two and three voltages supplied to the AC motor. $I_1,\ I_2,\ and\ I_3$ represents the phase one, two, and three currents to operate the motor. Also, *rms* is the “root-mean-square” value, which represents the method of calculation of the waveform data. The calculation works like this:

$$V_{rms} = \sqrt{\frac{\sum_{i=1}^{n} v_i^2}{n}} \tag{3.3}$$

Also, the output power (W) is shown as

$$Power\ Out = \frac{T\ \omega}{9.549} \tag{3.4}$$

where T (Nm) and ω (RPM) is the developed torque and speed as the power output components of the motor. 9.549 is just the unit conversion factor of speed.

3.4 Motor Losses

No matter how complex the combination of the mechanical system is the calculation of the efficiency is simply obtained from Equation (3.1). The best test procedures are fully explained in Method B of IEEE Standard 112-1996 [43]. Identifying the losses is also one of the valuable criteria to improve the actuator performance from the point of view of heat generation. Basically, a no-load test will determine the stator core losses, the mechanical friction and windage losses. The test motor is run on no load at rated voltage and frequency, and then the input electrical power is calculated as the stator primary losses and additional constant losses. At this time, the mechanical output power will be zero because there is no torque output. Once the stator copper losses are determined from the measurements of the derived currents in three phases of the stator windings with the knowledge of the resistance, the constant losses will be obtained from the subtraction of the input power from the stator copper losses. The stator copper losses are determined by the test under load. Moreover, the friction and windage losses are separable from the core losses by reading voltage, current, and power input at rated frequency and at reduced voltage. Efficiency and motor losses are combined together to represent the evaluation of heat effect on the motor.

3.4.1 Copper Loss

Compared to the brushed DC motor, the permanent magnet synchronous motor offers several advantages for applications which require high acceleration and a good torque quality, namely a high torque-to-inertia ratio and an excellent power factor close to unity, since the copper losses are essentially located only in the stator [31]. The copper loss is due to the armature winding resistance [104] as follows

$$P_c = R(i_d^2 + i_q^2) \tag{3.5}$$

where i_d and i_q are d and q axis components of armature current, which are mentioned in Section 2.1.2. Equation (3.5) can be formulated using the resistance R and *rms* value of the armature current I_{rms}. Using $\sqrt{i_d^2 + i_q^2} = \sqrt{3}I_{rms}$, Equation

(3.5) becomes [63]

$$P_c = 3RI_{rms}^2 \tag{3.6}$$

The winding resistance R is obtained by measuring two end wires out of three phases.

3.4.2 Core Loss

As illustrated in Figure 3.4, copper losses constitute for approximately 60% of the total losses. On the other hand, the core losses, in other words, iron losses, accounts for 20-25% of the total losses. The rest of the losses are friction and windage losses, and stray load losses, which are about 10-15% [65]. Copper losses are dependent on the loads, but the core losses, generated in active iron and other metal parts, are no-load losses.

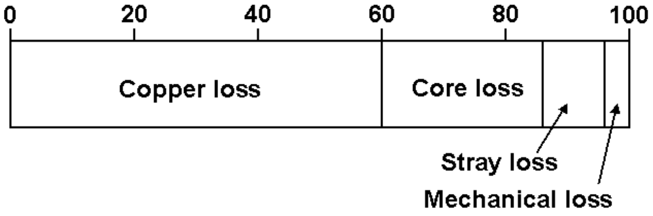

Figure 3.4: Energy loss components for a brushless DC motor

The core losses are the result of energy dissipated when the rotating magnetic field of the motor is applied to the stator core. Note that the rotor core loss is quite small compared with the stator core loss. Especially, in a permanent magnet synchronous motor, the stator core loss only exist because the slip[1] frequency for this motor equals to zero [45]. The core losses P_i in ferromagnetic materials

---

[1] The difference between the synchronous speed and the full load motor speed is called slip. The synchronous speed is the speed of the rotating electrical field, not the actual rotor speed.

are separated into a hysteresis component P_h and a dynamic or eddy current loss component P_d, i.e.,

$$P_i = P_h + P_d \tag{3.7}$$

The hysteresis loss is caused by very localized irreversible changes during the magnetization process, which make it dependent only on the maximum induction. While the flux density varies cyclically and the magnetic state forms a locus in the $B - H$ diagram, the hysteresis loss results as the material changes its magnetic state. The eddy current loss is also caused by the variation in flux densities, which locally induces currents in the laminated core [21]. According to [59], [91], the fundamental core loss density is expressed in the following form for sinusoidally varying magnetic flux density with angular frequency ω_s:

$$P_i = k_{hy}\omega_s B_m^{\alpha} + k_{ed}\omega_s^2 B_m^2 \tag{3.8}$$

where B_m is the peak value of the flux density, and k_{hy}, k_{ed} and α are constants determined by the manufacturer provided loss data.

Based on Urasaki et. al. [104], the core loss can also be formulated as follows.

$$P_i = \frac{\omega_e^2(\lambda_d^2 + \lambda_q^2)}{R_i} \tag{3.9}$$

where λ_d and λ_q are the stator winding d and q- axis phase of magnetic flux linkages. Also, R_i is the core loss resistance and ω_e is the stator winding voltage electrical angular speed (synchronous speed)[2]. The square of speed-EMF $\omega_e^2(\lambda_d^2 + \lambda_q^2)$ can be calculated by using the electrical input power P_{in}, RMS value of the voltage in the stator winding V_{rms}, and RMS value of the current in the stator

---

[2] ω_e is the electrical angular speed and ω_m is the mechanical angular speed.

winding I_{rms} [104]

$$\omega_e^2(\lambda_d^2 + \lambda_q^2) = (v_q - Ri_q)^2 + (v_d - Ri_d)^2 = 3V_{rms}^2 - 2RP_{in} + 3R^2I_{rms}^2 \qquad (3.10)$$

Note that the core loss can be measured in no-load condition. In this report, Equation (3.8) will be used to calculate the core loss in Section 5.1.2.

3.5 Rise Time

As one of the actuator criteria, the motor users in industry might also be interested in the rise time for a given input command. The rise time, as one of the transient responses, tells users how fast they can change the dynamic state of a given load (force, inertia, etc.) and how well the responses follow the desired motion program. The rise time mostly depends on the mechanical inertia and the performance of the controller. The motion controller will be included as parasitic equipment for criteria evaluation because the combination of a prime mover (i.e., electric motor) and an amplifier must be considered as a system including the motion controller.

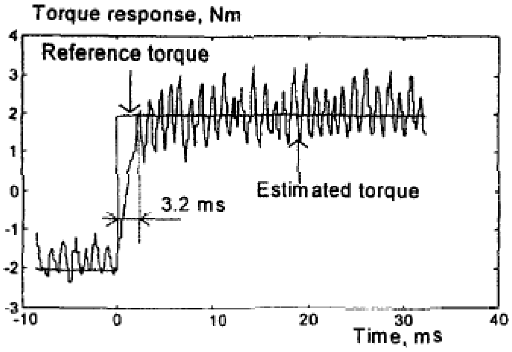

Figure 3.5: Step response of torque at standstill (experimental result) [78]

From a no-load test, the speed rise time will be obtained. The test motor runs at a certain speed without any connection of load and the amplifier provides a ceratin voltage in a steady state. Then, the motor speed will be increased to a certain desired value. The time difference between these two speeds is the rise time for the motor speed. Also, the torque rise time is estimated by the same method but in this case, the test motor needs a brake load. The brake load is developed by the load motor through the motor shaft and generates an increased torque at a certain speed. The measurement of the time difference between the lower torque and higher torque will be the torque rise time. Figure 3.5 shows the torque response for a step change of the reference torque from -2 to 2 Nm when the rotor is blocked. As shown in Figure 3.5, the torque response is very fast (in a unit of millisecond) and there is no overshoot. In this report, the torque rise time for a permanent magnet synchronous motor is driven based on different speeds and torque increments.

3.6 Torque-Current Ratio

The basic equation for torque is derived from the equation for force, which is Equation (2.1), in a manner similar to that used in obtaining the voltage equation. The torque produced by a motor with a given winding and physical geometry is directly related to the voltage it produces when the rotor is externally driven, or when the motor is used as a generator. After the appropriate substitutions are made, the torque equation becomes

$$T = K_T I \tag{3.11}$$

where K_T stands for torque constant (or torque sensitivity) and is expressed in Nm/A. T is the developed motor torque and I is the average current in the motor.

However, the relation between the torque and current of the motor might not be constant and it will be identified experimentally based on Torque-Current Ratio criterion. Figure 3.6 shows the torque and current responses for the motors of the third and fifth axes of the KUKA KR150 [99]. All wrist axis motors are identical but each of them responds in a different way depending on the motor velocity, acceleration, torque and inertia. Thus, the torque constant K_T becomes a nonlinear function of current, torque and speed.

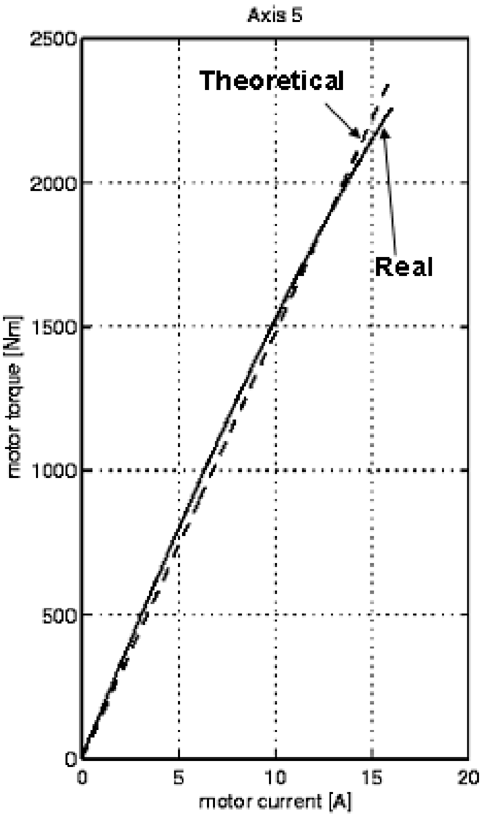

Figure 3.6: Current and torque responses of the permanent magnet synchronous motors in axis 5 of KUKA KR150 robot. [99]

Mademlis and Agelidis [54] experimentally obtain the torque and current plot and suggested the method to determine the maximum torque-to-current condition and ratio. They report the influence of magnetic saturation in maximum torque-current ratio controlled Interior PM (IPM) motor drives. The magnetic saturation will be explained in Section 3.9. The experimental results, taken from a three phase 3.4 kW IPM motor drive, are clearly presented to verify the nonlinear relation between the torque and current.

3.7 Torque Ripple

Permanent magnet motors are usually driven in one of two ways. Sinusoidal currents are applied in three phase windings when the motor has a sinusoidal back EMF (electromotive force), and rectangular currents are applied in three phase windings when the back EMF has a trapezoidal shape. If the electrical commutation is implemented perfectly, each of these drive schemes is capable of producing ripple-free torque. However, in reality, permanent magnet motors never exhibit perfectly sinusoidal or trapezoidal back EMF's [16].

The commutation points for the motor in Figure 2.3 are shown in Figure 3.7 (a). These commutation points center the peak of the back EMF waveform in the commutation zone, and provide equal sharing of the motor phases in the process of producing torque. However, due to the commutation points, the torque output over each commutation zone might be varied by 50% for a constant current input. To improve this variation of torque during commutation, (called torque ripple), consider the scheme shown in Figure 3.7 (b). In this case, the motor is commutated twice as often during one revolution by using the negative half of the back EMF waveform as well as the positive half. The torque now falls approximately 13% below the peak [47]. For a three phase motor with the simple commutation scheme shown, this is the torque ripple that can be obtained with the back EMF waveform of this particular brushless motor.

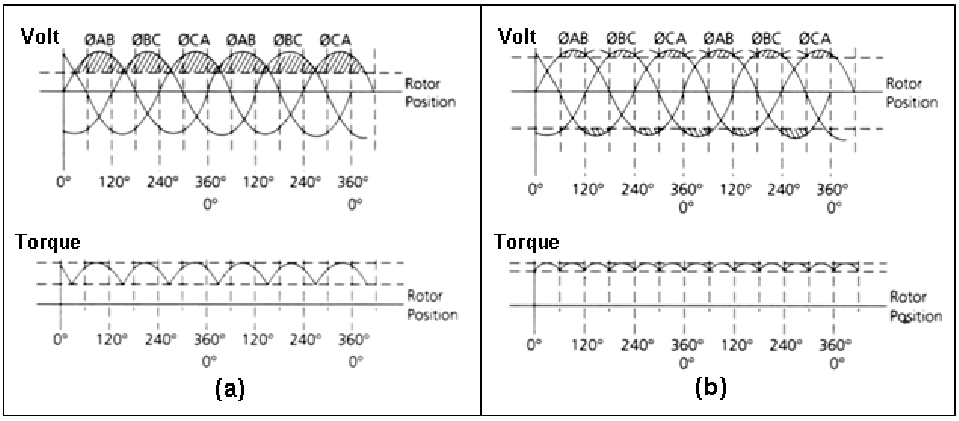

Figure 3.7: Torque ripple as a function of rotor position with constant current input [47]

There are other causes that generate parasitic torque ripple in a motor. The power electronics used to drive the motor have limitations that keep it from producing the required current waveform, especially as speed or load torque increases. In addition to these limitations, a permanent magnet motor often exhibits cogging torque that directly contributes to torque ripple. The cogging torque is independent of motor excitation and is caused by the interaction of the permanent magnet flux and the saliency of the stator [8], [33].

The torque ripple caused by the switching action of the commutation is calculated as follows

$$\%\ of\ torque\ ripple = \frac{amplitude\ of\ ripples}{average\ torque} \times 100 \tag{3.12}$$

The torque ripple will be developed from an experimental setting with static loading generated by a brake. By providing more current to the motor stator windings, keeping speed constant, the monitored torque output will show some ripple.

Moreover, the ripple test will show that the torque ripple is hardly changed as the temperature deviates because the ripple depends only on the motor geometry and the applied current.

3.8 Acceleration

Many robot applications require operation under dynamically changing conditions regarding the exact target position. For example, there are situations where the information about the target location is only available after the movement has begun or the original target position has been redefined after start. Such changes in target position either due to physical movement of the target or due to additional sensor information provided during the motion require on-line updating of the reference trajectory. Furthermore, in many applications it is very important to obtain a reference trajectory for smooth motion under constraints of maximum limiting values of velocity, acceleration, and jerk at the same time [52]. This requires monitoring the velocity, acceleration, and jerk signals to deal with abrupt changes to them. Figure 3.8 shows these responses for an induction motor. Shi et. al. [88] represents a method to control the acceleration to improve the dynamic performance of the motor.

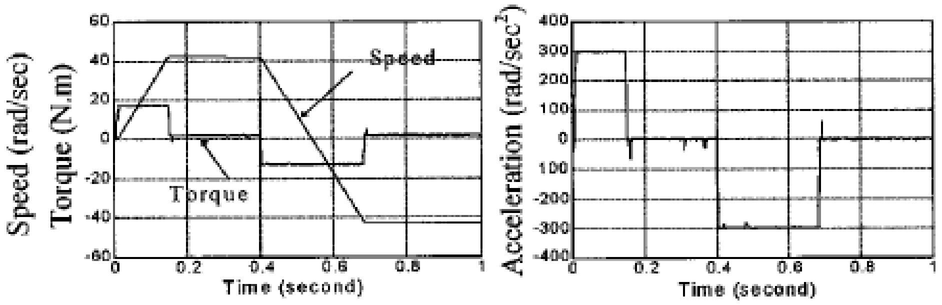

Figure 3.8: Speed, torque, and acceleration of 0.75 kW induction motor [88]

Acceleration defines how quickly the axis or axes come up to speed and is typically limited to avoid excessive stress on the motor, mechanical system, and load. A separate, slower deceleration is useful in applications where gently coming to a stop is most important. A high acceleration capability requires a high maximum torque combined with a constant polar moment of inertia for the motor and is expressed as follows

$$\alpha = \frac{d^2\theta}{dt^2} = \frac{1}{J}(T_e - F_b\frac{d\theta}{dt} - T_m) \tag{3.13}$$

where α is the acceleration, θ is the angular position, T_e is the electrically generated torque, F_b is the friction coefficient, and T_m is the load torque. Also, the acceleration capability of a permanent magnet motor is limited by the demagnetization of the magnets [90]. This can result from high temperature of the magnets and the winding insulation. For example, at a temperature around 150 $°C$, acceleration deteriorates as the torque generated by a reduced magnetic flux is lower due to higher temperature.

3.9 Max Magnetic Flux Energy

The waveform of the magnetic field in the core requires an exciting current in the stator windings. The nonlinear relationship between magnetic flux and current in Figure 3.9 means that the waveform of the exciting current differs from the sinusoidal waveform of the flux. A curve of the exciting current as a function of time can be found graphically from the desired magnetic characteristics as illustrated in Figure 3.10. Since magnetic flux density, B, and magnetic field intensity, H, are related to magnetic flux, φ, and current, i_φ, by known geometric constants, the hysteresis loop can be drawn using $\varphi = BA$ and $i_\varphi = Hl/N$ as shown in Figure 3.9.

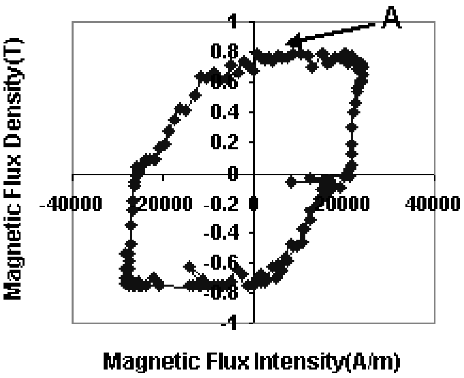

Figure 3.9: B-H curve of PMSM

At very low frequencies, the magnetic flux linkage and current loop can be obtained from the similar shape of the B-H loop (see Figure 3.9). At higher frequencies, the B-H loop is broadened due to the effect of eddy currents. Slemon explains this phenomenon more carefully in his book [92].

When the exciting current has more than one cycle and a constant RMS value, there is almost no variation of B with H. The magnetic material starts to be magnetized by the variation of magnetic flux density from the unmagnetized point as shown in Figure 3.11. If we look at Figure 3.11 more carefully, the arrow-head indicates the direction of movement of the point representing the magnetic state of the magnetized material as H alternates slowly [92]. At point 'A' in Figure 3.9, the magnetic flux is not increasing any more. It is said to be "Saturated". Then, as the strength of the magnetic field is reduced, the material does not go back to its former state because this process is irreversible. When the magnetic flux strength, which is the same as the magnetic field intensity, is zero, the value of the magnetic flux density is called the residual magnetic flux density. From this point, the curve will follow the demagnetization process as illustrated in the second quadrant. When

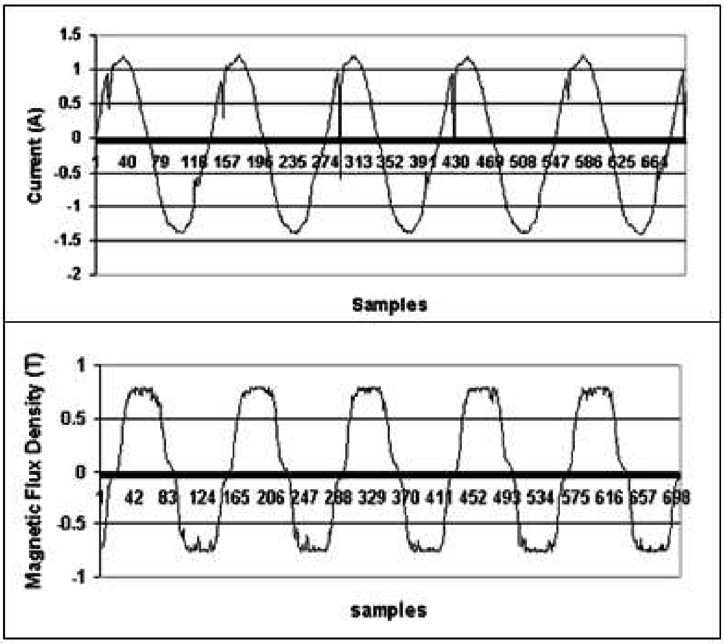

Figure 3.10: Current and magnetic flux density data in 150 RPM, 0.75 Amps (RMS)

the magnetic flux density is zero, it is defined by a coercivity force. Now, it follows to the negative direction of the pole. The complete loop is known as a hysteresis loop. Rotating the rotor of the PM motor creates this hysteresis loop at a constant speed.

The magnetic flux energy is defined as the area of the *B*-*H* curve as shown in Figure 3.11. The performance map of magnetic flux energy will be created based on torque and speed. The map will also be affected by temperature. In Section 3.10, changes to the magnetic flux curve depending on temperature will be discussed.

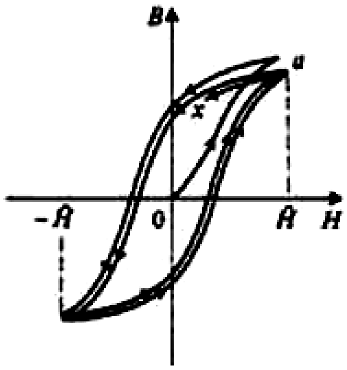

Figure 3.11: Variation of B with H [92]

3.10 Magnetic Flux Density

Tomy Sebastian mentions in [86] that temperature affects PM motors using rare earth magnets (including Nd-Fe-B and Sm-Co) with respect to their torque production capability and on the efficiency of the motor. If a careful design of a PM motor is performed, the irreversible demagnetization is avoidable at elevated temperatures. One of the ways to improve the design of the PM motor is to equip it with a better cooling system. When PM motors are designed to operate in a wide temperature range, the reversible demagnetization of the rare earth magnets due to temperature and the resulting increase in winding resistance influences the resulting maximum torque capability at rated speed and the efficiency of the motor. Figure 3.12 is the experimental result and represents the changes of magnetic flux density with sinusoidal current inputs in three phases. The flux density was saturated at 0.8 Tesla (Solid line in Figure 3.12), and it is reduced to a smaller value (Dotted line in Figure 3.12). Thus, the torque produced from this motor will be affected by the reduction of the magnetic flux density at higher temperatures because the torque is a function of flux and current. This result helps to demonstrate the temperature affects on the performance of the PM motor. In this criterion, the magnetic flux density always has the same maximum saturation value at any speed and reference current. This is because the flux measured by the sensor estimates the magnetic strength of the PM in the rotor.

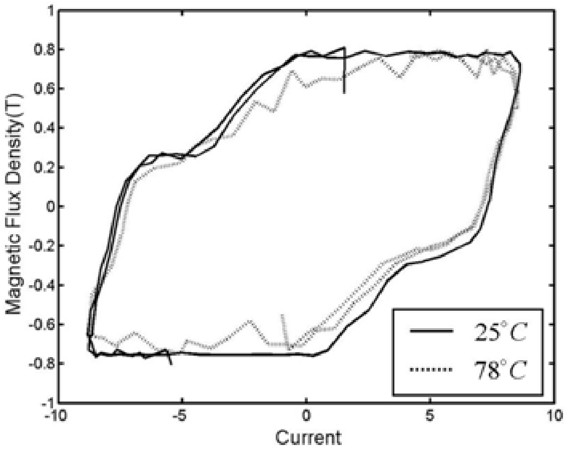

Figure 3.12: Magnetic flux density and current curve at two different temperatures (Solid line: 25°C, Dotted line: 78°C)

3.11 Temperature

Temperature is a sensitive and important parameter to describe the actual condition of an electromechanical motor and is a principal cause of failure. Motor temperature rise is a result of losses from various sources and is affected by the ability of the motor to dissipate heat or the efficiency of the cooling system of the motor. Significant temperature increase can be expected under load versus idle operation. Thus, applied loads with greater inertia will cause additional heat to build up during peak accelerations.

The thermal models for an electromechanical motors have been developed in [11], [38], [53]. Using the models, the temperature rise of a machine prior to

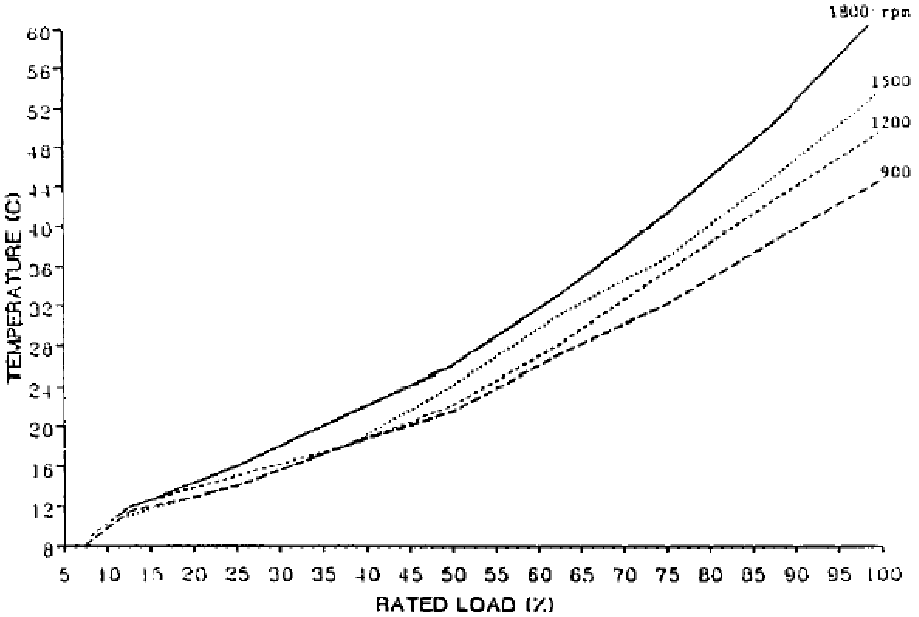

Figure 3.13: Temperature rise of the SRM for 900 to 1800 r/min as a function of load [60]

its construction is predicted and the overall performance is also predicted. Moghbelli et. al. [60] has tested a 10 HP switched reluctance motor (SRM) and measured total losses, efficiency, and temperature rise by changing the rotor speed and load. The temperature of the motor increases as the rotation speed increases as shown in Figure 3.13. In addition, Metwally [58] has measured the full load temperature rise of three phase induction motors. The result shown in Figure 3.14 represents the relationship between temperature rise and time at different values of supply voltage. The applied voltage is changed from 100% to 125% of the rated voltage in steps of 5%.

The stator winding temperature inside a motor can be measured by changing torque output with a fixed value of speed at each point. For the test scenario, four temperature sensors will be attached to the stator core and the three stator

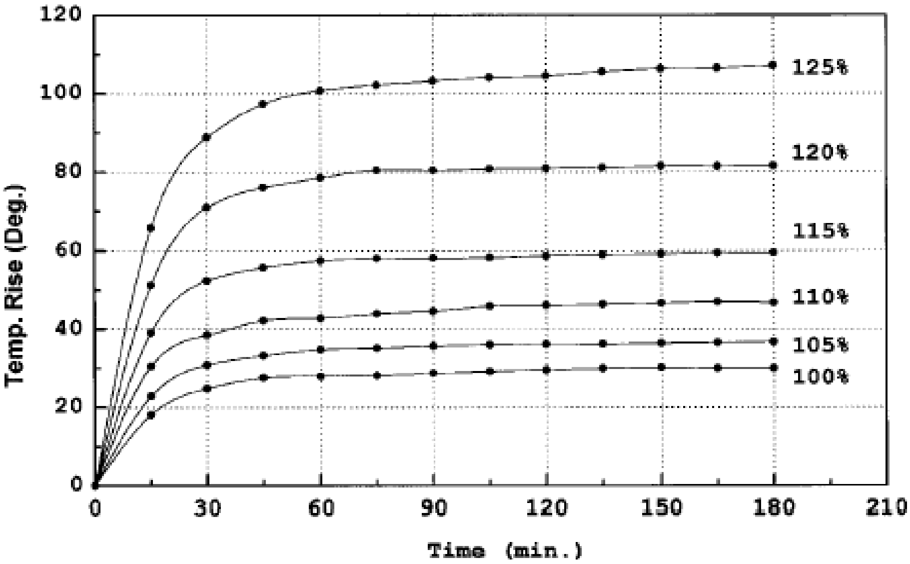

Figure 3.14: Temperature rise at different percent voltages [58]

windings. The converted voltage values obtained from the measured temperature will be one of the most important control parameters to decide the best operational condition for improving prime mover performance.

Chapter 4

Nonlinear Test Bed Development

In order to complete an actuator test architecture that considers all possible situations, a dynamic and nonlinear test environment is required. The Nonlinear Test Bed for Actuators (NTBA) is created to measure and record an array of physical properties during nonlinear load experiments. In order to simulate the most general situations during real operation of the actuator, two different types of loads can be applied: load motor with a programmed sinusoidal load and a constant load produced by a hysteresis brake. The NTBA is validated because the proposed prime mover criteria are accurately obtained through experimentation and are useful in developing the operational performance envelopes. In this section, the procedure to build the test bed is discussed as well as the capability of each component in the test bed to generate the required physical performance information.

4.1 Introduction

With the increased importance of actuator performance in robotic applications, many robot manufacturers have focused on assuring quality, reliability, conformance to design, and application suitability in their actuators. To evaluate the performance of a specific actuator, manufacturers need to thoroughly test the actuator. Morrell et. al. [64] proposed performance metrics for actuator evaluation. They mentioned that quantitative metrics for task performance will improve understanding of an actuator's nonlinear characteristics. More thorough testing can also provide necessary feedback information on the effectiveness of the electromechanical actuator for a specific task. This section describes the design of a new facility that provides extensive, automated test capability of electromechanical actuators.

Many researchers in the robot industry consider the electric motor (prime mover) to be the most important actuator component. Moreover, knowing the motor's capabilities, as discussed in Chapter 2, is important in order to verify design calculations and simulations and to improve future design efforts. Numerous articles describe the testing of actuators by independently testing the motors inside them. Newton et. al. [68] presented dynamometer simulation results for a DC machine with both steady state and dynamic loads. Stone et. al. [98] developed a way to emulate representative industrial loads. In both cases the load was generated using a simple inertia, friction and fixed torque load. The second order load was physically represented by an inertia connected to a driving machine via a compliant shaft. However, the load was only a fixed inertia, so it was impossible to generate highly nonlinear loads on the motor. Under prior research, the Robotics Research Group (RRG) at the University of Texas at Austin developed the Actuator Endurance and Reliability Test Bed including a dynamometer to test a robot actuator under a steady state load using a friction brake [46]. The torque-speed curve obtained from the experimental set-up showed the output curve was limited by a fixed maximum temperature. The torque-speed curve, however, has a different form under different loading conditions. The steady state performance tests of actuators in this test bed were insufficient to describe actuator performance under dynamic loading. Therefore, to complete an actuator test regime that considers all the possible situations, a dynamic and nonlinear environment is required.

This chapter is focused on the development of an experimental facility to test electromechanical actuators and to cover the nonlinear test region. To characterize the performance of each component inside the actuator, the modular type of test bed is necessary. Testing an electric motor with a gear train requires a higher torque rating than the rest of the test bed components. The next section explains the design and development of the Permanent Magnet Synchronous Motor (PMSM) test system in more detail. Section 4.3 describes the implementation of the mechanical and electrical components. Section 4.4 will discuss motion controller and operational software for a PMSM.

4.2 Overview of Permanent Magnet Synchronous Motor Test System

The RRG's initial motivation for building the Nonlinear Test Bed was to find the performance maps for permanent magnet synchronous motors. However, the test bed also had to be flexible enough to be used for a variety of prime movers as well as future research efforts involving Condition-Based Maintenance (CBM). Based on these objectives, the necessary operational characteristics of the test bed are specified. The maximum power is approximately 7.46 kW with a maximum speed up to 5000 RPM. Figure 4.1 shows the nonlinear test bed developed in this research. A schematic diagram of the test bed is shown in Figure 4.2. The diagram shows the signal flow from the sensor readings and the control reference signals are obtained from the motion controller.

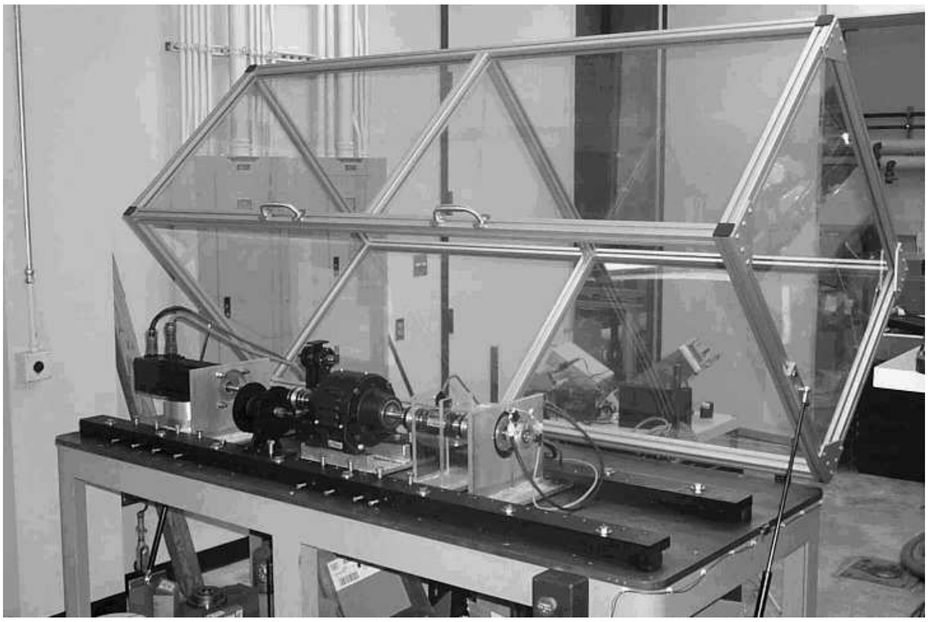

Figure 4.1: Nonlinear test bed

The test bed is designed to overcome misalignment problems caused by manufacturing tolerances and to be modular. The supporting blocks have four threaded screws that transfer the force to the surface of the test bed by finding the height and angle with respect to the horizontal surface of the test bed. The screws for the supporting blocks and the rails serve to accurately position each component. Additionally, the rails are designed to be modular, so a multitude of configurations can be achieved as long as the height from the surface of the test bed to the rotational center is less than 0.1524 meters (or 6 inches). All components are held rigidly against a variety of load profiles by long black steel rails. The rails have 0.0127 meter (or $\frac{1}{2}$ inch) threaded holes on the top to resist force in the vertical direction and 0.0064 meter (or $\frac{1}{4}$ inch) holes in the side to resist force in the horizontal direction. The screws allow for adjusting the alignment.

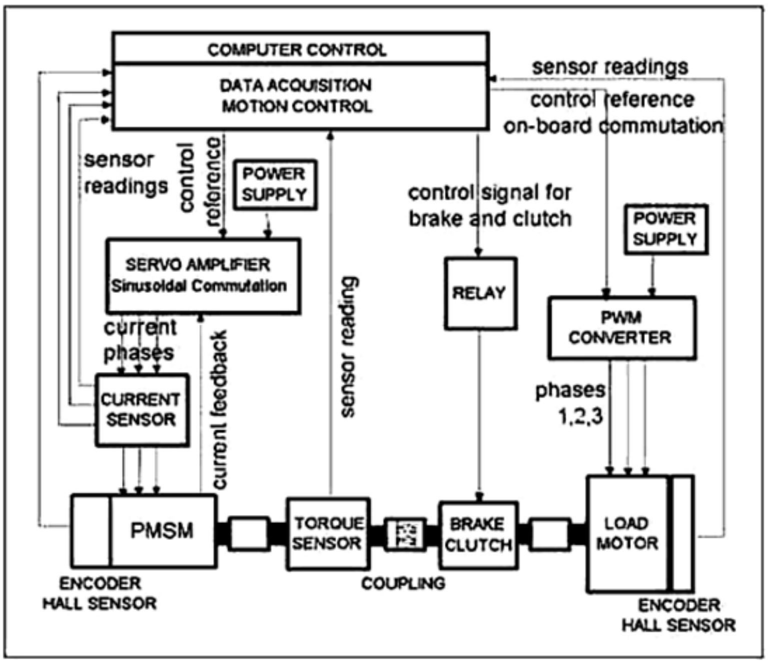

Figure 4.2: A schematic diagram of NTBA

Safety was an additional concern in building this test bed. To stop the operation of the test bed in the emergency situation, an emergency stop switch is built into the test bed. There are two power relays to disconnect the current to the amplifiers for the motors and an additional switch to stop the operation if the enclosure is opened. Also, the clutch is off by default to prevent the transfer of a large force from the load to the actuator under test. Eventually, this test bed will be used to test systems with large amounts of jerk motion so the potential for parts to fly off the system if they are not connected properly or break during testing is high. To protect the user, a large plexiglass enclosure was built that can be placed over the test bed when the system is running.

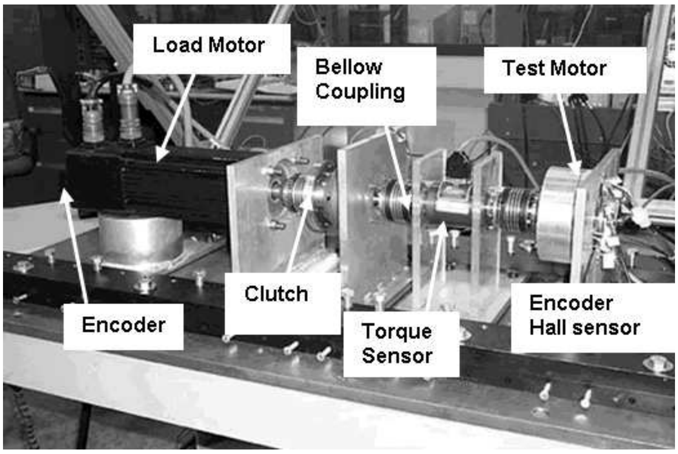

Figure 4.3: Mechanical components of NTBA

The mechanical component set-up for the test bed is shown in Figure 4.3. This test bed is for dynamic testing, so the load motor is used to generate a variety of load types. The four bar linkage creates the nonlinear periodic load. The special load type is selected to express a realistic situation for the given test motor. The mechanical clutch is engaged while the load motor provides a load to the test motor. The torque sensor is used to measure the torque between the load motor and the test motor. The encoders estimate the position, velocity and the acceleration. In addition, three Bellows couplings are used to connect each component to the rest of the system. The couplings were carefully chosen to endure more than 54 Nm in the rotational direction.

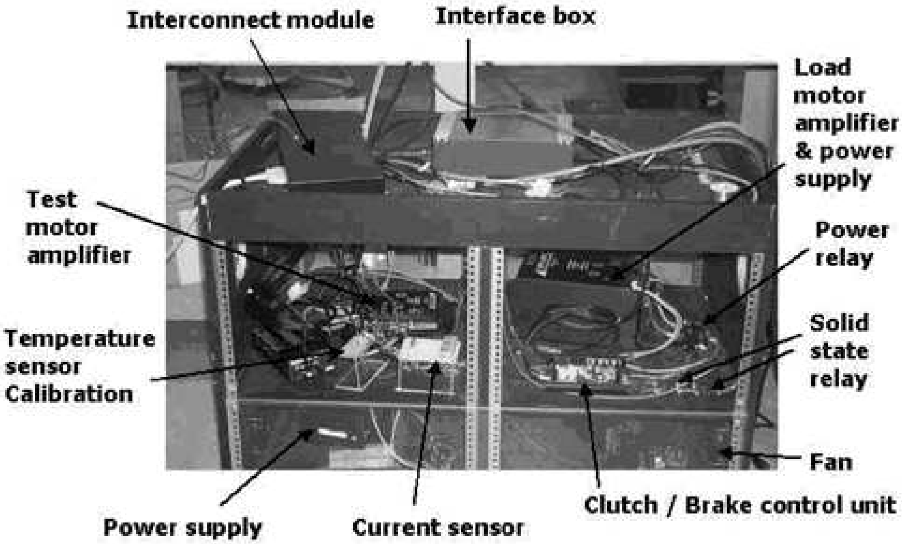

Figure 4.4: Electrical components of NTBA

Figure 4.4 shows the electrical component set-up for the test bed. The frame itself is made of the wood to avoid electrical hazard. The interconnection module is for the connection lines between the motion controller and each mechanical component. The interface box is for the torque sensor. This unit sends the torque signal from the sensor to the controller. The motor amplifiers and power supplies need the heat sink for cooling. During testing, the amplifiers and power supplies will generate a large amount of heat, so the four fans operate to reduce the heat. The solid state relay is used to control the clutch operation. The current sensor measures how much current is flowing through the wire from the amplifier to the test motor. Also, temperature sensors are attached inside the test motor, and the voltage signals transferred from temperature are scaled down by the calibration circuit. All of these components will be explained in detail later.

4.3 Hardware Implementation

The test bed is designed to accommodate actuators and electric motors up to 0.75 kW (or 1 HP) in capacity. As different 0.75 kW systems can have a large variation in torque-speed relationships, the mechanical components of the test bed are designed and selected for both high-speed and high-torque operations. A 4000 RPM, 7.46 kW (peak 5000 RPM and 48 Nm torque) motor is selected as the load motor. Its primary purpose is to provide a programmable dynamic load. The test motor and the load motor are connected through a series of Bellow couplings that are selected for minimal inertia, maximum stiffness, high torque and high speed capacity. In between the mechanical couplings are other components such as a brake, clutch, torque sensor, etc. Each coupling can endure more than 54 Nm in the torsion direction. All components are held rigidly against a variety of load profiles by long steel rails. Set screws are used for the fine adjustment of the pitch and yaw of each component. The current test bed set-up is shown in Figure 4.3.

Three current sensors, two position encoders, four thermistors, and one torque sensor are used to develop the performance data sets and to monitor the test motor state variables in real time. The current sensors measure three phase input currents to the test motor. A 12 bit incremental encoder is used to determine precise rotor position. A 1 kHz bandwidth Surface Acoustic Wave (SAW) torque sensor is used to fully measure the performance of an actuator and to enable torque control of the load motor. The specifications of these sensors will be discussed in detail later.

Figure 4.5: The test motor

4.3.1 Test Motor Selection

Permanent Magnet Synchronous Motors (PMSM) are useful prime movers in the field of robotics, because they have some distinct advantages compared to conventional DC motors that do not have permanent magnets on their rotors. PMSM are an attractive choice for heavy duty applications because large torque output can be obtained during high acceleration and deceleration rates. PMSM is chosen as the test motor for a practical robotic application. PMSMs have high torque and low speed compared with the motors used in manufacturing applications. The parameter values in the test motor are referenced from the Advanced Lightweight Prototype High-performance Arm (ALPHA) project of UTRRG in 1991 sponsored by the Defense Advanced Research Project Agency (DARPA) [56]. The motor inside of the 2 DOF Knuckle Module is used to develop performance criteria from the Nonlinear Test Bed [51].

The PMSM used for testing was provided by Kollmorgen. It has Samarium-Cobalt rare earth magnets, three phase wye connection and built-in Hall effect

Parameter	**Value**	**Unit**
Model number	RBE	03001-A50
Power at peak torque	1.98	kW
Peak torque	28.2	Nm
Max. Cont. Stall Torque	5.1	Nm
No Load Speed	650	RPM
Cont. current	7.6	Amps
Peak current	17.2	Amps
Rotor inertia	7.8×10^{-4}	kgm^2

Table 4.1: Test motor parameter values

devices for electronic commutation. As seen in the Table 4.1, the maximum power is 1.98 kW, the synchronous speed is 650 RPM, and the peak torque is 28.2 Nm. The continuous stall torque of this motor is measured by experiment.

Figure 4.6: The load motor - PMSM

4.3.2 Load Motor Selection

In order to select the load motor, various types of motors were investigated in terms of having a larger torque-speed curve range than the test motor. PMSM brushless DC motor was selected, because it has a larger torque and speed range than any other type of motor. This load motor was also chosen because its inertia is small when compared with an induction and DC brushed motor. Figure 4.6

shows the Kollmorgen GOLDLINE series motors that is used as a load motor in this experiment.

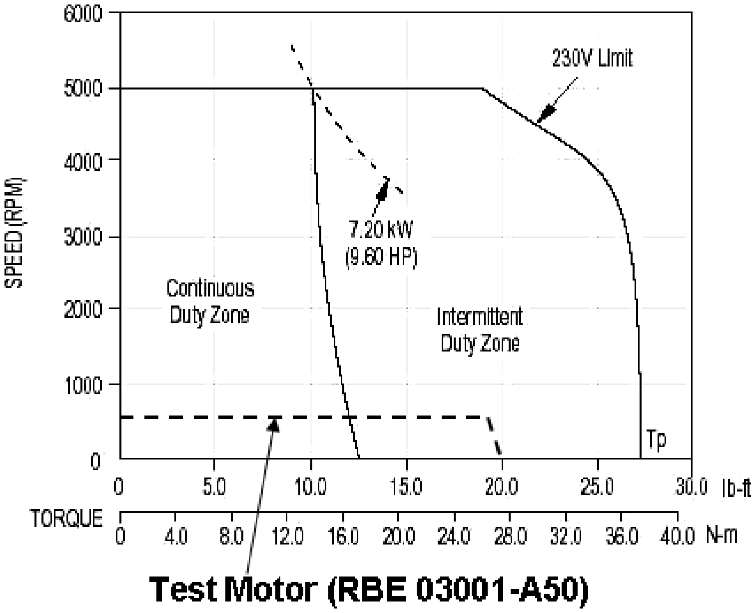

Figure 4.7: Load motor selection - BE-406-C

In Figure 4.7, the solid lines represent the load motor capacity, and the torque-speed curves are divided into continuous and intermittent cases. The intermittent rates are unknown but the curve shows the performance of the motor capacity in the intermittent zone is improved by two fold. The torque-speed curve for the test motor is shown in Figure 4.7. These two curves show the BE-406-C motor from Kollmorgen [47] is appropriate as a load motor in this experiment due to the larger capacity for torque and speed than the test motor. Table 4.2 shows the specification of the load motor being used for this test. Notice the power is almost 7.20 kW. The maximum speed is 5000 RPM and the maximum torque is 38.2 Nm. It has very small inertia and needs 250 VAC in order to run the motor at maximum speed. However, the wall outlet voltage in UTRRG laboratory only

Parameter	**Value**	**Unit**
Model number	Goldline	BE-406-C
Power at peak torque	7.16	kW
Speed at rated power	5000	RPM
Max speed	5000	RPM
Cont. stall torque	18.01	Nm
Peak torque	48.21	Nm
Cont. current	27.2	Amps RMS
Peak current	81.4	Amps RMS
Rotor inertia	0.000929	kgm^2
Weight	15.9	kg
Static friction	0.287	Nm
Max. line-to-line voltage	250	Volts RMS
Number of poles	4	pc

Table 4.2: Load motor specifications

provides 208 VAC so 5000 RPM is not possible. However, it is enough to test the motor. The maximum current that the motor will need is quite large so the amplifier should be carefully selected.

4.3.3 Amplifier Selection

The amplifier is the electronic power converter that drives the motor according to the controller reference signals. The test motor and load motor in this experiment are permanent magnet synchronous motors, so sinusoidal AC brushless amplifiers are used. These amplifiers use encoder signals for commutation feedback. The amplifier drives the motor with sinusoidal currents, resulting in smooth motion. Hall effect sensors are needed for startup since the encoder provides only incremental position information and not the current angular location of the rotor relative to the stator.

The first step in amplifier sizing is equating the power requirement of an

Parameter	**Test Motor Amplifier**	**Load Motor Amplifier**
Company name	Advanced Motion Control	Advanced Motion Control
Model number	SE30A40	S100A40AC
Peak current	30 A	100 A
Continuous current	15 A	50 A
AC Supply voltage	45 - 270 VAC	85 - 270 VAC

Table 4.3: Amplifier specifications

amplifier to that of a motor. Servo amplifiers typically have both continuous and peak current ratings along with a maximum voltage rating. The peak current rating is available for acceleration/deceleration requirements for transient loads and is typically available for two or more seconds. Voltage and current ratings of an amplifier need to be matched with a motor's winding constants to yield the desired performance. The amplifier voltage and current ratings are determined from the maximum motor voltage, maximum motor current and continuous motor current. It is recommended to select an amplifier with a voltage rating of at least 20% higher than the maximum voltage to allow for regenerative operation and power supply variations. The amplifier peak current rating should exceed the maximum motor current requirements. The peak current of the test motor amplifier is 30 Amps which exceeds the peak current value of the test motor. Also, the supply voltage that the amplifier needs is less than 270 VAC. In Table 4.3, the load motor amplifier is also selected by comparing the maximum peak currents of the motor and amplifier. The 100 Amps peak current of the load motor amplifier satisfies 81 Amps peak current of load motor. The supply DC voltage from power supply is 291 VDC.

Company Name	Advanced Motion Control
Model Number	PS30A
AC Supply Voltage	45 - 240 VAC, 1 or 3 phase, 50 60 Hz
Peak Current	30 Amps for single phase AC input
Continuous Current	15 Amps for single phase AC input

Table 4.4: Specifications of test motor power supply

4.3.4 Power Supply Selection

The power supply is sized to match the amplifier and motor power requirements and typically includes a logic power supply along with regeneration circuitry. The power output rating of a power supply must exceed or equal the combined average power of all servo drives operating simultaneously. Taking into account motor and drive losses for permanent magnet servos, PS30A in Table 4.4 is chosen as a test motor power supply because peak current and supply voltage exceed the requirements of the test motor amplifier specification. The power supply for the load motor is attached to the load motor amplifier. The load motor amplifier (S100A40AC) has the power supply in the model so the input DC voltage directly supplies to the amplifier through the internally connected lines.

4.3.5 Clutch Selection

Electromechanical clutch developed by Ogura is used as shown in Figure 4.8. The clutch operates via an electric actuation but transmits torque mechanically. When the clutch is required to actuate, voltage is applied to the clutch coil. The coil becomes an electromagnet and produces magnetic flux. Then, this magnetic flux is transferred through the small air gap between the field and the rotor. The rotor portion of the clutch becomes magnetized and sets up a magnetic loop that attracts the armature. The armature is pulled against the rotor and a frictional force is developed at contact. Within a relatively short time the load is accelerated to match the speed of the rotor, thereby engaging the armature and the output hub of the clutch. When current is released from the clutch, the armature is free to turn with the shaft. Springs hold the armature away from the rotor surface when power is released, creating a small air gap. Figure 4.9 describes the schematic diagram of the clutch.

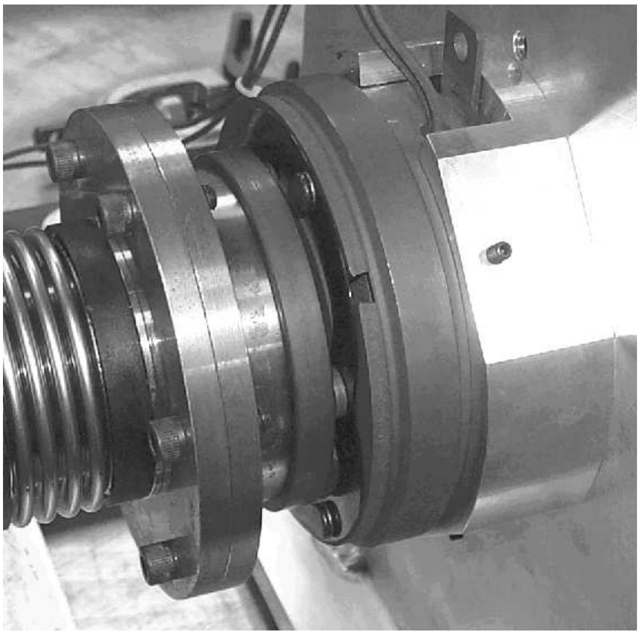

Figure 4.8: Ogura clutch installed in NTBA

To determine the selection of a clutch, we need to know how much torque and speed are governing the whole system. The maximum torque and speed handled by the clutch should be larger than the governed shaft torque and speed. Clutch selection charts provided by the manufacturer [69] help to choose the correct size of clutch. The following equation is a useful guide for selection of a clutch.

$$T = \frac{5250 \times HP \times K}{N} \tag{4.1}$$

where *HP* is the horse power for brake and clutch, *T* is the torque in Lb-ft, *N* is the speed at clutch location in RPM, and *K* is the motor overload factor for clutch.

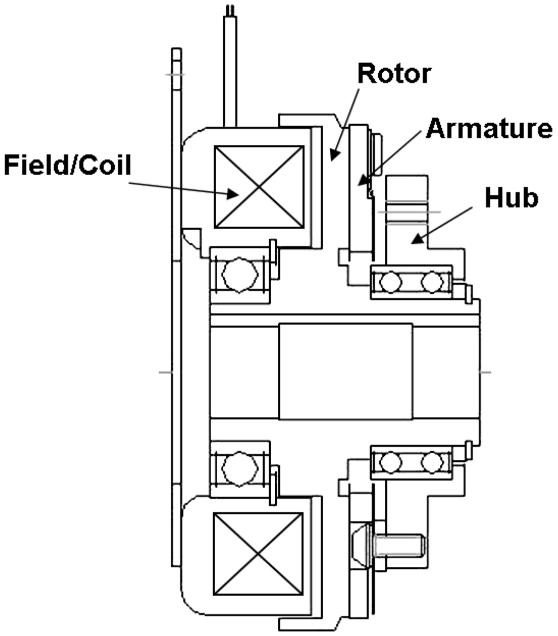

Figure 4.9: Electromechanical clutch [69]

The no load speed of the test motor is 650 RPM, and the maximum power is 1.98 kW. Also, because the motor overloading factor, K, is equal to 2, the acceptable torque for the clutch is approximately 40 Nm. Therefore, VCEH2.5P in Table 4.5 shows that the 29 Nm static torque for the clutch is larger than the value obtained from Equation (4.1). In addition, the maximum speed of the test motor is within the maximum range to be handled by the clutch module.

4.3.6 Coupling Selection

The NTBA uses Bellows couplings (Figure 4.10) to connect each component. The major characteristic of this specific coupling is high clamping forces to hold

Company Name	Ogura Industrial Corp.
Model Number	VCEH2.5P
Power	25 W
Static Torque	29 Nm
DC Voltage	24 V
Moment of Inertia	0.000017 kgm^2

Table 4.5: Specifications of electromechanical clutch

the shafts, so there is almost zero backlash. The way to hold the shaft is that the tapered conical sleeve slides inside the bore of the Bellows coupling and the outside shafts, and then by using the screws, the sleeve pushes into the body of the coupling. The tightening torque is 8 Nm and the stiffness of the coupling is 76000 Nm/rad in this application. The rated torque that can be handled by the chosen coupling is 60 Nm (or 44.3 Lb-ft). Also, the coupling is very light so it has very small inertia compared with the other type of couplings. The axial and lateral misalignment will be accommodated 1.5 mm and 0.2 mm respectively if necessary.

Figure 4.10: Bellows Coupling - R&W America

4.3.7 Torque Sensor Selection

In order to fully measure the performance of an actuator and to enable torque control of the load motor, a torque sensor is needed. The torque sensor is required to have a torque, speed range, and a torsional stiffness higher than the operational range of the test motor. The procedures for choosing the right torque sensor are as follows:

- Find the maximum average running torque.
- Estimate the peak torque.
- Check the extraneous loads.
- Verify the speed rating.
- Verify sensor accuracy.
- Specify the power source.
- Specify the output signal.
- Choose the optimum torque sensor.

By using the above procedure, the non-contact rotary torque sensor in Figure 4.11 was selected. Since the Nonlinear Test Bed is required to test a range of actuator sizes with their respective torque-speed curves, an accurate torque sensor was sought. Typical high quality industrial torque sensors are rated to 0.5% full scale accuracy. This means, for example, that if the torque sensor's full scale is 10 Nm, the output measurement will only be good to ±0.05 Nm. This is great if the operating point of the measured experiment is around 5-10 Nm. However, if the same sensor was used in an application with smaller torque magnitudes, the error would be a larger percentage of the measured quantity. A balance between accuracy and economy can be found in Surface Acoustic Wave (SAW) technology. Table 7 explains more about the specification of the torque sensor that we have chosen [24].

Figure 4.11: Torque sensor - Sensor Technology

SAW technology is a relatively new when used for sensing torque. SAW transducers are similar in appearance to strain gages but they operate on a completely different principle. Each transducer has two sets of interdigital electrodes etched on a piezo-electric substrate. One is excited at ultrasonic frequencies and the other receives this acoustic wave after it propagates along the surface of the shaft, converting back to an electrical signal.

In a half bridge configuration, these sensors are temperature compensated, and have an accuracy that is superior even to the strain bridge (0.25% of full scale) [103]. A radio frequency coupling reliably transfers the sensor signal from the half bridge to a signal conditioning circuit. Since the radio frequency coupling is non-contact, the sensor is highly reliable. The change in torque is reflected in the change of frequency of the transducer signal. For this reason, signal conditioning

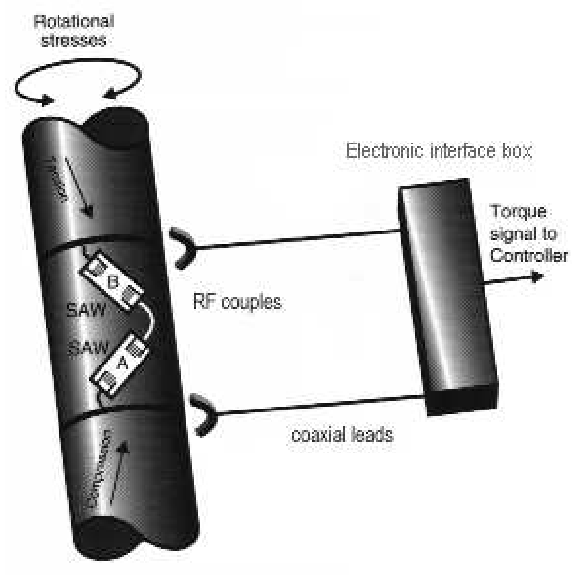

Figure 4.12: SAW transducer arrangement and electronic connection [24]

Manufacturer	WEN technology
Model Number	E300RWT1-3
Max.Torque	40Nm = 29.5 Lb-ft
Operational Speed	15000RPM
Accuracy	±0.5%
Analog Torque Output	±5 V

Table 4.6: Torque sensor specifications

circuitry is needed to convert the signal to a form that can be used by a controller.

4.3.8 Position Sensor Selection

The Test Bed required two encoders, one for the load motor and the other for the test motor. The load motor encoder was obtained from Kollmorgen and is embedded inside of the load motor. A through hole encoder is required for the test motor for accurate measurement of the output shaft position. Both of the encoders are incremental optical encoders and have 2048 cycles per turn resolution. Model

260 from Accu-Coder encoder company is used as the test motor encoder. This encoder has three Hall sensors with up to 12 pole commutation available.

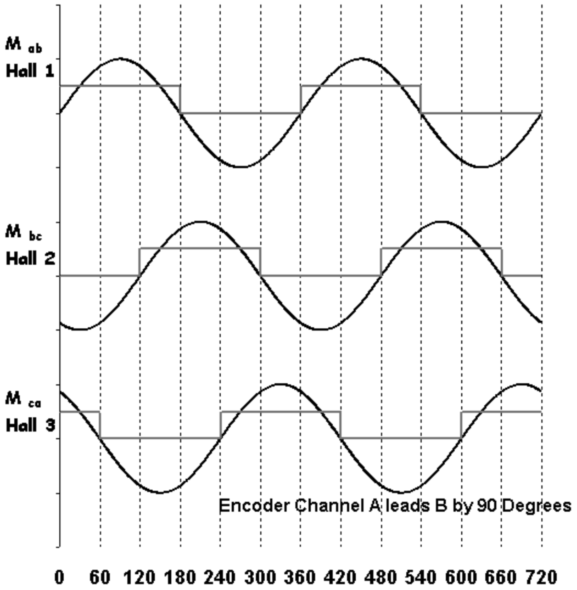

Figure 4.13: A typical method of determining rotor position using Hall switches

In brushless motors, commutation is performed by electronically sending the motor current to the appropriate winding. To do this, the rotor position is determined using an Accu-Coder encoder. Figure 4.13 shows a typical method of determining rotor position using Hall sensors. The encoder containing Hall devices is aligned with a magnet on the rotor, so that the relationship shown between the Hall outputs and the motor back EMF can be established. The mounting instructions for the Model 260 encoder to the test motor is as follows:

- Slide the Model 260 encoder over the motor shaft.
- Tighten the socket head screw in the clamping collar.

Manufacturer	Encoder Products Co.
Model Number	Model 260 Ultra Versatile Commutated Thru-Bore
Resolution	2048 CPR
Number of Channels	Dual with Index
Max. Speed	7500 RPM
Accuracy	0.01° mechanical angle from one cycle to any other cycle

Table 4.7: Specification of test motor encoder

- Lock the motor rotor to hold the motor shaft in a fixed position for alignment to the commutation channels.
- Rotate the motor shaft while viewing encoder signals on an oscilloscope.
- Check the alignment by turning the motor shaft and comparing the back EMF and Hall signals as shown in Figure 4.14.

The specifications of the test motor encoder are contained in Table 4.7. The encoder signals provide feedback to control the position and speed for the operation of the motors.

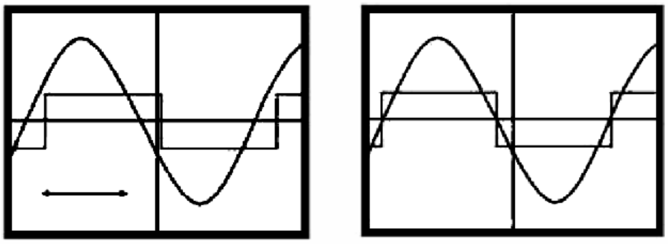
(a) Commutation not aligned with motor winding

(b) Proper commutation alignment with motor winding

Figure 4.14: Commutation alignment with motor winding

4.3.9 Current Sensor Selection

Though current may be measured by inference using a known phase resistance and inductance and measuring the voltage across it, this inference is not accurate enough for a variable temperature environment like an actuator (both resistance and inductance change with temperature). In order to obtain a direct measurement of current, a current sensor was needed. Typical direct methods of measuring current include using a calibrated shunt resistor (by measuring the voltage across it), an inductive coil, or a Hall-effect current sensor. The shunt resistor offers simplicity but changes the phase resistance substantially. Both the inductive coil and Hall-effect sensor use the magnetic field of the current-carrying wire to produce a voltage indicating the current. Between inductive and Hall-effect current sensors, the Hall sensor offers faster response time (less than a micro-second). The Hall-effect current sensor is also the industry standard, benefiting from the refinement of competition and low cost.

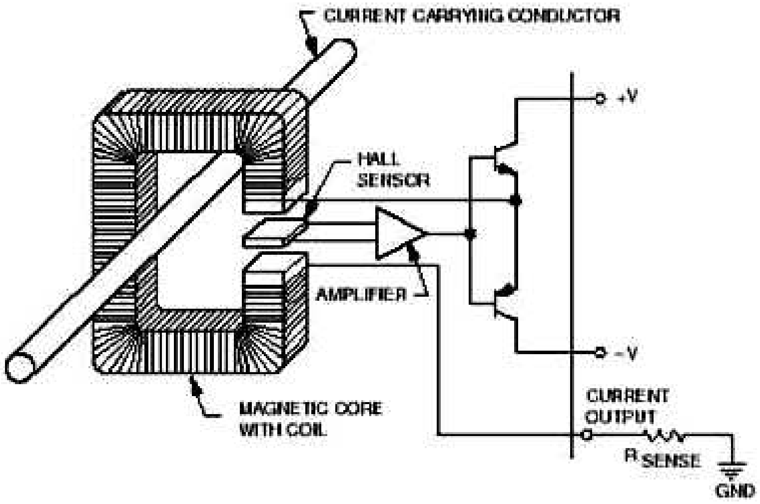

Figure 4.15: Schematic of closed loop current sensor [37]

Hall-effect current sensors come in two varieties: open loop and closed loop.

Manufacturer	FW Bell
Model Number	CLN-25
Nominal Current	25 A
Peak Current	36 A
Nominal Output Current	25 mA
Accuracy at ±15 V	±0.5 %
Sense Resistor	218 Ohms

Table 4.8: Specification of current sensor

Both have similar construction with a ferromagnetic core that provides a closed magnetic circuit in line with the Hall-effect sensor. In the case of the open loop sensor, the Hall-effect sensor produces a voltage proportional to the magnetic flux (and therefore the current) of the circuit. Since the measurement is passive, it is subject to drift and electromagnetic interference. A closed loop current sensor has an active inductive coil wrapped around the magnetic core providing an equal and opposite flux. A control loop is built into the sensor that continuously seeks to cancel the flux in the wire by generating an equal and opposite flux in the inductive coil (see Figure 4.15). The measured value of the current in the inductive coil is proportional to the current flowing in the phase being measured. The Hall-effect sensor is only used as part of the control loop. It does not provide the output signal as with the passive variety. The close loop sensor is the superior choice in this application. Figure 4.15 shows a schematic diagram for a closed loop current sensor using the Hall-effect phenomenon.

One current sensor is needed to measure the current in each phase of the actuator. Since the current is the same throughout the circuit, these sensors may be located anywhere between the amplifier and the actuator. Inductive current sensors operate best when the wire being measured passes through orthogonal to the sensor. For this reason, an FW Bell closed loop current sensor was purchased (see Table 4.8). These sensors route the current-carrying conductor through the Hall sensor loop at a right angle. Table 4.8 represents the specification for the closed loop of current sensor provided by FW Bell.

4.3.10 Temperature Sensor Selection

In order to facilitate the measurement of criteria for an actuator, system testing must reflect temperature dependencies of the actuator system. A temperature sensor was needed to enable this testing. There are three types of temperature transducers that provide a temperature-dependent voltage signal. These are thermocouples, thermistors, and RTD's. All of these have similar geometries and are available in the temperature range that the PMSM phase windings will experience. EMF interference is one factor that helps in deciding the best temperature sensor for this application. Thermocouples are passive devices (not powered) that provide a small voltage signal due to the Seebeck effect [46]. Since the signal is small, it requires shielding from EMF noise and preamplification. These two factors made thermocouples the least desirable of the three options for this application.

Both thermistors and RTDs are temperature sensitive resistors. By placing them in a simple voltage divider circuit, they provide a simple clean signal. RTDs are superior both in accuracy (fractions of a degree) and in temperature range (up to $400°F$) than the thermistor, but they are more expensive. Because the application demands no more than ±1 degree of accuracy, and the upper range is well within the bounds of standard thermistors, a thermistor is used for temperature measurements.

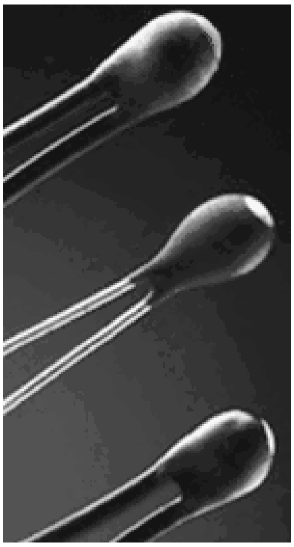

Figure 4.16: Thermistors [77]

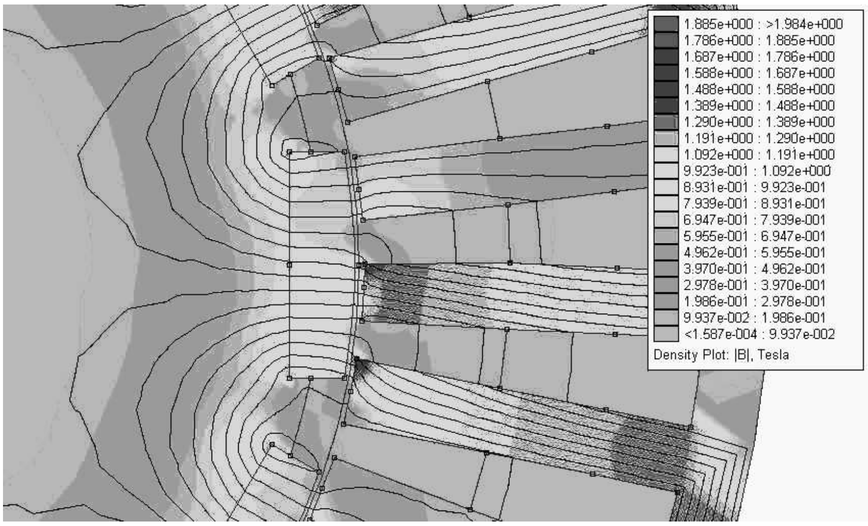

Figure 4.17: FE analysis in the test motor (3 phases, 12 poles PMSM)

4.3.11 Magnetic Flux Density Sensor Selection

The Hall generator is used to measure magnetic flux density. This sensor provides an output voltage proportional to the magnetic flux density. The Hall effect develops a voltage across a conductor when current is flowing and the conductor is placed in a magnetic field. The voltage generated across the width of the conductor is called the Hall voltage. The Hall voltage can be given as follows.

$$V_H = \gamma_B B \sin\theta \tag{4.2}$$

where V_H is Hall voltage (mV), γ_B is the magnetic sensitivity (mV/kG), B is the magnetic field flux density (kG), and θ is the angle between magnetic flux vector and the plane of Hall generator. The sensor used in this research was the Lake Shore Hall Generator (HGT-1010). The sensor needed a current source (100 mA) and its sensitivity was set as 8.60 mV/kG.

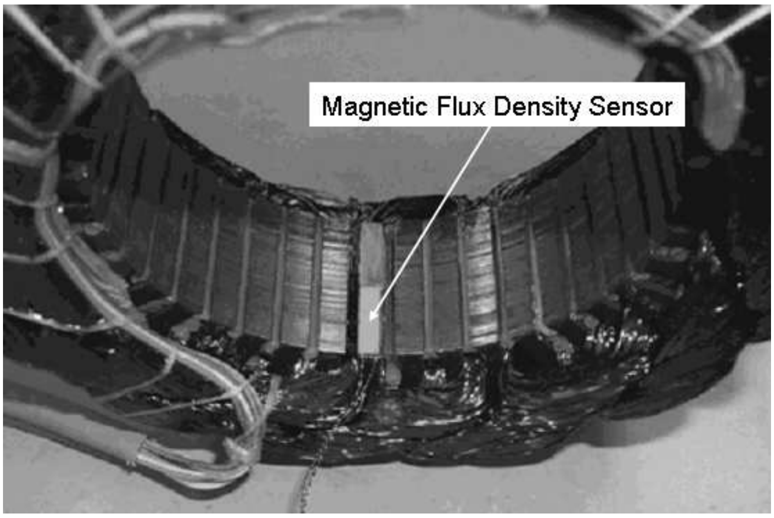

Figure 4.18: Installation of magnetic flux density sensor inside the stator of a PMSM

Figure 4.17 shows the FE analysis of magnetic flux distribution generated inside the PM motor. The values shown in the right-hand corner represent the physical values of magnetic flux density in Teslas (T). Based on these values, the best location to obtain the maximum value of the magnetic flux is the air gap

Manufacturer	Lake Shore Cryotronics, Inc.
Model Number	HGT-1010
Description	Transverse Hall generator, 0.02 inch thick
Nominal Control Current	100 mA
Magnetic Sensitivity	8.60 mV/kG
Operating Temperature Range	-40 to 100°C

Table 4.9: Specification of magnetic flux density sensor

between the rotor and stator poles. Thus, the magnetic flux sensor was mounted on the surface of the stator poles as shown in Figure 4.18. The air gap between the rotor and stator poles of the motor was 0.03 inches and the thickness of the Hall sensor was 0.02 inches. Therefore, the sensor was barely able to be installed in the air gap without causing a mechanical problem. For the current position of the sensor shown in Figure 4.18, the maximum theoretical flux density was 0.9 T on the stator pole.

4.3.12 Hysteresis Brake Selection

A hysteresis brake is used to perform torque ripple and acceleration tests as mentioned in Chapter 5. The load motor is not appropriate for the torque ripple test, because the torque ripple from the test motor might be confused with the torque ripple from the load motor. Also, acceleration tests need a device to control the motor torque independent of the rotor speed. The Magtrol hysteresis brake [55], which is used in these tests, provides absolutely smooth, infinitely controllable torque loads, independent of speed, and they operate without any physical contact with components in the test bed. Figure 4.19 represents the schematic diagram for Magtrol hysteresis brake.

The hysteresis brake is made up of two primary members, the pole structure and the rotor, that interact magnetically to produce a braking or clutching force. The pole structure, which is made up of an inner pole, an outer case, and a coil, form the fixed member of a brake assembly or the driven member of a clutch assembly. The geometry of the pole structure is such that it forms an inner and outer pole structure with a close tolerance air gap into which a drag cup (or rotor) is fitted. The rotor is affixed to a shaft and suspended in the air gap by a set of shaft bearings and forms the rotating member of a brake assembly or the output member in a clutch assembly.

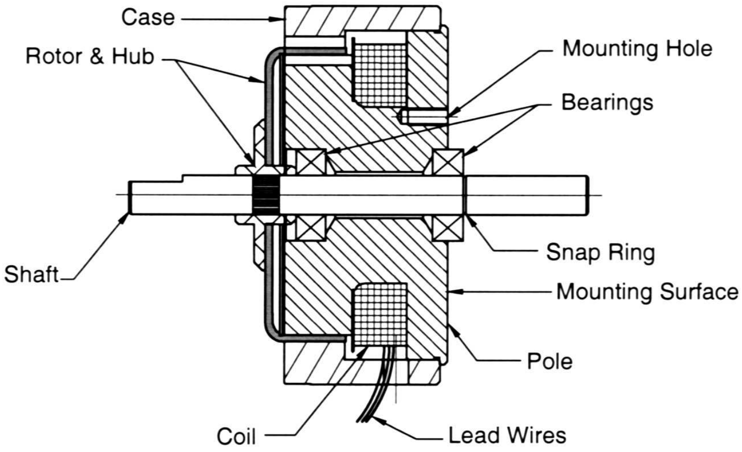

Figure 4.19: Hysteresis brake

As current is applied to the coil, a magnetic field proportional to current is established within the air gap. The rotor, which is located within the air gap, becomes magnetized. Due to its specific hysteresis properties, the rotor resists movement, creating a braking torque between the pole structure and rotor. The transmitted torque remains constant and smooth as the rotor is forced to rotate within the air gap and will respond to increases or decreases in coil current with corresponding increases or decreases in torque. The removal of coil current and changes in coil current result in a smooth transition from one torque level to the next. Under certain operating conditions, however, it is possible to set up a salient pole condition on the brake rotor that can result in “Cogging Torque”. Cogging torque is an inherent characteristic of a hysteresis brake that should be avoided by a proper operation shown in [55].

4.4 System Motion Controller and Operational Software

4.4.1 Motion Controller

The PMSM is sinusoidally commutated. Commutation is implemented electrically with a drive amplifier that uses semiconductor switches to change current in the windings based on rotor position feedback [2]. There are two common methods to vary the current supplied to the motor windings. The traditional method depends on the amplifier to commutate the current based on position feedback. The second method is to use a motion controller to commutate the first two phases and to allow the amplifier to determine the value of the third phase [26]. Since the sum of the currents at any time is zero, the current in the third phase equals the inverse of the first two currents. Figure 4.20 shows this schematically. A National Instruments (NI) motion controller is used to provide a sinusoidal commutation to the load motor [66].

NI products have proved to be extremely useful to the instrumentation, control, and software development of this test bed. For motion control, NI’s PXI-7358 8-axis motion control card is used. Two axes of this board are used for the load motor and one for the test motor. The load motor drive does not need an encoder and Hall sensor feedback, because the sinusoidal commutation of the load motor

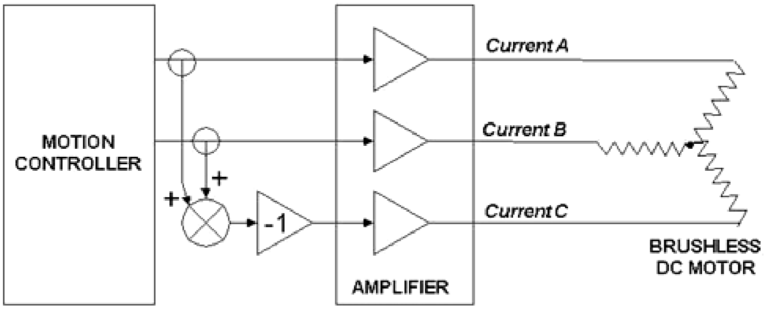

Figure 4.20: Sinusoidal commutation of the motion controller [26]

is done by the motion controller. As such, the Hall and position feedback signals are directly sent to the PXI-7358. For the test motor, encoder and Hall signals are needed for feedback to the amplifier and complete the sinusoidal commutation loop to run the test motor. Also, in order to control the test motor in torque mode, the torque sensor analog signal is connected to one of the analog input channels on the NI motion controller. This channel is then used as a feedback signal for the test motor. With this arrangement, the load motor is speed controlled while the test motor is torque controlled. The clutch is instrumental in the safe operation of the test bed. The operational command for the clutch is provided by the motion controller. Default for the clutch is “off”. This is done to prevent the unintentional transfer of large torques from the load motor to the test motor during initialization.

4.4.2 Data Acquisition

The values of interest from sensors in the test bed are position, velocity, acceleration, torque, temperature, voltage, and current. An NI-SCXI signal preconditioning module cleans up the noisy raw data from the test bed. The SCXI 8th order programmable Bessel filter is installed for this purpose in the test system. The SCXI-1142 Bessel lowpass filter provides 80 dB attenuation and the

Manufacturer	National Instruments
Model Number	PXI-7358
Description	Brushless motor controller with sinusoidal commutation
System processor	Motorola 32 bit microprocessor, DSP and FPGA
Communication interface	PXI with bi-directional FIFO
Analog I/O	8 channel multiplexed, 16 bit ADC
Minimum Servo Loop Update Rate	62.5 microseconds

Table 4.10: Specification of motion controller

passband magnitude response begins to drop off immediately with 7 kHz cutoff frequency. A Bessel filter has almost zero phase shift and it is not sensitive to overshoot or ringing in the step response. For data acquisition, an NI-PXI-6040E multifunctional DAQ board is used to read the 11 analog input signals at 22.7 kHz per channel, 12-bit resolution. The Real Time System Integration (RTSI) bus connected internally in the PXI machine is used for high speed data synchronization. NI-Motion and Measurement & Automation Explorer (MAX) configuration utility is used to provide complete control over the characteristics of the actuator control system. MAX uses a Graphical User Interface (GUI) to initialize the motion board, configure each axis, set control loop gains and set motion thresholds [66].

4.5 Operations of Nonlinear Test Bed for Actuators

Once the test bed has all of the required mechanical and electrical parts, signal wires are connected from the controller to each component. The power lines for each piece of measurement equipment and amplifiers are connected with power supplies. Encoders and Hall sensors need 5V, and their power is provided from the controller interconnection block as shown in Figure 4.4. Current sensor needs ±15V, so it has its own power supply. In addition, thermisters require ±15V and the power is provided by the same power supply. Two power relays are used to disconnect the current flow if there is a power surge as represented in Figure 4.21. Each of the power relays is connected in series between amplifier and power supply.

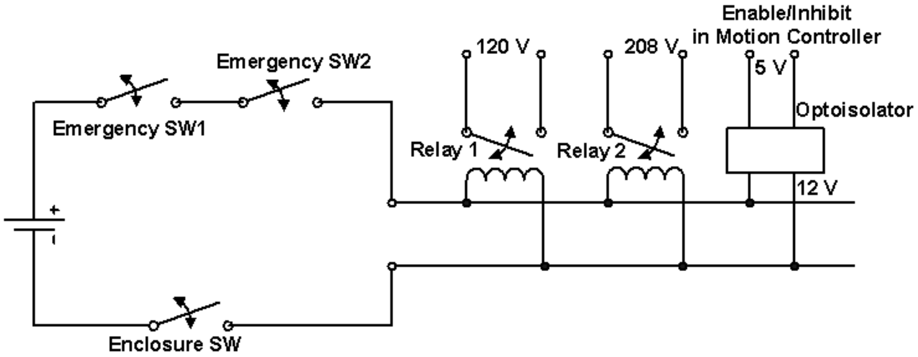

Figure 4.21: Analog circuit for emergency stop

A voltage divider circuit is also fabricated in order to take the voltage signals from the test motor. These signals are scaled down to ±10V. The sensor signals are sent to the motion controller through the interconnection block. There are 12 input signals that will be collected: three voltage signals, three current signals, four temperature signals, one magnetic flux density signal and one torque signal. In the test motor, encoder and Hall signals are needed for feedback to the amplifier. These signals are needed to complete the sinusoidal commutation loop to run the test motor. The load motor does not need to feedback the position signals and Hall signals to the amplifier, because the load motor commutates the current signals in the motion controller and not in the amplifier. The test motor amplifier ground is not isolated from the power line, so the grounds for the amplifier and motion controller are connected to earth. Moreover, the one to one ratio of the isolated power transformer is used to transfer the voltage range of between ±76VDC to the voltage output range of 0VDC to 169VDC. Finally, in order to control the engagement of the clutch, one of the digital output channels is used. This signal will be sent to the clutch in an emergency case or during operation.

The NI motion controller provides over 100 commands for specifying motion and machine parameters. Commands are included to initiate action, interrogate status and configure the controllers and filters. These commands can be sent in Virtual Instruments (VIs) using the Labview program. These VI commands help the user to generate, store and execute many complex application programs. Additionally, NI provides example files to develop the program easily for motion control, data acquisition, and signal processing. All of these features helped us to build a real time operation system with fast sampling and feedback update speed.

Chapter 5

Test Regime and Stochastic Processes

In practice, motors, used for complex operations as found in robotics and automation, operate under conditions where parameters such as room temperature, load and velocity profile, and task type are constantly changing. As a result, the motor loading is driven by nonlinear, nonstationary and stochastic variables. However, the influence of load variation on motor performance has not received proper attention from engineers. This can be seen from the fact that motor catalogs and brochures do not present enough information about the response to nonlinear, periodic loadings [41]. Therefore, the first goal of this study will be development of the test protocol to generate the motor performance maps under variable loadings. Additionally, the stochastic processes are discussed to support the test results presented in Chapter 6. All of the test regimes established in this report are based on the performance criteria developed in Chapter 3. Table 5.1 presents the symbols of the sensors, test motor and load motor parameters that used to describe the test procedures and test results.

5.1 Test Regime for Permanent Magnet Synchronous Motor

5.1.1 Dynamic Loading Test

Generally, the torque-speed curve is obtained by increasing the load torque, T_m, with a fixed value of speed, ω_L, in current mode. However, this torque-speed

Symbols	**Descriptions**
i_{T1}	Current in phase 1 of the test motor.
i_{T2}	Current in phase 2 of the test motor.
i_{T3}	Current in phase 3 of the test motor.
V_{T1}	Voltage in phase 1 of the test motor.
V_{T2}	Voltage in phase 2 of the test motor.
V_{T3}	Voltage in phase 3 of the test motor.
V_b	Voltage applied to the hysteresis brake to generate a reaction torque.
T_L	Torque generated at the load motor.
T_m	Torque generated at the test motor. The test motor controls the torque of the whole system.
T_a	Torque measured in torque sensor.
T_r	Torque ripple amplitude.
ω_L	Rotor speed of the load motor. The load motor controls the speed of the whole system.
ω_T	Rotor speed of the test motor.
ω_w	Speed of the whole system including test motor, load motor, bellows couplings, and clutch. s_w equals to s_L and s_T when the test motor and the load motor are engaged by the clutch, and they are operated together.
ω_b	Speed of the mechanical components including test motor, hysteresis brake, bellows couplings, clutch.
a_L	Rotor acceleration of the load motor.
a_T	Rotor acceleration of the test motor.
a_w	Acceleration of the whole system including test motor, load motor, bellows couplings, clutch.
a_b	Acceleration of the mechanical components including test motor, hysteresis brake, bellows couplings, clutch.
t_r	torque rise time.
C_T	Temperature inside the test motor.
M_T	Magnetic flux density of the test motor.

Table 5.1: Symbols used in electromechanical motor testings

plot does not show the effect of several different kinds of dynamic loads such as sinusoidal, ramp, and arbitrary nonlinear periodic loads. In this research, given one of these loading types, several tests are performed with different peak magnitudes and cyclic frequencies. The whole loading period for each test is at least one minute in order to see the effect of different torque profiles. The generated torque, T_a, is recorded as a state at each time step to compare the value of the measured state with the monitored state values obtained from a Condition Based Maintenance system in real time [42]. In all of the tests with different dynamic loadings, it should be noted that both the amplifier and motion controller influence the performance of the test motor. Using this test protocol, only sinusoidal loading is applied and the operational margin of torque-speed performance map is obtained.

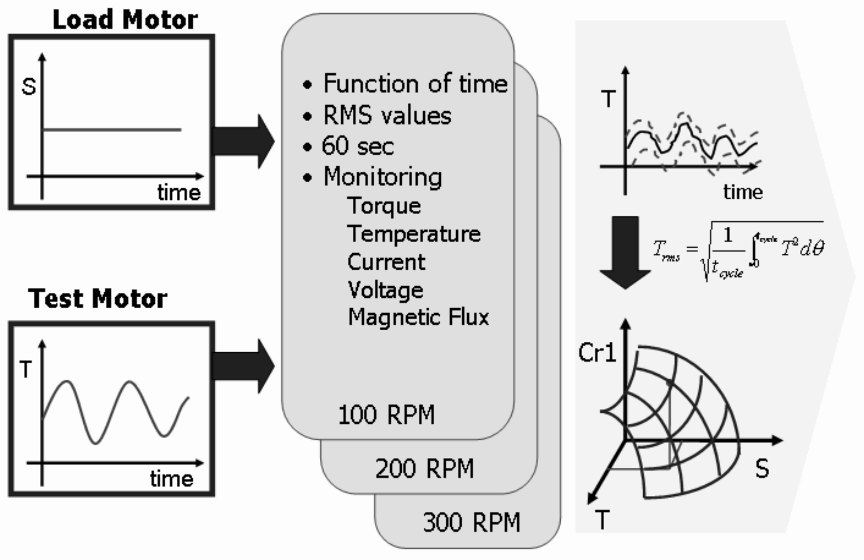

Figure 5.1: Torque-speed curve with dynamic loading

The conceptual diagram of the test procedure for the operational margin criterion is represented in Figure 5.1. The amplifiers for the test motor and the load motor use current feedback. The motion of the load motor disturbs the motion of the test motor. Thus, the side effect generated between these two torque-generators is the output shaft torque, T_a. Increasing or decreasing speed, ω_L, in the load motor can change the output torque, T_a, measured from the torque sensor. Also, varying the magnitude and cyclic frequency of the load torque, T_m, in the test motor can affect the measured torque, T_a, obtained between these two motors. The test motor and the load motor cannot run independently at the start of the test. Because they are connected by a clutch, the position and velocity feedback signals have to be used only in the load motor controller which has a higher power capacity. The test motor has only a torque feedback control loop. The torque-speed curve is obtained by increasing and decreasing the speed of the load motor. In each speed region, the electrical torque command from the test motor is increased until it produces the highest value of torque, T_a, without changing the speed, ω_w, provided by the load motor. Figures 5.2 and 5.3 represent Labview[1] programs to control the test motor and the load motor separately. Currents, i_{T1}, i_{T2}, i_{T3}, voltages, V_{T1}, V_{T2}, V_{T3}, torque, T_a, temperature, C_T, and magnetic flux density, M_T, signals are collected in the Labview program for the load motor controller as shown in Figure 5.3. Also, velocity, ω_w, and acceleration, a_w, signals are measured in the Labview program for the test motor controller as shown in Figure 5.2.

An operational performance map is obtained as a range of torque-speed curve values corresponding to several different cyclic frequencies in sinusoidal loadings at the test motor. The nonlinear sinusoidal loading is performed by programmed torque, T_m, at the test motor. In order to measure the loading torque, T_a, the test bed has a torque sensor which can measure up to 40 Nm. Each test is

---

[1] The graphical development environment for creating flexible and scalable test, measurement, and control applications rapidly and at minimal cost.

repeated at least 20 times to allow for statistical analysis. The data obtained from all of the tests is analyzed by generating the mean and standard error values with the proper assumption of a normal distribution.

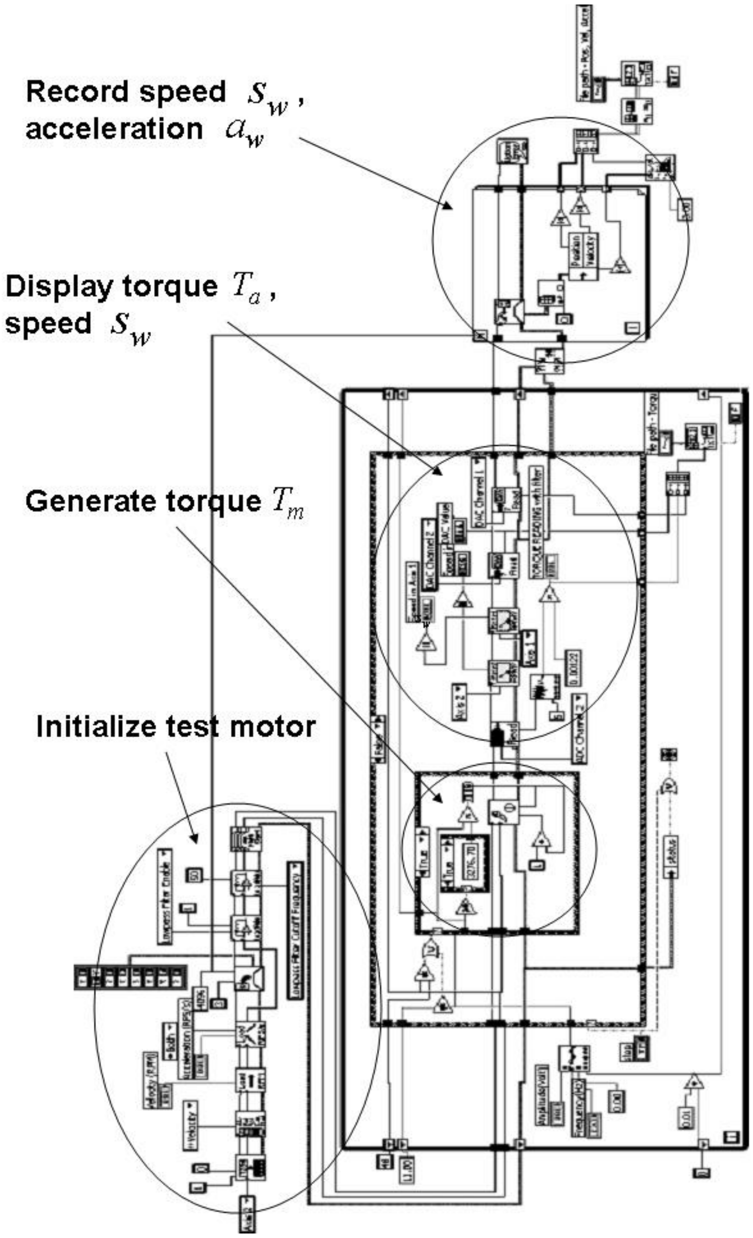

Figure 5.2: Labview program to control the test motor

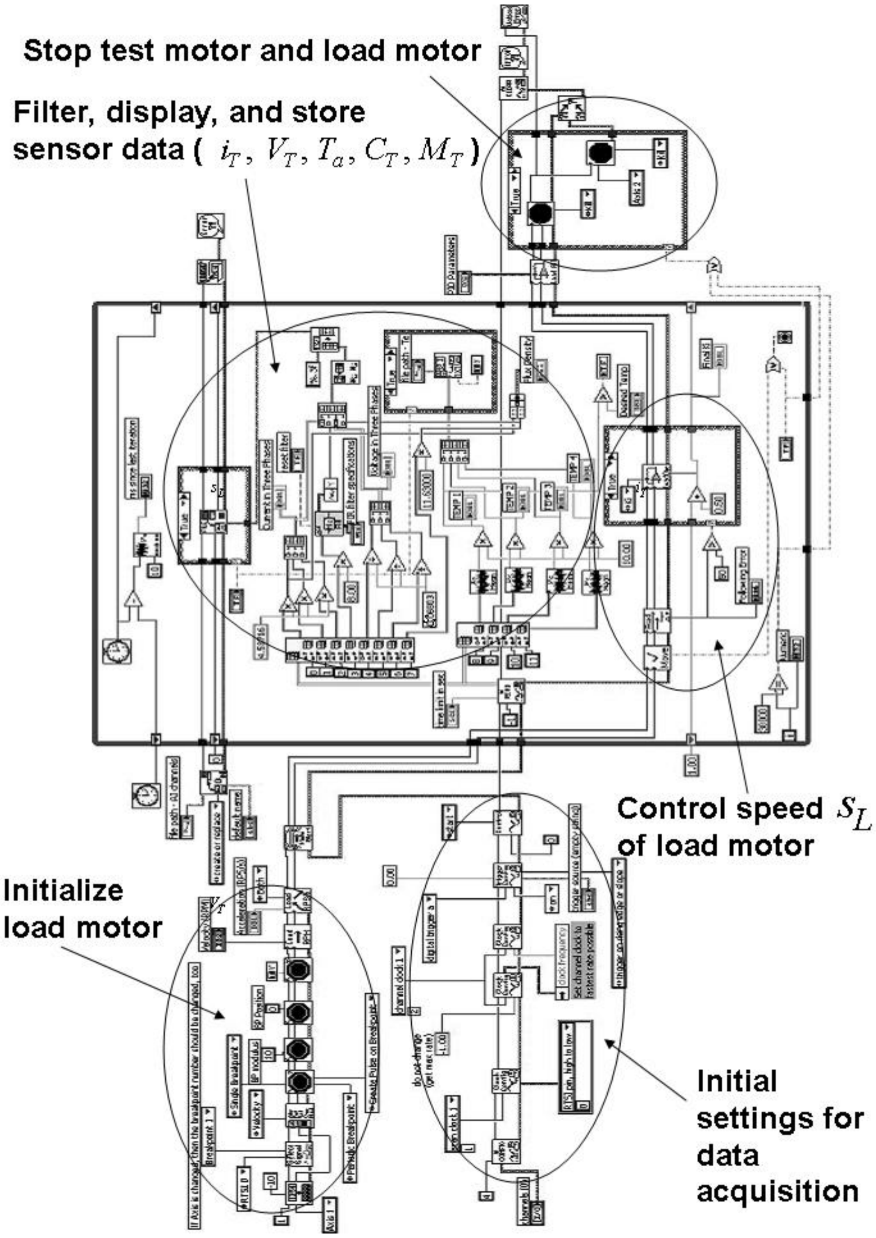

Figure 5.3: Labview program to control the load motor

5.1.2 Loading Test Using Constant Torque, T_a

The test set-up for the generation of constant torque, T_a, to obtain the performance maps for motor efficiency, power loss, temperature, C_T, magnetic flux density, M_T, magnetic flux energy, $(BH)_{max}$, and torque, T_a,-current, i_{T1}, ratio is quite direct. The mechanical torque output signal, T_a, from the torque sensor and the speed, ω_w, of the load motor from the encoder are monitored at the same time. Also, the currents, i_{T1}, i_{T2}, i_{T3}, and voltages, V_{T1}, V_{T2}, V_{T3}, signals in each of three phases of the test motor are measured and recorded in three current sensors and three voltage divider circuits wired through the test motor power lines in real time. In addition, the temperature and magnetic flux sensors installed in the test motor are monitored in this test. For the constant torques, T_a, measured in the torque sensor, the electrical torques[2] from the test motor develop different magnitudes of nonlinear torque profiles. By changing the amplitude in each load profile, the currents, i_{T1}, i_{T2}, i_{T3}, provided from the test motor amplifier influence the output power of the test motor. The test procedures are as follows.

- At rest, both motors are connected by engaging the clutch.
- The load motor starts to run at a constant speed, ω_L. The speed, ω_w, of the system is governed by the load motor.
- At the same time, the test motor is operated in a certain repeating torque profile. This torque, T_m, is generated by providing the current command required to run the motor to the test motor amplifier. The torque, T_a, applied to the system is controlled by the test motor.

---

[2] Electrical Torque: command voltage output to the test motor amplifier

- The measured data during the operation is recorded by the DAQ board.
- This test is repeated for different speeds, ω_L, of the load motor.
- The torque sensor measures the output torque, T_a, of the test motor.

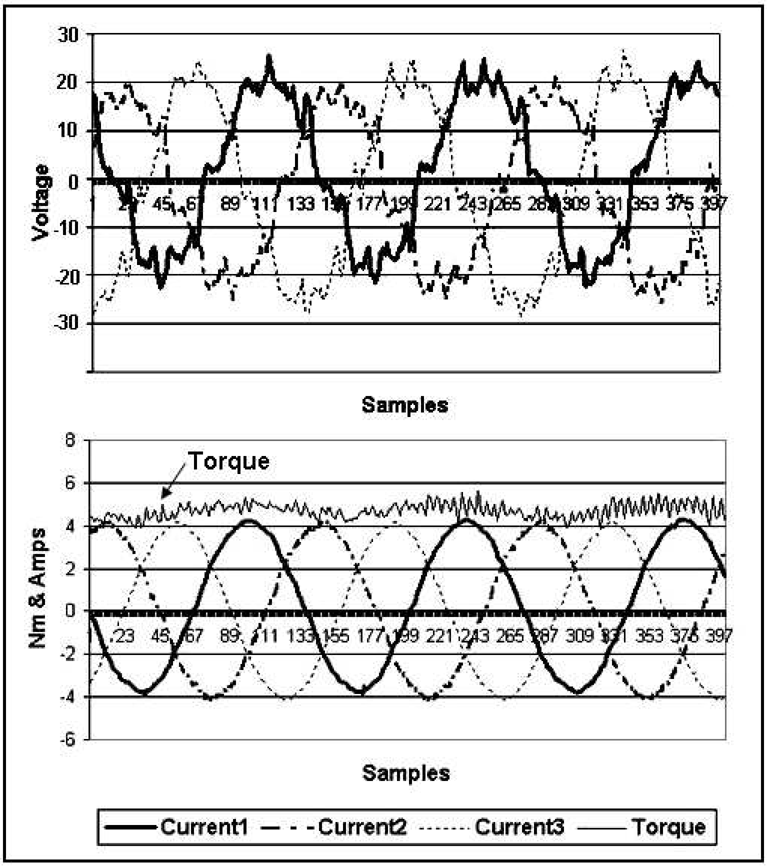

Figure 5.4: Experimental results of voltage, current, and torque responses in the constant motor speed of 100 RPM and the desired constant torque of 4.5 Nm

The Labview program of Figure 5.2 is modified to develop constant torque output, T_m, in the test motor. The sinusoidal command input is applied in the sinusoidal loading test of Section 5.1.1 and the voltage input is commanded to control the constant torque, T_m, in the test motor. In Figure 5.4, three currents,

i_{T1}, i_{T2}, i_{T3}, in three phases from the test motor amplifier were provided to generate a torque, T_a, of 4.5 Nm in the test motor. Three sinusoidal voltage signals, V_{T1}, V_{T2}, V_{T3}, were driven in 120° phase lags. The torque, T_a, curve shown in Figure 5.4 has some ripples in it. The loading test using constant torque, T_m, developed in the test motor describes several different levels of torque profiles used to develop efficiency and motor loss performance maps. The procedures to obtain these maps are as follows.

- From the tests in this section, three currents, i_{T1}, i_{T2}, i_{T3}, three voltages, V_{T1}, V_{T2}, V_{T3}, speed, ω_w, and torque, T_a, signals for the test motor are collected.
- To obtain the efficiency map, the input and output powers to the motor are calculated using Equation (3.1).
- Copper loss is determined based on Equation (3.6). A RMS value of armature current, i_T, per phase in the test motor is calculated from the test data.
- To obtain the core loss, the values of power input and copper loss are needed. They have been already determined in the previous procedures.
- The sum of core loss and mechanical friction loss are acquired by subtracting copper loss from the power input to the test motor.
- To determine the core loss, Equation (3.10) is used and a square of speed EMF and a core resistance should be defined. They are properly explained in Section 3.4.2 and Figure 5.5.
- To find a core resistance of the rotor in the test motor, no-load testing is performed [43]. Power output is zero due to no load.

- As shown in Figure 5.5, the slope is the reciprocal of the core resistance as mentioned in IEEE-112 [43]. The core resistance is determined as 29.5 Ω. Additionally, the friction loss is acquired by the area bounded below by zero and above by the y-intercept[3]. It is not bounded in x-direction.

- The core loss is calculated by multiplying the core resistance and the square of speed EMF.

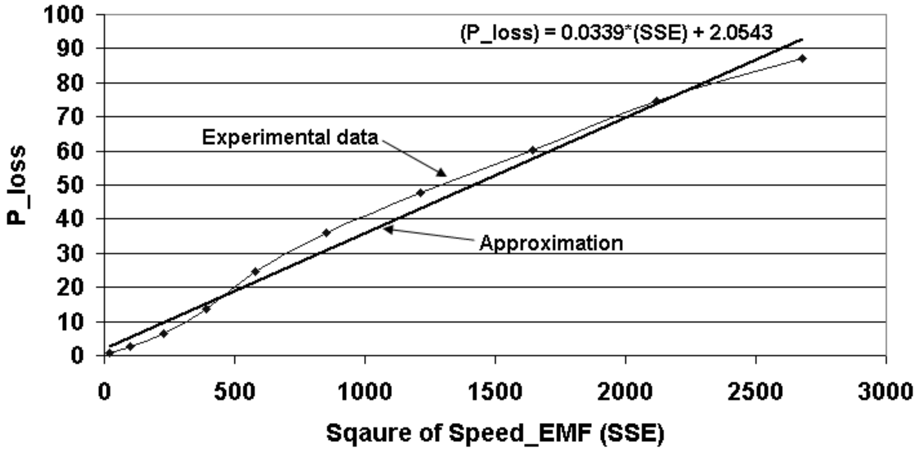

Figure 5.5: No load test at reduced voltage

Torque-current ratio and magnetic flux density performance maps are also obtained in this constant torque test. The torque-current ratio map is determined from torque, T_a, current, i_T, and speed, ω_w, data in sensors attached in the test motor. The magnetic flux density and maximum magnetic flux energy performance maps are obtained as follows.

---

[3] y-axis is the P_{loss} axis. x-axis is the SSE axis in Figure 5.5. The square of back EMF is used in x-axis in order to obtain the slope of P_{loss} with respect to the square of the speed EMF (SSE). P_{loss} is almost proportional to the SSE [43].

- The magnetic flux density, M_T, signals are measured in Hall sensors attached in the stator of the test motor, and they are sent to the DAQ board by the motion controller as the other sensor signals are collected.
- The temperature, C_T, is measured at 11 minutes after starting the test. The magnetic flux density is affected by the increment of temperature.
- The 3D plot of magnetic flux density map is drawn based on torque, speed and temperature.
- B-H curve is generated from the magnetic flux density data and one of three current signals in the test motor stator.
- The area of B-H curve is the $(BH)_{max}$. The 3D plot of max magnetic flux energy map is obtained with respect to torque and speed.

5.1.3 Temperature Test

The temperature distribution is affected by the properties of the conductors and magnetic materials in an electromechanical motor and the performance of the electromagnetic force, which is generated from the reaction between stator and rotor. The most temperature sensitive parameters are the stator winding resistance and the iron core of the stator [92]. The resistance variation is determined over the operational temperature range of the motor.

Figure 5.6 shows the test motor stator and four locations chosen for the measurements of the temperature inside the test motor. There are four holes through the front cover face of the stator and four thermisters are attached on the stator windings and core by using epoxy. The temperature sensors are attached to the stator as shown in Figure 5.6(b). The winding wires have insulation so the

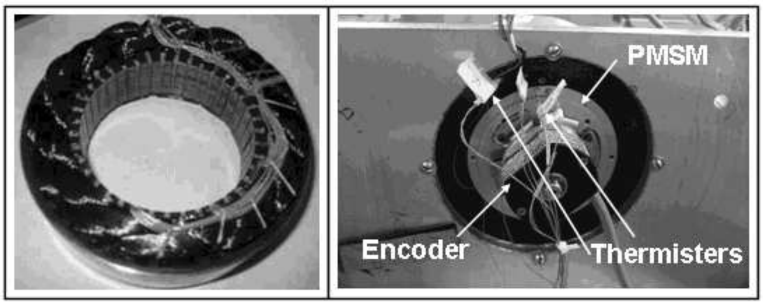

(a) Stator of the test motor (b) Installation of thermisters

Figure 5.6: Installation of temperature sensors

sensors actually measure the temperature on the insulation of the wires. However, it is too hard to find a way to measure the actual temperature of the wires, so in this report, when the temperature calculation is performed, it is assumed that the insulation temperature equals to the wire temperature.

As mentioned in Section 5.1.2, the same torque, T_m, profiles are generated in the test motor while the load motor runs at a certain speed, ω_L, to produce the torque-speed curve. At this time, there is one more measurement parameter, which is temperature, C_T. The operating temperature, C_T, of the test motor is considered between $25°C$ (an ambient temperature) and $90°C$. The temperature values measured in four different locations inside the test motor. They measure the temperatures for phase one, phase two, phase three and the stator core, and they are recorded with respect to torque, T_a, and speed, ω_w, values to generate the 3D performance map.

5.1.4 Transient Response Test

As one example of the transient response tests, the rise time, t_r, is measured at several torque, T_a, and speed, ω_w, levels in this report. A step torque, T_m, input to the test motor is applied to clearly identify the changes of the torque magnitude. The response time for torque changes is as fast as predicted earlier (less than 10 msec) and there is almost no overshoot. Also, there are some torque ripples with signal noise, which are discussed in Section 3.7. In Figure 5.7, the rise time for the torque, T_a, response can clearly be identified as 0.24 msec. This criterion test generates performance maps for a number of torque, T_a, and speed, ω_w, values.

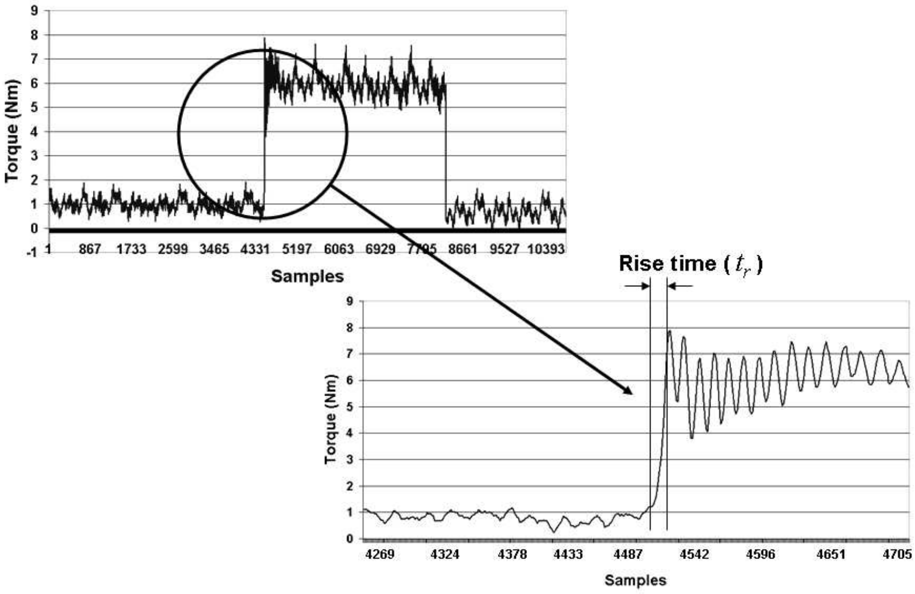

Figure 5.7: Measurement of rise time, t_r, at the reference inputs of 300 RPM and 6 Nm

The torque rise time, t_r, is limited by the mechanical inertia and the performance of the motion controller as mentioned in Section 3.5. However, the exact value of the system inertia is not required to be known because the torque rise time can be directly obtained from one of the Labview programs used in this report. The Labview program shown in Figure 5.3 has a triggering command to the DAQ board which pulls out the torque, T_a, signals at a steady rate. The collection of the sensor data is performed synchronously and the sampling rate can be estimated. These values are fixed and never changed during the test. The data from the torque rise time test is generated from the test set-up to create constant torque, T_a, values using the test motor and the load motor. The procedures for this transient response test are as follows.

- At rest, both of motors are connected by engaging the clutch.
- The load motor starts to run at a constant speed, ω_L. The speed, ω_w, of the system is governed by the load motor. At this time, the test motor is off.
- After a few seconds, the test motor energizes to develop a certain torque, T_m. The torque increases to a certain value as commanded by the controller and stays there for a few seconds to obtain enough data.
- The measured data during the operation is recorded by the DAQ board. The test data are recorded for a certain time in an equidistant period of a sampling rate.
- This test is repeated for different speeds of the load motor.
- The torque sensor measures the output torque, T_a, of the test motor. Figure 5.8 represents the control of the torque, T_a, generated in the test motor.

5.1.5 Hysteresis Brake Test

Using the hysteresis brake, torque ripple, T_r, and acceleration, a_b, performance maps are obtained. The hysteresis brake can be installed in the test bed instead of using the load motor. The reason that the hysteresis brake is used for these particular tests is to generate the torque, T_a, passively independent of the

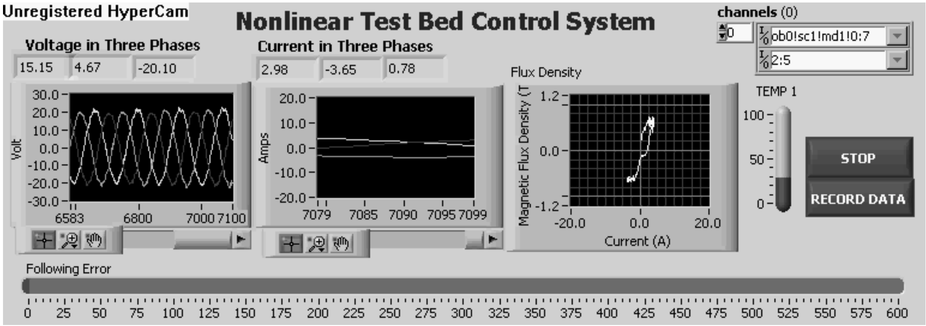

Figure 5.8: Labview program to control torque output in the test motor

speed, ω_T, of the test motor. In this test, the test motor requires speed feedback, ω_T, from the test motor encoder in closed loop[4]. The acceleration test needs to have a feature to increase the speed, ω_b, without changing the operating torque, T_a. Also, there are no salient poles in a hysteresis brake, so the ripple and cogging torques do not exist. Because the load motor, which has salient poles, is removed, the torque ripple, T_r, is measured only in the test motor.

For the acceleration test, the Labview programs in Figures 5.2 and 5.3 are modified as shown in Figures B.1 and B.2. In Figure B.1, the speed, ω_T, of the test motor increases from the base speed to the target speed and the acceleration data is obtained by differentiating the speed with respect to the time between two data points of the speed measurements as shown in Figure 5.9. To create the torque, T_a, the brake is engaged and the voltage input provides the increments of torque. The procedure to control the hysteresis brake and the load motor for the acceleration, a_b, test is as follows.

- At a stop position, the test motor and hysteresis brake are connected by

---

[4] When the load motor was used, the test motor controlled only torque signals measured in torque sensor in an open loop. The load motor controlled speed signals in a closed loop.

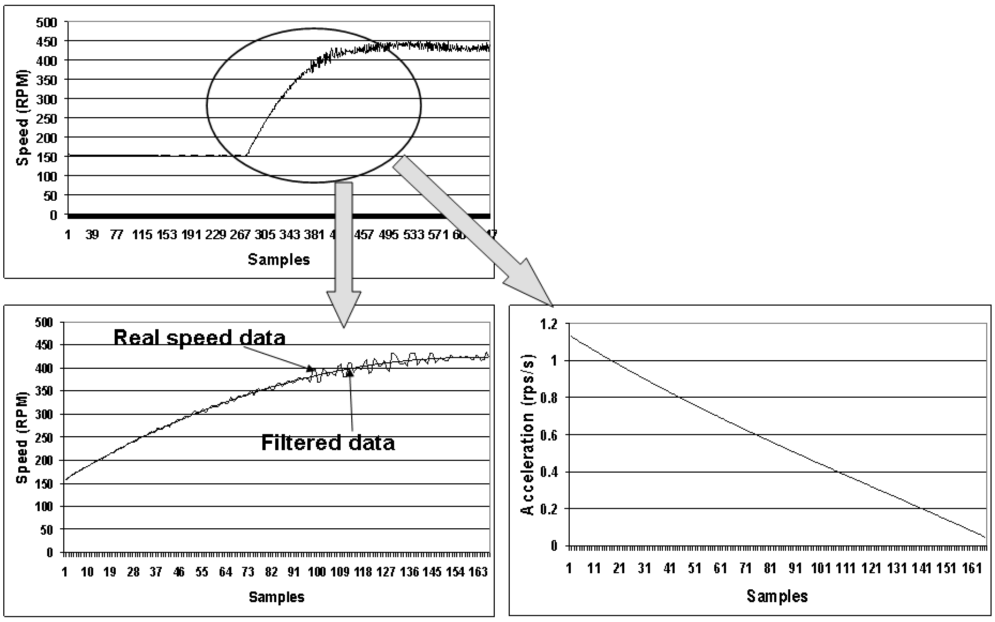

Figure 5.9: Representation of acceleration at 286 RPM of speed and 7.0 Nm of torque

engaging the clutch.

- The test motor starts to run at a constant speed, ω_b. The speed of the system is mostly governed by the inertia and friction of the test motor and hysteresis brake at the beginning. The speed is set by monitoring the torque response.
- After a few seconds, the hysteresis brake is applied to develop a certain torque, T_a. The torque increases to a certain value as commanded by the controller unless the motor runs at enough speed to overcome the inertia and friction of the test system.
- In the control program for the test motor, the command signal, which is the voltage signals provided in the motion program for the test motor, is provided to create the increment of speed. By doing this, the average and

maximum accelerations, a_b, are obtained.

- The measured data during the operation is recorded by the DAQ board. The test data is recorded in a time period of 3 msec.
- This test is repeated for different increments of speeds and torques of the test motor.

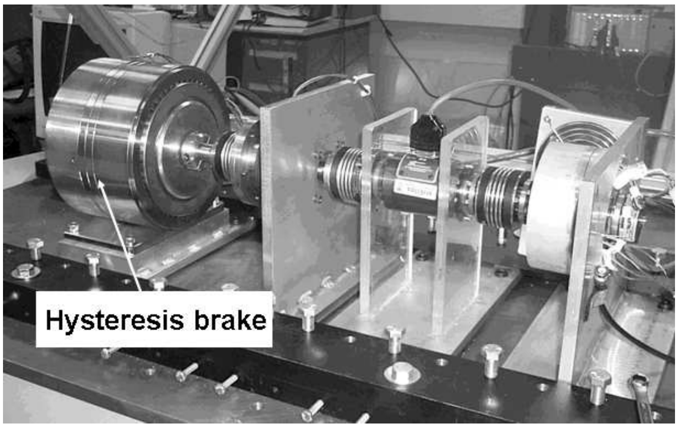

Figure 5.10: Hysteresis brake test bed to obtain acceleration and torque ripple performance maps

The biggest reason that the hysteresis brake is used in this test regime is to develop the torque ripple, T_r, performance map. A permanent magnet synchronous motor (PMSM), which is the test motor, generates parasitic torque pulsations owing to variable magnetic reluctance, distortion of the stator flux linkage distribution, and deficiencies of feasible winding geometries. The torque ripple is particularly undesirable in some demanding motion control applications, and it leads to speed oscillations which cause deterioration in the performance [40]. Continuous constant torque, T_a, from the test motor is generated in order to identify the ripple on the output torque curve. The torque ripple, T_r, will be measured in Equation

(3.12). The amplitude of torque ripple, ,T_r is obtained as shown in Figure 5.11. The RMS torque was 1.434 Nm and peak-to-peak torque was 0.355 Nm, which is $2T_r$. Therefore, the ripple was 12.36% based on Equation (3.12).

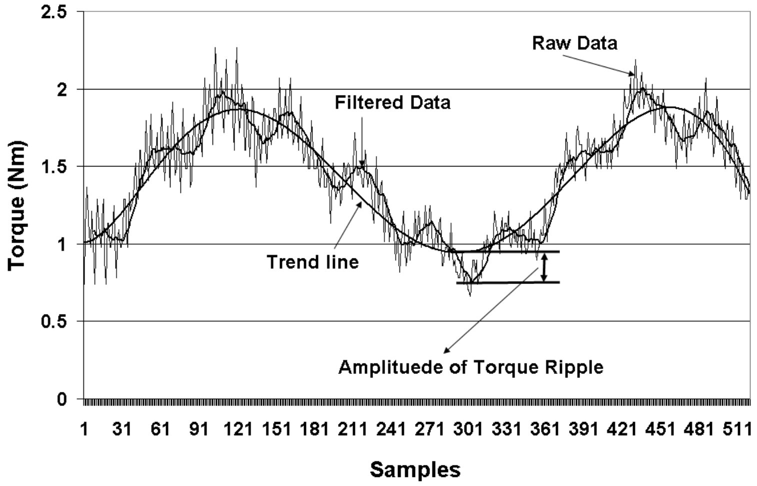

Figure 5.11: Representation of torque ripple at 180 RPM of speed and 1.43 Nm of RMS torque

The hysteresis brake is used to generate the constant torque, T_a, during the test. The torque, T_a, developed in the reaction of the test motor against the passive brake is controlled by the governing speed, ω_b, and applied voltage, V_b. The output signals measured in the torque sensor are filtered using an active filter to eliminate measurement noise. This test procedure is almost the same as the procedure for the acceleration performance map, except following the point where the test motor and the brake are connected and generate a certain torque, T_a.

- The test motor control program commands constant movement. The imbalance of the test bed system causes the sinusoidal response as shown in Figure 5.11.

- The torque data during the operation is recorded by the NI DAQ board. By investigating the 2D plots of the torque vs samples, the RMS and amplitude of torque ripple values are obtained.
- This test is repeated for different increments of speed and torque for the test motor.

If the speed, ω_b, of the test motor is less than 100 RPM, the speed is not enough to overcome the system inertia, so the speed should be increased to provide enough mechanical power to overcome the overall inertia. The measured signals should be as clean as possible to identify the torque ripple, T_r, from the sinusoidal torque, T_a, response.

5.2 Stochastic Processes on Test Data

In order to create a statistical model of the experimental data and to develop upper and lower error bounds for the sensor data, the Time Series Analysis is used. Section 5.2.1 represents the process in order to develop the statistical modeling of experimental data using regression analysis. In Section 5.2.2, the theory of Time Series Analysis (TSA) is concisely described and the error bounds are drawn by using the covariance matrix in Section 5.2.4. The stochastic model obtained from the Auto-Regressive and Moving Average (ARMA) equation is developed in Section 5.2.3.

5.2.1 Generation of Statistical Models

Statistical modeling assumes that information contained in experimental data can be extracted, analyzed, and reduced to one or more equations that can be used to replicate historical patterns. The patterns of experimental data are very clear to discriminate but sometimes they are disturbed by noise and uncertainties. The most popular technique used to represent the statistical model is regression analysis.

Regression attempts to model the relationship between two variables by fitting an equation to the observed data. One variable is considered to be an independent variable, and the other is considered to be a dependent variable. The experimental data of torque response, T_a, in a sinusoidal input command is shown in Figure 5.12. At this time, the torque profile was obtained at a speed of 100 RPM and the sinusoidal electrical torque input with the cyclic frequency of 0.5 Hz and the magnitude of 2.5 Volt. The regression analysis is used to fit a statistical model to the observed data.

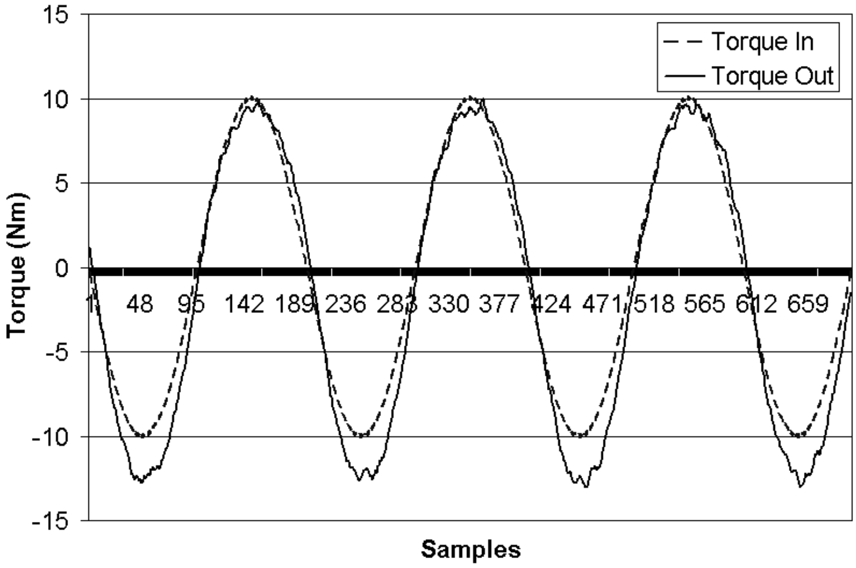

Figure 5.12: Torque, T_a, data about a sinusoidal input for regression analysis

The most common method for fitting a regression line is the method of least-squares. This method calculates the best fitting line for the observed data by minimizing the sum of the squares of the vertical deviations from each data point to the line (if a point lies on the fitting line exactly, then its vertical deviation is 0). Because the deviations are first squared, then summed, there are no cancelations between positive and negative values. In matrix algebra notation, a regression model is written as

$$Y = X\beta + \epsilon \tag{5.1}$$

where X is the $n \times k$ design matrix (rows are observations and columns are the regressors), β is the $k \times 1$ vector of unknown parameters, and ϵ is the $n \times 1$ vector of unknown errors. The first column of X is usually a vector of 1s used in estimating the intercept term [44]. Parameter estimates are formed using least-squares criteria by solving the normal equations as shown in Equation (5.4). First of all, the regression model should be expressed in terms of the sums of square error.

$$Min \;\; LS = \sum e_j^2 = e^T e = (Y - X\beta)^T (Y - X\beta) \tag{5.2}$$

By applying the partial derivative with respect to β, the least-square value can be minimized as follows

$$\frac{\partial LS}{\partial \beta} = 0 \tag{5.3}$$

Then,

$$X^T X\beta = X^T Y \tag{5.4}$$

for the parameter estimates β, yielding

$$\beta = (X^T X)^{-1} X^T Y \tag{5.5}$$

Assume for the present that $(X^T X)$ is full rank.

A least-square criterion refers to a methodology which evaluates the relationship between a set of values and alternative estimators of those values by choosing that estimator for which the sum of the squared differences between the actual values and the estimated values is lowest. The REG procedure in SAS fits least-square estimates to regression model equations as shown above. Figure 5.13 presents a set of torque data estimated by regression and actual torque data. Also, the proposed method does not fit exactly because the deviations of the actual and estimated data are monitored as shown in Figure 5.13. Base on this, something is either wrong with the data (errors in measurement), or the model is inadequate (errors in specification). Therefore, another statistical modeling method is presented in Section 5.2.2.

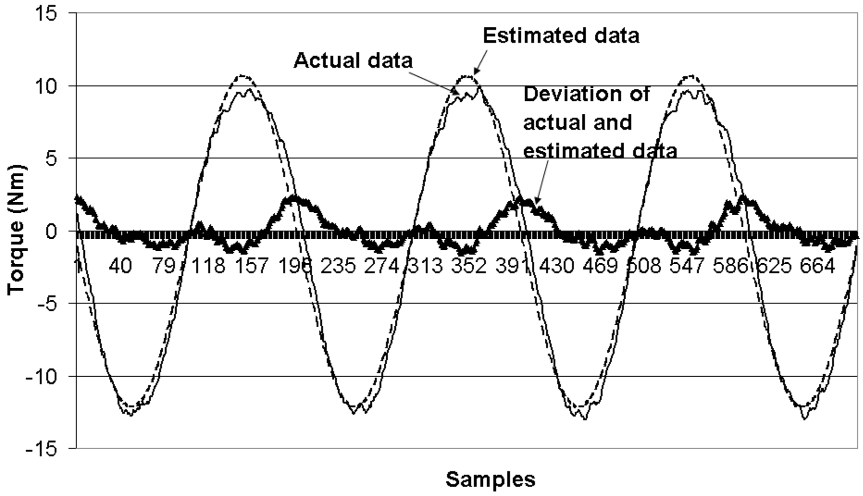

Figure 5.13: Measured and estimated torque curve

5.2.2 Time Series Analysis: Model Identification

A discrete time series consists of a set of random variables, which are observed at equally spaced time periods and which are ordered and indexed by time.

The experimental data appear as time series which is a sequence of observations taken sequentially in time. The selected method used in this research is Box-Jenkins ARMA models. The detailed information about this method is explained in [12].

The first thing that should be discussed is the difference between stationary and nonstationary system. The stationary process has the property that the mean, variance and autocorrelation structure do not change over time. On the other hand, most of the real applications are nonstationary systems which describe the system status changes in time. Many time series also display seasonality. Each experimental data should be checked to detect seasonality and properly described in the model. Once a time series model is decomposed into a trend, seasonal and residual component, the autoregressive (AR) and moving average (MA) model can be obtained. There are three stages that perform the autoregressive integrated moving average (ARIMA) process corresponding to that described in references of [12], [13]. Box and Jenkins recommend differencing nonstationary series one or more times to achieve a stationary series. Doing so produces an ARIMA model, with the "I" standing for "Integrated". All of these statistical processes are performed in SAS which is a very popular statistical computational software package.

In the identification stage, the IDENTIFY[5] statement in SAS is used to specify the response series and identify candidate ARIMA models for them [85]. The IDENTIFY reads time series data that are used in later statements, possibly difference them for nonstationary data, and compute autocorrelations, inverse autocorrelations, and partial autocorrelations. Stationary tests can be performed to determine if differencing is necessary. The analysis of the IDENTIFY statement

---

[5] One of SAS commands, SAS statements requests predefined routines called a PROC [85].

suggests two or three ARIMA models that can be fit and one of them should be selected as the system model based on three autocorrelation plots. The IDENTIFY statement in SAS first prints descriptive statistics for “Deviation” torque data represented in Figure 5.13. This part of the IDENTIFY statement is shown in Figure 5.14.

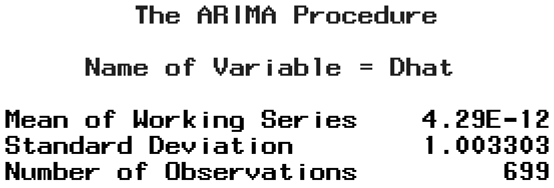

```
                The ARIMA Procedure

             Name of Variable = Dhat

      Mean of Working Series    4.29E-12
      Standard Deviation        1.003303
      Number of Observations         699
```

Figure 5.14: IDENTIFY statement descriptive statistics output

The IDENTIFY statement next prints three plots of the correlations of the series with its past values at different lags. The sample autocorrelation function plot output of the IDENTIFY statement is shown in Figure 5.15. The autocorrelation plot shows how values of the series are correlated with past values of the series. For example, the value 0.98494 in the “Correlation” column for lag 1 row of the plot means that the correlation between “Dhat”, which is the variable name of “Deviation” torque data, and the Dhat value for the previous period is 0.98494. The rows of asterisks show the correlation values graphically. Also, the confidence interval is generated, which is approximately $\pm\frac{2}{\sqrt{N}}$ with N denoting the sample size.

This plot is called an autocorrelation function because it shows the degree of correlation with past values of the series as a function of the number of periods in the past (that is, the lag) at which the correlation is computed. In this case, there

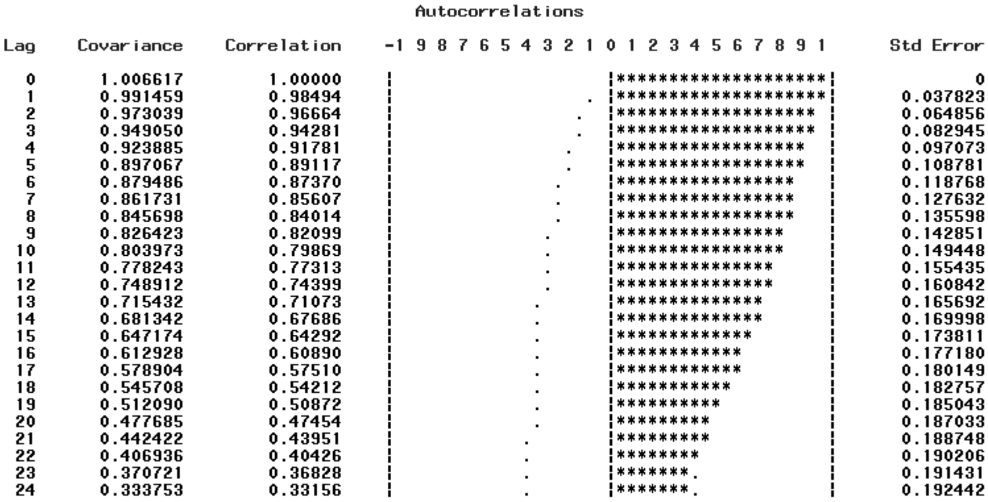

```
                                              Autocorrelations

Lag    Covariance    Correlation    -1 9 8 7 6 5 4 3 2 1 0 1 2 3 4 5 6 7 8 9 1       Std Error

  0      1.006617        1.00000    |                    |********************|              0
  1      0.991459        0.98494    |                  . |********************|       0.037823
  2      0.973039        0.96664    |                 .  |******************* |       0.064856
  3      0.949050        0.94281    |                 .  |******************* |       0.082945
  4      0.923885        0.91781    |                .   |******************  |       0.097073
  5      0.897067        0.89117    |                .   |******************  |       0.108781
  6      0.879486        0.87370    |               .    |*****************   |       0.118768
  7      0.861731        0.85607    |               .    |*****************   |       0.127632
  8      0.845698        0.84014    |               .    |*****************   |       0.135598
  9      0.826423        0.82099    |              .     |****************    |       0.142851
 10      0.803973        0.79869    |              .     |****************    |       0.149448
 11      0.778243        0.77313    |              .     |***************     |       0.155435
 12      0.748912        0.74399    |              .     |***************     |       0.160842
 13      0.715432        0.71073    |             .      |**************      |       0.165692
 14      0.681342        0.67686    |             .      |**************      |       0.169998
 15      0.647174        0.64292    |             .      |*************       |       0.173811
 16      0.612928        0.60890    |             .      |************        |       0.177180
 17      0.578904        0.57510    |             .      |************        |       0.180149
 18      0.545708        0.54212    |             .      |***********         |       0.182757
 19      0.512090        0.50872    |             .      |**********          |       0.185043
 20      0.477685        0.47454    |             .      |*********           |       0.187033
 21      0.442422        0.43951    |            .       |*********           |       0.188748
 22      0.406936        0.40426    |            .       |********            |       0.190206
 23      0.370721        0.36828    |            .       |*******.            |       0.191431
 24      0.333753        0.33156    |            .       |*******.            |       0.192442
```

Figure 5.15: IDENTIFY statement Autocorrelations plot

are only 24 lags by default but the lag can be shortened or expanded by the NLAG[6] command. By examining this plot, we can judge whether the series is stationary or nonstationary. A visual inspection of the autocorrelation function (ACF) plot indicates that the Dhat series is nonstationary, since the ACF decays very slowly. Therefore, the ACF plot helps to evaluate the “stationarity” of the test data and provides how many differencings the system needs to achieve stationarity.

The inverse and partial autocorrelation plots are presented in Figure 5.16 and 5.17. These plots have the same form as the autocorrelation plots, but display inverse and partial autocorrelation values instead of autocorrelations and autocovariances. The mathematical expressions of these correlations are referred to [12].

The last part of the default IDENTIFY statement output is the check for white noise. This is an approximate statistical test of the hypothesis that none of

---

[6] NLAG is the order of AR process in SAS.

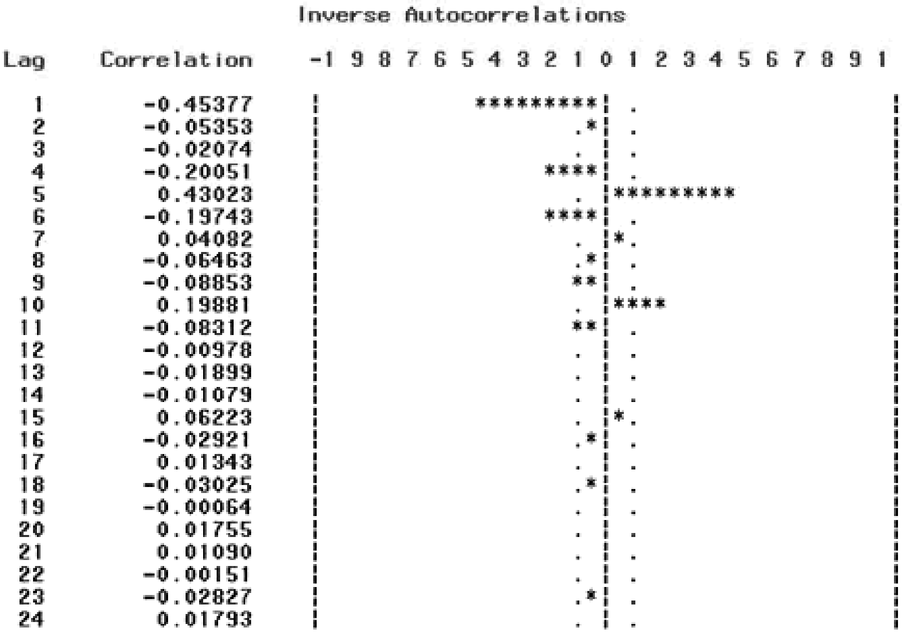

```
                        Inverse Autocorrelations

Lag     Correlation    -1 9 8 7 6 5 4 3 2 1 0 1 2 3 4 5 6 7 8 9 1

 1         -0.45377    |          *********| .                 |
 2         -0.05353    |                 .*| .                 |
 3         -0.02074    |                 . | .                 |
 4         -0.20051    |               ****| .                 |
 5          0.43023    |                 . |*********          |
 6         -0.19743    |               ****| .                 |
 7          0.04082    |                 . |*.                 |
 8         -0.06463    |                 .*| .                 |
 9         -0.08853    |                 **| .                 |
10          0.19881    |                 . |****               |
11         -0.08312    |                 **| .                 |
12         -0.00978    |                 . | .                 |
13         -0.01899    |                 . | .                 |
14         -0.01079    |                 . | .                 |
15          0.06223    |                 . |*.                 |
16         -0.02921    |                 .*| .                 |
17          0.01343    |                 . | .                 |
18         -0.03025    |                 .*| .                 |
19         -0.00064    |                 . | .                 |
20          0.01755    |                 . | .                 |
21          0.01090    |                 . | .                 |
22         -0.00151    |                 . | .                 |
23         -0.02827    |                 .*| .                 |
24          0.01793    |                 . | .                 |
```

Figure 5.16: Inverse Autocorrelation Function (IACF) plot for Dhat

the autocorrelations of the series up to a given lag are significantly different from 0. The numbers of "Autocorrelations" should be close to 0 in order not to have a significant relationship between a current lag value and a previous lag value. The autocorrelations are checked in groups of six, and the number of lags checked depends on the NLAG. The check for white noise output is shown in Figure 5.18. The white noise stochastic process is simply a normal random variable with zero mean and variance, σ^2. In this case, the white noise hypotheses in each lags are rejected, which is expected since the series is nonstationary.

Since the series is nonstationary, the next step is to transform it to a stationary series by differencing. That is, instead of modeling the Dhat series itself, the change in Dhat from one period to the next is modeled. To difference the Dhat series, use another IDENTIFY statement and specify that the first difference of

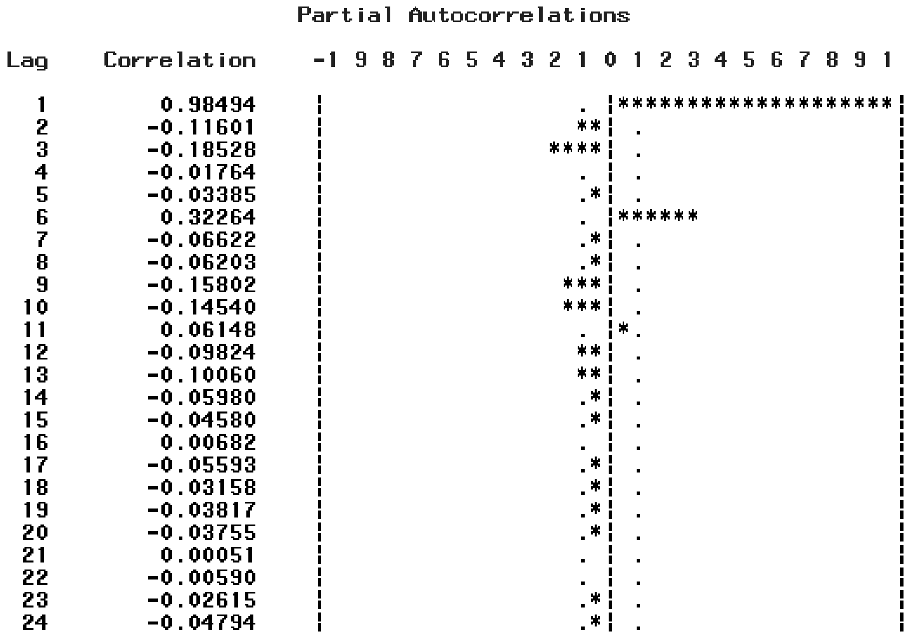

```
                          Partial Autocorrelations

 Lag    Correlation    -1 9 8 7 6 5 4 3 2 1 0 1 2 3 4 5 6 7 8 9 1

   1        0.98494     |                  . |********************|
   2       -0.11601     |                  **| .                  |
   3       -0.18528     |                ****| .                  |
   4       -0.01764     |                  . | .                  |
   5       -0.03385     |                  .*| .                  |
   6        0.32264     |                  . |******              |
   7       -0.06622     |                  .*| .                  |
   8       -0.06203     |                  .*| .                  |
   9       -0.15802     |                 ***| .                  |
  10       -0.14540     |                 ***| .                  |
  11        0.06148     |                  . |*.                  |
  12       -0.09824     |                  **| .                  |
  13       -0.10060     |                  **| .                  |
  14       -0.05980     |                  .*| .                  |
  15       -0.04580     |                  .*| .                  |
  16        0.00682     |                  . | .                  |
  17       -0.05593     |                  .*| .                  |
  18       -0.03158     |                  .*| .                  |
  19       -0.03817     |                  .*| .                  |
  20       -0.03755     |                  .*| .                  |
  21        0.00051     |                  . | .                  |
  22       -0.00590     |                  . | .                  |
  23       -0.02615     |                  .*| .                  |
  24       -0.04794     |                  .*| .                  |
```

Figure 5.17: Partial Autocorrelation Function (PACF) plot for Dhat

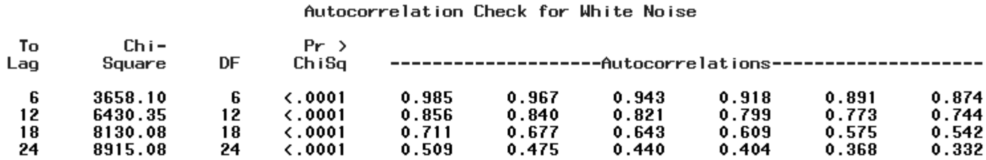

```
                                  Autocorrelation Check for White Noise

  To        Chi-             Pr >
 Lag      Square     DF     ChiSq    --------------------Autocorrelations--------------------

   6     3658.10      6    <.0001     0.985      0.967      0.943      0.918      0.891      0.874
  12     6430.35     12    <.0001     0.856      0.840      0.821      0.799      0.773      0.744
  18     8130.08     18    <.0001     0.711      0.677      0.643      0.609      0.575      0.542
  24     8915.08     24    <.0001     0.509      0.475      0.440      0.404      0.368      0.332
```

Figure 5.18: IDENTIFY statement check for white noise

Dhat be analyzed. The second IDENTIFY statement produces the same information as the first but for the change in Dhat from one period to the next rather than for the total Dhat in each period. The summary statistics output from this IDENTIFY statement is shown in Figure 5.19. Notice that the period of differencing is given as 1, and one observation is lost through the differencing operation.

The autocorrelation function (ACF) plot for the differenced series is shown in Figure 5.20. The autocorrelations in the ACF plot of Figure 5.20 decrease

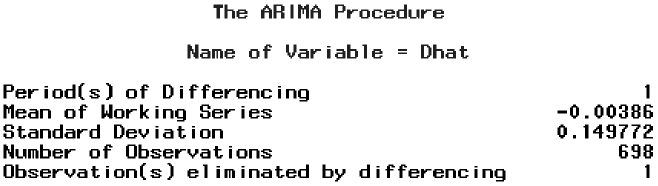

```
                The ARIMA Procedure

              Name of Variable = Dhat

Period(s) of Differencing                         1
Mean of Working Series                     -0.00386
Standard Deviation                         0.149772
Number of Observations                          698
Observation(s) eliminated by differencing         1
```

Figure 5.19: IDENTIFY statement output for differenced series

rapidly compared with the ACF plot shown in Figure 5.15, indicating that the change in Dhat becomes a stationary time series. For a discrete process of the stationary time series data, the joint distribution of any set of observations, which indicates the number of lags in Figure 5.20, is unaffected by shifting all the times of observation by the differencing operation.

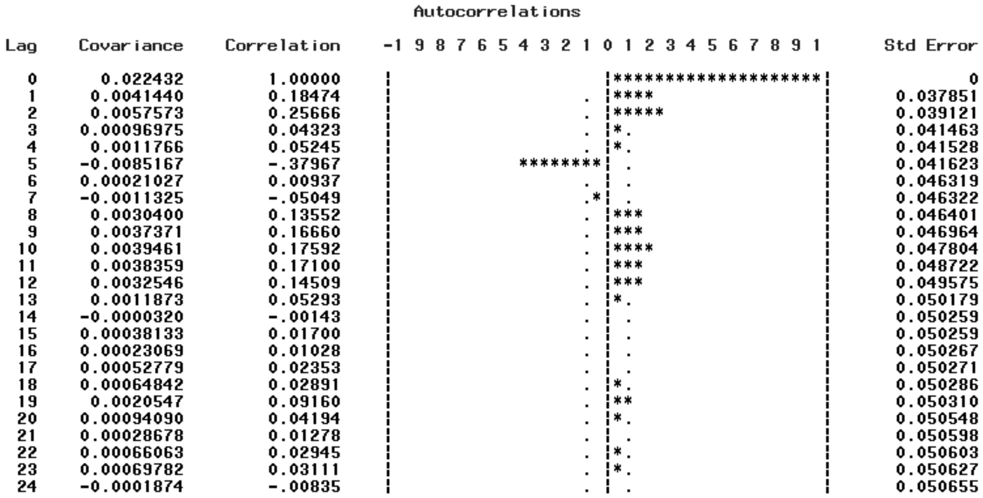

```
                                                               Autocorrelations

Lag    Covariance    Correlation    -1 9 8 7 6 5 4 3 2 1 0 1 2 3 4 5 6 7 8 9 1         Std Error

  0      0.022432        1.00000    |                    |********************|            0
  1     0.0041440        0.18474    |                  . |****                |     0.037851
  2     0.0057573        0.25666    |                  . |*****               |     0.039121
  3    0.00096975        0.04323    |                  . |*.                  |     0.041463
  4     0.0011766        0.05245    |                  . |*.                  |     0.041528
  5    -0.0085167        -.37967    |            ********| .                  |     0.041623
  6    0.00021027        0.00937    |                  . | .                  |     0.046319
  7    -0.0011325        -.05049    |                  .*| .                  |     0.046322
  8     0.0030400        0.13552    |                  . |***                 |     0.046401
  9     0.0037371        0.16660    |                  . |***                 |     0.046964
 10     0.0039461        0.17592    |                  . |****                |     0.047804
 11     0.0038359        0.17100    |                  . |***                 |     0.048722
 12     0.0032546        0.14509    |                  . |***                 |     0.049575
 13     0.0011873        0.05293    |                  . |*.                  |     0.050179
 14    -0.0000320        -.00143    |                  . | .                  |     0.050259
 15    0.00038133        0.01700    |                  . | .                  |     0.050259
 16    0.00023069        0.01028    |                  . | .                  |     0.050267
 17    0.00052779        0.02353    |                  . | .                  |     0.050271
 18    0.00064842        0.02891    |                  . |*.                  |     0.050286
 19     0.0020547        0.09160    |                  . |**                  |     0.050310
 20    0.00094090        0.04194    |                  . |*.                  |     0.050548
 21    0.00028678        0.01278    |                  . | .                  |     0.050598
 22    0.00066063        0.02945    |                  . |*.                  |     0.050603
 23    0.00069782        0.03111    |                  . |*.                  |     0.050627
 24    -0.0001874        -.00835    |                  . | .                  |     0.050655
```

Figure 5.20: Autocorrelations plot for change in Dhat

The next step in the Box-Jenkins methodology [12] is to examine the patterns in the autocorrelation plot to choose candidate ARIMA models to the series. The inverse and partial autocorrelation function plots are also useful aids in identifying appropriate ARIMA models for the series. The inverse and partial autocorrelation function plots for differenced data are shown in Figure 5.21 and 5.22.

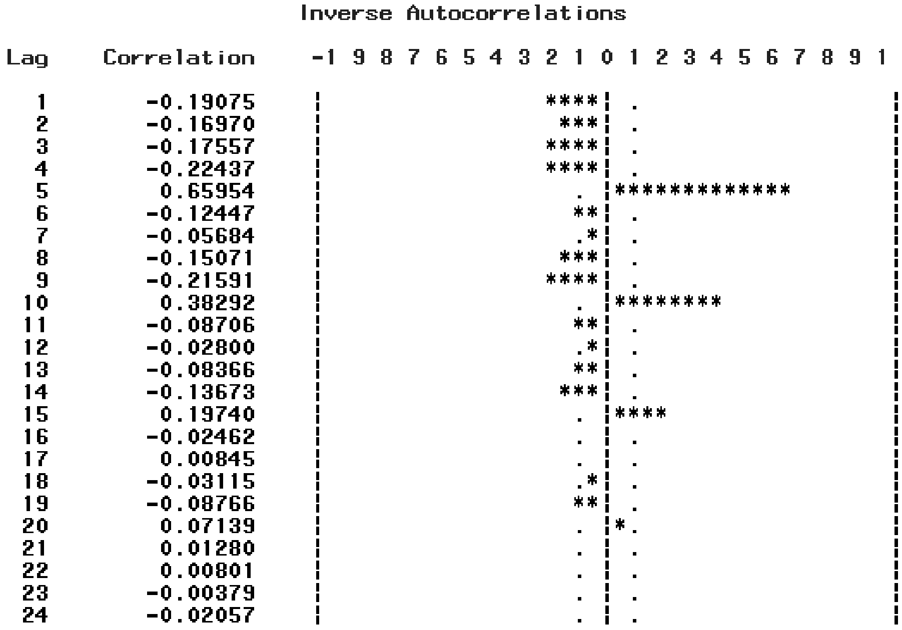

```
                           Inverse Autocorrelations

 Lag    Correlation    -1 9 8 7 6 5 4 3 2 1 0 1 2 3 4 5 6 7 8 9 1

   1       -0.19075     |                ****| .                  |
   2       -0.16970     |                 ***| .                  |
   3       -0.17557     |                ****| .                  |
   4       -0.22437     |                ****| .                  |
   5        0.65954     |                  . |*************       |
   6       -0.12447     |                  **| .                  |
   7       -0.05684     |                  .*| .                  |
   8       -0.15071     |                 ***| .                  |
   9       -0.21591     |                ****| .                  |
  10        0.38292     |                  . |********            |
  11       -0.08706     |                  **| .                  |
  12       -0.02800     |                  .*| .                  |
  13       -0.08366     |                  **| .                  |
  14       -0.13673     |                 ***| .                  |
  15        0.19740     |                  . |****                |
  16       -0.02462     |                  . | .                  |
  17        0.00845     |                  . | .                  |
  18       -0.03115     |                  .*| .                  |
  19       -0.08766     |                  **| .                  |
  20        0.07139     |                  . |*.                  |
  21        0.01280     |                  . | .                  |
  22        0.00801     |                  . | .                  |
  23       -0.00379     |                  . | .                  |
  24       -0.02057     |                  . | .                  |
```

Figure 5.21: IACF plot for change in Dhat

In the usual Box and Jenkins approach to ARIMA modeling [13], the sample ACF, IACF, and PACF are compared with the theoretical correlation functions expected from different kinds of ARIMA models. This matching of theoretical autocorrelation functions of different ARIMA models to the sample autocorrelation functions computed from the response series is the heart of the identification stage of Box-Jenkins modeling.

If the series is white noise (a pure random process), then there is no need to difference the data any more. The check for white noise, shown in Figure 5.23, indicates that the change in Dhat is not significantly autocorrelated because the autocorrelation values are very small compared with the autocorrelation values

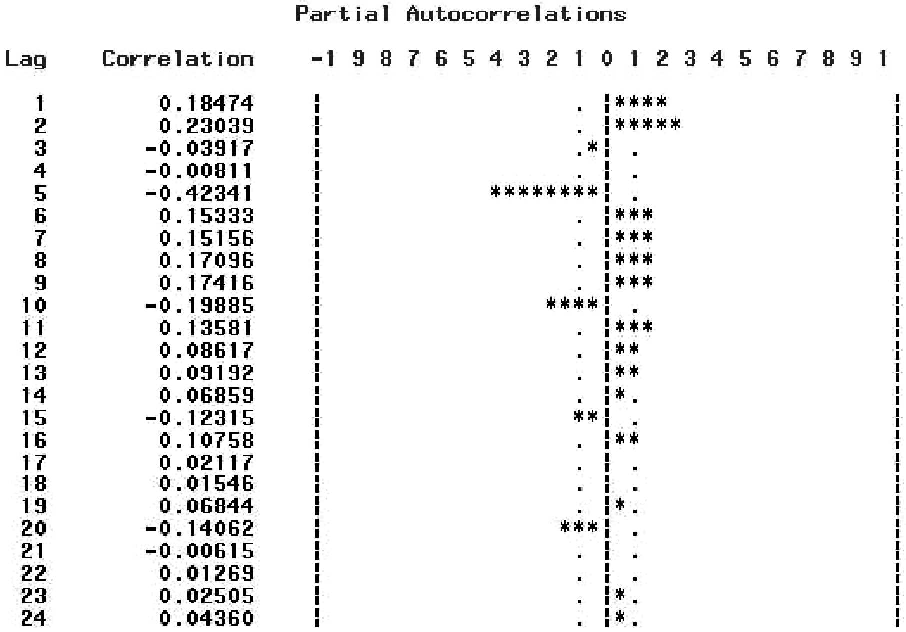

```
                          Partial Autocorrelations

 Lag    Correlation    -1 9 8 7 6 5 4 3 2 1 0 1 2 3 4 5 6 7 8 9 1

   1        0.18474    |                   . |****                |
   2        0.23039    |                   . |*****               |
   3       -0.03917    |                   .*| .                  |
   4       -0.00811    |                   . | .                  |
   5       -0.42341    |             ********| .                  |
   6        0.15333    |                   . |***                 |
   7        0.15156    |                   . |***                 |
   8        0.17096    |                   . |***                 |
   9        0.17416    |                   . |***                 |
  10       -0.19885    |                 ****| .                  |
  11        0.13581    |                   . |***                 |
  12        0.08617    |                   . |**                  |
  13        0.09192    |                   . |**                  |
  14        0.06859    |                   . |*.                  |
  15       -0.12315    |                   **| .                  |
  16        0.10758    |                   . |**                  |
  17        0.02117    |                   . | .                  |
  18        0.01546    |                   . | .                  |
  19        0.06844    |                   . |*.                  |
  20       -0.14062    |                  ***| .                  |
  21       -0.00615    |                   . | .                  |
  22        0.01269    |                   . | .                  |
  23        0.02505    |                   . |*.                  |
  24        0.04360    |                   . |*.                  |
```

Figure 5.22: PACF plot for change in Dhat

shown in Figure 5.18. Thus, one differencing operation is enough to turn the nonstationary estimated values into stationary series.

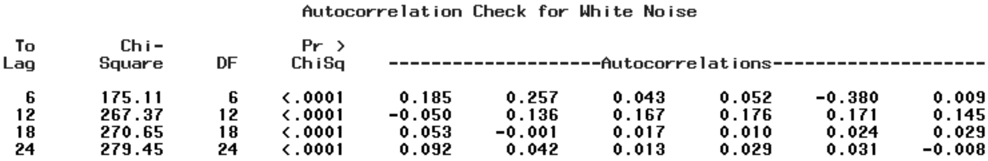

```
                          Autocorrelation Check for White Noise

 To        Chi-             Pr >
Lag      Square     DF     ChiSq     --------------------Autocorrelations--------------------

  6      175.11      6    <.0001      0.185      0.257      0.043      0.052     -0.380      0.009
 12      267.37     12    <.0001     -0.050      0.136      0.167      0.176      0.171      0.145
 18      270.65     18    <.0001      0.053     -0.001      0.017      0.010      0.024      0.029
 24      279.45     24    <.0001      0.092      0.042      0.013      0.029      0.031     -0.008
```

Figure 5.23: White noise check for change in Dhat

Seasonality (or periodicity) is also detected in IACF and PACF plots in Figure 5.21 and 5.22. By seasonality the time series display periodic fluctuations. The ICAF and PACF plots show spikes at lags equal to the period of five (lag 5, 10, 15, 20). In Section 5.2.3, the seasonal effect is considered to develop the ARIMA equation.

5.2.3 Time Series Analysis: Estimation and Diagnostic Checking

In the estimation and diagnostic checking stage, the ESTIMATE statement specifies the ARIMA model to fit to the variable specified in the previous IDENTIFY statement, and to estimate the parameters of that model [85]. The ESTIMATE statement also produces diagnostic statistics to judge the adequacy of the model. Significance tests for parameter estimates using t-statistics indicate whether some terms in the model are necessary [44].

Once stationary and seasonality have been addressed in Section 5.2.2, the next step is to identify the order of the Auto-Regressive(AR) and Moving Average(MA) terms. The primary tools for doing this are the autocorrelation, inverse autocorrelation and partial autocorrelation plots. The general rules to determine the order of AR and MA are explained as follows.

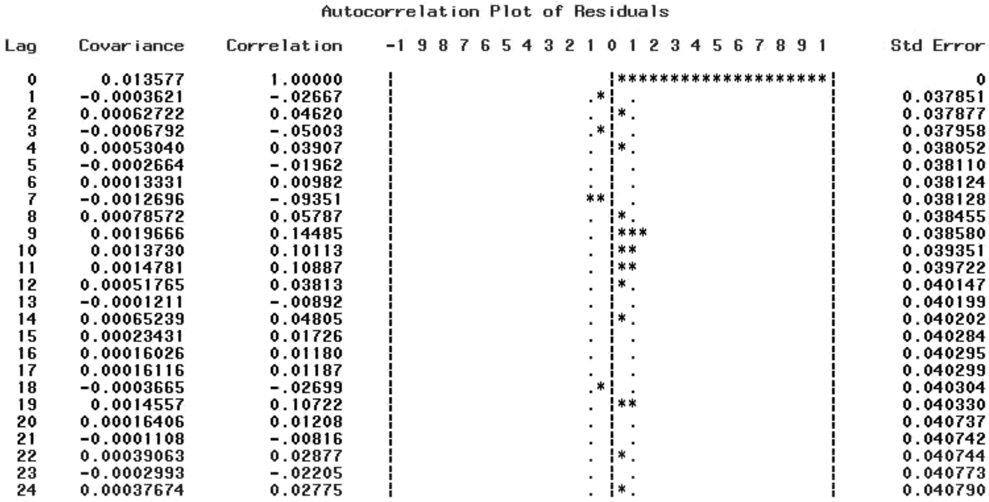

```
                              Autocorrelation Plot of Residuals

 Lag    Covariance    Correlation    -1 9 8 7 6 5 4 3 2 1 0 1 2 3 4 5 6 7 8 9 1      Std Error

   0      0.013577        1.00000    |                    |********************|             0
   1    -0.0003621        -.02667    |                  .*|  .                 |      0.037851
   2    0.00062722        0.04620    |                  . |* .                 |      0.037877
   3    -0.0006792        -.05003    |                  .*|  .                 |      0.037958
   4    0.00053040        0.03907    |                  . |* .                 |      0.038052
   5    -0.0002664        -.01962    |                  . |  .                 |      0.038110
   6    0.00013331        0.00982    |                  . |  .                 |      0.038124
   7    -0.0012696        -.09351    |                  **|  .                 |      0.038128
   8    0.00078572        0.05787    |                  . |* .                 |      0.038455
   9     0.0019666        0.14485    |                  . |***                 |      0.038580
  10     0.0013730        0.10113    |                  . |**                  |      0.039351
  11     0.0014781        0.10887    |                  . |**                  |      0.039722
  12    0.00051765        0.03813    |                  . |* .                 |      0.040147
  13    -0.0001211        -.00892    |                  . |  .                 |      0.040199
  14    0.00065239        0.04805    |                  . |* .                 |      0.040202
  15    0.00023431        0.01726    |                  . |  .                 |      0.040284
  16    0.00016026        0.01180    |                  . |  .                 |      0.040295
  17    0.00016116        0.01187    |                  . |  .                 |      0.040299
  18    -0.0003665        -.02699    |                  .*|  .                 |      0.040304
  19     0.0014557        0.10722    |                  . |**                  |      0.040330
  20    0.00016406        0.01208    |                  . |  .                 |      0.040737
  21    -0.0001108        -.00816    |                  . |  .                 |      0.040742
  22    0.00039063        0.02877    |                  . |* .                 |      0.040744
  23    -0.0002993        -.02205    |                  . |  .                 |      0.040773
  24    0.00037674        0.02775    |                  . |* .                 |      0.040790
```

Figure 5.24: ESTIMATE statement ACF plot at p=1, q=(1)(5)

Specifically, for the AR(1) process, the sample autocorrelation function should have an exponentially decreasing appearance. However, higher order AR processes are often a mixture of exponentially decreasing and damped sinusoidal components. For higher order autoregressive processes, the sample autocorrelation needs to be supplemented with inverse autocorrelation and partial correlation plots. The partial autocorrelation of an AR(p) process becomes zero at lag p+1 and greater, so the sample partial autocorrelation function is examined to see if there is evidence of a departure from zero. The inverse autocorrelation plot is applied in the exactly same way [12].

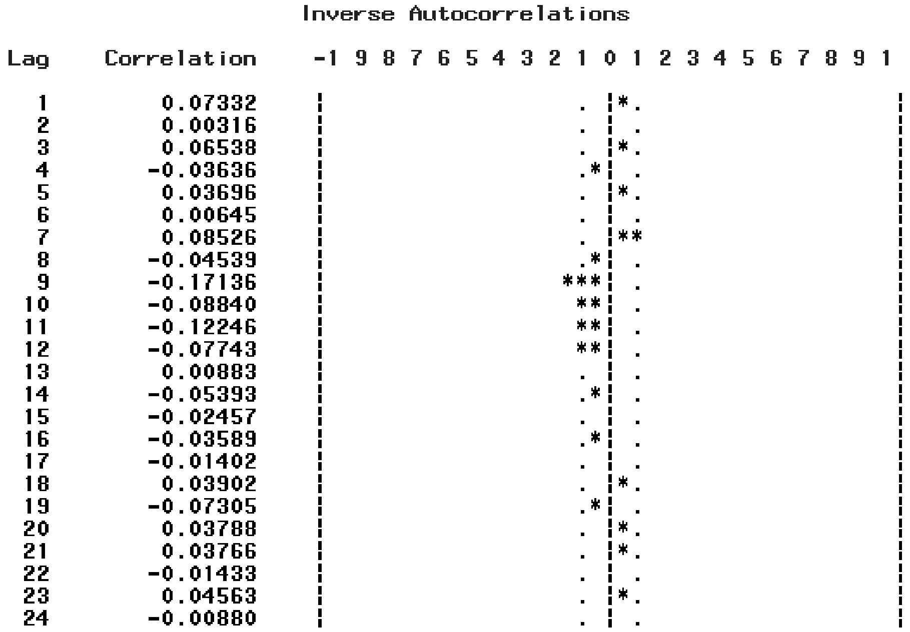

```
                        Inverse Autocorrelations

  Lag    Correlation    -1 9 8 7 6 5 4 3 2 1 0 1 2 3 4 5 6 7 8 9 1

    1        0.07332     |                 . |*.                 |
    2        0.00316     |                 . | .                 |
    3        0.06538     |                 . |*.                 |
    4       -0.03636     |                 .*| .                 |
    5        0.03696     |                 . |*.                 |
    6        0.00645     |                 . | .                 |
    7        0.08526     |                 . |**                 |
    8       -0.04539     |                 .*| .                 |
    9       -0.17136     |                ***| .                 |
   10       -0.08840     |                 **| .                 |
   11       -0.12246     |                 **| .                 |
   12       -0.07743     |                 **| .                 |
   13        0.00883     |                 . | .                 |
   14       -0.05393     |                 .*| .                 |
   15       -0.02457     |                 . | .                 |
   16       -0.03589     |                 .*| .                 |
   17       -0.01402     |                 . | .                 |
   18        0.03902     |                 . |*.                 |
   19       -0.07305     |                 .*| .                 |
   20        0.03788     |                 . |*.                 |
   21        0.03766     |                 . |*.                 |
   22       -0.01433     |                 . | .                 |
   23        0.04563     |                 . |*.                 |
   24       -0.00880     |                 . | .                 |
```

Figure 5.25: ESTIMATE statement IACF plot at p=1, q=(1)(5)

The autocorrelation function of a MA(q) process becomes zero at lag q+1 and greater, so the sample autocorrelation function is examined to see where it essentially becomes zero. The sample autocorrelation function on the sample autocorrelation plot is placed in the 95% confidence intervals. The partial autocorrelation function is generally not helpful for identifying the order of the moving

Shape	Indicated Model
Exponential, decaying to zero	AR model. Use the PACF plot to identify the order of the AR model.
Alternating positive and negative, decaying to zero	AR model. Use the PACF plot to help identify the order.
One or more spikes, rest are essentially zero	MA model. The order is identified by where plot becomes zero.
Decay, starting after a few lags	Mixed AR and MA model.
All zero or close to zero	Data is essentially random.
High values at fixed intervals	Include seasonal AR term.

Table 5.2: Shape of autocorrelation function

average process. Table 5.2 summarizes how the autocorrelation function for model identification is used.

Practically, the ACF, IACF, and PACF are random variables and will not give the same pictures as the theoretical functions as shown in Table 5.2. Especially, the mixed models are more difficult to identify. Based on the theories learned above, the mixed ARIMA model of Dhat in Figure 5.13 is estimated and the process to determine the model involves much trial and error.

In Figure 5.20, the shape of autocorrelation plot includes alternating positive and negative ACF, which means the AR(1) component is involved, and one or more spikes, and the rest of them are zero, which indicate the MA(1) component in the model. The spikes at fixed five intervals indicate the seasonal effect is involved in the MA term in IACF and PACF plots as mentioned in Section 5.2.2. By performing computational trials with different combinations of AR and MA orders, the order of AR is 1 and the order of MA is 1. Also, the seasonal value in the MA part is determined as 5. Then, ACF in most of the lags stays within 95% confidence intervals as shown in Figure 5.24. Also, IACF and PACF plots are

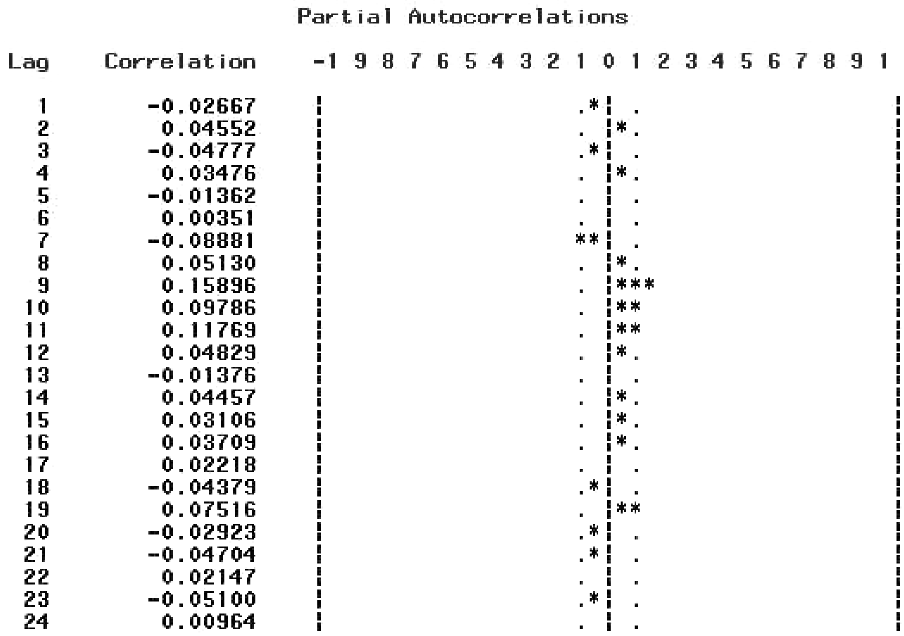

```
                      Partial Autocorrelations

 Lag    Correlation    -1 9 8 7 6 5 4 3 2 1 0 1 2 3 4 5 6 7 8 9 1

   1       -0.02667     |                 .*| .                 |
   2        0.04552     |                 . |*.                 |
   3       -0.04777     |                 .*| .                 |
   4        0.03476     |                 . |*.                 |
   5       -0.01362     |                 . | .                 |
   6        0.00351     |                 . | .                 |
   7       -0.08881     |                 **| .                 |
   8        0.05130     |                 . |*.                 |
   9        0.15896     |                 . |***                |
  10        0.09786     |                 . |**                 |
  11        0.11769     |                 . |**                 |
  12        0.04829     |                 . |*.                 |
  13       -0.01376     |                 . | .                 |
  14        0.04457     |                 . |*.                 |
  15        0.03106     |                 . |*.                 |
  16        0.03709     |                 . |*.                 |
  17        0.02218     |                 . | .                 |
  18       -0.04379     |                 .*| .                 |
  19        0.07516     |                 . |**                 |
  20       -0.02923     |                 .*| .                 |
  21       -0.04704     |                 .*| .                 |
  22        0.02147     |                 . | .                 |
  23       -0.05100     |                 .*| .                 |
  24        0.00964     |                 . | .                 |
```

Figure 5.26: ESTIMATE statement PACF plot at p=1, q=(1)(5)

given in Figures 5.25 and 5.26, and show that the spikes are removed for the best estimation of ARIMA model.

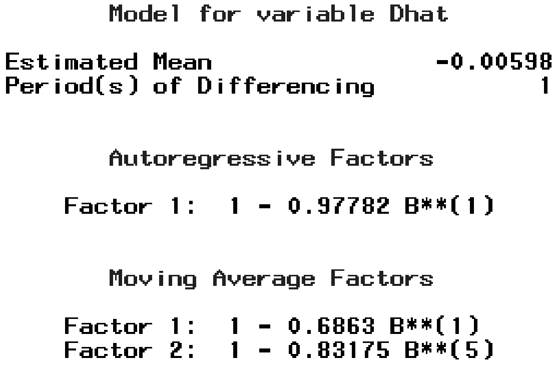

```
             Model for variable Dhat

      Estimated Mean                -0.00598
      Period(s) of Differencing            1

             Autoregressive Factors

         Factor 1:  1 - 0.97782 B**(1)

             Moving Average Factors

         Factor 1:  1 - 0.6863 B**(1)
         Factor 2:  1 - 0.83175 B**(5)
```

Figure 5.27: ESTIMATE ARIMA model for Dhat at p=1, q=(1)(5)

The list of factors in Figure 5.27 combines the differencing specification given in the IDENTIFY statement with the parameter estimates of the model for the change in Dhat. The estimated model shown in this output is written as

$$(1-B)Y_t = -0.00598 + \frac{(1-0.6863B)(1-0.83175B^5)}{(1-0.97782B)}a_t \tag{5.6}$$

where B stands for the back shift operator[7]. Y_t is the response series and a_t is the independent disturbances. Based on Appendix A, ARIMA$(1,1,1)\times(0,0,1)_5$ is expressed in Equation (5.6).

5.2.4 Development of Upper and Lower Error Bounds

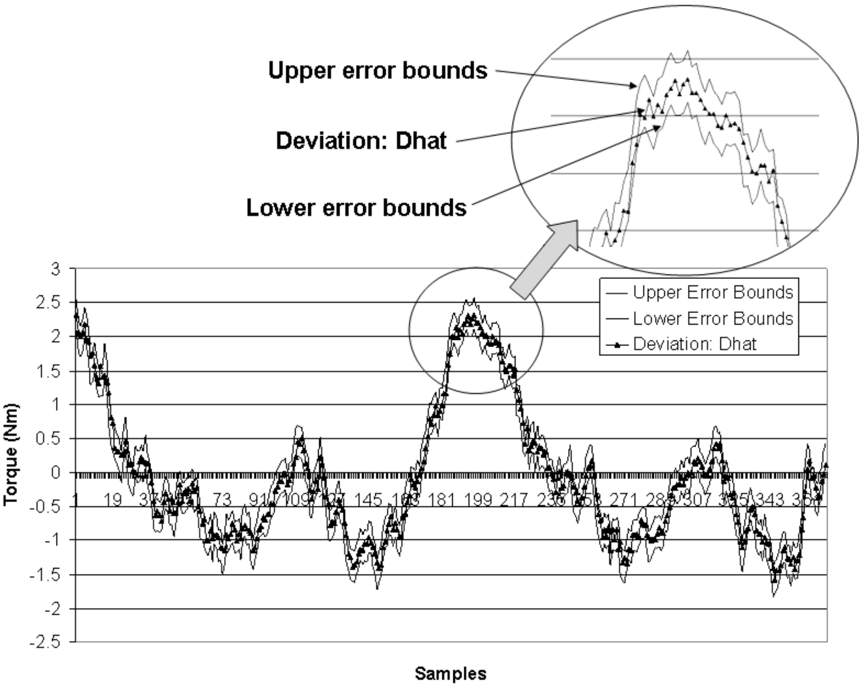

Figure 5.28: Dhat plot with 95% confidence interval

The standard error of the mean is used to indicate a confidence interval about the mean, which is useful when motor test data represent a sample of real

---

[7] B is also mentioned as magnetic flux density in Section 2.1.1.

values from some candidates. Figure 5.28 shows 95% confidence interval about a torque test result.

When data are independently sampled from a normal distribution, the confidence interval for the mean relies on a probability distribution called *t distribution* [44]. For large degrees of freedom, the t distribution and the normal distribution are equal. The $100(1-\alpha)\%$ confidence interval for mean μ is defined as follows

$$L_l = x - (s)(t_{1-\frac{\alpha}{2},n-1}) \tag{5.7}$$

$$L_u = x + (s)(t_{1-\frac{\alpha}{2},n-1}) \tag{5.8}$$

where $t_{1-\frac{\alpha}{2},n-1}$ is the value for which the area under the t_{n-1} distribution. s is the standard error of x. Based on Equation (5.7), the confidence interval curves are driven as shown in Figure 5.28.

Chapter 6

Development of Performance Maps and Performance Envelopes

There are no generalized data on the motor performance maps in the literature. The only data available are the separate results for different motors obtained from the nonlinear test bed for actuator (NTBA) run under constant loading conditions. Accordingly, one of the goals of this effort is to present the data in a form of generalized motor performance maps which could cover the whole family of motors with different power ratings under dynamic load operation.

In Chapter 5, the test regime for electromechanical machines was discussed, and the statistical method to analyze the test data was described. The ARIMA equation shown in Equation (5.6) was used to identify the control parameter values as a function of time, which are displayed as points which construct the performance map in 3D space. Each of the performance map plots based on the test regime is described in Chapter 6. All of the maps are derived based on the results of the test motor only and not the load motor. Therefore, the torque, current, speed, magnetic flux density, temperature, position, velocity, and acceleration values belong to the test motor only. After ten performance maps are created, the maps are compared with the plots obtained from trade literatures and papers. The comparisons show how this test data supports the trade literatures and papers, and find how this data expand the meaning of them. Additionally, the changes of trade literature to support future development of intelligent actuators can be suggested.

6.1 Development of Performance Map Plots

6.1.1 Operational Margin Map

For the operational margin test sinusoidal loads will be supplied, and the torque response monitored. This test demonstrates how the mechanical torque is generated by the motion between the test motor and the load motor. Figure 6.1 shows the response of the three phase currents and torque in the cyclic frequency of 1.3 Hz and a base rotational speed of 100 RPM. Based on the different values of speed and cyclic frequency, the mechanical torques are monitored and plotted as represented in Figures 6.2 and 6.3.

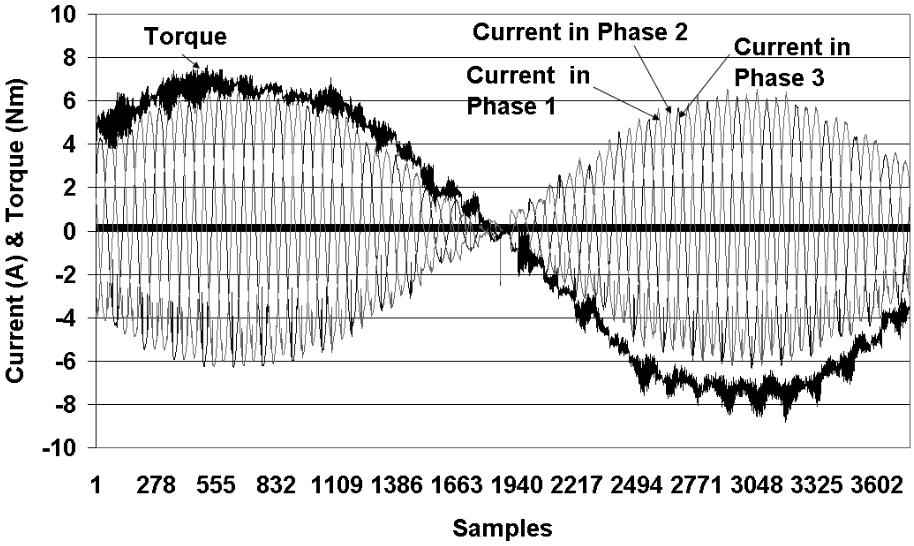

Figure 6.1: Torque and current responses in the sinusoidal loading

The root mean square value of torque is increased as the current is increased, as shown in Figure 6.2. The relationship between the torque and the current in the test motor is designated as a torque-current performance map as shown in Section 6.1.5. The changes in cyclic frequency does not have an appreciable affect on the torque in each layer of the tests up to 5 Hz. However, higher torque values are generated with higher current input values. There is a modest variation of the torque with respect to speed and frequency. To obtain the root mean square value of the generated torque for a certain period, more than 40,000 samples were gathered with a sampling rate of less than 1 msec.

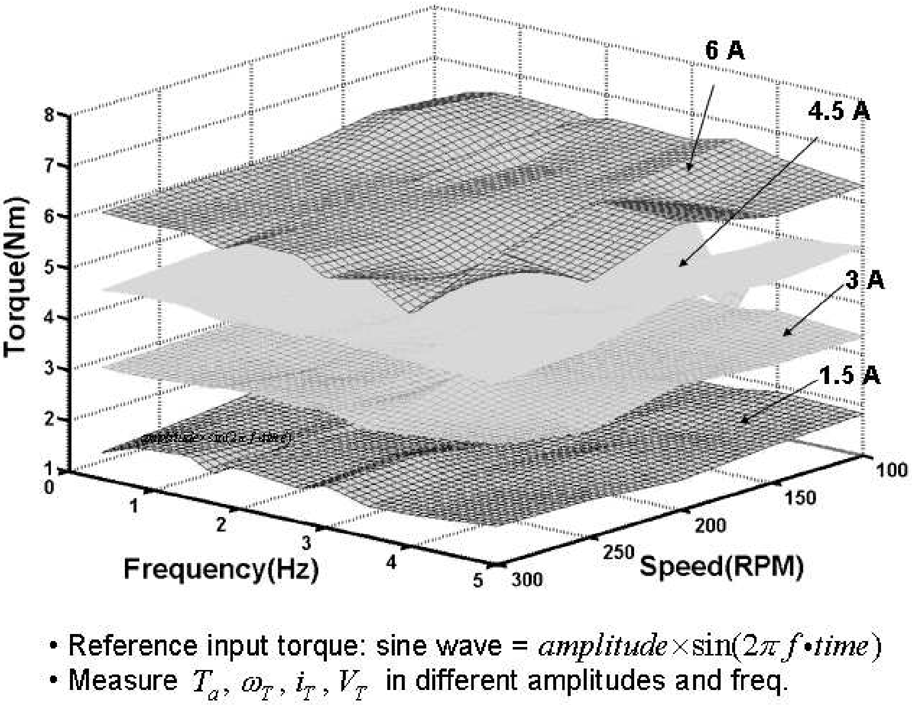

- Reference input torque: sine wave = $amplitude \times \sin(2\pi f \bullet time)$
- Measure T_a, ω_T, i_T, V_T in different amplitudes and freq.

Figure 6.2: Torque response based on changes of speed and sinusoidal loading frequency at constant current commands

In Figure 6.3, the supply voltage to operate the test motor is shown as a function of frequency and speed. The voltage is measured from the voltage divider circuit which is used to drop the high voltage down to a ±10 V signal voltage. The voltage is decreased as the frequency of sinusoidal input torque increases, especially at higher input currents. Referring to [83], the relationship between voltage and speed in a motor is linear and the ratio of them is called “back EMF constant”. However, the speed in the test motor is nonlinearly changing by applying the voltage, V_T. Specifically, at higher current (such as 6 Amps), the surface in Figure 6.3 is not smooth and it can be seen that the frequency affects the voltage applied to the motor.

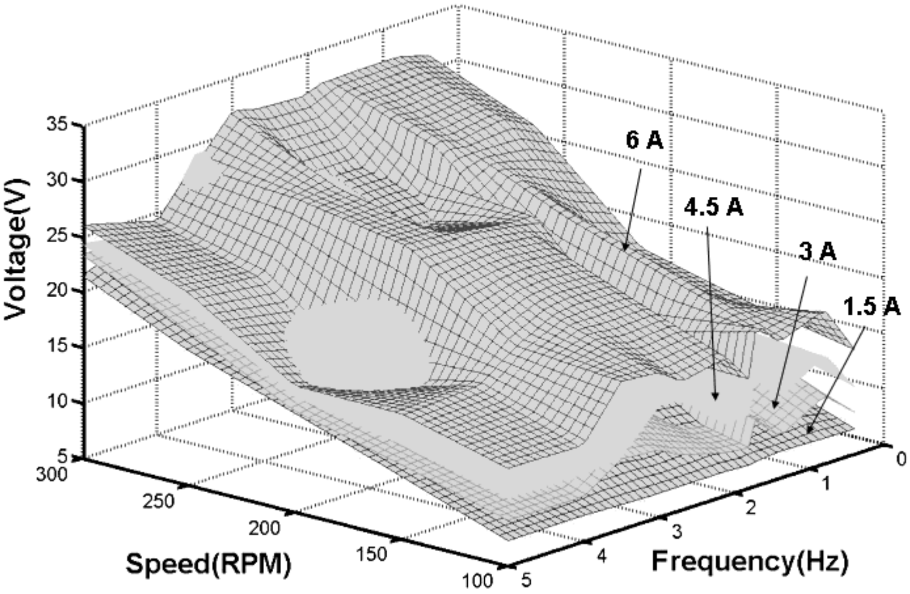

Figure 6.3: Voltage response based on changes of speed and sinusoidal loading frequency at constant current commands

The operational margin performance maps shown in Figures 6.2 and 6.3 do not cover the whole range of the test motor. Four desired torque reference signals (reference currents) are applied for each test. More torque reference inputs should be used in future tests. Also, different types of torque loading such as trapezoidal motion should be applied with different cyclic frequencies. The test bed is modular, so additional components, such as a gear train, higher capacity couplings and torque sensors, can be added.

6.1.2 Efficiency Map

Operating efficiency is the most commonly used performance metric to evaluate motors, and different motor loads help to identify energy efficiency gains and possible reliability improvements. To calculate exact and realistic values of efficiency, Equation (3.1) is used in this testing.

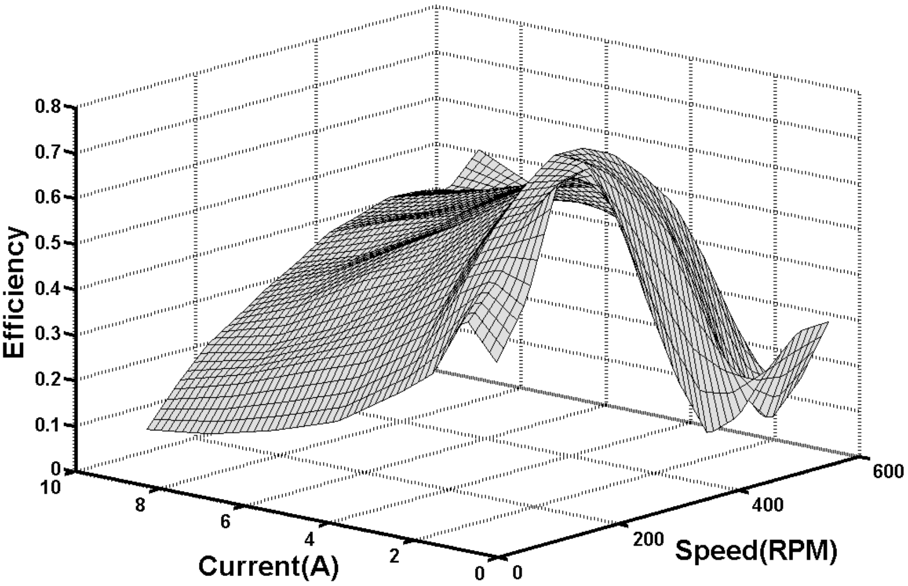

Figure 6.4: Efficiency plot with respect to current and speed

The shaft output power is the input power minus any losses. How to assess losses is another test regime that is discussed in Section 6.1.3. The shaft output can be measured at the torque sensor which is located between the load motor and the test motor in the test bed. Also, the electrical input power is obtained from required current and voltage values generated in the test motor. The test set up to obtain the performance maps for motor efficiency is elementary. The mechanical torque output, T_a, signal is measured from the torque sensor and the speed, ω_T, of the test motor is monitored at the same time. Additionally, the current, i_T, and voltage, V_T, in the three phases are measured and recorded in real time. The measured current and voltage data are applied in Equation (3.2) for a power input and the torque and speed data are plugged in Equation (3.4) for a power output.

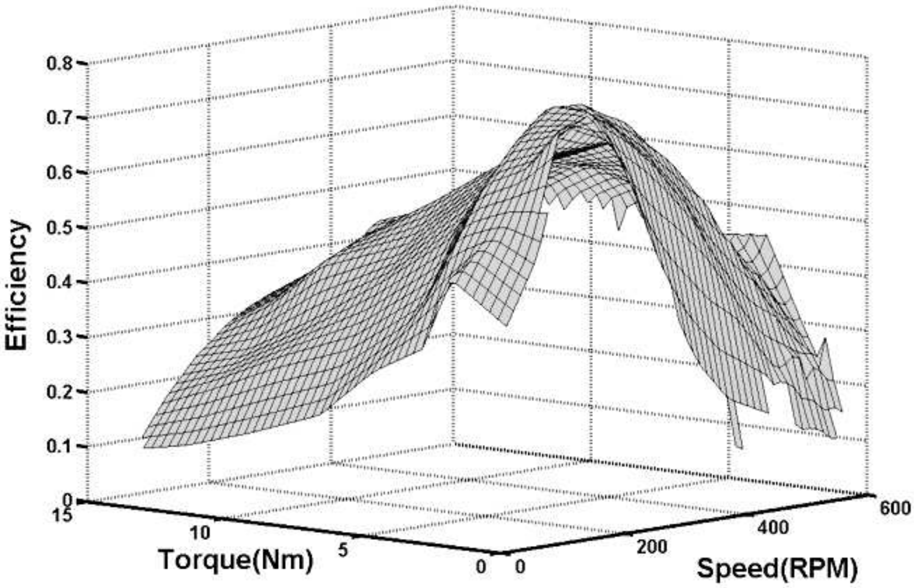

- Reference input: Constant loading torque
- $\mathit{Efficiency} = \frac{\mathit{Power\ Output}}{\mathit{Power\ Input}} = \frac{\mathit{Power\ Output}}{\mathit{Power\ Output} + \mathit{Power\ Loss}}$

Figure 6.5: Efficiency plot with respect to torque and speed

The efficiency of the test motor is 80% at 200 RPM of the rated speed, 4 Nm of the rated torque, and 2.5 Amps of the current as shown in Figures 6.4 and 6.5. At less than 150 and higher than 300 RPM, the efficiency drops dramatically. Also, at higher than 7 Nm, the efficiency is less than 50%. The motor losses, including core losses, copper losses, and mechanical losses, cause the reduction of the efficiencies in these areas. These losses are expressed in nonlinear equations using control parameters (such as voltage, current, speed) and the nonlinear terms in each equation will be identified in the future research. Also, note that the test motor in this research needs to have a better cooling mechanism implemented[1].

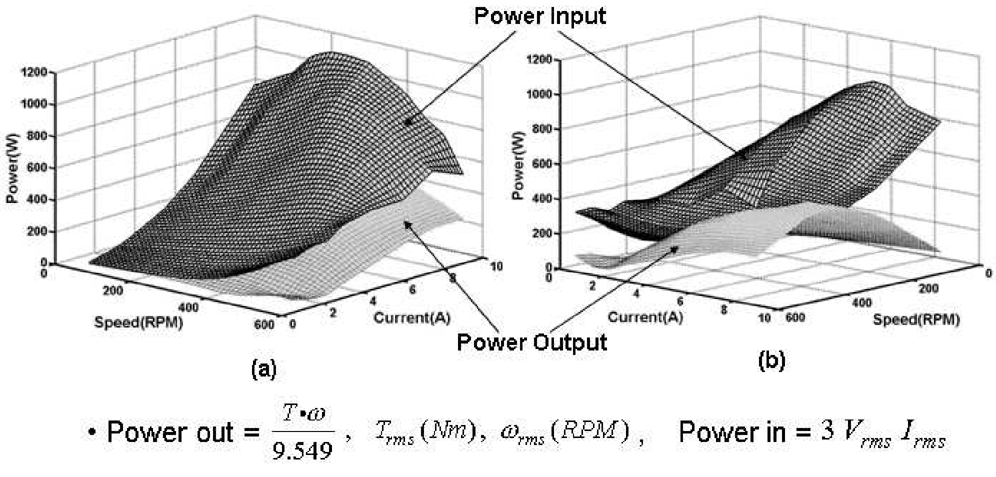

• Power out = $\frac{T \cdot \omega}{9.549}$, $T_{rms}(Nm)$, $\omega_{rms}(RPM)$, Power in = $3\, V_{rms}\, I_{rms}$

Figure 6.6: Power input and output plots in a different viewpoint

6.1.3 Motor Loss Map

The difference between power input and power output is due to electrical losses, friction and windage. Even though higher power motors are typically more efficient, their losses are significant and should not be ignored, as shown in Figure 6.6. The equations needed to calculate power output and power input from the test data use instantaneous values of torque, speed, voltage and current signals to create the representative performance surfaces of power input and power output. In order to explain the reduction of the power input at the region of the high speed and high current in Figure 6.6, further research should be going on. The differences between the power input and power output plots are identified by describing the motor losses in this section.

---

[1] In the future research, the following question should be answered: how will it affect this efficiency plot if it is cooled?

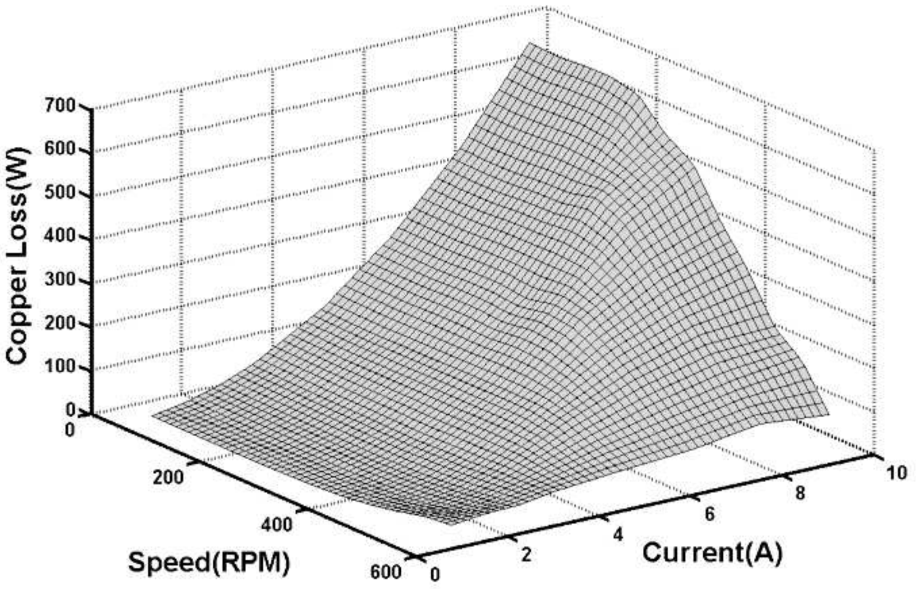

- Copper loss = $3RI_{rms}^2$

Figure 6.7: Copper loss map with respect to current and speed

Power losses are converted into heat which is dissipated by the motor frame through radiation, conduction, and convection. Stator copper losses are caused by current flowing through the motor winding and are proportional to the product of the current squared and the winding resistance as represented in Equation (3.6). Core losses are mainly confined to the laminated core of the stator and rotor. Friction and windage loss is due to all sources of friction and fluid movement in the motor. In this testing, copper loss and core loss maps are obtained as shown in Figures 6.7, 6.8, 6.9, and 6.10.

Figures 6.7 and 6.8 represent the copper loss with different control variables. Copper loss is very small at low current and torque, but by increasing the current to the motor, copper loss increases significantly. The second order copper loss equation shown in Figure 6.7 creates the parabolic shape of copper loss performance

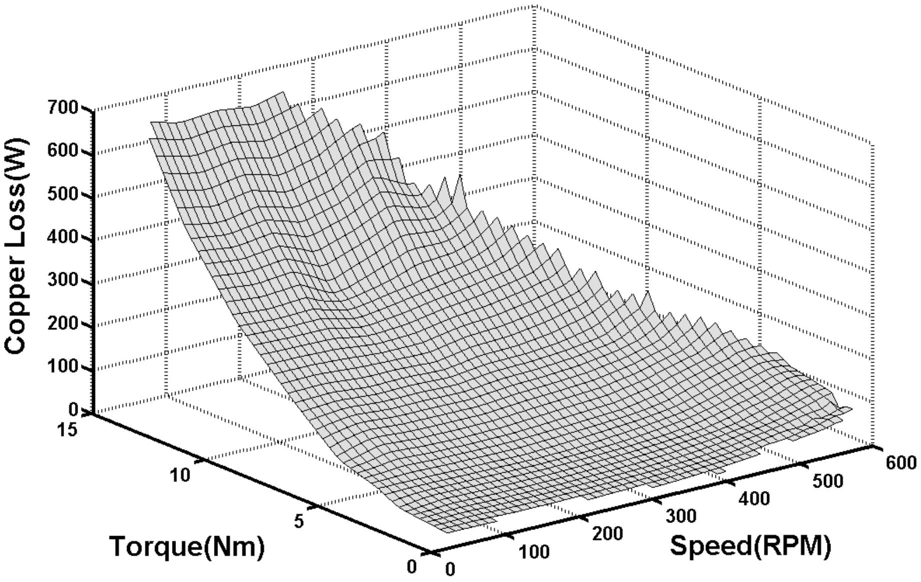

Figure 6.8: Copper loss map with respect to torque and speed

map as a function of current, i_T. This equation is not always applicable in the speed and current axes as shown in the figure. In a certain region of high current, some other factors affect in the development of copper loss map, so the copper loss is generated much less than in the other areas. Copper loss is also affected by speed. Specifically, copper loss at low speed (i.e., less than 200 RPM), with 10 Amps current, is quite high. In Figure 6.8, the plot is not completed above 200 RPM and 10 Nm because the torque, T_m, could not be generated as commanded in the nonlinear test bed for actuator (NTBA). Torque control is done by feeding back the current signals, i_{T1}, i_{T2}, i_{T3} and not by direct control of the torque, T_a, signal.

In general, the core loss values are much smaller than the copper loss values. However, core loss is also an important criteria to consider because it is one of the parasitic disadvantages developed during the operation of the motor and increases

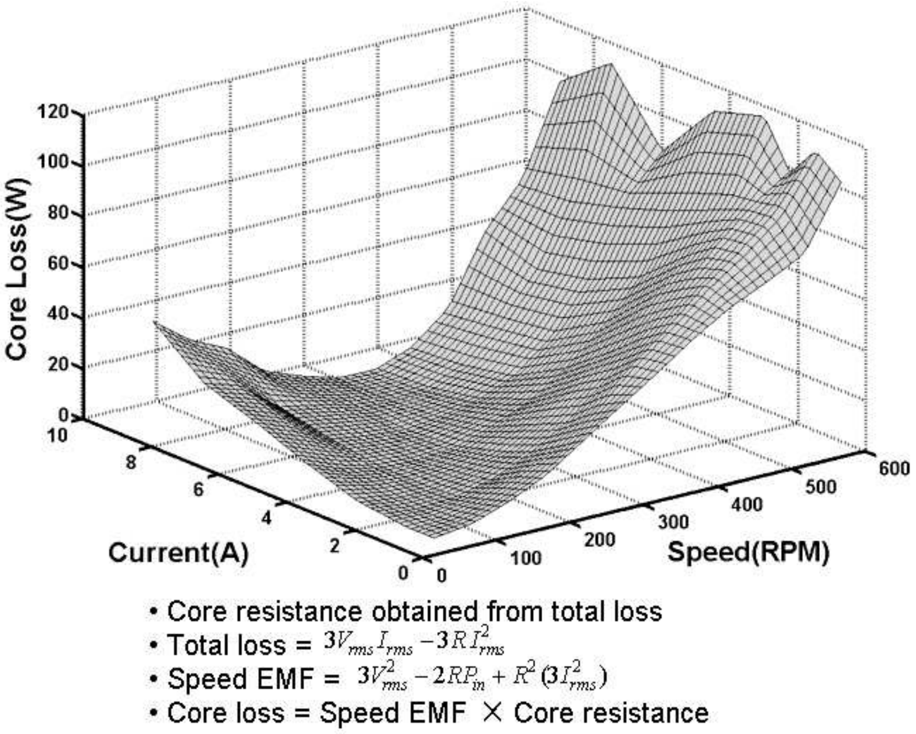

- Core resistance obtained from total loss
- Total loss = $3V_{rms}I_{rms} - 3RI_{rms}^2$
- Speed EMF = $3V_{rms}^2 - 2RP_{in} + R^2(3I_{rms}^2)$
- Core loss = Speed EMF × Core resistance

Figure 6.9: Core loss map with respect to current and speed

rapidly at higher magnetic switching speeds. Figures 6.9 and 6.10 show the core loss with different reference control parameters. The shapes of the core loss performance maps are parabolic due to the square terms of voltage and current as shown in Figure 6.9. These two terms are multiplied together to create the core loss surface as mentioned in Section 5.1.2. Notice the core loss is low at the rated values of torque, T_a, and speed, ω_w, but it increases under low torque-high speed and high torque-low speed conditions. Speed, ω_m, has the greatest affect on core loss while torque, T_m, which is directly dependent on the control current, has the greatest affect on copper loss[2] during the operation of the motor.

---

[2] It is closely correlated with current while generates the level of torque produced.

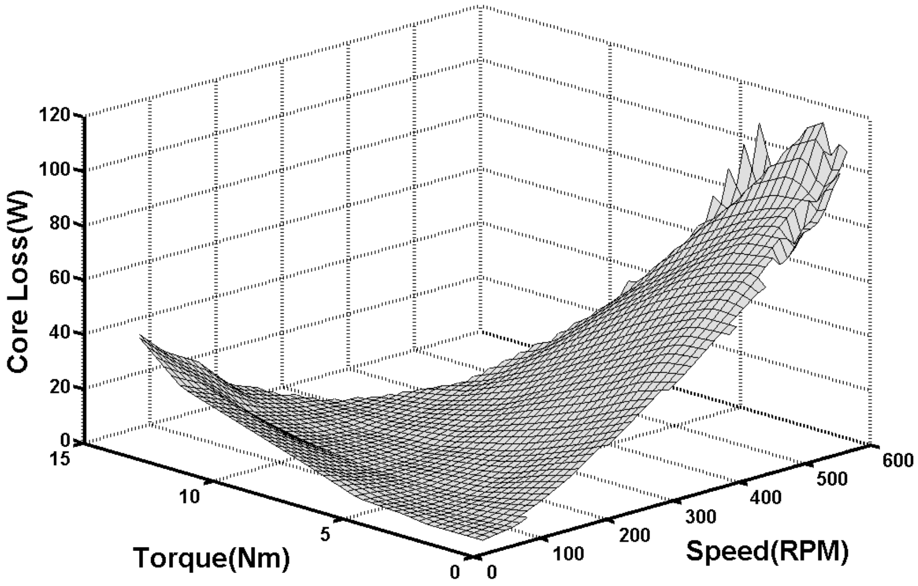

Figure 6.10: Core loss map with respect to torque and speed

6.1.4 Rise Time Map

The rise time is one of the traditional transient performance criteria used to evaluate the response time due to a magnitude change in the required load torque, T_m. Rise time is measured for a variety of torques and speeds to establish one of the performance criteria. Figure 6.11 shows that the rise time is very much dependant on the speed. When the test motor was running at 400 RPM, the rise time was less than 1 msec. As can be seen, the rise time decreases by increasing the torque at low speed, but it increases by decreasing the torque at high speed. The turning point is close to the rated speed, which is 200RPM. Also, as shown in Figure 6.11, the base torque is 1 Nm and the base torque might affect the rise time in the step input torque. Therefore, the useful reference parameter[3], $\frac{\triangle T_m}{T_m}$, is

---

[3] The step torque, $\triangle T_m$, is the applied torque to develop the rise time performance map, and additionally the base torque, T_m, in the denominator can be another control parameter.

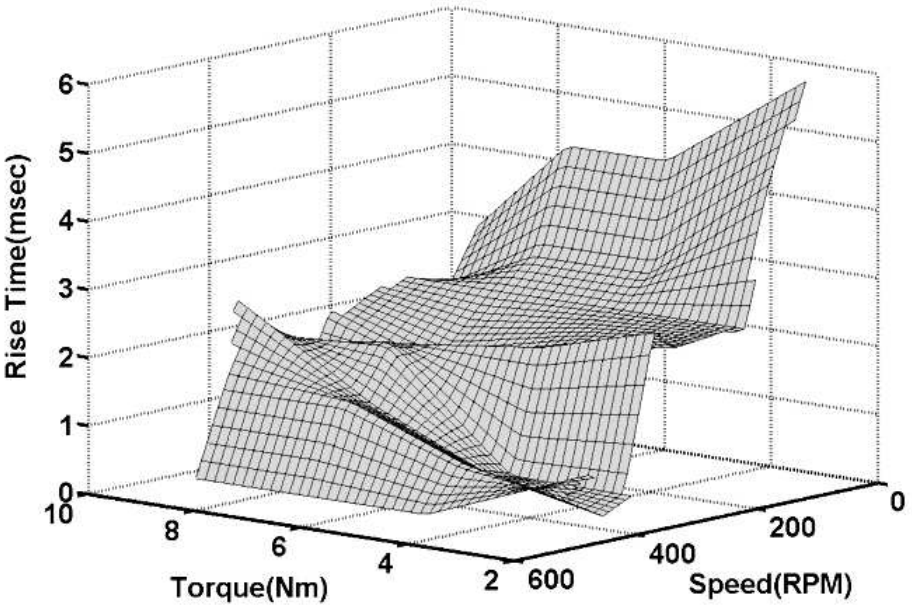

- Base torque: 1 Nm
- Step input torque is applied.
- Measured the time to rise from 5% to 95% of its final torque.

Figure 6.11: Rise time performance map

used as one of the control parameters. More rise time performance maps will be created by using $\triangle T_m$ in the future.

6.1.5 Torque-Current Map

In this map, the relationship between torque and current is tested by changing the speed of the motor. As mentioned in Section 3.6, torque and current responses do not have a linear relationship, which is verified in Figure 6.12. Specifically, torque for this test motor is not generated as a first order differential response to current commands above 500 RPM.

In Section 2.3.1, the torque and back EMF constants were fixed values during commutation due to the assumption of the linear relationship between torque

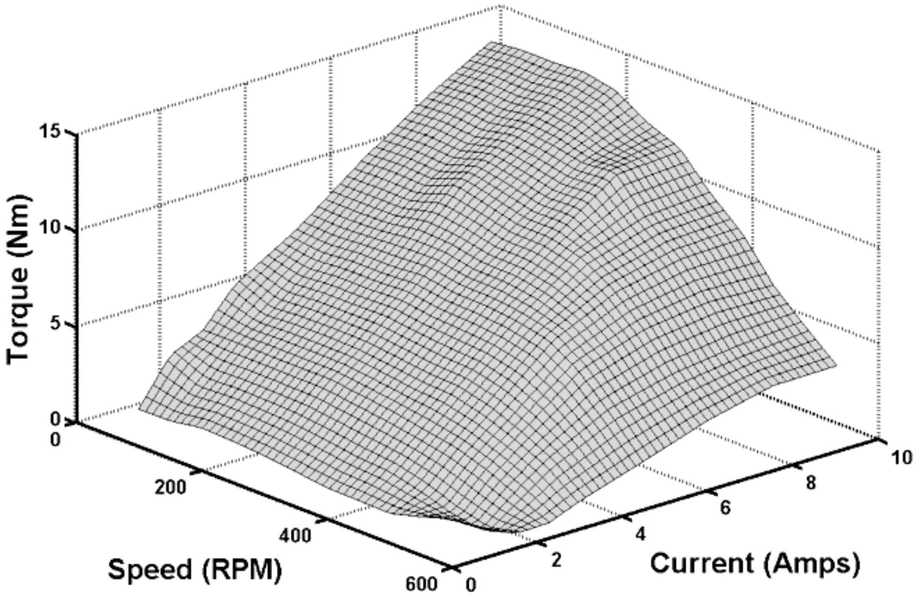

- Obtain RMS value of torque, current, speed.
- $\frac{T_m}{i_T}$ is determined

Figure 6.12: Torque-current performance map

and current. However, the torque-current performance map proves that the motor equation developed in Equation (2.23) cannot be applied in a real system because of the uncertainties of the torque and back EMF constants. At more than 200 RPM and 6 Amps in Figure 6.12, the torque-current has an even more severe nonlinear curve.

6.1.6 Torque Ripple Map

As mentioned in Equation 3.12, the torque ripple is the percentage ripple of the torque response in the test motor divided by the average torque, T_m, applied. The torque ripple performance map is obtained using the hysteresis brake to create a steady loading as shown in Figure 5.10. The ripple was almost 45% at the test

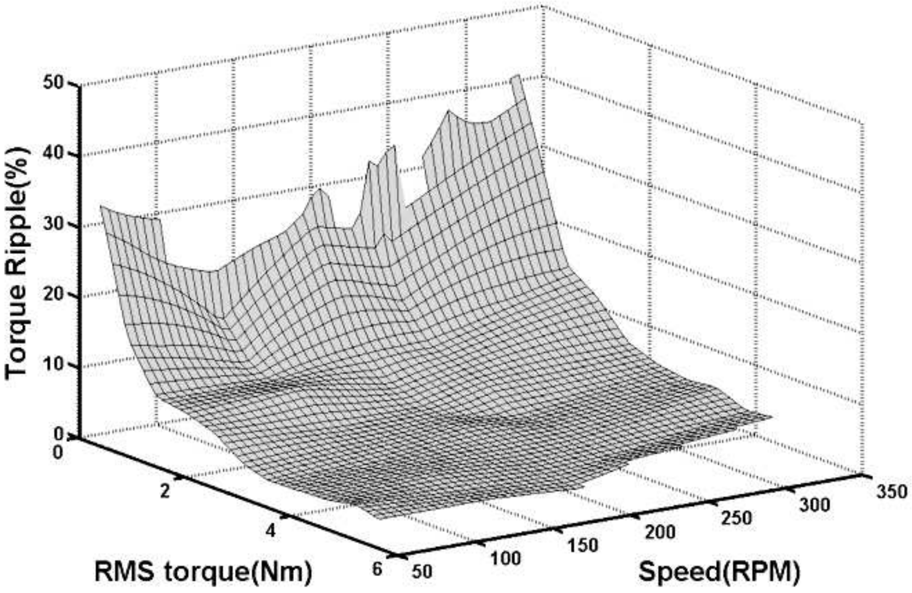

- Hysteresis brake is used for testing.
- % of torque ripple = $\frac{amplitude\ of\ ripples}{average\ torque}$

Figure 6.13: Torque ripple performance map

motor speed of 300 RPM and a low torque of 0.42 Nm. The smallest ripple was 3%, obtained at 200 RPM and 5 Nm. The ripple was small at the rated speed but increased to 30% at low torque output. In overall torque ripple responses, the ripple was less than 5% at higher torque output, T_a, from the test motor. It slightly increased as the speed, ω_w, of the motor increased. More than 25% of torque ripple was shown at less than 1 Nm of the torque output from the test motor. This plot might be better normalized by plotting the ratio, $\frac{\triangle T_m}{T_m}$.

6.1.7 Acceleration Map

The acceleration performance map is presented in two different output plots depending on the method used to show the acceleration of the inertia of the test motor, three bellows couplings, clutch, and the hysteresis brake. The test motor inertia is 15% of the total inertia including all of the mechanical components in the test bed. In Figures 6.14 and 6.15, notice that the total inertia of the test system is considered when calculating the acceleration at each speed, ω_T, and torque, T_m, of the test motor.

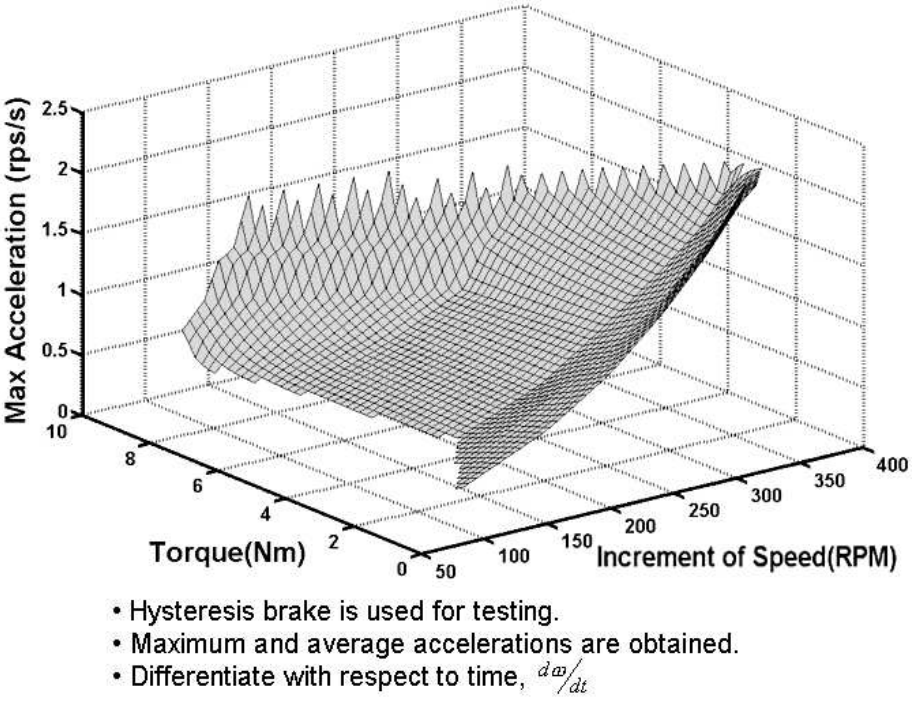

Figure 6.14: Maximum acceleration performance map

The way to get the acceleration performance maps is explained in Section 5.1.5 in detail. Maximum acceleration is obtained by selecting the largest value in the transient region when increasing the speed, ω_w, from a low value to a higher value. The average acceleration is determined by averaging the acceleration values in the transient region between two different magnitudes of speed. These two plots have a very similar shape and trend. In Figure 6.14, the maximum acceleration is almost 2.3 rps/s at 1 Nm of torque, T_a, output (between the test motor and the hysteresis brake) and 340 RPM of the speed increment. By looking at the trend of the maximum acceleration plot, as torque of the test motor is increased, the maximum acceleration is increased. When a initial speed increases to the target speed, the acceleration has the highest value at first time and then it decrease by approaching to the target speed as shown in Figure 5.9. On the other hand, in acceleration performance maps (Figures 6.14 and 6.15), the acceleration keeps increasing with respect to speed because only maximum and average accelerations are chosen as a function of different torque and speed values. The average acceleration has almost the same tendency as the maximum acceleration as shown in Figures 6.14 and 6.15. The average acceleration plot is mostly affected by high speeds. At 400 RPM, the average acceleration is 1 rps/s, and the same acceleration is developed over all torque values.

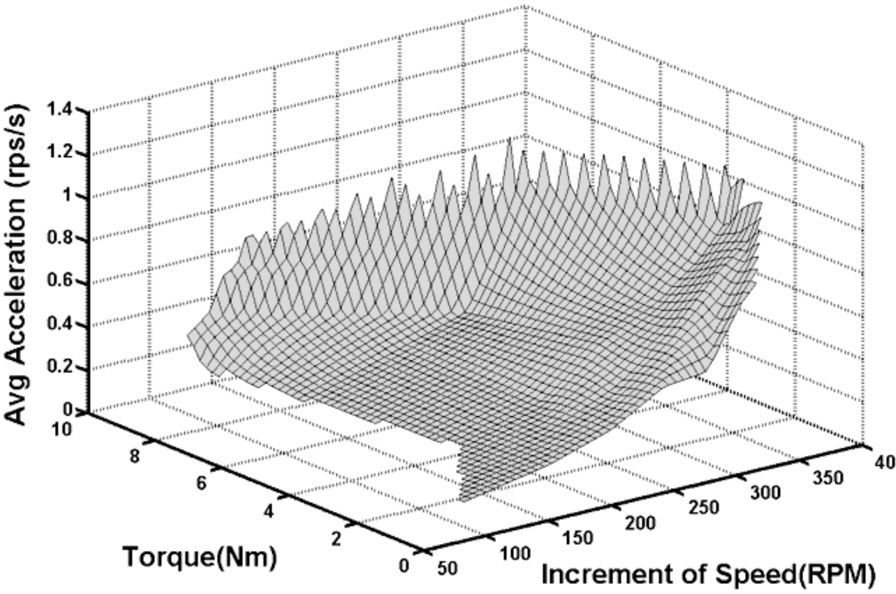

Figure 6.15: Average acceleration performance map

6.1.8 Max Magnetic Flux Energy Map

Magnetic flux energy is expressed as the area surrounded by the *B*-*H* hysteresis curve in the production of magnetic energy during the operation of the test motor. The maximum value for the magnetic flux energy, $(BH)_{max}$, is derived from the largest area that covers the whole range of one of the currents passing through the three phases for one cycle of the test motor. This flux energy is shown in the experimental data plot of Figure 3.9. As shown in Figure 6.16, the torque output from the test motor has the greatest affect on the magnetic flux energy.

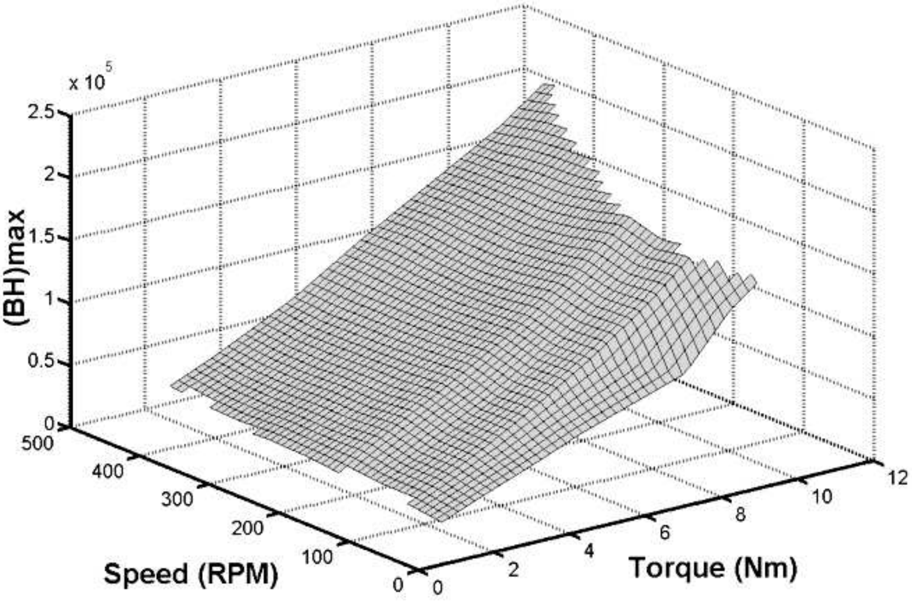

- Use magnetic flux density sensor.
- Create *B-H* curve.
- Calculate the area of *B-H* hysteresis plot in one cycle.

Figure 6.16: Maximum magnetic flux energy performance map

The magnetic flux energy, which is the function of current and magnetic flux density, ranges from 30000 to 220000 Joules (J) during the tests of different torques in the test motor. The magnetic flux energy directly produces torque, T_m, based on the following relationship [92]:

$$T \propto BJ \tag{6.1}$$

where B stands for the RMS value of magnetic flux density (Wb/m^2), and J is defined as the RMS value of current density (A/m). H in $(BH)_{max}$ is the magnetizing force and has the same unit as the current density. Therefore, the torque developed during the test should be proportional to the magnetic flux energy, $(BH)_{max}$ as represented in Figure 6.16. Also, the energy is slightly increased by the increments of the test motor speed.

6.1.9 Magnetic Flux Density Map

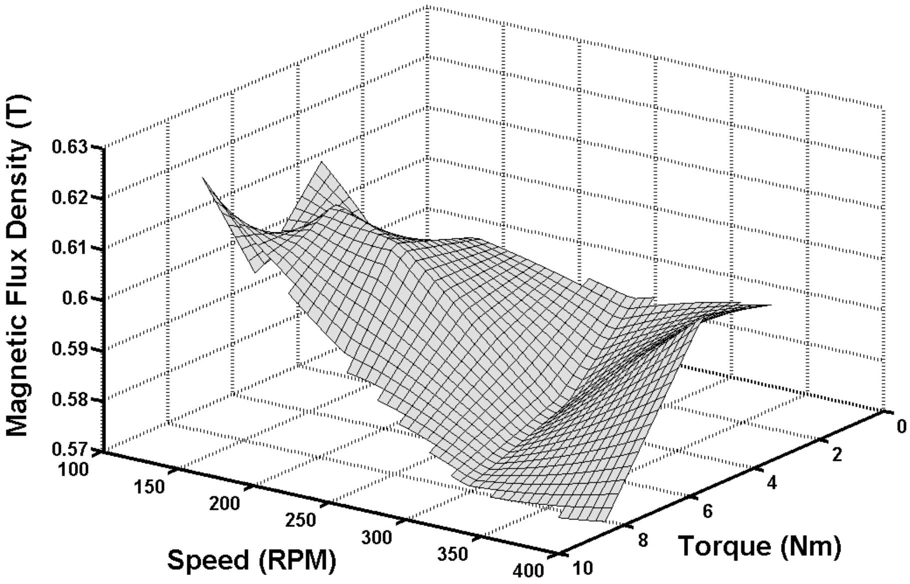

Figure 6.17: Magnetic flux density performance map

Another performance map using magnetic flux density signals is the magnetic flux density map as represented in Figures 6.17 and 6.18. There are two performance maps for this criteria because the maps can be drawn with respect to several control parameters such as speed, torque, and temperature. As shown in Figure 6.17, the magnetic flux density is slightly reduced at higher rated torques and speeds at the elapsed time of 11 minutes. The magnitude of the reduced value is very small (about 6-7 %) but this plot explains that magnetic flux density B is affected by torque and speed. Further research will be performed to find the relationship among the magnetic flux density, torque and speed in the future. In Figure 6.18, the magnetic flux density, as a function of temperature and speed, measured at 11 minutes is lower than 0.6 Tesla (T) measured at the start. Specifically, at $80°C$, the magnetic flux density is reduced to 6%. The temperature effects on the test motor is explained in detail in Section 6.1.10.

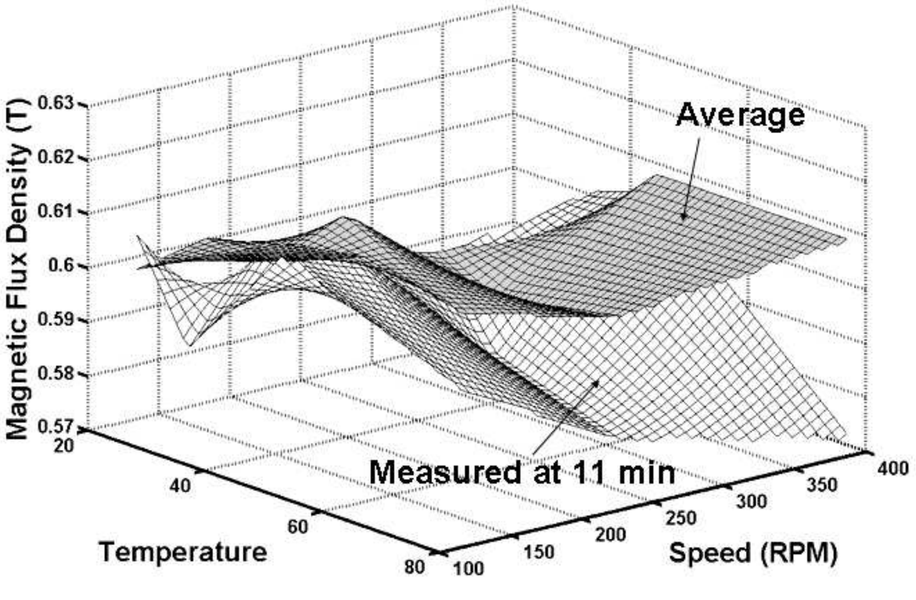

- Magnetic flux density measured at 11 minutes
- Use RMS value of magnetic flux density signals

Figure 6.18: Magnetic flux density affected by temperature

6.1.10 Temperature Map

In the temperature performance map, the temperatures were measured after an elapsed time of 11 minutes for different sets of torques and speeds. The performance map shows how quickly the temperature increases as the torque and speed increase. Figure 6.19 shows that the temperature reaches 80°C if 9 Nm of torque is applied to the test motor for 11 minutes. It is shown that the temperature almost linearly increases by increasing the torque[4].

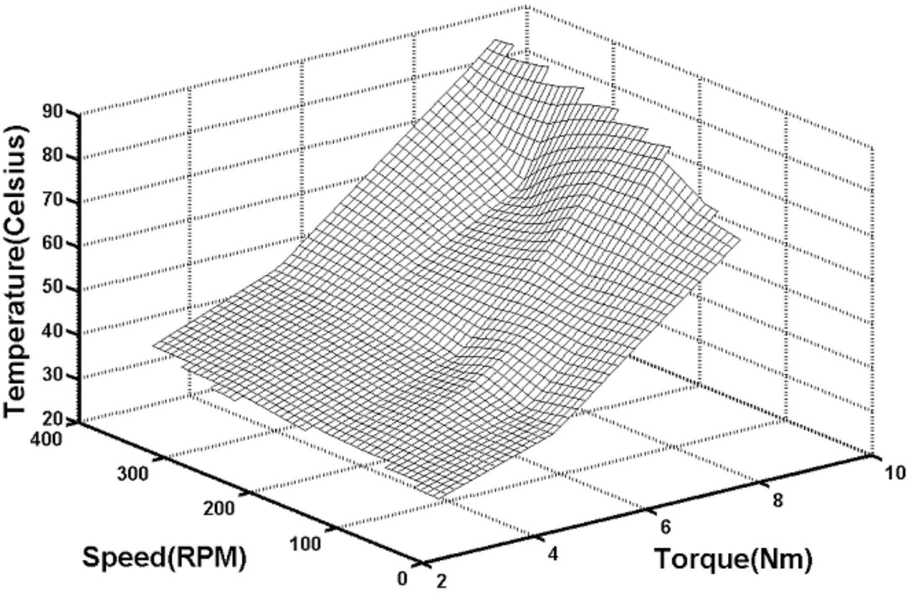

• Use a thermometer to measure the temperature inside the test motor at 11 minutes.

Figure 6.19: Temperature performance map

Also, the temperature plot is affected by the speed. Especially, at torque higher than 6 Nm, the temperature inside the test motor reaches 50°C for any speed. From this map, it can be deduced that the test motor has a very bad

---

[4] More torque means more current which means more losses.

ventilation system. Installation of a fan or fins to remove the heat during operation is needed.

6.1.11 Error Bounds for a 3D Surface

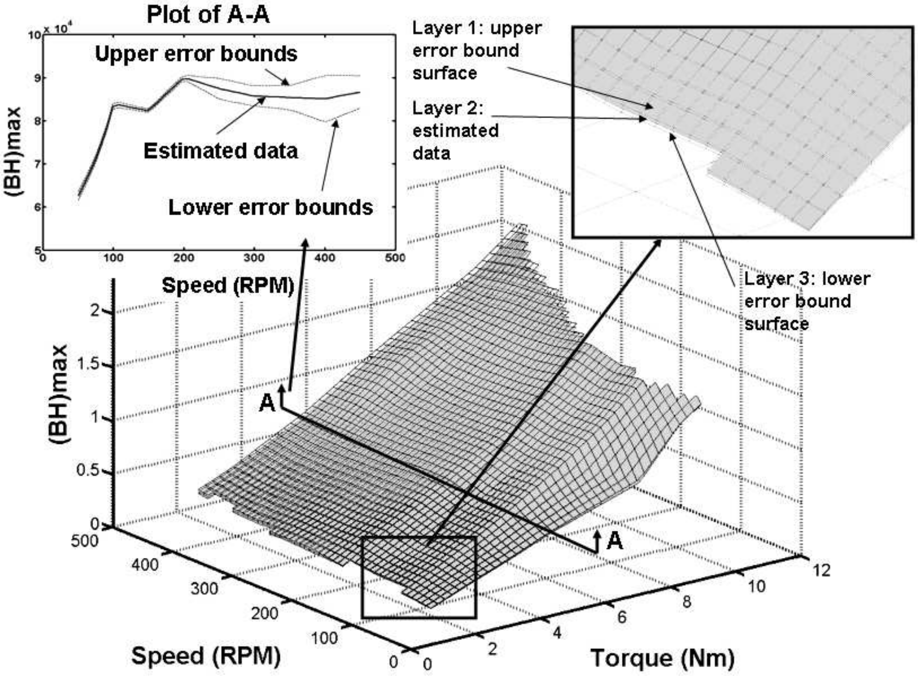

Figure 6.20: Determination of error bounds for the experimental data of magnetic flux energy

The experimental data obtained in previous sections is treated with a statistical method in order to consider the uncertainties of estimating real physical system parameters. Based on the test protocol in Chapter 5, each test should be repeated to create the error bounds. The performance maps can be completed only when they have the upper and lower error bounds which shows the percentage of uncertainty. However, to develop the error bounds, the test should be performed more than 20 times for enough data to apply a statistical analysis. In this report, only one performance map, which is the maximum magnetic flux energy performance map, is presented to demonstrate the usefulness of the error bounds for the experimental data.

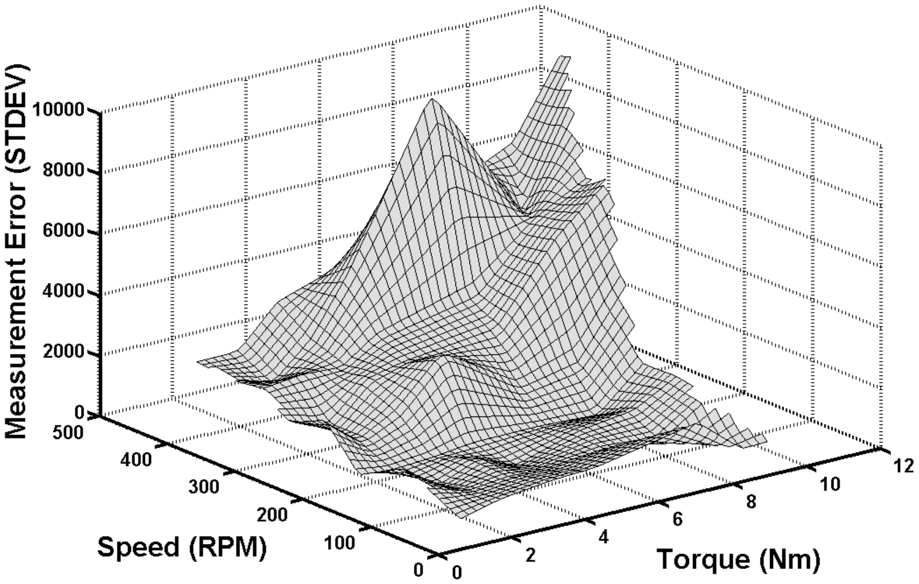

Figure 6.21: Magnitude of measurement error of $(BH)_{max}$

Figure 6.20 shows how the error bounds are represented in the performance map. The tests for building the magnetic flux energy map were repeated 299 times in different torque, T_a, and speed, ω_w, settings of the test motor and the load motor. Once the average value of magnetic flux energy in a particular torque and speed is calculated, the error bounds, which is sometimes called as standard deviation, are determined using the following equation:

$$STDEV = \sqrt{\frac{\sum(x-\overline{x})^2}{(n-1)}} \tag{6.2}$$

where x is the sample data measured in the test bed, $\overline{x}$ is the average value of the sample data, and n is the sample size. The standard deviation is calculated using the unbiased equation, which includes “n-1” in the equation.

Using Equation 6.2, the upper and lower error bound surfaces are drawn as shown in Figure 6.20. $(BH)_{max}$ is represented with two other layers where the upper layer is obtained by adding the standard deviation values to the average values and the lower layer is obtained by subtracting the standard deviation values from the average value of $(BH)_{max}$. The plot “A-A” represented in Figure 6.20 shows how error bounds change with respect to the speed, ω_w at 5 Nm of fixed torque, T_a. Based on the plot “A-A”, error bounds are increased at higher speeds. These error bounds are clearly shown in the overall range of torque and speed values in Figure 6.21. The standard deviation is substantially increased as the torque, T_a, and speed, ω_w, are increased because the values of T_a and ω_w in this area include more measurement error and noise.

6.2 Generation of Performance Envelopes

Once all the performance maps based on the suggested operational criteria are obtained for several different kinds of phenomena, performance envelopes have to be built based on the maps. Even though the torque-speed curve with respect to temperature and efficiency at a given speed and torque are specified in the trade literature (or arrived at through simulation), actual values depend on the type of load torque, T_a, and environmental variables. Therefore, if the performance envelope including all of these cases is completed, it will become the functional decision map to guide the operation of the motor.

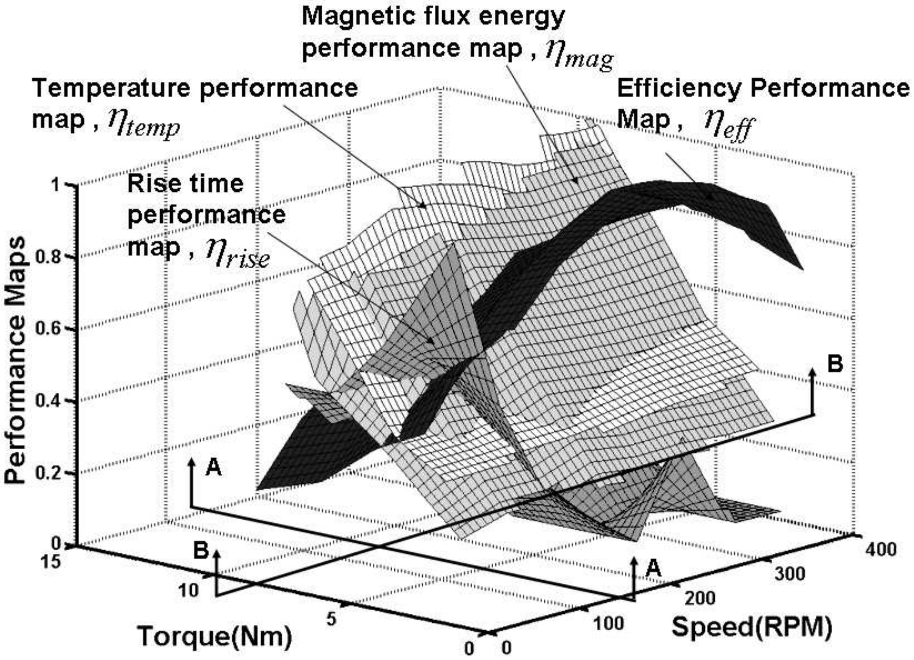

Figure 6.22: Four performance maps with respect to torque and speed

Figure 6.24 represents how each performance envelope is obtained from several performance maps. In this research, the actuator test bed has been developed in order to obtain enough information to evaluate the performance of a permanent magnet synchronous motor. The data obtained from the sensors in the test bed are plotted with respect to time. The data sets obtained from the repetition of testing the test motor are ready to insert in the statistical analysis. The mean value with high confident intervals (95%) are calculated and then several different plots of mean values in different loading conditions are derived in Section 6.1.11. Along with the curves, upper and lower boundaries are determined from the statistical calculation. Once all of the data sets are collected from the sensors, they are combined together based on each actuator criterion. Then performance maps can be completed based on appropriate independent parameters. From the performance maps built in the suggested test methods in Section 5.1, we find out which of the independent parameters will be used as the controllable axis in the performance envelope graphs. These graphs need to demonstrate the actual performance in the test motor.

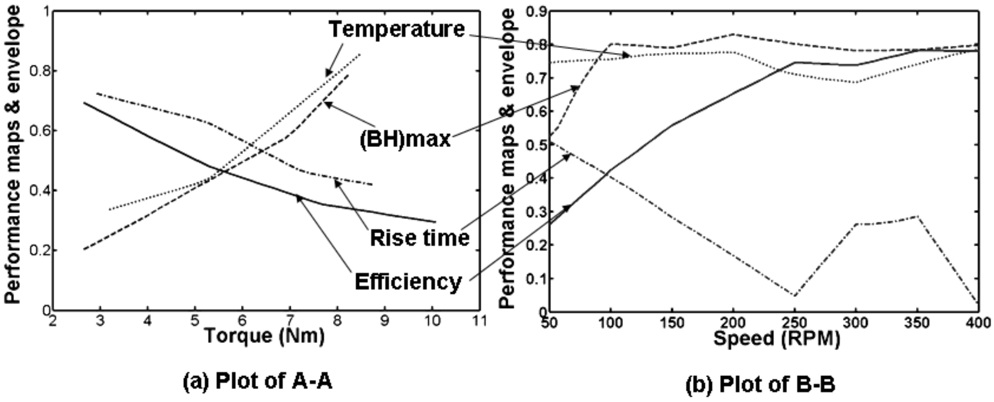

(a) Plot of A-A

(b) Plot of B-B

Figure 6.23: 2D plots of performance maps shown in Figure 6.22

As an example of how the performance envelope is generated, four performance maps were combined together and the performance envelope was generated with respect to torque and speed as shown in Figures 6.22 and 6.24. Each performance map is expressed as the ratio of the estimated value over the maximum value in each torque, T_a, and speed, ω_w, in the test region. In order to present four maps in the same vertical axis, each of the performance maps is normalized with its maximum value as follows[5]:

$$\eta_{eff} = \frac{E_{act}}{E_{max}} \tag{6.3}$$

$$\eta_{rise} = \frac{t_{act}}{t_{max}} \tag{6.4}$$

$$\eta_{mag} = \frac{M_{act}}{M_{max}} \tag{6.5}$$

$$\eta_{temp} = \frac{T_{act}}{T_{max}} \tag{6.6}$$

where

E_{act}: current efficiency of the test motor

t_{act}: current torque rise time of the test motor

M_{act}: current magnetic flux energy in the test motor

T_{act}: current temperature of the test motor

E_{max}: maximum efficiency in the test range

t_{max}: maximum rise time in the test range

M_{max}: maximum magnetic flux energy during the test

T_{max}: maximum temperature rise in the test range

As shown in Figure 6.22, four different normalized performance maps are created using Equations (6.3), (6.4), (6.5) and (6.6).

Figure 6.23 shows the 2D plots of performance maps originated from Figure 6.22. Figure 6.23(a) is the cutaway view in A-A direction and four different curves

---

[5] Note that the weighting factors will be multiplied to each of normalized terms based on their relative importance to the user in the future research.

are shown with respect to the torque output, T_a. Also, the cutaway view in B-B direction is represented as a function of speed as shown in Figure 6.23(b). These two cutaway views just represent one possible performance mapping with respect to one control variable. If the maximum performance envelope is selected to evaluate the test motor, the maximum surfaces out of four different performance map surfaces in each region of torque and speed are chosen as represented in Figure 6.24. As shown in the maximum performance envelope, the temperature performance map governs the management of torque and speed in the region of more than 6-10 Nm of the torque output, T_a. After the test motor operates at the speed of 350 RPM and the applied torque of 10 Nm, the temperature map is dominant in the region and it indicates that the temperature increases up to $80°C$ in 11 minutes. $80°C$ is determined by Figure 6.19 and Equation (6.6). Also, in the region of less than 100 RPM and less than 5 Nm, the rise time is the main control map to be referred to by the controller in the operation of the test motor. The user of the test motor should notice that the rise time is about 8 millisecond at 2 Nm and 50 RPM from Figure 6.11 and Equation (6.4). Efficiency is very low in the region of less than 5 Nm and it is critically noted to the test motor user based on Figure 6.24.

All of these four surfaces, which come from four actuator criteria, are plotted along two reference parameters (torque and speed). In summary, actuator performance maps must be obtained by experiment based on several independent control parameters. These basic reference parameters for PMSM drives are desired torque and rotor speed. There exist more possible control parameters such as voltage and current. The voltage, V_T, is needed to develop current, i_T, in the test motor amplifier, so one of them is used as the independent parameter and it will

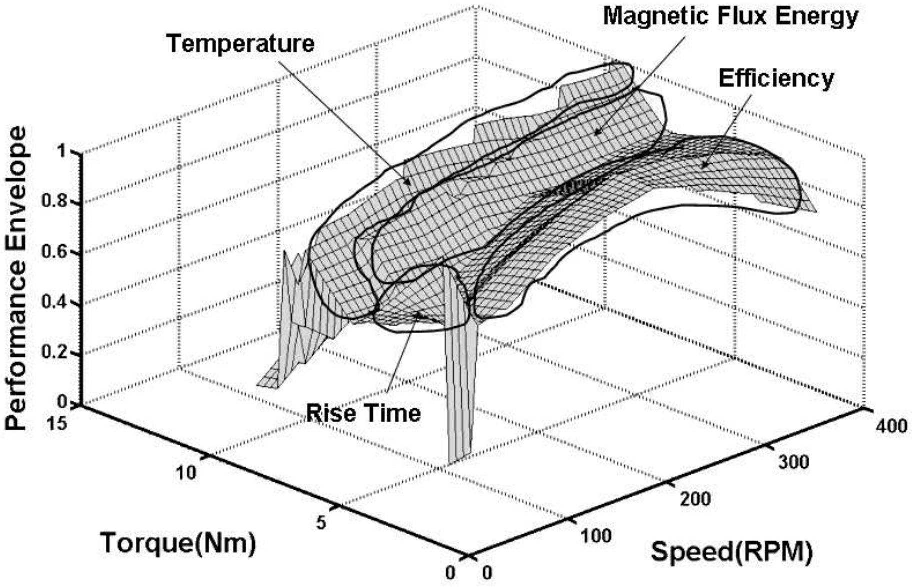

Figure 6.24: Development of performance envelope

be shown in more performance maps in the future. Also, the measured dependent parameters are output torque, temperature, magnetic flux density, acceleration, and response time. The reference parameters are one of the x-y axes. Also, the combination of dependent parameters is plotted in the third axis as shown in Figure 6.22. In order to manage the control parameters when considering all of the possible scenarios, the performance envelope should be developed on the basis of the construction of a decision making algorithm, which will be developed by a future study.

6.3 Comparison of Test Results with the Trade Literature

In this section the actuator performance maps obtained from ten experiments are compared with the traditional plots which represent the electromechanical performance criteria such as the torque-speed curve and efficiency. Motor manufacturers provide electromechanical motors with the specifications and applications of the specific motor. These specifications are then used to pick the right size and capacity motor for a given application. However, the user often requires the motor to operate in abnormal conditions, which may not result in the best or expected output from the motor. In this report, a way to solve this problem is suggested and more than ten test result plots prove that these precious performance maps can correctly guide and evaluate the operation of the motor for better responses. The traditional plots utilized in this section originate from the trade literature and papers written by motor researchers and scientists.

6.3.1 Comparison of Operational Margins: Torque-Speed Curves

In general, electromechanical motor manufacturers provide torque-speed curves to indicate the performance of the selected actuator. The torque-speed curve is sometimes enough of a reference to verify the capacity of the motor at peak and continuous loadings. However, the torque-speed plot is not a perfect guide when considering all of the unusual conditions a motor may be subjected to.

Figure 6.25 shows the performance curves for the Parker Hannifin and Bodine brushless DC motors. The lines represent maximum values which indicate the limitations of the motor capacity. These lines were determined by repeatedly testing the motor until peak torque and speed values, for static loadings, were found. However, the torque-speed performance line does not give insight into how

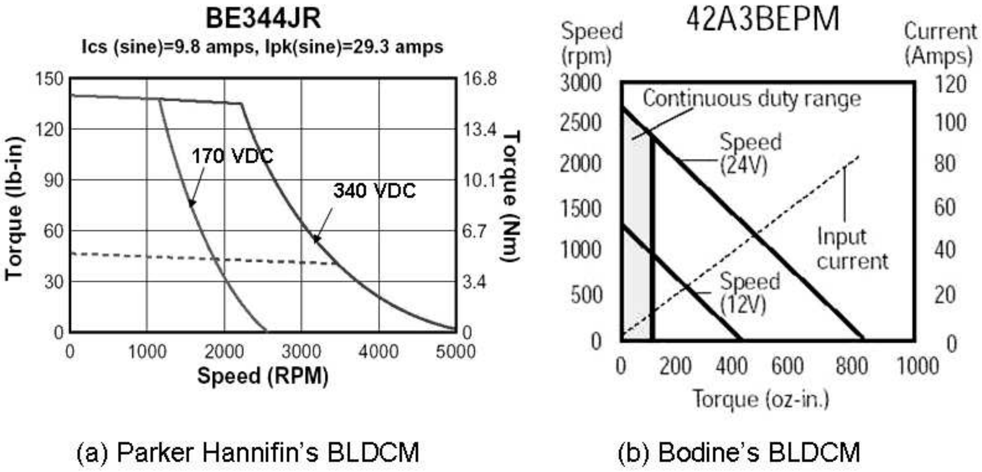

(a) Parker Hannifin's BLDCM (b) Bodine's BLDCM

Figure 6.25: Torque-speed curve of commercialized brushless DC motor [34], [9]

the line will change for periodic sinusoidal loadings. As shown in Section 6.1.1, there is an additional control parameter, load cyclic frequency. The 3D plot in Figure 6.2 is incomplete because the performance surface does not cover the whole range of the test motor. However, it is enough to show the cyclic frequency also affects the torque and speed responses, especially at higher currents (load).

In addition, the suggested performance envelope, which includes four different performance maps shown in Figure 6.24, can be presented as 2D contour plot. As represented in Figure 6.26, the control parameters are torque and speed, and each contour line represents the same normalized performance value. The way to apply the performance envelope and performance maps is as follows.

- For example, 250 RPM and 8 Nm are selected to evaluate whether they are a good combination to generate enough power from the motor.
- The point at 250 RPM and 8 Nm belongs to the magnetic flux energy performance map. Also, the normalized value is 0.8, which means 80% of the

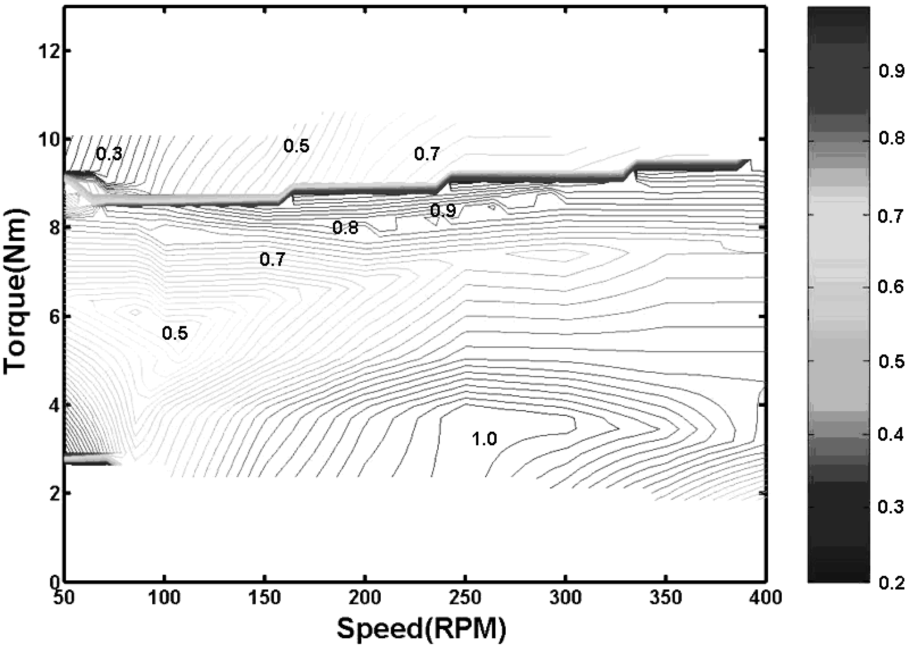

Figure 6.26: Torque speed contour of the performance envelope

maximum magnetic flux energy is generated. It might cause a reduction in torque production after operating for a long time.

- At the same torque and speed, other performance maps can be considered, too. Specifically, temperature inside the test motor is almost 90% of the maximum value ($80°C$), which provides a precaution when the motor is operated in this region.

If there are more performance maps created from the motor testing, a motor user can have more precise guidance and operate the motor with the best performance (i.e., the goal of intelligence).

6.3.2 Comparison of Efficiencies

Efficiency is a commonly used indicator of energy usage and operating costs in the motor industry, so it is another useful reference used to choose the proper motor for a specific application. Most motor efficiency plots are presented with respect to speed or applied torque as shown in Figures 6.27(a) and 6.28. Figure 6.27 compares two kinds of efficiency maps. One is from Reliance Electric's web site, represented in Figure 6.27(a), and the other is created experimentally using the NTBA, represented in Figure 6.27(b).

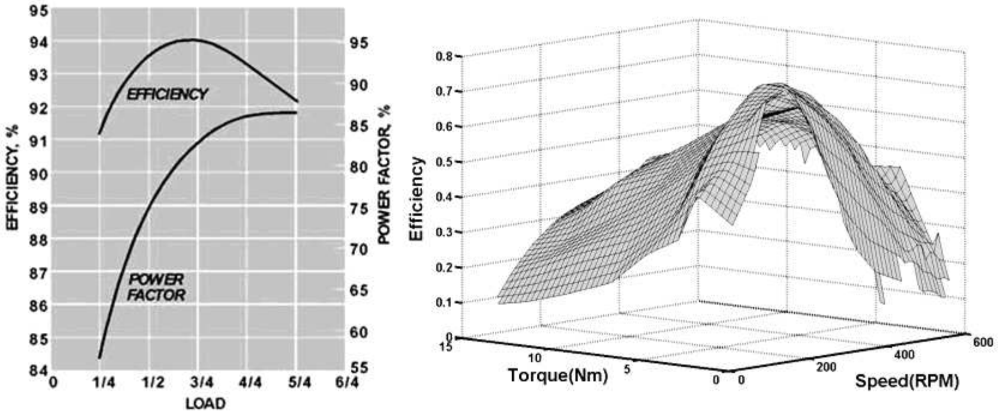

(a) Reliance Electric's XE series AC motor – 30HP, 1800 RPM

(b) Efficiency performance map

Figure 6.27: Comparison of efficiency plots [81]

The XE series of Reliance Electric's AC motor is energy efficient, and the largest efficiency (94%) exists at three quarter load. The overall efficiency of the Reliance Electric's motor is more than 20% higher than the efficiency of our test motor. The test motor has a critically low efficiency at more than 10 Nm. The test motor does not have fans or fins on its outer case. The heat generated during the operation of the motor is hardly dissipated through the surface, so motor losses are greater than the commercialized electric motor installed with fans and fins.

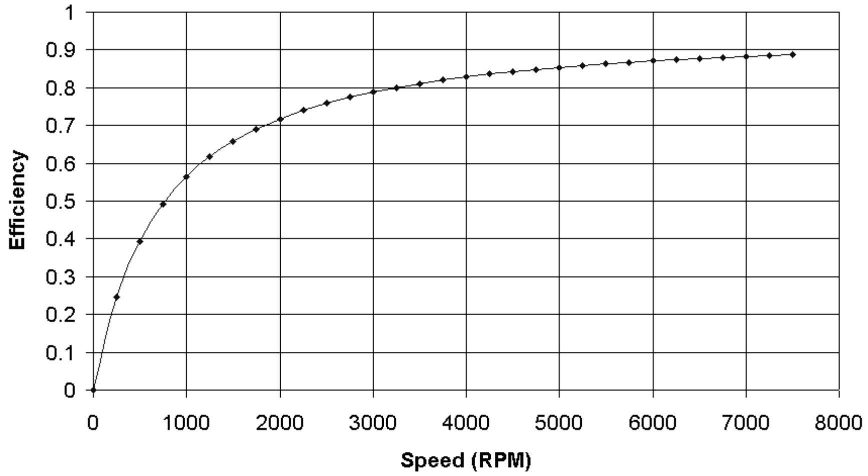

Figure 6.28: Efficiency curve of Parker Hannifin's brushless DC servo motor - SM232B [34]

An efficiency curve as a function of speed is displayed in Figure 6.28. The motor, built by Parker Hannifin, is an SM232B brushless DC servo and the specifications of the motor have 2.34 Nm of peak torque, 16 Amps of peak current, and 7500 RPM maximum speed. On the other hand, the specifications of the test motor has 28.2 Nm of peak torque, 17.2 Amps of peak current, and 650 RPM of no load speed as shown in Table 4.1. The efficiency of the test motor is 70% at the rated speed, which is the highest value in the overall range of speed as shown in Figure 6.27(b). However, the maximum efficiency of the Parker Hannifin motor exists at the rated speed, which is 7500 RPM.

Each of the performance 2D plots shown above represents its maximum feasible efficiency value only regarding one axis, torque or speed, so the efficiency at a given speed and torque is not easy to obtain. Relatively, the test result plot of the efficiency performance map in Figure 6.27(b) is very easy to interpret for a certain combination of torque and speed and evaluate the performance for each combination. The efficiency maps can also be created in different control parameters, such as current or voltage as shown in Figure 6.4.

6.3.3 Comparison of Core Losses

The trade literature in Sections 6.3.1 and 6.3.2 involves only torque-speed curves and efficiency plots to describe the performance of electric motors. The comparisons between the 2D performance plots and the 3D performance maps presented in the rest of Section 6.3 refer to the research papers previously published in the field of electric motors for the last 10 years.

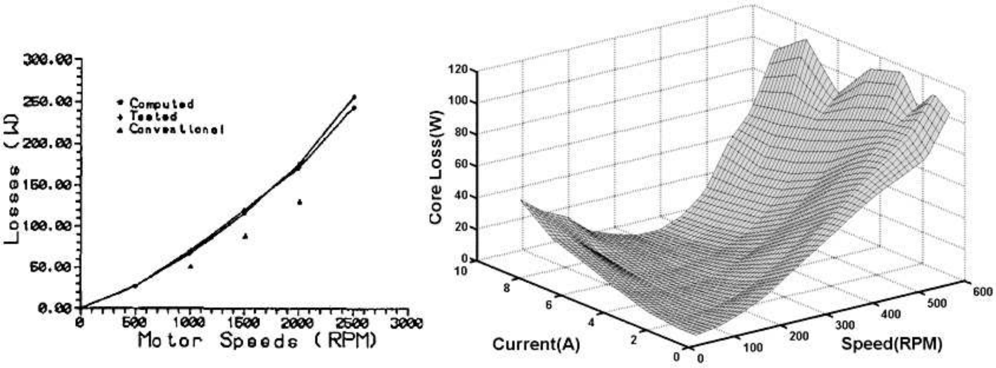

(a) Core loss plot generated in General Motors

(b) Core loss performance map developed in this research

Figure 6.29: Comparison of core loss plots [21]

As mentioned in Section 3.4, the core loss plot along with the copper loss plot determine efficiency of an electromechanical motor. Fang Deng [21] tested a brushless DC motor and developed a core loss plot with respect to motor speeds as shown in Figure 6.29(a). Based on this core loss plot, it can not be seen explicitly whether the loss depends on the applied torque to the motor. Therefore, using the nonlinear test bed for actuators (NTBA), two separate control parameters were manipulated and 3D plots of the core loss performance map were created, as shown in Figure 6.29(b). Additionally, Figure 6.10 involves torque and speed as additional control parameters.

6.3.4 Comparison of Torque Ripple Plots

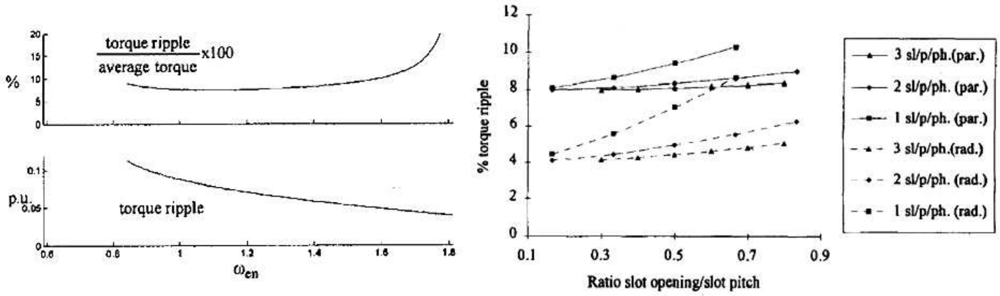

(a) Torque ripple as a percentage of average torque and peak to peak torque ripple for PMSM

(b) Torque ripple from various motor designs depending on slot and tooth structure of a stator

Figure 6.30: Torque ripple plots of two commercialized brushless DC motors [87] [62]

There are many papers describing the parasitic torque ripple occurrences in an electromechanical motor and most of them include a torque ripple test of a specific motor. As mentioned in Section 3.7, the magnitude and frequency of ripples very much depend on the structure of the stator and rotor design in an electric motor. Figure 6.30(b) shows how ripples change depending on the ratio of slot opening and slot pitch of a stator. In this report, the structure of the test motor has already been chosen as mentioned in Section 4.3.1, so it is seen if the torque ripple can be changed depending on the operational control parameters. The torque ripple 2D plot in Figure 6.30(a) is compared with the torque ripple performance map in Figure 6.13. The definition of the torque ripple in Figure 6.30(a) is the peak-to-peak torque ripple over the average torque value, which is different than the definition used to create the torque ripple map shown in Figure 6.13. In this research, the torque ripple is calculated as the ratio of the amplitude of ripples and the average torque. Torque ripple increases as the speed of the motor increases as shown in both Figure 6.30(a) and Figure 6.13. In Figure 6.13, the additional control parameter is used to display the torque ripple with respect to two independent parameters.

6.3.5 Comparison of Acceleration Plots

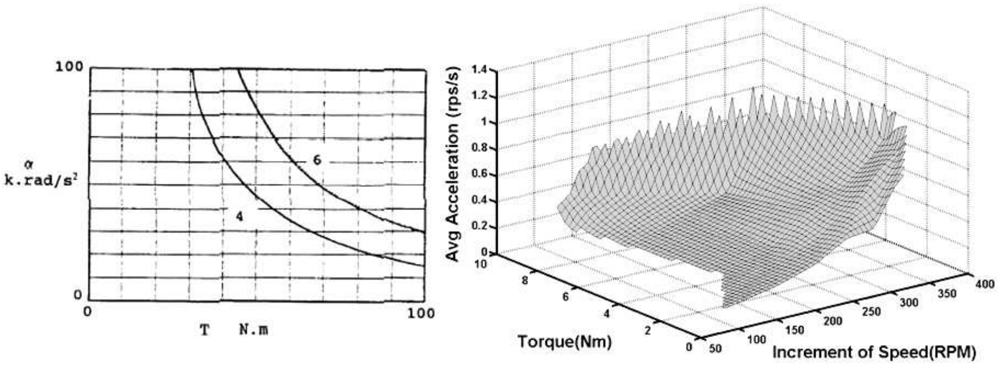

(a) Acceleration – Torque relations for 2 pole motors

(b) Acceleration performance map

Figure 6.31: Comparison of acceleration plots [90]

In this section, the maximum acceleration is represented in two different axes. The BLDC motor compared with the test motor in this research is Slemon's permanent magnet synchronous motor as presented in [90]. Figure 6.31(a) shows limiting values of achievable angular acceleration for the maximum torque capability up to 100 Nm. Two acceleration curves depend on the number of poles as shown in Figure 6.31(a). The acceleration capability decreases as the torque rating is increased. However, the acceleration depends on an additional control parameter which is speed as shown in Figure 6.31(b). By increasing speed, the available acceleration is increased. The acceleration performance map is also created in Figure 6.14 to describe the maximum acceleration at the same control parameters as in Figure 6.31(b).

6.3.6 Comparison of Magnetic Flux Density Plots

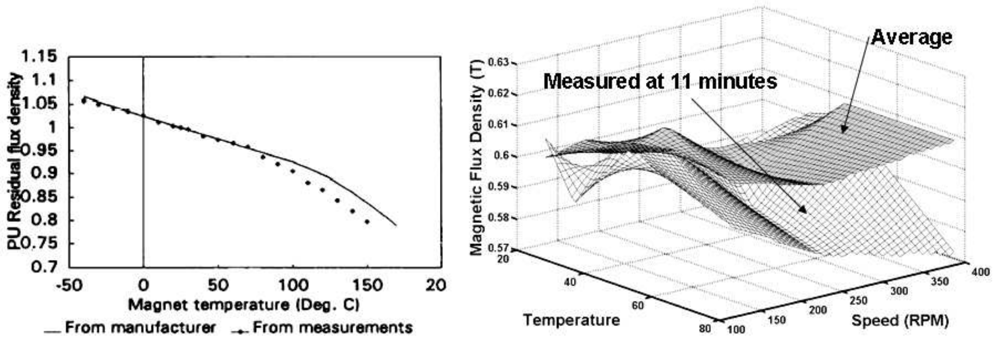

(a) Temperature effects on magnetic flux density in Tomy Sebastian's paper

(b) Magnetic flux density map

Figure 6.32: Comparison of magnetic flux density plots [86]

The magnetic flux density is measured by the flux density sensor installed inside the stator of the test motor. Using this sensor, a B-H hysteresis curve is created and it is useful to evaluate if the magnetic energy is efficiently being transferred to the mechanical energy of the electromechanical motor. The magnetic flux energy is affected by increased temperature as mentioned in [86]. Figure 6.32(a) shows that the flux density is reduced to 20% at 150°C. Referring to this result, the magnetic flux density performance map is created as represented in Figure 6.32(b). Based on the figure, the magnetic flux density also depends on the motor speed. In Figure 6.17, torque is an additional control parameter to display the magnetic flux density performance map.

6.3.7 Comparison of Temperature Plots

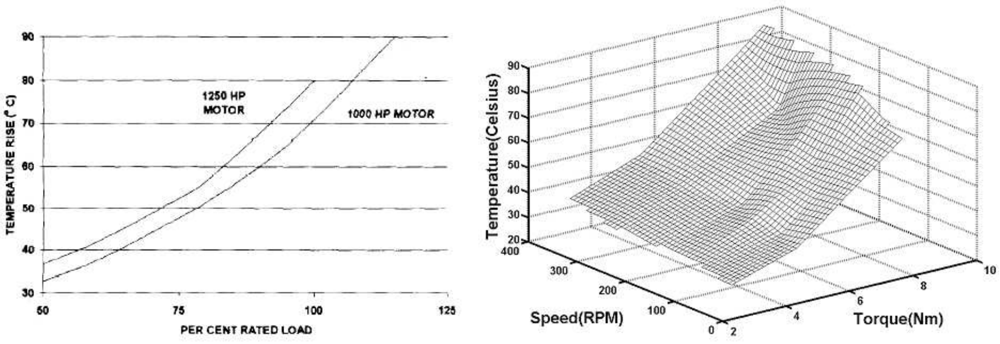

(a) Temperature rise plot of Campbell's paper (b) Temperature performance map

Figure 6.33: Comparison of temperature plots [14]

The temperature performance map is one of the core performance maps used to evaluate the operation of an electromechanical motor and check the temperature inside the motor. The temperature map used as an operational reference is created as shown in Figure 6.33(a). In this figure, the temperature rise mostly depends on the applied loadings (i.e., higher torque is due to higher current which leads to higher wiring losses). Also, the temperature plots shown in Figures 3.13 and 3.14 support the idea that the temperature increases as the more torque is applied. Figure 3.14 presents the temperature plot as a function of torque and time. On the other hand, the time to measure the temperature is fixed at 11 minutes shown in Figure 6.33(b) in this report. The temperature performance map developed in Figure 6.33(b) changes with respect to applied torque and speed. Specifically, this map shows that the temperature is changed by the increase of rotor speed.

Chapter 7

Conclusions and Recommendations for Future Work

7.1 Research Summary and Conclusion

These major topics are summarized in this chapter and the conclusion is described in each individual section. In the second part of this chapter, recommendations and suggestions for future directions of research are discussed.

7.1.1 Background Study on Electromechanical Actuators

In Chapter 1, the major topics, performance criteria and maps, are introduced through existing literature and technical papers. The papers presented in Table 7.1 describe the concept and usage of performance criteria and maps used in different types of electromechanical machines. Table 7.2 lists the papers closely related to the performance map methods of automobile engines. Each paper suggested the test regime for the specific engine and built the test methods and performance maps to control the operational parameters. Some other applications for the performance criteria and maps are represented in Table 7.3. The performance maps of turbine engines are created in Ref. [89].

A detailed study of brushless DC motors has been presented in Chapter 2. The past research has involved modeling, analysis, and control of brushless DC motors. For modeling of the electromechanical motor control system, the permanent magnet synchronous motor equations are derived and the mechanical

Literature Review	**Descriptions**
Morrell and Salisbury [64]	Quantitative metrics for the task performance would improve understanding of an actuator's nonlinear characteristics.
Reinert et. al. [80]	The performance criteria of the switched reluctance motor (SRM) were described.
Neumeyer et. al. [67]	Introduced seven performance limiting factors for electric machines to evaluate if the operational conditions of a motor were out of range.
Smith and Jacobsen [94]	Nine quantitative performance criteria for electromechanical actuators were presented.
Kuribayashi [50]	Used power and energy divided by mass and volume to evaluate ten linear and rotary actuators.

Table 7.1: Literature review for performance criteria and maps in electromechanical actuators

equations including all of the test equipment are considered. To build the motor equation, fundamental electric and magnetic energies are studied. Based on the force equation developed in Equation (2.1), the generation of torque has been explained by describing the sinusoidal commutation. To perform the simulation using PMSM before the practical experiment, the following equations (such as Equations (2.23), (2.27), (2.28), and (2.29)) were used:

- $\frac{di_q}{dt} = -\frac{R}{L-M} i_q - n i_d \omega - \frac{n k_e}{L-M}\omega + \frac{1}{L-M} V_q$
- $\frac{di_d}{dt} = -\frac{R}{L-M} i_d + n i_q \omega + \frac{1}{L-M} V_d$
- $T_m = (J_l + J_m)\frac{d\omega_l}{dt} + (B_l + B_m)\omega_l + T_e$
- $T_m = \frac{3}{2} n k_e i_q$

Literature Review	**Descriptions**
Baker and Daby [7]	Developed an engine mapping method to determine engine calibration.
Stevens et. al. [97]	Built a map of engine stability and combustion performance parameters.
Golverk [29], [30]	Generated the generalized normalized diesel engine performance maps through experiments.
Onder et. al. [70]	Generated loop-up tables to represent the nonlinear operational conditions for the internal combustion engine using a dynamic test bench.
Cuddy et. al. [19]	Created the performance maps for the operational regime and predicted the electric vehicle performance, range, and fuel economy.
Rizzoni et. al. [82]	Developed a simulation package using performance maps to find the operational optimizing solution of the control parameters for hybrid electric vehicles.
Paganelli et. al. [72]	Used the concept of engine performance maps for parallel hybrid vehicles.

Table 7.2: Literature review for performance criteria and maps in the automotive industry

Literature Review	**Descriptions**
Sieros et. al. [89]	Described a method to model the performance maps of compressors and turbines in a jet engine.
Chen et. al. [15]	Presented the effect of the power loss of a rubber V-belt continuous variable transmission (CVT)

Table 7.3: Literature review for performance criteria and maps in other industries

In this case, T_e is ignored because this term is considered as a disturbance.

Then magnetism in the permanent magnet of the rotor has been discussed.

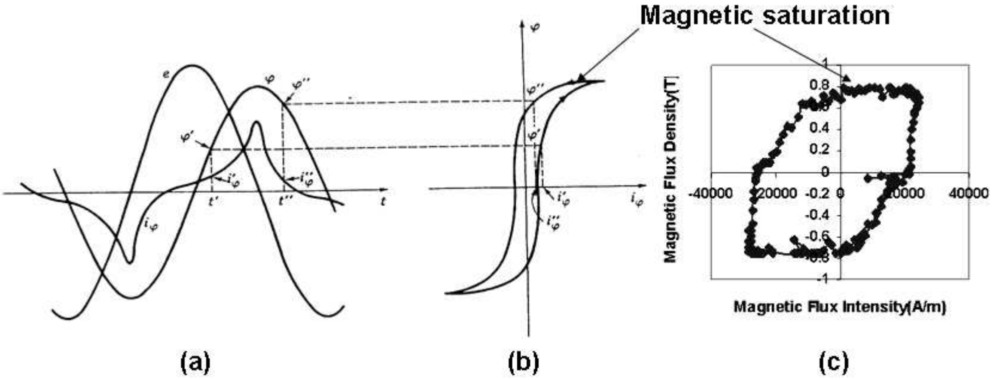

Figure 7.1: Magnetic exciting current curve. (a) Back EMF, Magnetic flux, Exciting current, (b) Corresponding hysteresis loop [25], (c) *B*-*H* hysteresis loop obtained from the magnetic flux test

The magnetization of ferromagnetic material is explained by providing the concept of magnetic saturation in Section 2.2. The magnetic saturation was verified in a permanent magnet synchronous motor by experiment as shown in Figure 7.1.

Based on the motor equations developed in Section 2.3.1, simulation of the brushless DC motor in the test bed was performed. The simulation model was built to represent the electrical and mechanical modeling of the electromechanical motor using Matlab Simulink block diagrams and the differential equations describing its dynamic motions. The mathematical model for this simulation used the following assumptions:

- The flux established by the permanent magnets in the stator is sinusoidal.
- The electromotive forces are sinusoidal.
- Friction in bearings, windage, etc. loss is not considered.
- Most of losses depend on core and copper losses.

- Temperature distribution is followed by Equation (2.36).
- Magnetic saturation is ignored.
- The stator windings have the same resistances and inductances.
- The self inductances and mutual inductances between windings are equal.

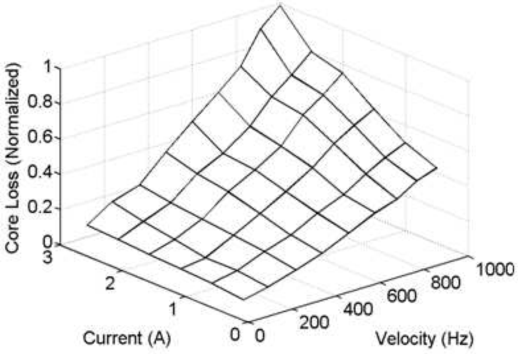

- **Core Loss Reduces Efficiency**
  - Temperature Is an Issue
- **Efficiency Depends on Speed and Torque**
  - Increases with Current (Amps)
  - Speed Generates Mechanical Losses
- **Heavy Duty Cycle Increases Losses**
  - High Average Torque and Speed

Figure 7.2: Core loss plot from simulation

The simulation result plots are represented in Figures 2.12, 2.13, and 7.2 using Matlab and Simulink programs. The simulation for the core loss plot is performed as presented in Equation 2.35 as follows:

- $Power\ Loss = Core\ Loss + Copper\ Loss$
- $Power\ Loss = \frac{\omega_e^2}{R_c}[(L_1I_1)^2 + (L_2I_2)^2 + (L_3I_3)^2] + R_s[I_1^2 + I_2^2 + I_3^2]$

The core loss term represented in this equation applied the assumption of $\lambda = Li$ where λ is the magnetic flux linkage and is defined in Equation (2.5). The core loss performance map obtained by simulation affects the efficiency map as represented in Figure 2.12. Heavy duty cycles including the motor operation with high torque and fast speed increase losses as seen in Figure 7.2.

7.1.2 Development of Actuator Performance Criteria

This report presents a work-in-progress that aims to develop an intelligent control methodology whose basic premise is that an actuator is a highly nonlinear device with redundant resources and that its performance can be improved by using a nonlinear model and extensive sensory information. A collection of performance criteria shown in Chapter 3 is the approach taken to represent the complexity of the actuator (both as an original model reference and as a real time sensor reference) and the metrics for measuring the actuator state.

The actuator control architecture, which uses a decision-making system to determine the best performance output for an intelligent control system, is shown in Figure 7.3. The key building blocks of the intelligent control approach are the actuator criteria and performance maps which were constructed in this research. The performance criteria are defined as the decisive factors to define, anticipate, and evaluate the performance responses of the system. The quality of an actuator's outputs can be evaluated quantitatively based on the properly defined performance criteria. The criteria, built in this research, are diverse enough to characterize as many aspects of performance as can be deduced from the physical state of an actuator during the task. These criteria become the basis to create the performance maps, which is the metric visual expression of performance criteria, considering all possible situations and conditions. The performance maps developed from tests were based on independent operational parameters and states, and represent the most important nonlinear properties of the actuator. A generalized actuator parametric model that represents these nonlinear properties will be developed using performance maps. Also, in order to complete the intelligent control, the decision-making algorithm necessitates sensor models that are based on real-time sensor

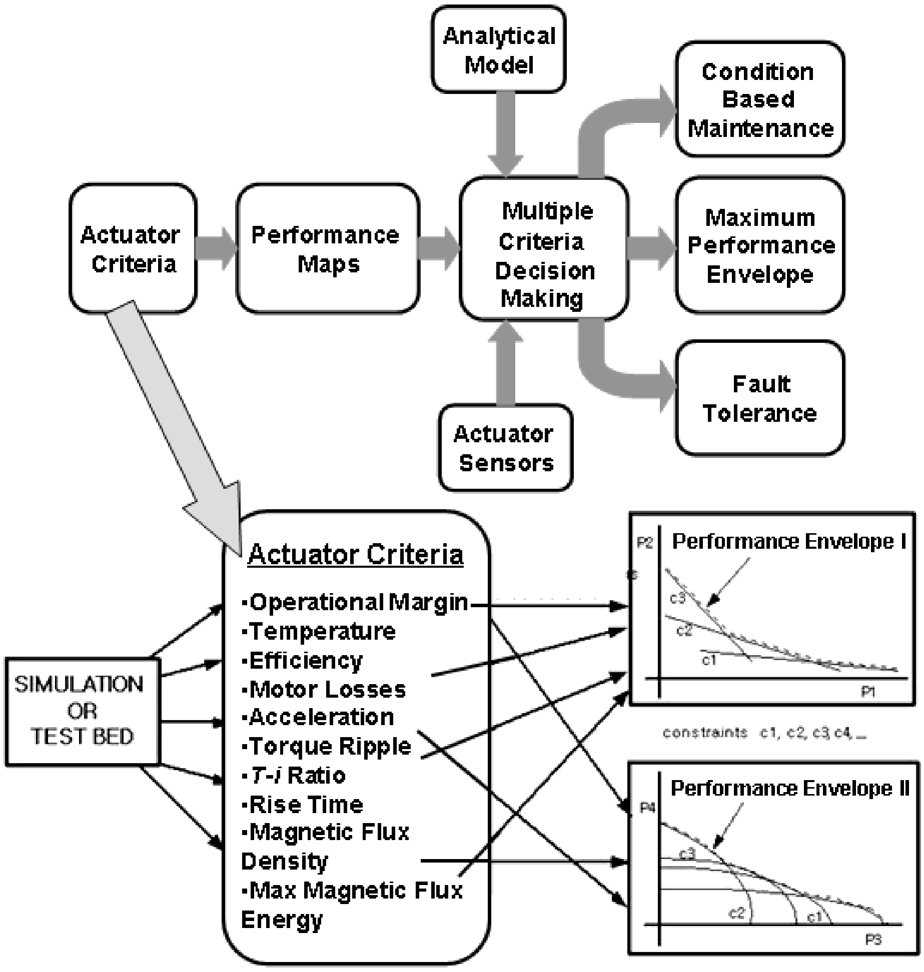

Figure 7.3: Importance of actuator criteria

data. Actuator criteria, which were the focus of this research, will be the references to collect the sensor data based on the parametric models.

The initial listing of 10 electromechanical motor performance criteria was presented in Table 3.1. Development of these criteria and the identification of the relationships among them are the basic foundation to build an actuator management architecture. Actually, an electromechanical motor has a multitude of parameters that affect its overall performance. A detailed understanding of these cross-couplings and parameters is an essential first step towards increased performance. For example, the torque generated by a motor is closely tied to its temperature. Understanding of this relationship suggests a need to address the cooling needs of the actuator. Also, of interest is the acceleration response of a motor under a given load. Analysis of this property can provide an operational acceleration margin that is used to determine how fast the acceleration follows the input torque command (i.e., in terms of step input). Superimposed cyclic variations in the normal load (called torque ripple) affect actuator performance. This torque ripple has a distinct sound signature that can be detrimental for low noise applications.

Actuator performance criteria have been suggested for experiment based on several independent control parameters. These independent parameters for PMSM drives are desired torque, T_m, rotor speed, ω_L, and current, i_T, (or voltage, V_T). The measured dependent parameters are output torque, T_a, temperature, C_T, magnetic flux density, M_T, acceleration, a_b, and rise time, t_r. The independent parameters were one of the x-y axes in performance map plots as shown in Figures 7.5 – 7.10. Also, the combinations of dependent parameters were plotted in the third (z) axis.

7.1.3 Fabrication of the Actuator Test Bed

In this report, the approach for representing the complexity of actuator performance is a collection of performance maps corresponding to each motor or actuator. Using flexible hardware and software to integrate the motion control for two motors and the hysteresis brake, test data has been obtained using the actuator test bed. The procedure for building the test bed, which has been named the Nonlinear Test Bed for Actuators (NTBA) and represented in Figure 7.4, was described in Chapter 4. For experimental data measurements, the gains have been carefully chosen and various signal processing methods have been used to filter out signal noise.

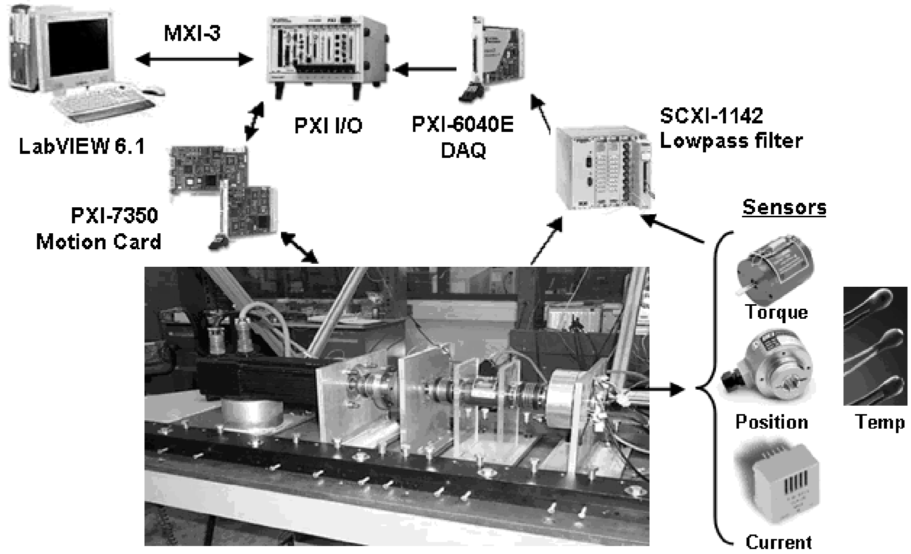

Figure 7.4: Actuator test system overview

Each mechanical component has been carefully chosen and its specifications are introduced and used to explain why the specific component has been selected as shown in Table 7.4. The load motor was selected first, then couplings, a brake, a clutch, and a torque sensor were chosen. The amplifier and power supply for the test motor and the load motor were selected based on the maximum power capacity of the overall management system. The maximum speed was 650 RPM, the maximum applied torque was 15 Nm, and the system frequency was 20 Hz. A high bandwidth torque sensor has been used to accurately measure the torque signals. Also, 12 bit resolution encoders were used to estimate the velocity and acceleration. The current signals in three phases were measured in three current

Key Components	**Features**
Load Motor	7.16 kW, 48.2 Nm (Peak), 5000 RPM (No Load Speed), 81 Amps (Peak)
Test Motor	1.98 kW, 28.2 Nm (Peak), 650 RPM, 17.2 Amps (Peak)
Torque Sensor	40 Nm (Max), 15000 RPM, ±0.5% (Accuracy)
Encoder	12 Bit (Resolution), 6000 RPM (Max)
Clutch	29 Nm (Static torque), 5000 RPM
Current Sensor	Current Sensor 36 Amps (Peak), ±0.5% (Accuracy)
Motion Controller	16 kHz (Sampling Rate), 8 AIO (16 Bit), 16 DIO.

Table 7.4: Specifications of major components

sensors. To measure magnetic flux density signals affected by high temperatures, the Hall sensor was installed inside the air gap of the test motor. Four thermisters were used to monitor the increment of the temperature in the three phase currents and the stator core. To control the overall mechanical and electrical system in NTBA, an NI motion controller is used and the Labview programs help the test bed operator provide proper commands to generate a mechanical power from an electrical power source.

To create performance maps, test regimes have been developed in Chapter 5. Five test methods have been suggested to test the electromechanical motor and create ten performance maps in this report. Test regimes include the most general case in the operation of the motor and the applied torques consider two different type of loads. Dynamic torque measured in a torque sensor has been developed by the test motor and generates sinusoidal periodic loads which represent a nonlinear periodic load. Table 7.5 describes the procedure of this test protocol. On the other hand, the static constant torque was developed in the test motor to provide

Test Regime I

- The load motor starts to run at a constant speed, ω_L. The speed, ω_w, of the system is governed by the load motor.
- At the same time, the test motor is operated in a certain repeating torque profile. This torque, T_m, is generated by providing the current command required to run the motor to the test motor amplifier. The torque, T_a, applied to the system is controlled by the test motor.
- The measured data during the operation is recorded by the DAQ board. The test data are recorded for a certain time.
- This test is repeated for different frequencies of cyclic voltage input and different speeds of the load motor.
- The torque sensor measures the output torque, T_a, of the test motor.

Table 7.5: Test regime for dynamic loading test

Test Regime II

- At rest, both motors are connected by engaging the clutch.
- The load motor starts to run at a constant speed, ω_L. The speed, ω_w, of the system is governed by the load motor.
- The torque, T_m, is generated by providing the current command required to run the motor to the test motor amplifier. The static torque command from the test motor amplifier is provided to generate constant torque, T_a.
- The measured data during the operation is recorded by the DAQ board.
- This test is repeated for different speeds, ω_L, of the load motor.
- The torque sensor measures the output torque, T_a, of the test motor.

Table 7.6: Test regime for static loading test using constant torque, T_a

Test Regime III

- At rest, both motors are connected by engaging the clutch. Thermisters are attached on the stator windings and core as shown in Figure 5.6. Also, thermometer is inserted inside the test motor to monitor visually the rise of temperature.
- As mentioned in Test regime II, the same torque, T_m, profiles are generated in the test motor while the load motor runs at a certain speed, ω_L.
- The measured data during the operation is recorded by the DAQ board. At this time, there is one more measurement parameter, which is temperature, C_T.
- The operating temperature, C_T, of the test motor is considered between $25°C$ (an ambient temperature) and $90°C$.
- This test is repeated for different speeds, ω_L, of the load motor.
- The torque sensor measures the output torque, T_a, of the test motor.

Table 7.7: Test regime for temperature test using constant torque, T_a

constant loading to create the peak torque at each speed, which is controlled by the load motor. The test protocol for the static loading test is represented in Table 7.6. Also, in order to determine the rise of temperature inside the motor, the temperature is measured for 11 minutes. At less than 5 Nm, the temperature increases very slowly, but at more than 5 Nm, the temperature increases somewhat faster. The temperature performance map created in this test is a very important limiting factor to generate a torque in the motor during a certain time, so the temperature should be monitored while the motor is operated. The test protocol for the temperature test just adds the procedure to measure temperature using thermisters when the test data are collected in the sensors installed in the test bed as described in Table 7.7.

Test Regime IV
• At rest, both of motors are connected by engaging the clutch. • The load motor starts to run at a constant speed, ω_L. The speed, ω_w, of the system is governed by the load motor. At this time, the test motor is off. • After a few seconds, the test motor energizes to develop a certain torque, T_m. The torque increases to a certain value as commanded by the controller and stays there for a few seconds to obtain enough data. • The measured data during the operation is recorded by the DAQ board. The test data are recorded for a certain time in an equidistant period of a sampling rate. • This test is repeated for different speeds of the load motor. • The torque sensor measures the output torque, T_a, of the test motor. Figure 5.8 represents the control of the torque, T_a, generated in the test motor.

Table 7.8: Test regime for transient response test

The transient test has been suggested as shown in Table 7.8. In this report, the torque rise time is described as a transient test and the torque developed in the test motor is increased to a certain higher level of static loading from a no-load condition. This test has been performed for various values of speed, controlled by the load motor. Finally, the hysteresis brake was used to develop acceleration and torque ripple performance maps. The hysteresis brake test is named after the usage of the hysteresis brake. The hysteresis brake is used instead of using a load motor because there is no cogging torque in the hysteresis brake. The cogging torque, mentioned as a parasitic property in an electromechanical motor, is the major source of the torque ripple in an electromechanical machine as mentioned in Section 3.7. The test protocol for the hysteresis brake test is represented in Table

Test Regime V

- At a stop position, the test motor and hysteresis brake are connected by engaging the clutch.
- The test motor starts to run at a constant speed, ω_b. The speed of the system is mostly governed by the inertia and friction of the test motor and hysteresis brake at the beginning. The speed is set by monitoring the torque response.
- After a few seconds, the hysteresis brake is applied to develop a certain torque, T_a. The torque increases to a certain value as commanded by the controller unless the motor runs at enough speed to overcome the inertia and friction of the test system.
- In the control program for the test motor, the command signal, which is the voltage signals provided in the motion program for the test motor, is provided to create the increment of speed. By doing this, the average and maximum accelerations, a_b, are obtained.
- The measured data during the operation is recorded by the DAQ board. The test data is recorded in a time period of 3 msec.
- This test is repeated for different increments of speeds and torques of the test motor.

Table 7.9: Test regime for hysteresis brake test

7.9.

7.1.4 Analysis of Test Results

Based on the test regimes presented in Tables 7.5, 7.6, 7.7, 7.8, and 7.9, actuator tests were performed. Chapter 6 describes the test results, and performance maps and performance envelopes were created. Each set of torque and speed values, as presented in Section 5.1, were applied to the test motor and the load motor and they were connected by engaging the clutch as shown in Figure

7.4. Several sensors were installed in the test bed, and began operating with the motion of both motors. The sensor signals were collected using a synchronously fixed sampling rate and they were stored in the DAQ board. Using an NI-SCXI signal conditioning machine, the signals were cleaned by removing 95% of the signal noises generated in the measurement. The cleaned signals are identified as a function of control parameters using time series analysis, which is described in Section 7.1.6.

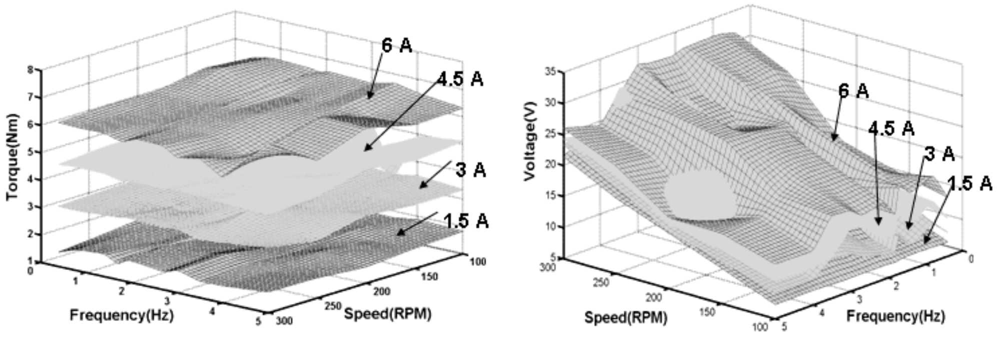

(a) Torque response **(b) Voltage response**

Figure 7.5: Test result I: Operational margin maps

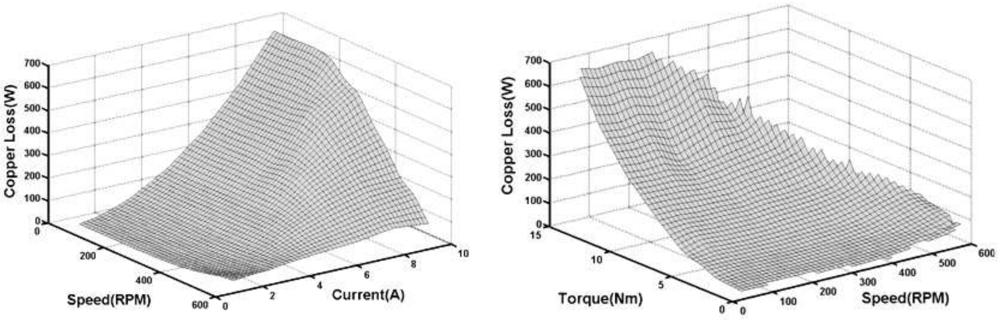

(a) Copper loss map I **(b) Copper loss map II**

Figure 7.6: Test result II: Copper loss maps

Ten performance maps were obtained through experiments using NTBA

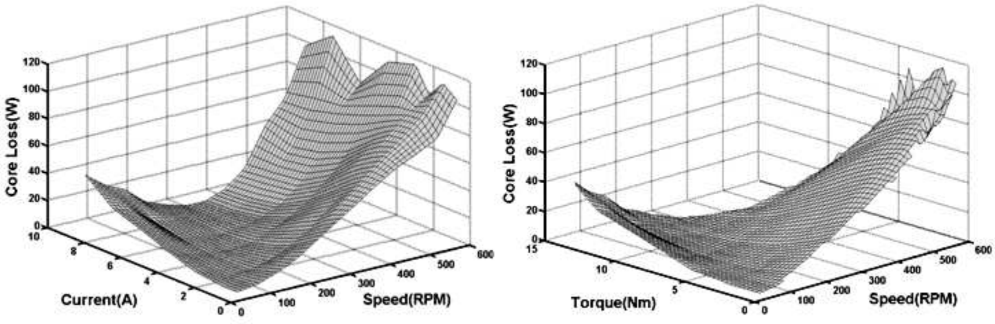

(a) Core loss I (b) Core loss II

Figure 7.7: Test result III: Core loss maps

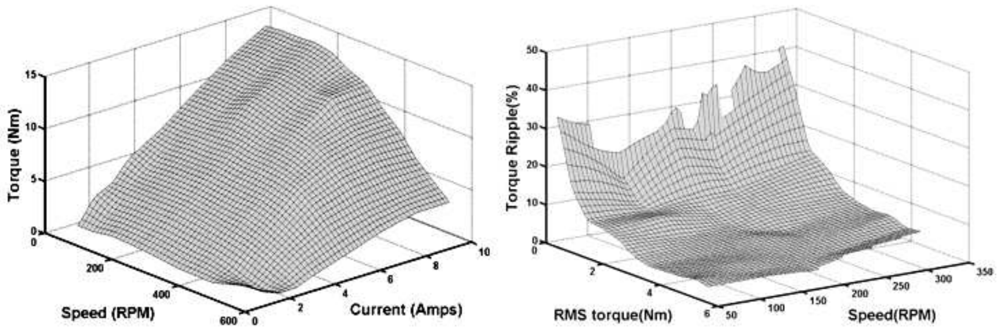

(a) Torque-current map (b) Torque ripple map

Figure 7.8: Test result IV: Torque response maps

as shown in Chapter 6. Some parts did not show up in the 3D surface of a performance map because the test bed could not adequately test the permanent magnet synchronous motor in that area (it was speed or load capacity limited). The test motor was supposed to generate up to 26 Nm of peak torque but only achieved 14 Nm. Because the power transformer of the test motor was not able to provide enough peak current, the maximum torque was not generated in the test motor. This current limitation of the NTBA is illustrated in test results as shown in Figures 7.5-7.10.

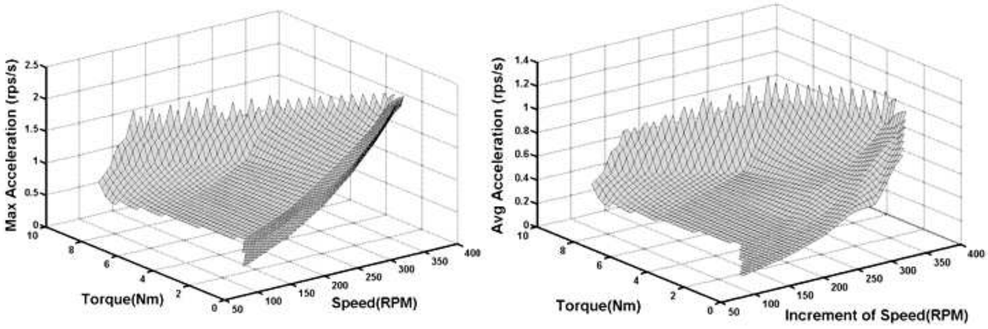

(a) Maximum acceleration map **(b) Average acceleration map**

Figure 7.9: Test result V: Acceleration maps

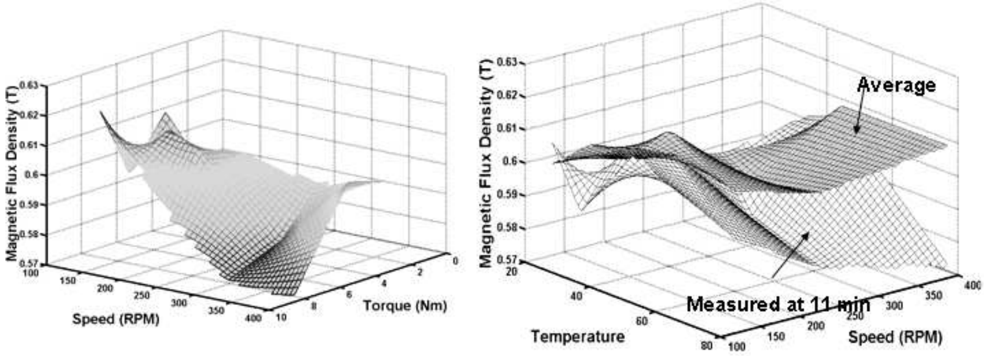

Figure 7.10: Test result VI: Magnetic flux density maps

Most of the performance maps did not cover all of the test range of the test motor, but the surfaces created using the test bed had very nonlinear, meaningful and practical properties, which were reasonable in an engineering sense. In fact, their nonlinearity must be taken into account to accurately create valid operational performance envelopes. Operational performance maps have been presented in Figure 7.5. The maximum current used in the tests was 6 Amps because the test bed started vibrating at this amperage. This problem can be solved by replacing the power transformer for the test motor. Also, Figure 7.6 represents the incomplete surface with respect to the torque variable because the power transformer did not provide enough current to generate the torque in the test motor. As shown in Figure 7.6, copper loss was very small at low current and torque, but by increasing the current to the motor, copper loss increased significantly with the square of the current. The second order copper loss equation shown in Figure 6.7 created the parabolic shape of copper loss performance map as a function of current, i_T. The shapes of the core loss performance maps were parabolic due to the square terms of voltage and current as shown in Figure 7.7. Core loss was low at the rated values of torque, T_a, and speed, ω_w, but it increased under low torque-high speed and high torque-low speed conditions.

The relationship between torque and current was described by changing the speed of the motor and it was represented in Figure 7.8(a). At more than 200 RPM and 6 Amps in Figure 6.12, the torque-current had an even more severe nonlinear curve. Also, the torque ripple performance map was obtained using the hysteresis brake as shown in Figure 7.8(b). The ripple was almost 45% at the test motor speed of 300 RPM and a low load torque of 0.42 Nm. In overall torque ripple responses, the ripple was less than 5% at higher torque output, T_a, from the test motor.

The acceleration performance map has been created using the test set-up including the hysteresis brake as shown in Figure 7.9. Maximum acceleration was obtained by selecting the largest value in the transient region when increasing the speed, ω_w, from a low value to a higher value. The average acceleration was determined by averaging the acceleration values in the transient region between two different magnitudes of speed. In Figure 7.9(a), the maximum acceleration was almost 2.3 rps/s at 1 Nm of torque, T_a, output and 340 RPM of the speed increase. In addition, the average acceleration had almost the same tendency as the maximum acceleration as shown in Figure 7.9.

The magnetic flux density performance maps, which are the last test example plots, are shown in Figure 7.10. As shown in Figure 7.10(a), the magnetic flux density was slightly reduced at higher rated torques and speeds at the elapsed time of 11 minutes. The magnitude of the reduced value was very small (about 6-7 %) but this plot explained that magnetic flux density B was affected by torque and speed. In Figure 7.10(b), the magnetic flux density, as a function of temperature and speed, measured at 11 minutes was lower than the 0.6 Tesla (T) measured at the start.

An actuator test framework has been discussed and test methods for building performance maps are presented in this report. In this section, performance maps have been created through five different test regimes and these maps represent the operational performance of the test motor. The motor has a number of operational references, so it can be managed to generate high quality responses during operation. The performance envelope created by using performance maps provides and guides optimum output responses by controlling the motor. The procedure to create a performance envelope has been discussed in Section 6.2.

7.1.5 Development of performance envelope

The NTBA fabricated in this research has been used to create electromechanical motor performance maps utilized to develop performance envelopes. The procedure to create a performance envelope is shown in Figure 7.11. Test regimes have been established to provide test procedures and develop these performance maps, and using the NTBA, performance map plots have been created. The first result from the dynamic loading test, which is one of the presented test regimes, was for building the operation margin performance map. To compare with the torque-speed curve in the trade literature, two control axes were cyclic frequency and speed, and the third axis was torque. The cyclic frequency changed up to 5 Hz and could be increased more[1]. Also, the torque-speed contour plot developed in Figure 6.26 is one kind of performance envelope and it can be compared with the torque-speed curve introduced in traditional trade literature. Four performance maps, such as efficiency, rise time, magnetic flux energy, and temperature, were used as examples to show how to create the performance envelope based on these maps as described in Section 6.2.

Using constant static torque test, the efficiency and motor loss performance maps have been created. Based on loss performance maps, efficiency has been considered as one of electromechanical motor performance maps because the power input becomes power output and power loss. In this research, the efficiency obtained through the testing has been very low compared with values in trade literature as shown in Figure 6.27. The maximum efficiency has been estimated as 70% in the test of the brushless DC motor. Figure 7.12 describes the normalized efficiency performance map which can be used to establish a performance envelope. There are some other tests performed in this test protocol.

The magnetic flux density signal has been monitored to create magnetic flux energy. Flux energy has been obtained by calculating the area of the B-H hysteresis curve developed during the test. As shown in Figure 7.14, the torque output from the test motor has the greatest affect on the magnetic flux energy. The magnetic flux energy, which is the function of current and magnetic flux density, ranges from 30K to 220K Joules (J) during the tests of different torques in the test

---

[1] The test motor bandwidth is 20 Hz.

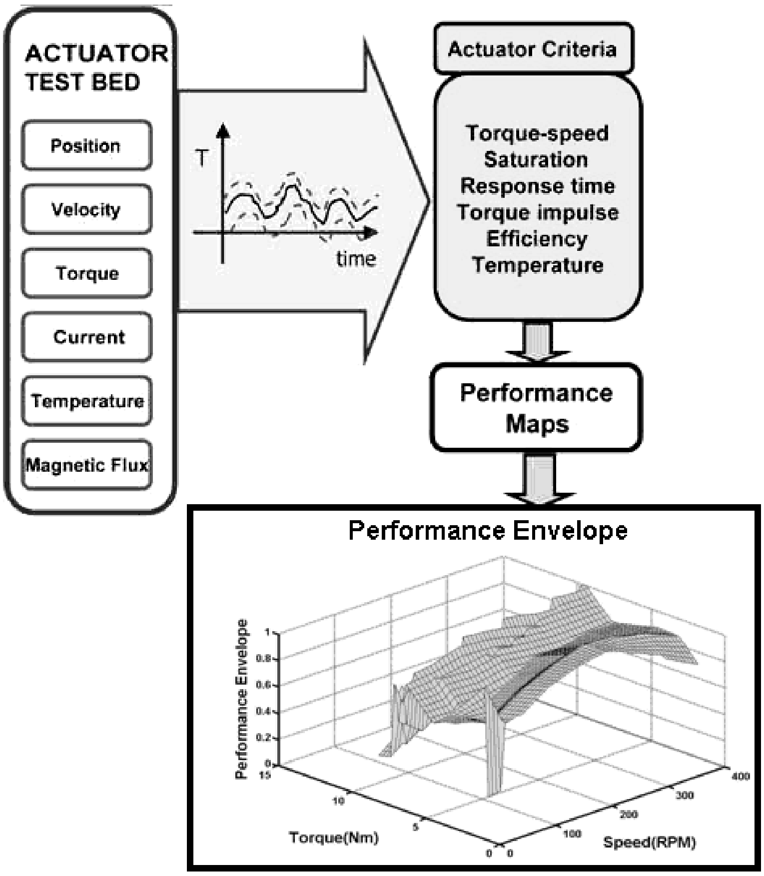

Figure 7.11: Procedure to develop performance envelope

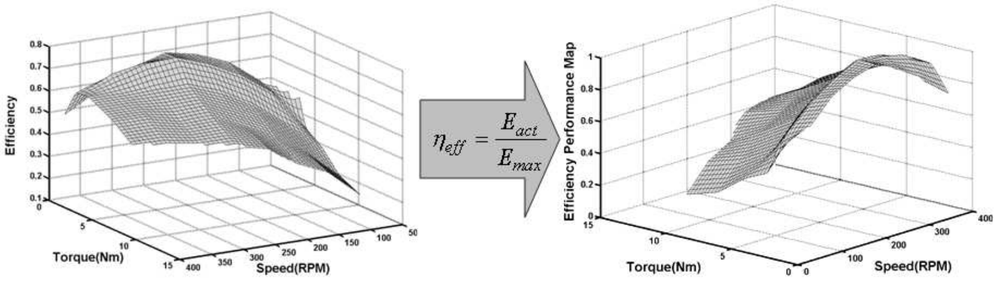

Figure 7.12: Development of efficiency performance map

motor. The normalized magnetic flux density performance map is also presented in Figure 7.14.

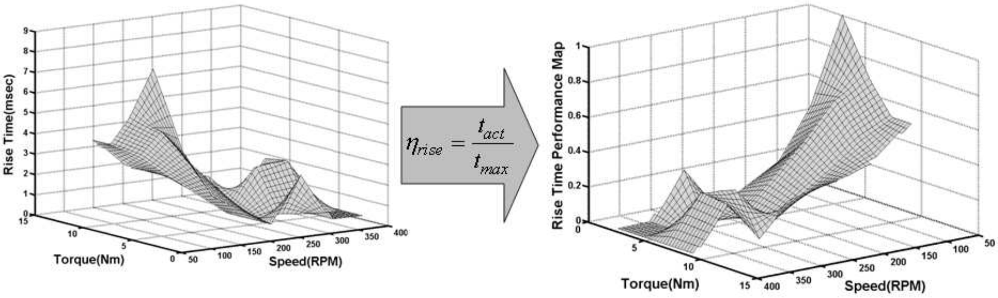

Figure 7.13: Development of rise time performance map

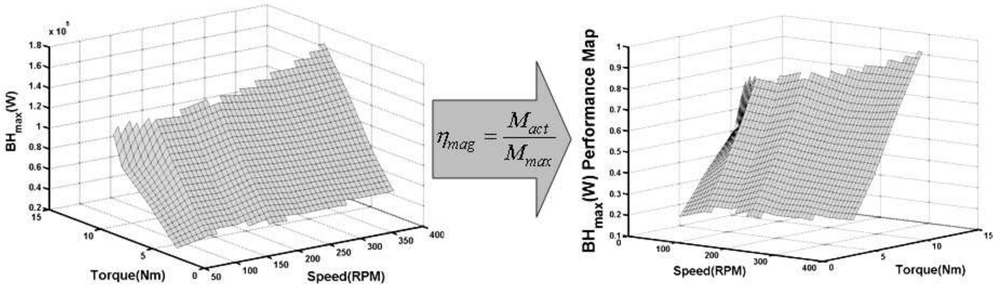

Figure 7.14: Development of magnetic flux energy performance map

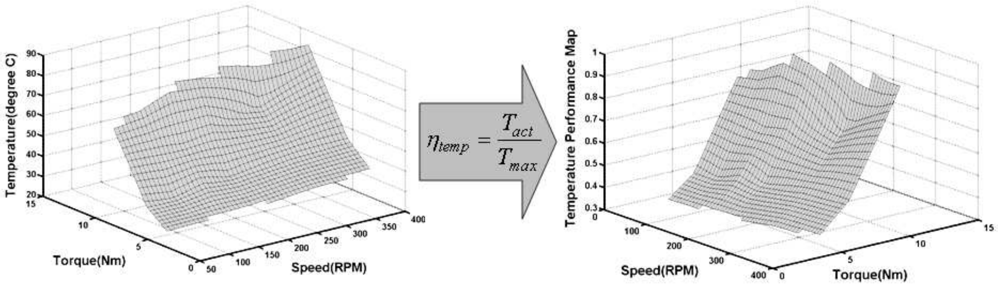

Figure 7.15: Development of temperature performance map

Using the temperature test protocol developed in Section 5.1.3, the temperature performance map has been developed as shown in Figure 7.15. Using this map, it is possible to judge how fast the temperature increases at higher levels of torque and higher speeds. Specifically, from the map, it is seen that the temperature almost linearly increases by increasing the torque. In the temperature performance map, the temperatures were measured after an elapsed time of 11 minutes for different sets of torques and speeds. The temperature reaches 80°C if 9 Nm of torque is applied to the test motor for 11 minutes. The temperature performance map is normalized using the maximum temperature, then the scaled map is created as shown in Figure 7.15.

A rise time test has been suggested as one of the transient test protocols. The rise time performance map shows the torque response time by increasing the static torque as shown in Figure 7.13. In this report, only the step-up of torque has been applied, but the step-down of the torque should also be applied and the response to it will be different than the test results found in this research. As can be seen, the rise time decreases by increasing the torque at low speed, but it increases by decreasing the torque at high speed. When the test motor was running at 400 RPM, the rise time was less than 1 msec. The normalized rise time performance map is presented in Figure 7.13.

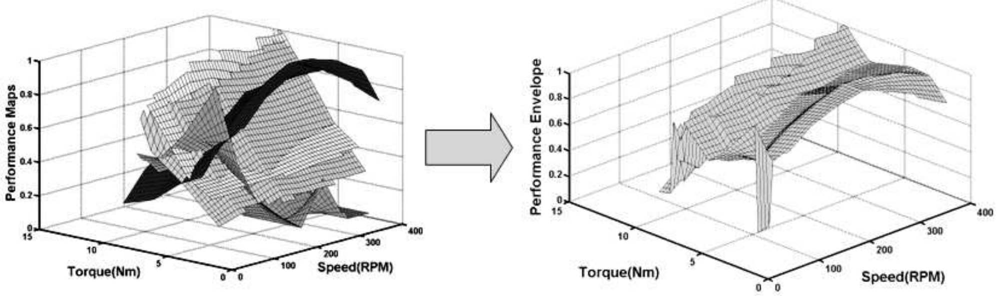

(a) Four performance maps with respect to torque and speed

(b) Development of performance envelope

Figure 7.16: Development of actuator performance envelope using four performance maps

After completing the development and analysis of ten performance maps, building the performance envelope has been discussed. To generate a performance envelope plot, all of the performance map plots driven at the same control parameters should be normalized with a properly defined normalizing factor[2]. The 3D normalized performance map plots are represented in Figures 7.12 through 7.15. The normalized performance maps have been combined together in torque and speed axes as shown in Figure 7.16(a). In this report, maximum values in each data point have been chosen as a governing performance value during the operation of the motor. Then, combining together all of the data points selected based on the knowledge of maximum values, the performance envelope is established as shown in Figure 7.16(b). The performance envelope plot with respect to torque and speed is also presented in torque-speed contour plot as shown in Figure 7.19(b). The performance envelope guides the motor controller to manage for the proper command without hitting any safety border line during operation. The performance envelope can be improved by proving a rule to select the optimum operational map in a certain application. This will be done in the future by creating a decision-making algorithm.

Statistical processes have been utilized to supplement the uncertainties of the raw data obtained from tests of the brushless DC motor. The standard deviation and average values have been calculated and used to develop the upper and lower error bounds of the magnetic flux energy performance map as shown in Figure 7.17. The tests for building the magnetic flux energy map were repeated 299 times in different torque, T_a, and speed, ω_w, settings of the test motor and the load motor. $(BH)_{max}$ is represented with two other layers where the upper layer is obtained by adding the standard deviation values to the average values and the

---

[2] In this research, peak value in overall test ranges of the control parameters is used.

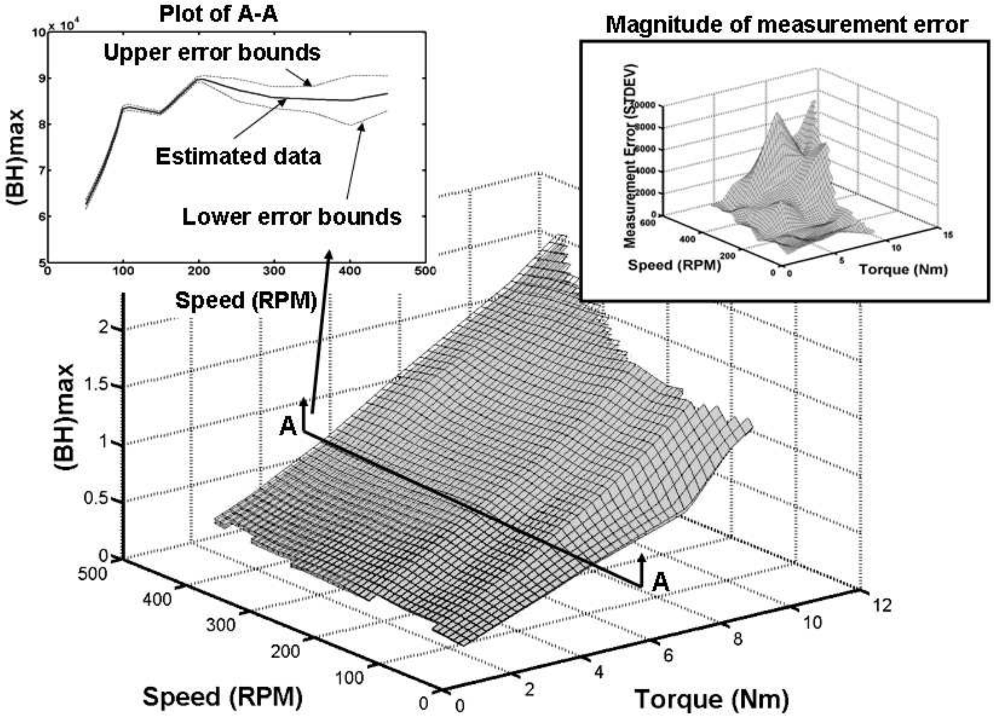

Figure 7.17: Determination of error bounds and magnitude of measurement error

lower layer is obtained by subtracting the standard deviation values from the average value of $(BH)_{max}$. Each performance map needs to have this error analysis because the data point in each 3D surface of performance maps is calculated by taking the RMS of the time dependent raw data measured in each sensor. These error bounds should be created for the other performance maps in the future.

7.1.6 Usage of performance envelope

All of the performance maps built in this report can be parametrically expressed in a nonlinear polynomial form. The Box-Jenkins statistical method has been used to retrieve all of the test data and build the mathematical representation of the sensor response with respect to time for creating each data point in a performance map. The example polynomial equation (Equation (5.6)) representing the sinusoidal torque response data has been developed using the stochastic ARIMA model.

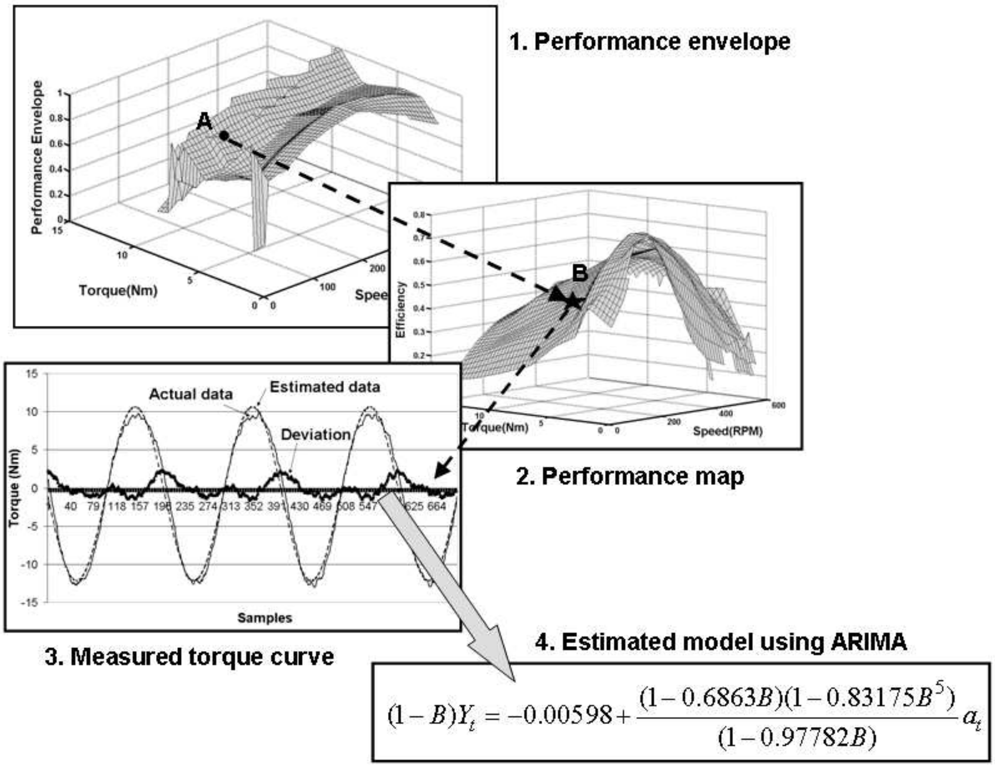

Figure 7.18: Identification of a performance equation

In Section 5.2, the Box-Jenkins ARIMA method is presented by solving an example problem. The test data is obtained using NTBA and the numerical model is obtained using the ARIMA procedure. The nonlinear equation representing the test data as a function of time will be created in other test data by repeating the ARIMA procedure. Once the parametric descriptions are ready for the identification of statistical data, the performance map is developed using the test data obtained from the tests. Figure 7.18 represents how the equation is used to manage the test data. A performance envelope has been built by testing an electromechanical actuator. The performance envelope used four performance maps and independent parameters and operational characteristics of each map have been confirmed by repeated tests. There is a certain point, "A", as a reference point in the performance envelope. The point "A" belongs to a point "B" of a performance map which is one of the normalized map components of the performance envelope. The point "B" is developed by a torque response of the given sinusoidal torque, T_m, command in the test motor. The point "B" is the representative of a specific performance map with respect to two independent parameters. The identification of this point is known as a time series equation written in time variables. The torque data curve as shown in Figure 7.18 is expressed as the estimated model equation number "4". The equation is obtained by ARIMA method presented in Section 5.2 and used as the reference model for performance evaluation and for condition based maintenance.

7.1.7 Comparisons of Test Results with the Trade Literature

Performance maps have been developed to construct the performance envelope for specific control parameters. In this report, torque and speed have been picked as control parameters and the performance envelope using these parameters is represented in Section 6.2. It was originally suggested that a decision-making algorithm should be used to create performance envelopes, as mentioned in Section 1.1, but this method is not built yet in RRG. Therefore, in this report, the maximum value is chosen for a set of torque and speed values, and by doing this a preliminary procedure to create the performance envelope is developed and is shown in Figure 7.11. Also, each performance map is normalized to be combined together in a performance envelope as represented in Figure 7.16. The performance envelope as shown in Figure 6.24 has maximum values in four different areas (such as efficiency, rise time, magnetic flux energy, and temperature performance maps) representing motor performance when it is operated. In each operational region, the magnitudes of four normalized performance maps are different, so the main role for guiding the motor operation keeps changing depending on the maximum value in each set of torque and speed axes. In Section 6.3, the performance maps built using the NTBA are compared with the performance plots introduced in the trade literature and research papers.

Trade Literature	**Test Results**
• Lack of operational values in normal and abnormal conditions.	• Provide enough metric values to manage the optimum performance of the test motor.
• Lack of the number of referencing plots.	• Generate many performance map plots depending on the environmental conditions.
• Lack of displacement of performance plots (2D plots).	• All of the performance maps are established in 3D surfaces.
• Lack of considerations of possible real operational events.	• Many test regimes have been developed to emulate real application conditions.

Table 7.10: Contrasts between performance plots obtained by trade literature and experimental data obtained by test result

The performance data plots used in the trade literature and research papers are compared with the test result plots presented as actuator performance maps. As listed in Table 7.10, the performance plots in the literature had several drawbacks for users, which are the lack of control parameters, the lack of operational values in normal and abnormal conditions, and the lack of the number of referencing plots to fully describe and enable the management of the performance

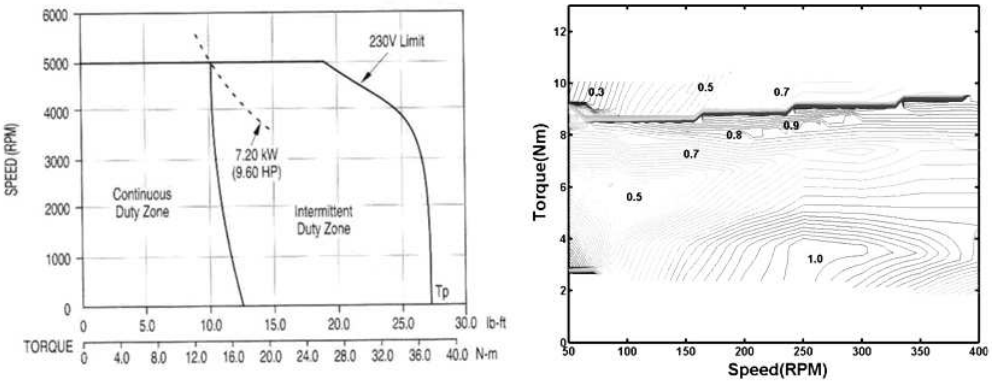

(a) Torque speed curve for Kollmorgen motor : BE-406-C

(b) Performance envelope contour for test motor

Figure 7.19: Comparison of torque-speed plots

of the motor considering all of the operational conditions. The maps obtained in the experiments using NTBA provide the metric values of maximum operation ranges and the control values at any instant in time. Also, the performance maps and envelopes have been built in separate tests before deploying the motor, so the user knows the operational properties of the motor and can control the motor to best meet various environmental conditions. In addition, more performance maps should be created for the test motor. The current set of performance maps provide much better information about the test motor than the information in the data sheet of the trade literature. However, in order to manage and evaluate the operation of an electromechanical motor, more performance maps need to be generated.

7.2 Recommendations

The performance maps created in this research provide an expanded level of understanding of a brushless DC motor. This section recommends the modification of the test bed for improving and extending the ability of the actuator tests. Also, in order to improve management and guidance for the operation of the motor, it is suggested that more performance maps and envelopes are created. Table 7.11 represents the additional performance criteria, which may be very useful to develop a more complete set of performance maps for a motor.

7.2.1 Recommendations for Additional Actuator Criteria

Criteria	**Descriptions**
Torque Impulse	Shock in a short time relative to a given duty cycle.
Torque Saturation Limit	Torque saturation based on duty cycle norm.
Friction Torque	Friction causes tracking error at low speed.
Internal Noise	A measure of the noise inside the actuator as an indicator of overall degradation.

Table 7.11: Additional actuator performance criteria

As mentioned in Table 7.11, $Peak\ torque \times \triangle t$ defines torque impulse. Torque impulse indicates the capacity of an actuator to suddenly create large torques for very short periods of time. The actual response can be obtained only through extensive testing. In normal operation, the rated current to generate torque is limited by the maximum heating from the resistive power loss. When a peak torque is to be generated for a very short period of time, the question is not heating (the basis for the rated current) but the ability of the motor to increase to some level of torque over the rated torque (200%, 300%, or etc), which is limited by the peak current in the brushless DC motor driver. What duty cycle is feasible? How many peak torque impulses will be allowed during the duty cycle? How much energy content is in each pulse relative to the normal energy content of a given duty cycle? Given these values, then the operator will know exactly what can be accomplished on demand (i.e., the system becomes intelligent) and how far beyond the performance envelope one can go for very short bursts of torque [1].

The PM motors using temperature sensitive magnetic cores with a relatively low Curie temperature[3] have different speed and torque characteristics as compared with conventional motors when considering temperature changes as mentioned in Section 2.2.3. The torque saturation limit is obtained as the critical magnetic flux density at the critical temperature [86]. Two kinds of parameters in this case are introduced to analytically describe the torque saturation limit. First of all, the torque saturation value is defined. It is the torque expression of the model used in, as

$$T_{sat} = rAB_{rms}J_{rms} \tag{7.1}$$

where r is the radius of the rotor in the air gap, A is the area of normal flux direction in the air gap, B_{rms} is the RMS value of magnetic flux density, and J_{rms} is the RMS value of current density. Secondly, the duty cycle norm is defined with the root-mean-square (RMS) value, which takes into account the fluctuations of the signal about its average value. The operation of computing the average value of torque output corresponds to integrating the signal waveform over some period of the cycle. The cycle averaged value of a torque or duty cycle norm is defined as

$$T_{rms} = \sqrt{\frac{1}{t_{cycle}} \int_0^{t_{cycle}} T^2 d\theta} \tag{7.2}$$

where t_{cycle} is the period of a cycle, θ is a cycle, and T is any kind of torque cycle curve. $T_{rms} - T_{sat}$ indicates the difference between the RMS value of the applied

---

[3] The definition of Curie temperature is given as follows: Curie point is the temperature at which the transition from ferromagnetic to paramagnetic properties of a substance is complete.

torque and the torque saturation limit. The difference between these two terms is used to evaluate the torque saturation limit.

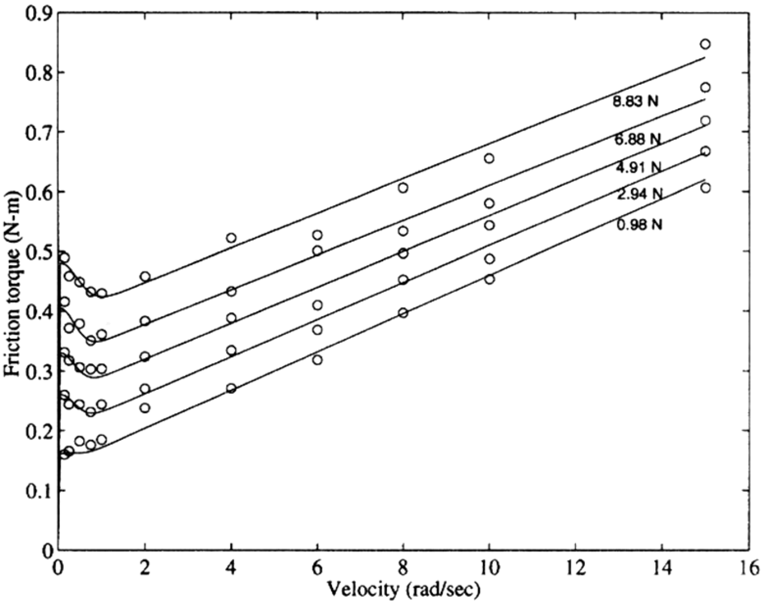

Figure 7.20: Steady-state friction torque vs. velocity models for normal loads of 0.98 N to 8.83 N [79]

Another actuator criteria that should be considered for future research is the friction torque. When the end effecter of a robot is tracking a reference trajectory at very low speeds, it does not perfectly follow its known path[4]. To identify the cause of this problem, the operation of the actuator inside of a robot needs to be investigated to compensate this tracking offset in dynamic motion. Especially, the present research only focused on the electric motor out of several components in actuator, so the cause of the tracking problem at a low speed may be found at the prime mover level. The common mechanical components in BLDCM are the rotor, stator, winding, shaft and bearing. Out of these components, the bearing

---

[4] Recall that at very low speeds, friction can be very dominant.

is the most likely candidate for the main cause of the tracking problem. However, the bearing friction inside the prime mover is too small effect on forward running of the motor. Therefore, in order to increase the friction effect, the experiment for this criterion will use a large mass on the ends of the motor shaft. The emulated vertical direction of loading will increase the friction torque in rotational direction of the motor. Additionally, the change of the mass size will give the effect of the vertical loading in dynamic motion at a very low speed. To make the situation close to the real situation, the sinusoidal and periodically nonlinear trajectory will be generated with different magnitudes and frequencies. From this experiment, the friction torque can be identified to help to find the tracking error. Figure 7.20 represents a published report on how the friction torque varies with increased speed and weight of the loads. This shows how to obtain the estimated values on the variation in normal load detected through the processing of the friction estimate.

Acoustic noise is one of the most important factors that determine acceptability and usage of motors. Magnetic noise caused by air gap radial forces is by far the most important contributor to the overall noise. The radial forces that create noise are mainly produced by space harmonics in the air gap magnetic field between stator and rotor. As the load is increased, the noise level increases at the rated flux as mentioned in [106]. At light loads, a reduction of the stator flux can significantly reduce the acoustic noise. However, as the load is increased the noise reduction becomes less significant, and a further reduction can result in higher noise emissions, and cause instability of the system. Also, Xu et. al. [106] mentioned that the noise increases noticeably with increasing speed.

7.2.2 Recommendations for Improving the Actuator Test Bed

The initial settings for the NTBA has been designed for testing an electromechanical motor, not an actuator. To test an actuator, a gear train needs to be installed, so the capacity of torque must be multiplied many times depending on the size of the gear train. For testing an actuator, an additional gear train is equipped in front of the load motor. Figure 7.21 shows the conceptual diagram of the dynamometer test bed for an actuator. The detailed procedure to change mechanical and electrical components are described in Table 7.12. The suggested values in each component are determined by the ratio of the gear train because the torque generated in the actuator mostly dominates the entire motion of the test system. The torque combined by the gear train and the load motor can overcome the torque generated in the test actuator. The torque-speed curve developed by testing the actuator will expand the outside limit of the test actuator. The test capacity is also increased, so the torque capacity of the torque sensor and clutch should be increased to cover two times larger than the maximum torque in the test actuator. As the electric power to the motor is increased, the power supply should be changed to provide enough electric power to generate the full amount of mechanical power. Unlike the motor, the test actuator needs a higher capacity power supply and power transformer to generate enough current for the development of the torque in the actuator.

During the operation of the actuator system, several Labview programs were used to control two electromechanical motors. The brushless DC motor in the test side controls the torque measured in the torque sensor and the brushless DC motor in the load side controls the velocity measured in an encoder. The position and velocity controls are correctly operated in both the load motor amplifier

Nonlinear Test Bed for Actuator including 100:1 ratio of gear train
• The peak torque of the test motor is 15 Nm and the maximum speed is 650 RPM. • Add a gear train, which has a 100:1 gear ratio in load motor side to test an actuator (100 times higher capacity of the actuator than the current test motor). • Replace the torque sensor. The governing torque of the test system is 100 times increased, so the allowable torque of a torque sensor should be 1500 Nm. • Bellows couplings should be replaced with a higher capacity coupling, which can endure more than 1500 Nm. However, the inertia increases 10 times than before. • Increase the size of the clutch for higher capacity. The maximum torque capacity of the Ogura clutch is 29.4 Nm. For the actuator testing, the static torque should be changed to more than 1500 Nm. • The isolated transformer should be changed for higher capacity in order to get higher torque output from the test motor. The current power capacity of the transformer is 5 kVA and it should be 10 kVA to develop the peak torque of 26 Nm. • Develop a torque control program in a closed loop. • Develop more Labview programs to provide different kind of nonlinear periodic loads.

Table 7.12: Recommendations for the improvement of NTBA

and the motion control program of the load motor. However, the torque control is not controlled in a closed loop in the motion control program of the test motor. The torque control was performed in an open loop, so the amount of torque had to be adjusted beforehand. In order to produce a more accurate torque, the torque control should be acquired in the motion control. Additionally, more motion pro-

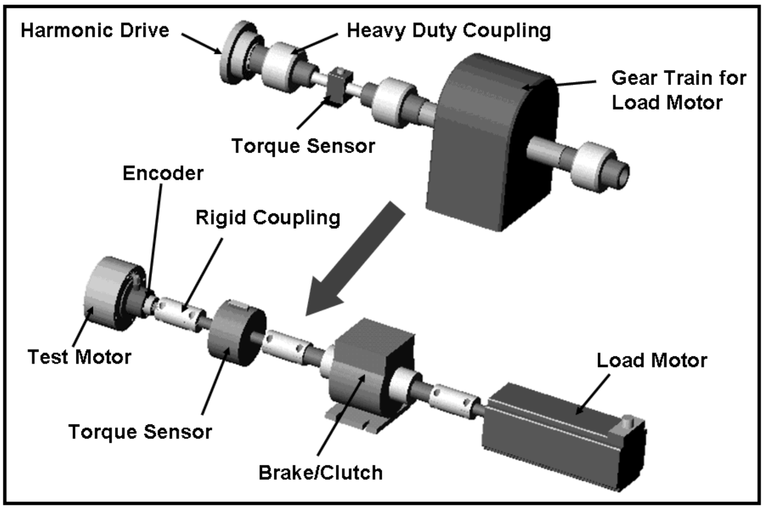

Figure 7.21: Installation of gear train in the test bed

grams should be developed to create some other types of nonlinear periodic loads using Labview. These generic loadings should be close to the realistically true loads which happen in the real application of an electromechanical motor.

7.2.3 Recommendations for Improving Development of Performance Maps

In this research, ten electromechanical motor criteria were developed. If there are more criteria to govern all other situations, more criteria should be defined in the future. Also, in this report, the test motor is a brushless DC motor, so other types of motors, such as induction AC motors, stepper motors, and switched reluctance motors, need their own performance criteria for proper operation considering all the possible situations. The following example of two different categories of how they produce torque provides why some other type of motor needs its own performance criteria. The motion of brushless DC motors is produced by the interaction of two magnetic fields, one generated by the stator and the other

Performance Maps
• More operational criteria should be defined in a permanent magnet synchronous motor as presented in Table 7.11. • Performance criteria will be defined for the actuator including gear train, bearing, clutch, and sensors. • Repeat current test regimes at the same conditions. • The same statistical analysis as the methods presented in Section 6.1.11 are used to create error bounds for nine more performance maps. • Each performance map surface has a nonlinear equation of the model developed by ARIMA time series analysis. • By improving the power supply capacity to the test motor, the performance maps developed in this research can be expanded to cover the whole range of torque and speed for the test motor. • Create performance maps with other control parameters such as current and voltage.

Table 7.13: Recommendations for the improvement of performance maps

by the rotor. Two magnetic fields, mutually coupled, produce an electromagnetic torque tending to bring the fields into alignment. On the other hand, the motion of switched reluctance motors is produced as a result of the variable reluctance in the air gap between the rotor and the stator. When a stator winding is energized, producing a single magnetic field, reluctance torque is produced by the tendency of the rotor to move to its minimum reluctance position. Because of these different working principles to produce a torque, a different type of a motor needs its own performance criteria. Likewise, an electromechanical actuator, including mainly gear train and associated bearings, needs to have performance criteria to manage the operation in a real application.

The test results developed in this research did not have enough error analysis except for the magnetic flux energy performance map. Some of the maps shown in Chapter 6 have uncertainties, so they need to have more test data to build error bound surfaces. These are operational margin, rise time, torque ripple, and magnetic flux density performance maps. Each test should be repeated using the same test protocol at the same test condition. Upper and lower error bounds are created by using the standard deviation of the test data. The test data should be large enough to follow normal distribution. Also, each performance map surface can be identified using the ARIMA time series method mentioned in Section 5.2. In this report, there is only one example to show how to find the stochastic analytic description from the test data. If a data point in a performance map needs to be identified as a function of time, the time series analysis should be applied and the governing equation obtained. However, this procedure is very tedious in order to accomplish all of the identification work for all of the data points needed. Some other method should be suggested by more research on statistics.

In addition, the isolated transformer used for the test motor has the power capacity of 5 kVA but it was not enough power to generate torque as commanded in the Labview program. The motor needs more current to develop the peak torque as referenced in the motor catalog. However, the torque is not generated because the current flowing into the motor is limited. This problem can be solved by replacing the current transformer with an isolated transformer of more than 10 kVA. The missing data shown in several performance maps can be recovered with the data developed with the new isolated transformer.

Performance Envelopes
• Decision-making algorithm should be developed to manage the operational control of an electromechanical motor. • Research some other mathematical method to normalize each performance map. • More performance envelopes can be created by joining performance maps in different sets of control parameters.

Table 7.14: Recommendations for the improvement of performance envelopes

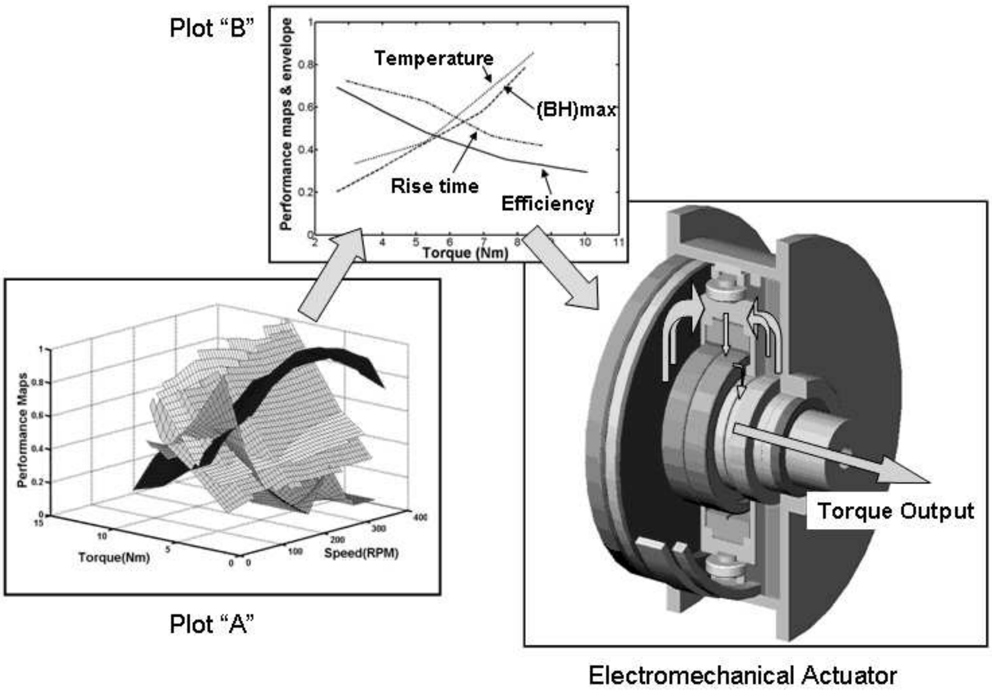

Figure 7.22: Application of the performance envelope

7.2.4 Recommendations for Improving Generation of Performance Envelopes

Engineering judgement is needed to decide optimum gain settings and determine the governing performance map in a certain control range. The decision-making system is supposed to pick the right combination of control parameters to manage all kinds of responses occurring in real situations. The operating rules in the decision-making system may be established off-line before applying them to the motor. Also, the decision-making will play the main role to decide the main reference surface in a certain operational area. As shown in Figure 7.22, four normalized performance maps are put together to develop a performance envelope (Plot "A"). The 2D plots (Plot "B") of performance maps originated from Plot "A" is a cutaway view of performance maps with respect to the torque output, T_a. If the maximum performance envelope is selected to evaluate the actuator, which is obtained from the reference of [100], as represented in Figure 7.22, the maximum surfaces out of four different performance maps are chosen with respect to torque and speed.

Based on the maximum performance envelope, the temperature performance map governs the management of torque and speed in the region of more than 6-10 Nm of the torque output, T_a. After the test motor operates at the speed of 350 RPM and the applied torque of 10 Nm, the temperature map is dominant in the region and it indicates that the temperature increases up to $80°C$ in 11 minutes. In this research, each performance map is normalized by the peak value of the overall components in the response matrix but sometimes the definition of normalization might be defined in a different way. Further research will be needed for the normalization of the performance maps. Finally, the performance envelope has been created with respect to applied torque and speed in this report, but more performance envelopes can be created based on the performance maps expressed in different control parameters such as current and voltage.

7.3 Tasks Accomplished in This Research

This report has provided a background study on electromechanical actuators, development of actuator performance criteria, a description of the fabrication of an actuator test bed, an analysis of test results using statistical tools, and the creation through extensive testing of performance maps and performance envelopes for an electromechanical actuator. The tasks accomplished in this research are as follows:

- Understood the principles for the operation of a PMSM.
- Researched the characteristics and operational range of a PMSM.
- Developed prime mover performance criteria.
- Collected position, torque, current, magnetic flux density, and temperature sensor information and determined appropriate sensors for the NTBA.
- Researched data acquisition board and micro-controller.
- Developed equations of motion for a PMSM when it was loaded. There were some references for constructing governing equations to describe the motion of a PMSM.
- Performed preliminary analysis by simulation using MATLAB.
- Used time series analysis to analyze the test data from experiments.
- Used ARIMA method to identify the governing equations of the statistical data.
- Developed and built the Nonlinear Test Bed for Actuator (NTBA).

- Developed five test regimes for an electromechanical motor.
- Performed experiments based on the test regimes using NTBA.
- Created ten performance maps based on the test data.
- Created upper and lower error bounds on the magnetic flux energy performance map using standard deviation analysis.
- Plotted a performance envelope with several parameters using four performance maps.
- Compared test results with the trade literature.

Appendices

Appendix A

General Notation for ARIMA Models

ARIMA is an acronym for AutoRegressive Integrated Moving Average. The order of an ARIMA model is usually denoted by the notation ARIMA(p,d,q), where p is the order of the autoregressive part, d is the order of the differencing, and q is the order of the moving-average process. If no differencing is done (d=0), the models are usually referred to as ARMA(p,q) models. The final model in the processing example is an ARIMA(1,1,1) model since the IDENTIFY statement specified d=1, and the final ESTIMATE statement specified p=1 and q=1 [85].

A.1 Notation for Pure ARIMA Models

Mathematically the pure ARIMA model is written as

$$W_t = \mu + \frac{\theta(B)}{\phi(B)} a_t \tag{A.1}$$

where t is indexes time, W_t is the response series, μ is the mean term, and B is the back shift operator; that is, BX_t=X_{t-1}, $\phi(B)$ is the autoregressive operator, represented as a polynomial in the back shift operator: $\phi(B)$=1-$\phi_1 B$-. . .-$\phi_p B^p$. $\theta(B)$ is the moving average operator, represented as a polynomial in the back shift operator: $\theta(B)$=1-$\theta_1 B - \ldots - \theta_q B^q$. a_t is the independent disturbance, also called the random error.

The series W_t is computed by the IDENTIFY statement and is the series processed by the ESTIMATE statement. Thus, W_t is either the response series

Y_t or a difference of Y_t specified by the differencing operators in the IDENTIFY statement. For simple differencing, W_t equals to $(1-B)^d Y_t$. For seasonal differencing W_t=$(1-B)^d(1-B^s)^D Y_t$, where d is the degree of nonseasonal differencing, D is the degree of seasonal differencing, and s is the length of the seasonal cycle [85]. For example, the mathematical form of the ARIMA(1,1,1) model estimated in the processing example is

$$(1-B)Y_t = \mu + \frac{(1-\theta_1 B)}{(1-\phi_1 B)} a_t \tag{A.2}$$

A.2 Notation for Seasonal Models

ARIMA models for time series with regular seasonal fluctuations often use differencing operators and autoregressive and moving average parameters at lags that are multiples of the length of the seasonal cycle. When all the terms in an ARIMA model factor refer to lags that are a multiple of a constant S, the constant is factored out and suffixed to the ARIMA(p,d,q) notation [85].

Thus, the general notation for the order of a seasonal ARIMA model with both seasonal and nonseasonal factors is ARIMA$(p, d, q) \times (P, D, Q)_S$. The term ($p$,$d$,$q$) gives the order of the nonseasonal part of the ARIMA model; the term $(P, D, Q)_S$ gives the order of the seasonal part. The value of S is the number of observations in a seasonal cycle. For example, the notation ARIMA$(1, 1, 2) \times (0, 1, 1)_{12}$ describes a seasonal ARIMA model with the following mathematical form:

$$(1-B)(1-B^{12})Y_t = \mu + \frac{(1-\theta_{1,1}B-\theta_{1,2}B^2)(1-\theta_{2,1}B^{12})}{(1-\phi_1 B)} a_t \tag{A.3}$$

Appendix B

Labview programs to control the Nonlinear Test Bed

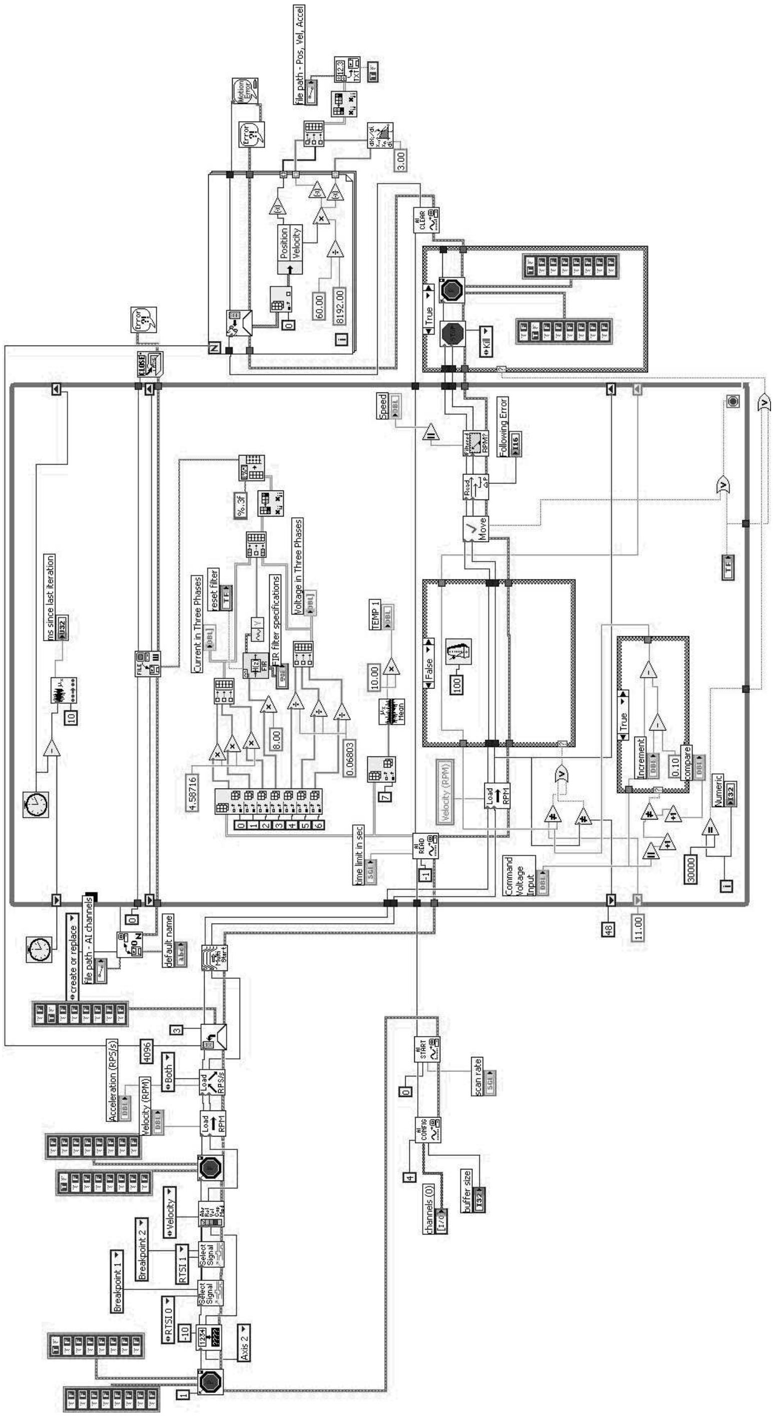

Figure B.1: Load motor control for acceleration test

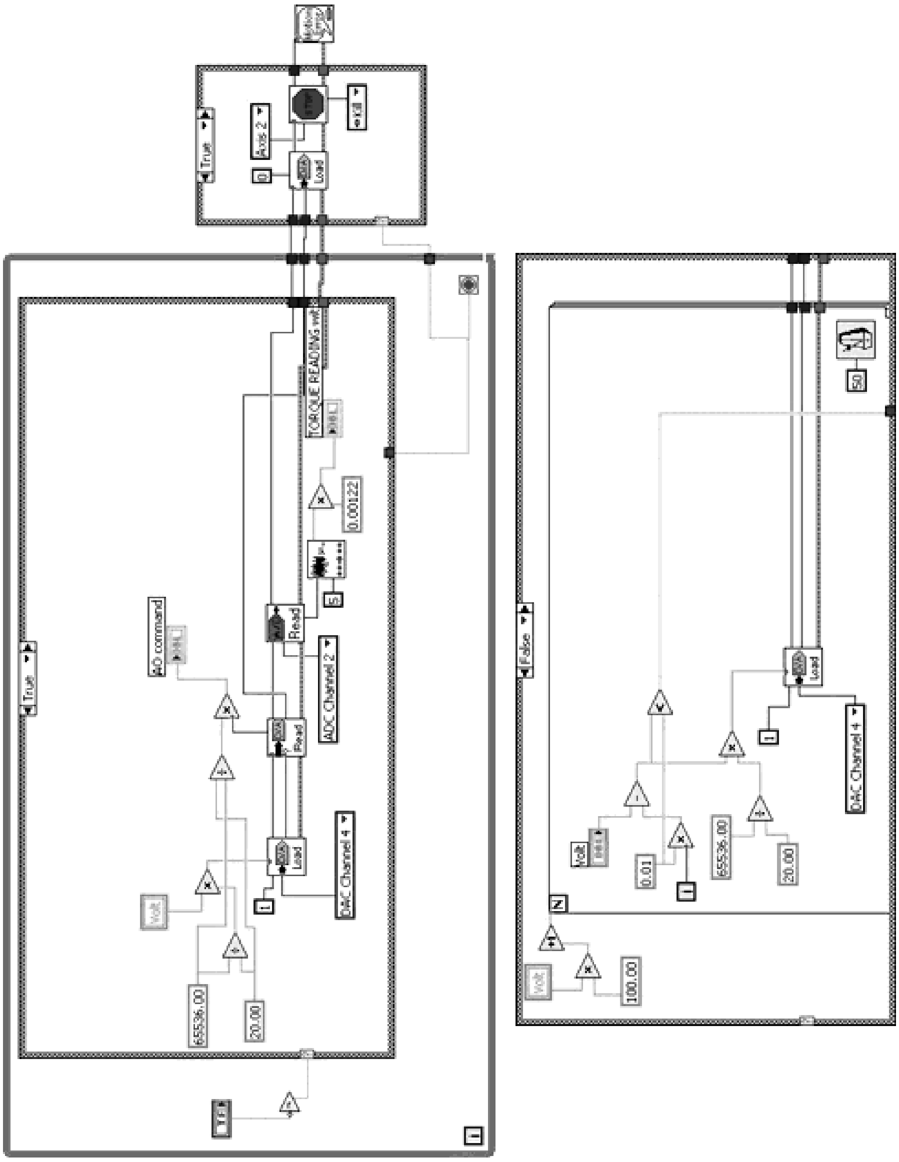

Figure B.2: Hysteresis brake control for acceleration test

Bibliography

[1] A. K. Adnanes, “Torque Analysis of Permanent Magnet Synchronous Motors”, IEEE Power Electronics Specialists Conference, PESC ’91 Record, 22nd Annual, pp. 695–701, 1991.

[2] Advanced Motion Controls, *PWM Servo Amplifiers - Engineering Notes*, AMC 1999-2000 Catalog and Technical Manual, California, 2000.

[3] I. Arsie, M. Gambino, C. Pianese, and G. Rizzo, “Development and Validation of Hierarchical Models for the Design of Engine Control Strategies”, Meccanica, Kluwer Academic Publishers, Vol. 32, pp. 397–408, 1997.

[4] A. V. Arvallo and D. Tesar, “Condition-Based Maintenance of Actuator Systems Using a Model-Based Approach”, Ph.D. Dissertation, University of Texas at Austin, 2000.

[5] K. J. Astrom and B.Wittenmark, *Adaptive Control*, Addison Wesley, 1995.

[6] K. Atallah, Z. Q. Zhu, and D. Howe, “The Prediction of Iron Losses in Brushless Permanent Magnet DC Motors”, International Conference on Electrical Machines (ICEM92), Manchester, England, pp. 814–818, 1992.

[7] R. E. Baker and E. E. Daby, “Engine Mapping Methodology”, International Automotive Engineering Congress and Exposition, SAE Technical Paper 770077, 1977.

[8] R. Carlson, A. A. Tavares, J. P. Bastos, and M. Lajoie-Mazenc, "Torque Ripple Attenuation in Permanent Magnet Synchronous Motors", IEEE Industry Applications Society Annual Meeting, Vol. 1, pp. 57–62, 1989.

[9] Bodine Electric, *DC Technical Information*, Catalog S-15, Chicago, IL.

[10] B. K. Bose, *Power Electronics and AC Drives*, Prentice Hall, 1986.

[11] A. Bousbaine, "Thermal Modelling of Induction Motors Based on Accurate Loss Density Distribution", Electric Machines and Power Systems, Vol. 27, pp. 311–324, 1999.

[12] G. E. P. Box, G. M. Jenkins, and G. C. Reinsel, *Time Series Analysis*, Pearson Education, 1994.

[13] P. J. Brockwell and R. A. Davis, *Introduction to Time Series and Forecasting*, Springer, 2001.

[14] B. Campbell and J. Galleno, "Motor Life: The Effects of Loading, Service Factor and Temperature Rise on Insulation Life", IEEE Annual Petroleum and Chemical Industry Conference, pp. 303–310, September 1998.

[15] T. F. Chen, D. W. Lee and C. K. Sung, "An Experimental Study on Transmission Efficiency of a Rubber V-Belt CVT", Mechanism and Machine Theory, Vol. 33, No. 4, pp. 351–363, 1998.

[16] S. Chen, C. Namuduri, and S. Mir, "Controller Induced Parasitic Torque Ripples in a PM Synchronous Motor", IEEE Transactions on Industry Applications, Vol. 38, No. 5, pp. 1273–1281, September/October 2002.

[17] W. H. Chen, D. J. Ballance, P. J. Gawthrop, and J. O'Reilly, "A Nonlinear Disturbance Observer for Robotic Manipulators", IEEE Transactions on Industrial Electronics, Vol. 47, No. 4, pp. 932–938, August 2000.

[18] K. A. Corzine, B. T. Kuhn, S. D. Sudhoff, and H. J. Hegner, "An Improved Method for Incorporating Magnetic Saturation in the q-d Synchronous Machine Model", IEEE Transactions on Energy Conversion, Vol. 13, No. 4, pp. 270–938, August 2000.

[19] M. R. Cuddy and K. B. Wipke, "Analysis of the Fuel Economy Benefit of Drivetrain Hybridization", SAE International Congress and Exposition Paper 970289, National Renewable Energy Lab., 1997.

[20] B. D. Cullity, *Introduction to Magnetic Materials*, Addison Wesley, Menlo Park, California, 1972.

[21] F. Deng, "An Improved Iron Loss Estimation for Permanent Magnet Brushless Machines", IEEE Transactions on Energy Conversion, Vol. 14, No. 4, pp. 1391–1395, December 1999.

[22] M. Van Doren and D. Tesar, "Criteria Development to Support Decision Making Software for Modular, Reconfigurable Robotic Manipulators", M.S. Thesis, University of Texas at Austin, 1992.

[23] R. C. Dorf and R. H. Bishop, *Modern Control Systems*, Addison Wesley, 1995.

[24] W. Drafts, *Acoustic Wave Technology Sensors*, Sensors Magazine, October, 2000.

[25] A. E. Fitzgerald, C. Kingsley and S. D. Umans, *Electric Machinery*, McGraw Hill, London, 1992.

[26] Galil Motion Control, *Sinusoidal commutation of brushless motors*, Application Note #3414, Rocklin, CA, 2002.

[27] D. Gray, *American Institute of Physics Handbook*, New York, 1972.

[28] A. A. Golverk, “Mathematical Calculation of the Performance Map of Internal Combustion Engine”, SAE Technical Paper 920683, 1992.

[29] A. A. Golverk, “The Method for Development of a Diesel Engine Universal Performance Map”, SAE Technical Paper 941928, 1994.

[30] A. A. Golverk, “Diesel Engine Performance Maps under Variable Loading”, ASME Internal Combustion Engine Division Spring Technical Conference, pp. 1–12, 1995.

[31] D. Grenier, L. Dessaint, O. Akhrif, Y. Bonnassieux, and B. Le Pioufle, “Experimental Nonlinear Torque Control of a Permanent-Magnet Synchronous Motor Using Saliency”, IEEE Transactions on Industrial Electronics, Vol. 44, No. 5, pp. 680–687, October 1997.

[32] S. G. Grupinski and D. Tesar, “Design of Low Cost Robotic Actuators for a Modular, Reconfigurable Six Degree-of-Freedom Robotic Manipulator”, M.S. Thesis, Dept. of Mechanical Engineering, The University of Texas at Austin, 1997.

[33] D. C. Hanselman, “Minimum Torque Ripple, Maximum Efficiency Excitation of Brushless Permanent Magnet Motors”, IEEE Transactions on Industrial Electronics, Vol. 41, No. 3, pp. 292–300, June 1994.

[34] Parker Hannifin, *Servo Motors BE Series Catalog 8000-4*, Parker Hannifin Corporation, CA.

[35] N. Hemati, “Modeling, Analysis, and Tracking Control of Brushless DC Motors for Robotic Applications”, Ph.D. Dissertation, Cornell University, 1988.

[36] N. Hemati, “A Complete Model Characterization of Brushless DC Motors”, IEEE Transactions on Industry Applications, Vol. 28, No. 1, pp. 172–180, 1992.

[37] Honeywell, *Technical Report for Hall Current Sensor*, Honeywell Inc.

[38] S. L. Ho, A. N. K. Nam, C. T. Tse, and T. K. Ho, “Thermal Studies of DC Traction Motors”, IEE International Conference on Developments in Mass Transit Systems, pp. 161–166, April 1998.

[39] H. Hochschwarzer, “Fully Automatic Determination and Optimization of Engine Control Characteristics”, SAE Technical Paper 920255, 1992.

[40] J. Holtz and L. Springob, “Identification and Compensation of Torque Ripple in High-Precision Permanent Magnet Motor Drives”, IEEE Transaction on Industrial Electronics, Vol. 43, No. 2, pp. 309–320, 1996.

[41] J. S. Hsu, J. D. Kueck, M. Olszewski, Don A. Casada, and L. M. Tolbert , “Comparison of Induction Motor Field Efficiency Evaluation Methods”, IEEE Transaction on Industry Applications, Vol. 34, No. 1, pp. 117–125, 1998.

[42] P. Hvass and D. Tesar, “Intelligent Actuator Condition Based Maintenance”, M.S. Thesis, Dept. of Mechanical Engineering, The University of Texas at Austin, August 2004.

[43] IEEE Power Engineering Society, *IEEE Standard Test Procedure for Polyphase Induction Motors and Generators*, IEEE Std 112, 1996.

[44] R. A. Johnson and D. W. Wichern, *Applied Multivariate Statistical Analysis*, Prentice Hall International, 1998.

[45] J. Jung and K. Nam, "A Vector Control Scheme for EV Induction Motors with a Series Iron Loss Model", IEEE Transactions on Industrial Electronics, Vol. 45, No. 4, pp. 617–625, August 1998.

[46] S. Kang, D. J. Cox, and D. Tesar, "Design of Actuator Endurance and Reliability Test Bed", Proceedings of ASME DETC'00, Design Engineering Technical Conferences, Baltimore, MD, 2000.

[47] Kollmorgen and Danaher Motion, *Brushelss Motors and Drive Systems*, Kollmorgen Inland Motor Handbook, Virginia.

[48] P. C. Krause, O. Wasynczuk, and S. D. Sudhoff, *Analysis of Electric Machinery*, IEEE Press, New York, 1994.

[49] B. C. Kuo and J. Tal, *DC Motors and Control Systems*, SRL Publishing Company, Champaign, Illinois, 1978.

[50] K. Kuribayashi, "Criteria for the Evaluation of New Actuators as Energy Converters", Journal of Advanced Robotics, VSP and Robotics Society of Japan, Vol. 7, No. 4, pp. 289–307, 1993.

[51] D. Le and D. Tesar, "Development and Integration of a Fault Tolerance Test Bed Environment for Space Application", M.S. Thesis, Dept. of Mechanical Engineering, The University of Texas at Austin, 1997.

[52] S. Liu, "An On-line Reference-Trajectory Generator for Smooth Motion of Impulse-Controlled Industrial Manipulators", IEEE 7th International Workshop on Advanced Motion Control, pp. 365–370, July 2002.

[53] Z. J. Liu, D. Howe, P. H. Mellor, and M. K. Jenkins, "Coupled Thermal and Electromagnetic Analysis of a Permanent Magnet Brushless DC Servo Motor", IEEE 6th International Conference on Electrical Machines and Drives, pp. 631–635, September 1993.

[54] C. Mademlis and V. G. Agelidis, "On Considering Magnetic Saturation with Maximum Torque to Current Control in Interior Permanent Magnet Synchronous Motor Drives", IEEE Transactions on Energy Conversion, Vol. 16, No. 3, pp. 246–252, September 2001.

[55] Magtrol Inc., *Hysteresis Brake Metric Product Guide*, Technical Note in Magtrol Inc., www.magtrol.com

[56] M. Marrs and D. Tesar, "Design of an Advanced, High-Precision. Seven Degree-of-Freedom Modular Robotic Manipulator", M.S. Thesis, Dept. of Mechanical Engineering, The University of Texas at Austin, 1997.

[57] C. Meskell and J. A. Fitzpatrick, "Errors in Parameter Estimates from the Force State Mapping Technique for Free Response Due to Phase Distortion", Journal of Sound and Vibration, Vol. 252, No. 5, pp. 967–974, 2002.

[58] H. M. B. Metwally, "Loadless Full Load Temperature Rise Test for Three Phase Induction Motors", Journal of Energy Conversion and Management, Vol. 42, No. 2001, pp. 519–528, August 2000.

[59] C. Mi, G. Slemon, and R. Bonert, “Modeling of Iron Losses of Surface-Mounted Permanent Magnet Synchronous Motors”, IEEE Industry Applications Conference, Thirty-Sixth IAS Annual Meeting, Vol. 4, No. 4, pp. 2585–2591, September-October 2001.

[60] H. Moghbelli, G. E. Adams, and R. G. Hoft, “Performance of a 10-Hp Switched Reluctance Motor and Comparison with Induction Motors”, IEEE Transactions on Industry Applications, Vol. 27, No. 3, pp. 531–538, May/June 1991.

[61] R. Monajemy, and R. Krishnan, “Control and Dynamics of Constant-Power-Loss-Based Operation of Permanent-Magnet Synchronous Motor Drive System”, IEEE Transactions on Industrial Electronics, Vol. 48, No. 4, pp. 839–844, August 2001.

[62] R. Monajemy, and R. Krishnan, “Performance Comparison for Six-Step Voltage and Constant Back EMF Control Strategies for PMSM”, IEEE Industry Applications Conference, Thirty-Fourth IAS Annual Meeting, Vol. 1, pp. 165–172, October 1999.

[63] S. Morimoto, Y. Tong, Y. Takeda, and T. Hirasa, “Loss Minimization Control of Permanent Magnet Synchronous Motor Drives”, IEEE Transactions on Industrial Electronics, Vol. 41, No. 5, pp. 511–517, October 1994.

[64] J. B. Morrell and K. Salisbury, “Performance Measurements for Robotic Actuators”, Proceedings of the ASME Dynamics Systems and Control Division, Vol. 58, pp. 531–537, 1996.

[65] R. L. Nailen, “Can Field Tests Prove Motor Efficiency?”, IEEE Transactions on Industry Applications, Vol. 25, No. 3, pp. 391–396, May 1989.

[66] National Instruments, *Measurement and Automation Catalog*, Austin, TX, 2003.

[67] C. Neumeyer, M. Awad, E. Baker, G. Bronner, and S. Ramakrishnan, “Load Monitor for TFTR Motor-Generator Sets”, IEEE Thirteenth Symposium on Fusion Engineering, Vol. 1, pp. 439–442, October 1989.

[68] R. W. Newton, R. E. Betz, and H. B. Penfold, “A Dynamic Dynamometer for Testing Variable Speed Drives”, IEEE Conference of Industry Applications Society Annual Meeting, Vol. 1, pp. 538–544, 1994.

[69] Ogura Clutch Company, *Ogura Electromagnetic Clutches and Brakes*, Technical Note in Ogura Industrial Corp.

[70] C. H. Onder and H. P. Geering, “Model-Based Engine Calibration for Best Fuel Efficiency”, Engine and Multidimensional Engine Modeling, SAE SP-1101, pp. 213–220, 1995.

[71] C. M. Ong, *Dynamic Simulation of Electric Machinery*, Prentice Hall, New Jersey, 1998.

[72] G. Paganelli, G. Ercole, A. Brahma, Y. Guezennec, and G. Rizzoni, “A General Formulation for the Instantaneous Control of the Power Split in Charge-Sustaining Hybrid Electric Vehicles”, Proc. of AVEC 2000, 5th International Symposium on Advanced Vehicle Control, Michigan, pp. 73–80, August 2000.

[73] G. Paganelli, G. Ercole, A. Brahma, Y. Guezennec, and G. Rizzoni, "General Supervisory Control Policy for the Energy Optimization of Charge-Sustaining Hybrid Electric Vehicles", SAE of Japan (JSAE) Review, Vol. 22, pp. 511–518, 2001. [13]

[74] R. J. Parker, *Advances in Permanent Magnetism*, John Wiley & Sons, New York, 1990.

[75] P. Pillay and K. Ramu, "Modeling Simulation and Analysis of Permanent Magnet Synchronous and Brushless DC Motor Drives", Ph.D. Dissertation, Virginia Polytechnic Institute and State University, 1987.

[76] P. Pillay, "Modeling, Simulation, and Analysis of Permanent-Magnet Motor Drives, Part I: The Permanent-Magnet Synchronous Motor Drive", IEEE Transactions on Industry Applications, Vol. 25, No. 3, pp. 265–273, 1989.

[77] Quality Thermisters, Inc., *NTC High Temperature Thermistors*, Application Note, http://www.thermistor.com/catalog/catlog09.htm, 2002.

[78] M. F. Rahman, and L. Zhong, "Comparison of Torque Responses of the Interior Permanent Magnet Motor Under PWM Current and Direct Torque Controls", The 25th Annual Conference of IEEE Industrial Electronics Society, IECON'99, pp. 1464–1470, December 1999.

[79] L. Ray, J. Townsend, and A. Ramasubramanian, "Optimal filtering and Bayesian detection for friction-based diagnostics in machines", ISA transactions, Elsevier Science, Vol. 40, pp. 207–221, 2001.

[80] J. Reinert, R. Inderka, M. Menne, and R. W. Doneker, “Optimizing Performance in Switched-Reluctance Drives”, IEEE Industry Applications Magazine, pp. 63–70, July/August 2000.

[81] Reliance Electric, *AC Motor Efficiency Guide - Part 7: A Motor as Part of a System*, Rockwell Automation, 2001.

[82] G. Rizzoni, L. Guzzella, and B. Baumann, “Unified Modeling of Hybrid Electric Vehicle Drivetrains”, IEEE/ASME Transactions on Mechatronics, Vol. 4, No. 3, pp. 246–257, 1999.

[83] Rockwell Automation and Electro-Craft, *DC Motors Speed Controls Servo Systems*, The Electro-Craft Engineering Handbook, 5th Edition, Minnesota.

[84] M. Sagawa, S. Fujimura, N. Togawa, H. Yamamoto, and Y. Matsuura, “New Material for Permanent Magnets on a Base of Nd and Fe”, Journal of Applied Physics, Vol. 55, No. 6, pp. 2083–2087, 1984.

[85] SAS Institute, *SAS/ETS User's Guide*, Ver. 8, SAS Publications, 1999.

[86] T. Sebastian, “Temperature Effects on Torque Production and Efficiency of PM Motors Using Nd-Fe-B Magnets”, IEEE Transactions on Industry Applications, Vol. 31, No. 2, pp. 353–357, March/April 1995.

[87] T. Sebastian and V. Gangla, “Analysis of Induced EMF Waveforms and Torque Ripple in a Brushless Permanent Magnet Machine”, IEEE Transactions on Industry Applications, Vol. 32, No. 1, pp. 195–200, January/February 1996.

[88] K. L. Shi, T. F. Chan, Y. K. Wong, and S. L. Ho, "A Rule-Based Acceleration Control Scheme for an Induction Motor", IEEE Transactions on Energy Conversion, Vol. 17, No. 2, pp. 254–258, June 2002.

[89] G. Sieros, A. Stamatis, and K. Mathioudakis, "Jet Engine Component Maps for Performance Modeling and Diagnosis", Journal of Propulsion and Power, Vol. 13, No. 5, pp. 665–674, 1997.

[90] G. R. Slemon, "On the Design of High Performance PM Motors", IEEE Conference of Industry Applications Society Annual Meeting, Vol. 1, pp. 279–285, October 1992.

[91] G. R. Slemon and X. Liu, "Core Losses in Permanent Magnet Motors", IEEE Transactions on Magnetics, Vol. 26, No. 5, pp. 1653–1655, September 1990.

[92] G. R. Slemon, *Electric Machines*, Addison-Wesley Publishing Company, Reading, Massachusetts, 1980.

[93] J. E. Slotine and W. Li, *Applied Nonlinear Control*, Prentice Hall, 1991.

[94] C. Smith and S. Jacobsen, "Design and Control of Electromechanical Actuation Systems", Modeling And Control of Compliant and Rigid Motion Systems, ASME, Vol. 31, pp. 137–144, 1991.

[95] T. Sokira, *Brushless DC Motors Electronic Commutation and Controls*, New York, TAB, 1990.

[96] G. C. D. Sousa, B. K. Bose, J. Cleland, R. J. Spiegel, and P. J. Chappell, "Loss Modeling of Converter Induction Machine System for Variable Speed

Drive", Proceedings of the International Conference on Industrial Electronics, Control, Instrumentation, and Automation, Vol. 1, pp. 114–120, San Diego, CA, November 1992.

[97] S. P. Stevens, P. J. Shayler, and T. H. Ma, "Experimental Data Processing Techniques to Map the Performance of a Spark Ignition Engine", Proceedings of the Institute of Mechanical Engineer, Part D, Journal of automobile engineering, Vol. 209, pp. 297–306, 1995.

[98] D. A. Stone, T. S. Birch, and K. N. Leonard, "A Versatile Computer Controlled Dynamometer Test System", Symposium on Power Electronics, Electrical Drives, Advanced Electrical Motors, pp. 353–358, 1994.

[99] J. Swevers, W. Verdonck, B. Naumer, S. Peiters, and E. Biber, "An Experimental Robot Load Identification Method for Industrial Application", International Journal of Robotics Research, Vol. 21, No. 8, pp. 701–712, August 2002.

[100] D. Tesar, *Electro-Mechanical Actuator Architecture*, Technical report in Robotics Research Group, Dept. of Mechanical Engineering, The University of Texas at Austin, 2001.

[101] D. Tesar, "Human Scale Intelligent Mechanical Systems", Proceedings of the 11th World Congress in Mechanism and Machine Science, China, 2003.

[102] M. Thomas and D. Tesar, "Dynamic Modeling of Serial Manipulator Arms", ASME Journal of Dynamic Systems, Measurement and Control, September, Vol. 104, No. 9, pp. 218–228, 1982.

[103] Torqsense, *Non-Contact Rotary Torque Measurement*, Wen Technology Inc., 2000.

[104] N. Urasaki,T. Senjyu, and K. Uezato, “An Accurate Modeling for Permanent Magnet Synchronous Motor Drives”, Applied Power Electronics Conference and Exposition, APEC 2000. Fifteenth Annual IEEE, Vol. 1, pp. 387–392, February 2000.

[105] H. Woodson and J. Melcher, *Electromechanical Dynamics*, Krieger Publishing Company, Florida, 1990.

[106] L. Xu, Z. Zhu and D. Howe, “Acoustic Noise Radiated from Direct Torque Controlled Induction Motor Drives”, IEE Proceedings of Electric Power Applications, Vol. 147, pp. 491–496, November 2000.

[107] G. Zhang, and J. Furusho, “Control of Robot Aims Using Joint Torque Sensors”, IEEE Control Systems Magazine, Vol. 18, No. 1, pp. 48–55, 1998.

Vita

Jae Gu Yoo was born on November, 14, 1969 in Kunsan, South Korea, the son of Mr. Chowoong Yoo and Mrs. Okjoo Oh. Upon completing the high school at Seoul, South Korea in February 1988, he then attended Sungkyunkwan University in Seoul, Korea. He received his B.S. degree in February 1994 from the Mechanical Engineering Department with high honors. He obtained his M.S. degree at the Mechanical Engineering at the University of Michigan at Ann Arbor in December 1997 with research in Control and Manufacturing. He joined the Robotics Research Group and started the Ph.D. program under the supervision of Prof. Delbert Tesar at the Mechanical Engineering Department at the University of Texas at Austin, in Spring 1998.

Permanent address: 11215 Research Blvd. #1111, Austin, TX 78759

This dissertation was typeset with LaTeX[†] by the author.

[†] LaTeX is a document preparation system developed by Leslie Lamport as a special version of Donald Knuth's TeX Program.